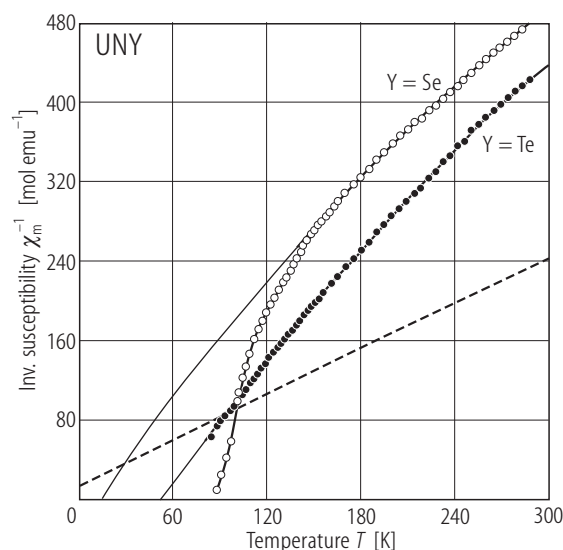


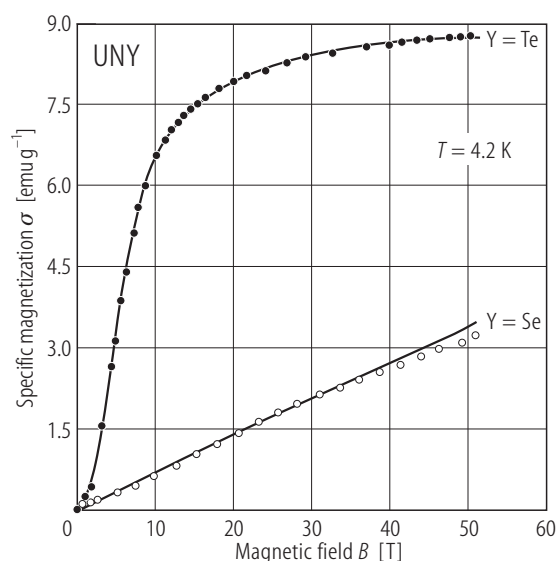
## 1.3.3.3.2 Figures and tables



**Fig. 1.** UNY, Y = Se, Te. Reciprocal molar magnetic susceptibility,  $\chi_m^{-1}$ , vs. temperature,  $T$  [87T]. Open circles: UNSe; full circles: UNTe. UNTe is a ferromagnet with  $T_C = 55$  K (see Fig. 3). UNSe does not order magnetically down to 4.2 K, though a magnetic phase transition could be suggested by a strong curvature of  $\chi_m^{-1}(T)$  near 90 K. The

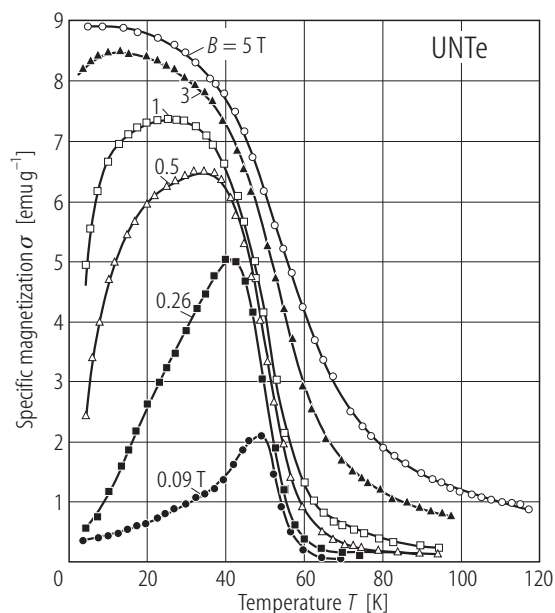
solid lines are fits to the formula  $\chi_m^{-1} = \left( \frac{A}{T} + B \right)^{-1} + \lambda$

with the parameters given in Table E. The dashed curve represents  $\chi_m^{-1}(T)$  calculated for both compounds using the crystal field parameters from Ref. [86ABBG] (see Table D).



**Fig. 2.** UNY, Y = Se, Te. Specific magnetization,  $\sigma$ , vs. magnetic field,  $B$ , measured at  $T = 4.2$  K [87T]. Open circles: UNSe; full circles: UNTe. Note a straight-line behaviour of  $\sigma(B)$  for UNSe, which indicates a paramagnetic ground state. The magnetization isotherm of UNTe shows a distinct tendency to saturation yielding the magnetic moment of  $0.65 \mu_B$ . See also Fig. 3.

**Fig. 3.** UNTe. Specific magnetization,  $\sigma$ , vs. temperature,  $T$ , measured in several different magnetic fields specified in the figure [87T]. The compound orders ferromagnetically at  $T_C = 55$  K. Note characteristic maxima, which broaden with increasing  $B$ , signaling a large magnetocrystalline anisotropy of the compound studied.



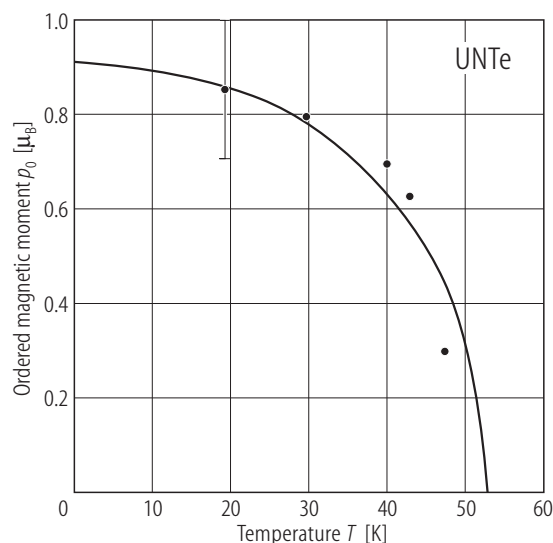


**Fig. 4.** UNTe. Ordered magnetic moment,  $p_o$ , vs. temperature,  $T$ , as determined by neutron powder diffraction (points; the error bar applies to all the data) and calculated from a perturbative crystal field model (solid curve) [86ABBG]. For description of the CF model see the original paper. The crystal field parameters used:  $B_2^0 = 7.326 \text{ cm}^{-1}$ ,  $B_4^0 = 0.3677 \text{ cm}^{-1}$ ,  $B_6^0 = 0.5279 \cdot 10^{-2} \text{ cm}^{-1}$ ,  $B_4^4 = 2.561 \text{ cm}^{-1}$ ,  $B_6^4 = -0.7843 \cdot 10^{-1} \text{ cm}^{-1}$ . The compound orders ferromagnetically at  $T_C = 52(3) \text{ K}$ . The ordered moment observed at 20 K is  $0.85(16) \mu_B$ . The CF model applied gives a singlet  $\Gamma_{14}$  as a ground state and a doublet  $\Gamma_{15}$  as a first excited state, separated by  $\Delta/k_B = 78 \text{ K}$ . The remaining crystal field levels originating from the  $^3H_4$  ground multiplet split in a tetragonal crystal field potential are located above 1000 K. For other crystal field models see Table D.

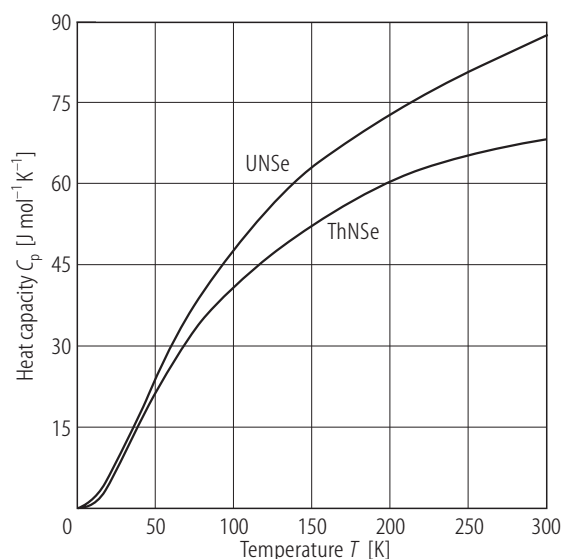


**Fig. 5.** UNSe. Heat capacity,  $C_p$ , vs. temperature,  $T$ , as compared to ThNSe [86ABBG]. The uranium compound remains paramagnetic down to 5 K. Note a very large difference between the two curves, ascribed by the authors to an enhanced electronic contribution ( $\gamma = 60 \text{ mJ/mol K}^2$ ). See the low temperature heat capacity data in Fig. 7 and the main thermodynamic characteristics given in Table C. For the crystal field model accounting for the thermodynamic and magnetic properties of UNTe refer to Table D.

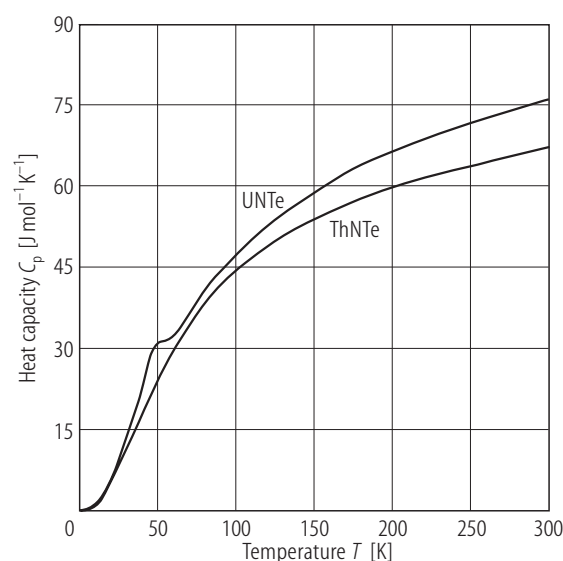


**Fig. 6.** UNTe. Heat capacity,  $C_p$ , vs. temperature,  $T$ , as compared to ThNTe [86ABBG]. Note that the ferromagnetic phase transition in UNTe at  $T_C = 52 \text{ K}$  (see Fig. 4) manifests itself not as a  $\lambda$ -shaped peak but only as a hump with  $C_p = 31.2 \text{ J/mol K}$ . The estimated entropy due to 5f electrons is of the order of  $7 \text{ J/mol K}$ . See the low temperature heat capacity data in Fig. 7 and the main thermodynamic characteristics given in Table C. For the crystal field model accounting for the thermodynamic and magnetic properties of UNTe refer to Fig. 4 and Table D.

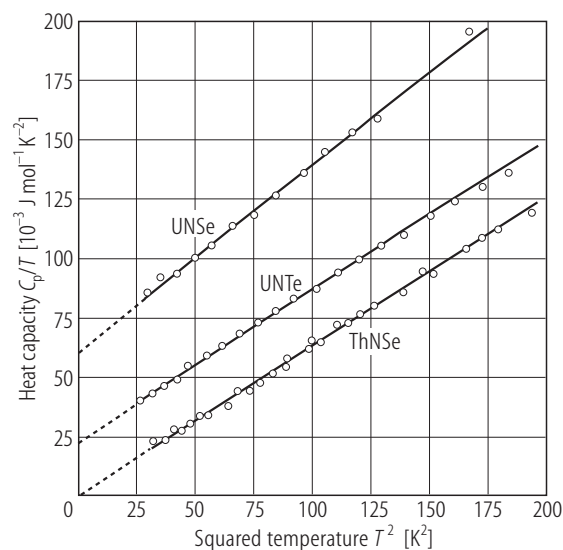


**Fig. 7.** UNY, Y = Se, Te. Low temperature heat capacity in the form  $C_p/T$  vs.  $T^2$  [86ABBG]. For comparison the data for ThNSe are also presented. The lines correspond to the dependence  $C_p = \gamma T + \beta T^3$  with the parameters given in Table C.

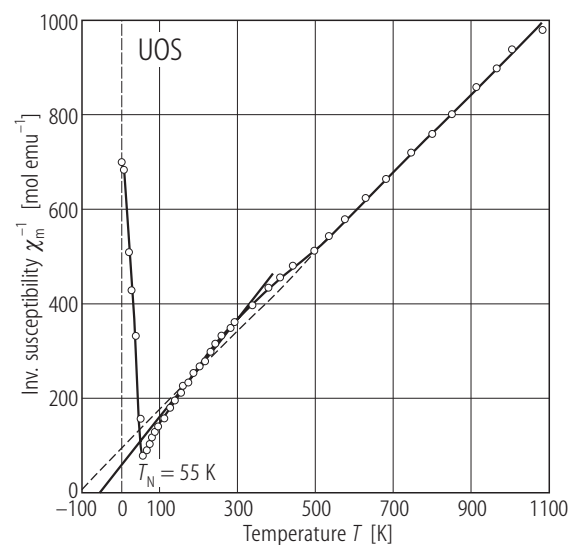


**Fig. 9.** UOS. Reciprocal molar magnetic susceptibility,  $\chi_m^{-1}$ , vs. temperature,  $T$  up to 1100 K [63BBP]. The compound orders antiferromagnetically at  $T_N = 55$  K. Note an inflection in  $\chi_m^{-1}(T)$  at about 450 K, the occurrence of which was explained in [63ABR] in terms of crystal field effect. The dashed and solid lines represent Curie-Weiss fits with the parameters given in Table B. From the value of the susceptibility when  $T \rightarrow 0$  the authors estimated the magnitude of the first anisotropy constant:  $K_1 \approx 7.5 \cdot 10^7$  erg/g.

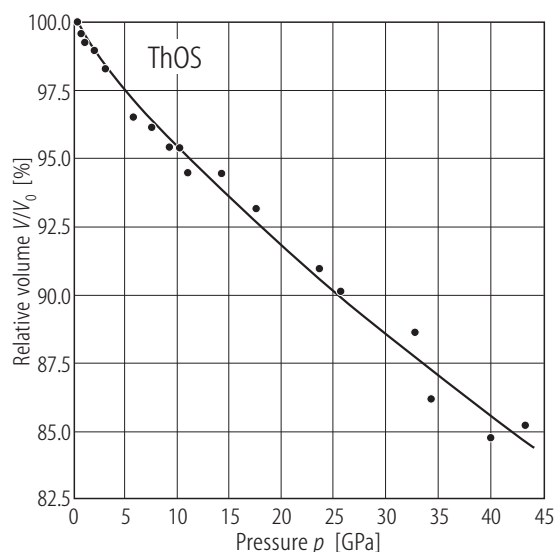


**Fig. 8.** ThOS. Relative volume,  $V/V_0$ , vs. pressure,  $p$ , up to 43.3 GPa [91GGBG]. Note that no phase transformation is observed.  $B_0 = 201.5$  GPa,  $B_0' = 3.0$ .

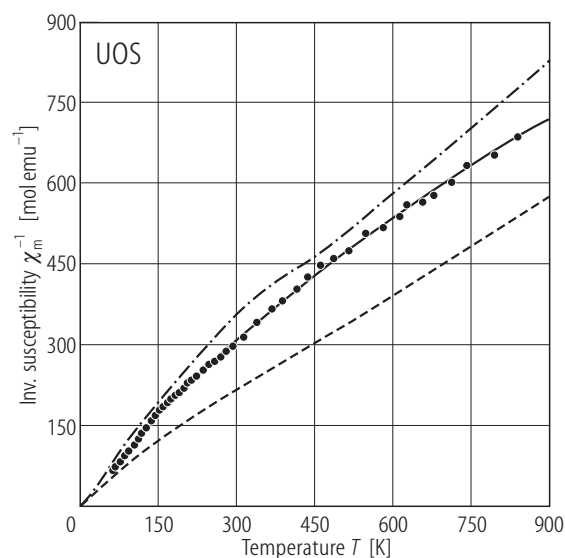


**Fig. 10.** UOS. Reciprocal molar magnetic susceptibility,  $\chi_m^{-1}$ , vs. temperature,  $T$ , up to 800 K [87T]. For comparison the experimental data from Ref. [63BBP] (see Fig. 9) are presented by the dash-dotted curve. The solid line is a fit of the susceptibility to the equation:

$$\chi_m = \frac{a/T + b - c \exp(-d/T)}{2 + \exp(-d/T)}, \text{ appropriate for the}$$

assumption of a doublet-singlet system of the crystal field levels, with the parameters:  $a = 1.00$  K emu/mol,  $b = 7.6 \cdot 10^{-3}$  emu/mol,  $c = 6.4 \cdot 10^{-3}$  emu/mol,  $d = 244$  K. For explanation see the original paper. The dashed curve represents  $\chi_m^{-1}(T)$  calculated using the crystal field parameters from Ref. [84ABCH] (see Table G).

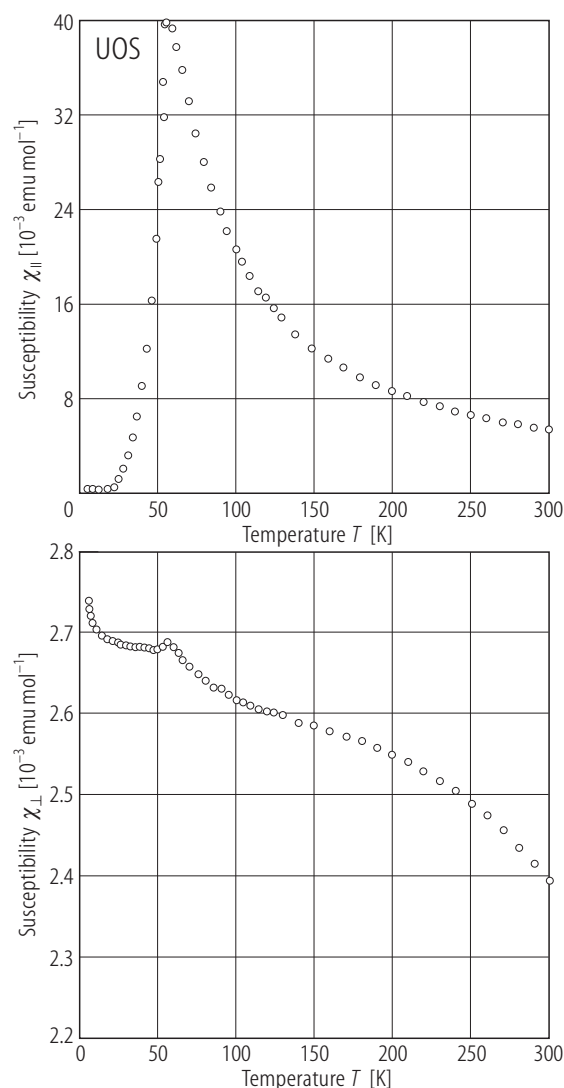


**Fig. 11.** UOS. Longitudinal,  $\chi_{||}$ , (upper panel) and transverse,  $\chi_{\perp}$ , (lower panel) molar magnetic susceptibility vs. temperature,  $T$ , measured on a single crystal in an applied magnetic field of 0.4 T [95ABBC]. The compound orders antiferromagnetically at  $T_N = 55$  K. For analysis of the susceptibility in terms of crystal field effect see Fig. 21a.

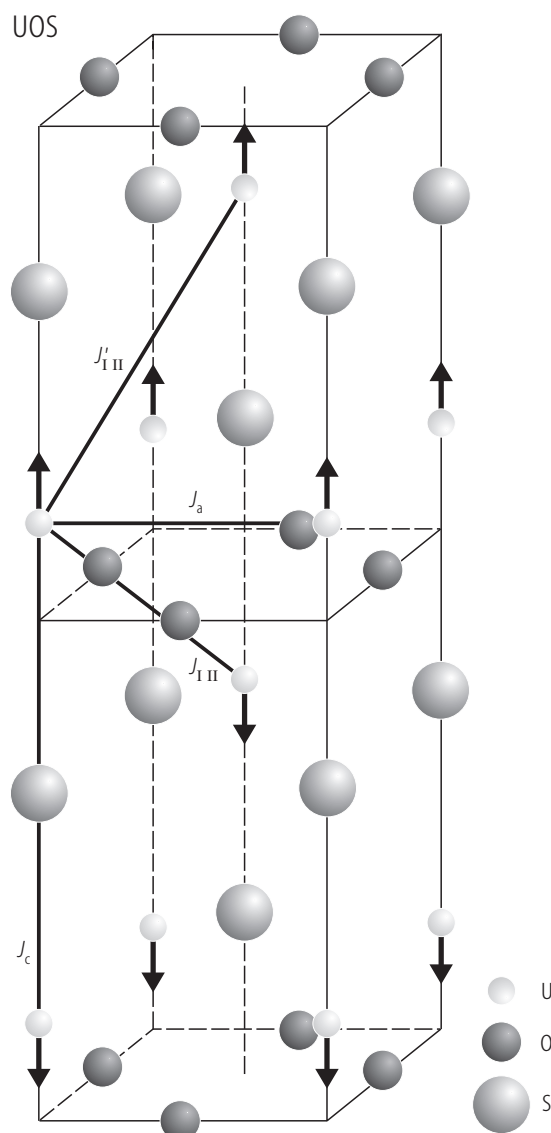


**Fig. 12.** UOS. Magnetic structure [63BBP]. The arrows indicate the direction of the uranium magnetic moments. The magnetic unit cell is doubled along the  $c$ -axis with respect to the chemical one [ $\mathbf{k} = (0,0,\frac{1}{2})$ ]. The moments are coupled ferromagnetically within the (001) planes, point along the  $c$ -axis with the sequence  $++--$ . The ordered moment  $p_o$  at 4.2 K amounts to  $1.9(1) \mu_B$ . The principal exchange interactions  $J_i$  between uranium atoms are marked. See the original paper for the analysis of the exchange integrals within the molecular field approximation.



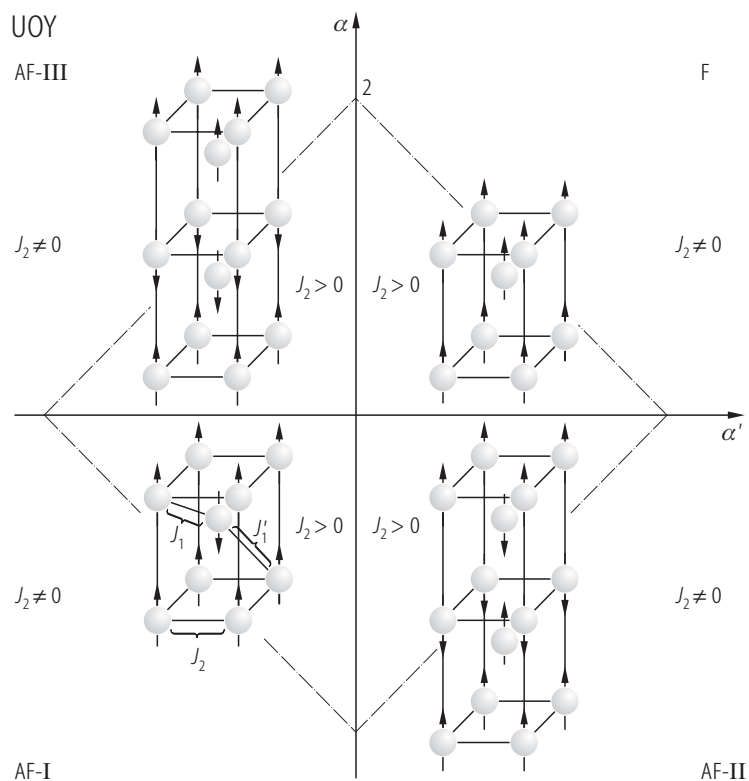


**Fig. 13.** UOY, Y = S, Se, Te. Stability diagram of the magnetic phases [65MN]. Possible magnetic moment configurations in a tetragonal structure of the PbFCl-type were analyzed in the framework of the Bertaut's matrix method. The three main exchange integrals,  $J_1$ ,  $J_1'$  and  $J_2$ , which were used in the calculations ( $\alpha = J_1/|J_2|$  and  $\alpha' = J_1'/|J_2|$ ) are defined in the bottom left quarter. There are four simple ordering schemes denoted by AF-I, AF-II, AF-III and F. The experimentally observed magnetic structures: UOS – AF-II (see Fig. 12), UOSe – AF-II (see Fig. 31) and UOTe – AF-I (see Fig. 36). For comparison see Fig. 14.

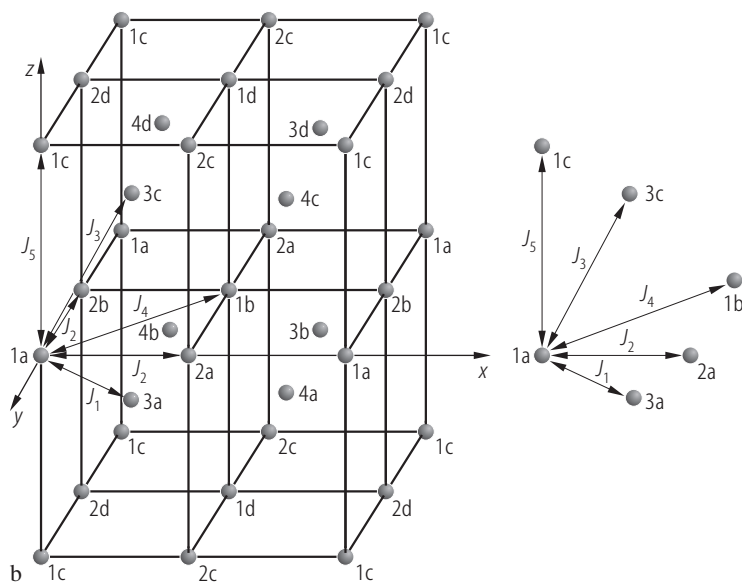


**Fig. 14 (b).** For caption see next page

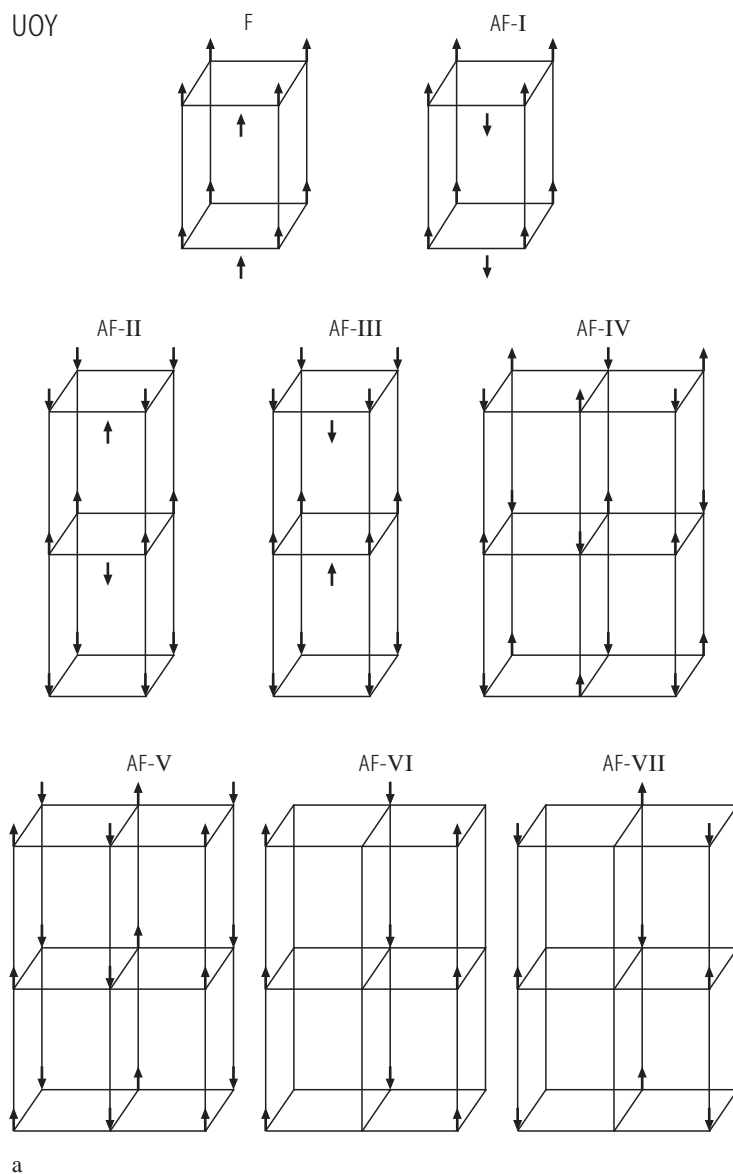


**Fig. 14.** UOY, Y = S, Se, Te. **(a)** Possible magnetic structures of the uranium compounds crystallizing with the tetragonal PbFCl-type crystal structure (s.g. P4/nmm), calculated by the Smart's method within the molecular field approximation [67PS]. The five different exchange integrals considered and a division of the crystal structure into sixteen Néel sublattices are shown schematically in panel **(b)**. Among UOY compounds the experimentally observed structures are AF-I (UOTe) and AF-II (UOS, UOSe). **(c)** Stability diagram of the structures presented in panel **(a)** obtained assuming that the stable structure is the one with the highest critical temperature and  $J_5 = 0$ .  $\alpha_1 = J_1/|J_2|$ ,  $\alpha_3 = J_3/|J_2|$ ,  $\alpha_4 = J_4/|J_2|$ ,  $c = 1 + 2\alpha_4$ . For the details see the original paper. Compare also Fig. 13.

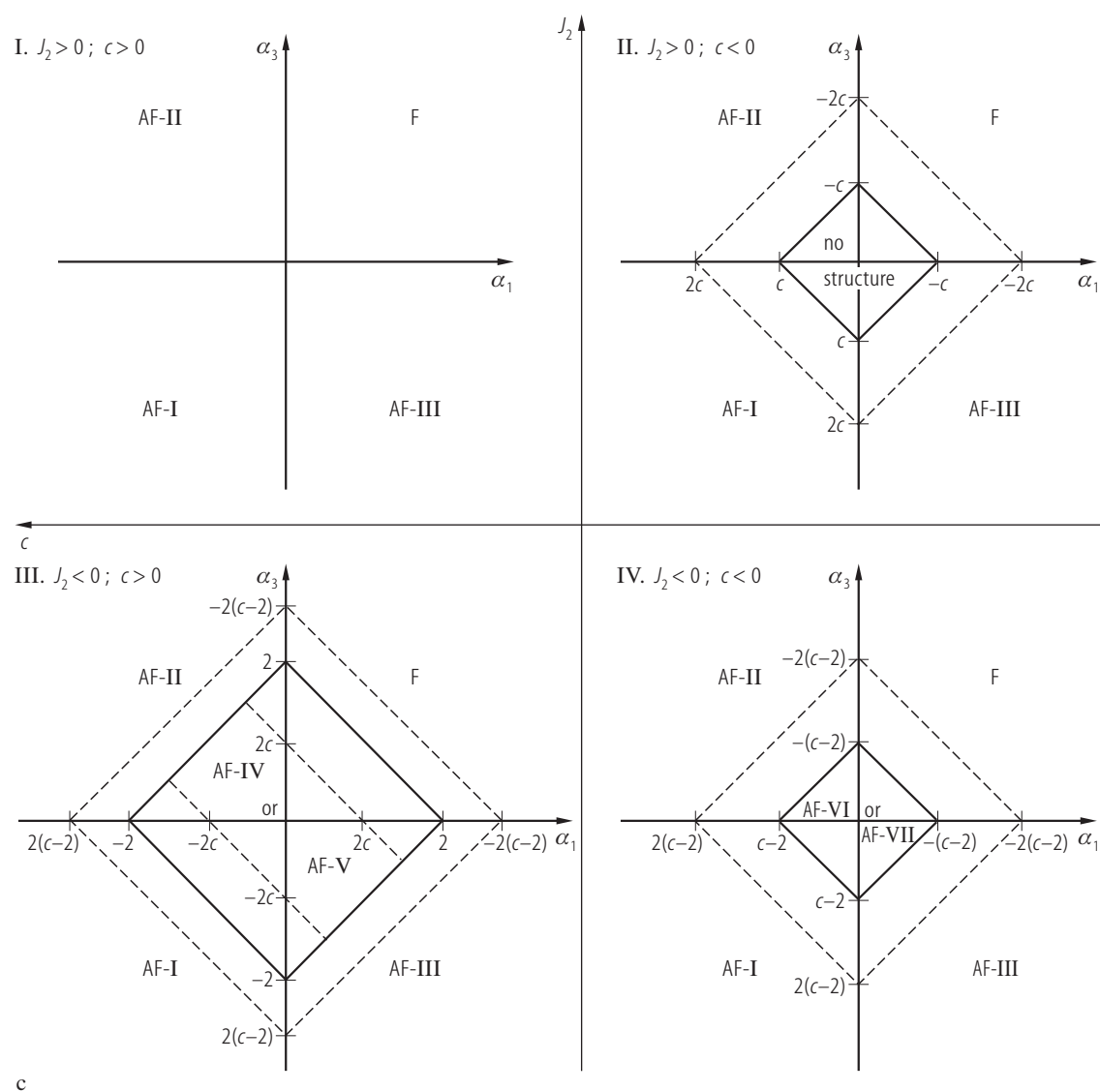


**Fig. 14 (c).** For caption see previous page.

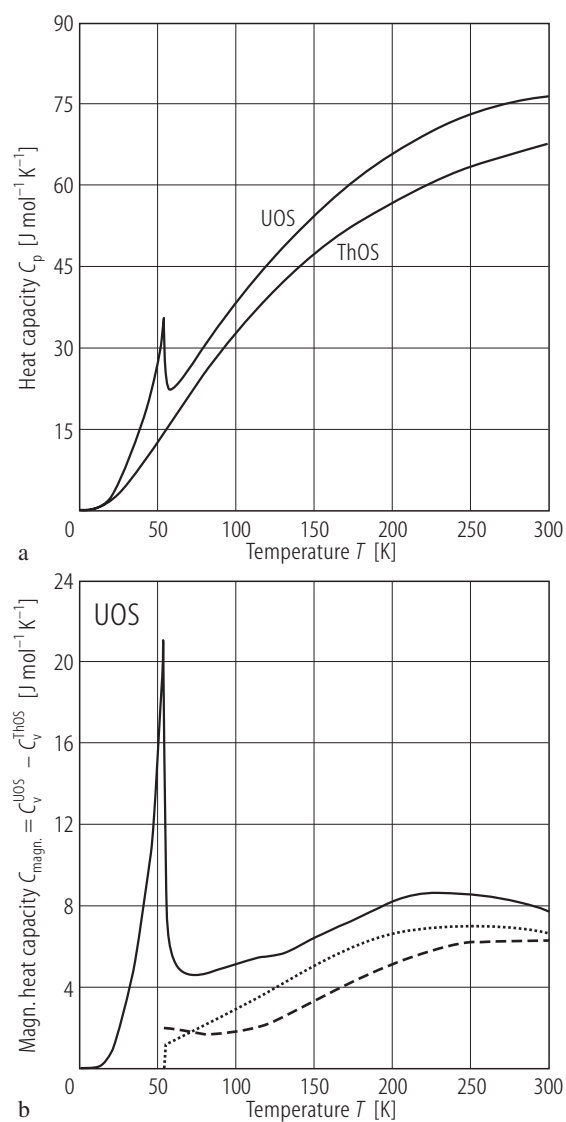


**Fig. 15.** UOS. (a) Heat capacity,  $C_p$ , vs. temperature,  $T$ , as compared to ThOS [84ABCH]. A sharp  $\lambda$ -shaped peak with  $C_p(\text{max}) = 35.6$  J/mol K manifests the antiferromagnetic phase transition at  $T_N = 55.35$  K. See the main thermodynamic characteristics given in Table E. (b) Comparison between the experimental  $(C_v^{\text{UOS}} - C_v^{\text{ThOS}})(T)$  curve and the calculated Schottky contribution, obtained in the framework of nearest neighbour (NN, dashed line) and lattice sum (LS, dotted line) point-charge models [84ABCH]. Note that better description of the experimental data gives the LS model. For the crystal field parameters see Table G.

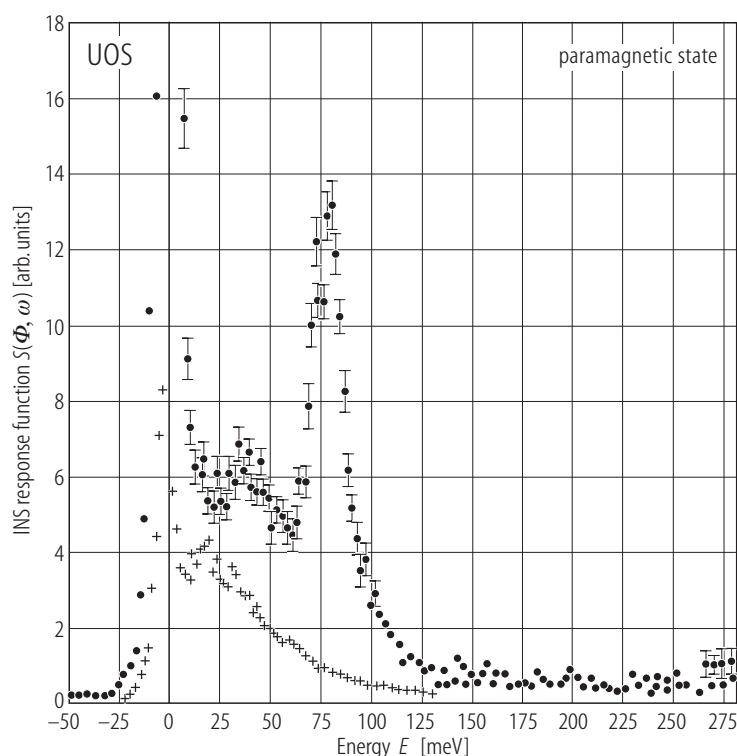


**Fig. 16.** UOS. Inelastic neutron scattering spectra,  $S(\Phi, \omega)$ , measured with incident energy  $E_0 = 290$  meV at  $T = 75$  K (paramagnetic state) at an average scattering angle  $\Phi = 5^\circ$  (full circles) and  $136^\circ$  (crosses) [88ABFC]. The spectrum recorded at  $\Phi = 136^\circ$  gives the shape of the phonon density of states. In the spectrum taken at  $\Phi = 5^\circ$  note an intense magnetic peak centered at about 80 meV, and the absence of any pronounced features above 100 meV. For high-resolution scans see Fig. 17.

For Fig. 17 see next page

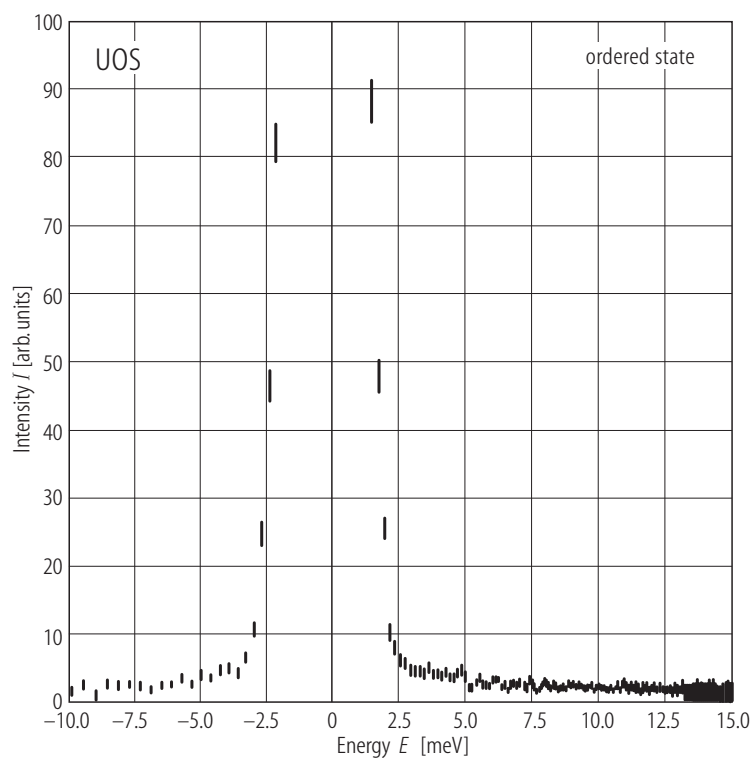


**Fig. 18.** UOS. Inelastic neutron scattering spectrum, intensity  $I$  vs. energy transfer  $E$ , measured with incident energy  $E_0 = 15$  meV at  $T = 35$  K (antiferromagnetic state) [95ABBC]. Note the absence of any intense magnetic transition at about 8 meV, which could be expected on the basis of the crystal field model A proposed in Ref. [89ABCF] (see Fig. 20).

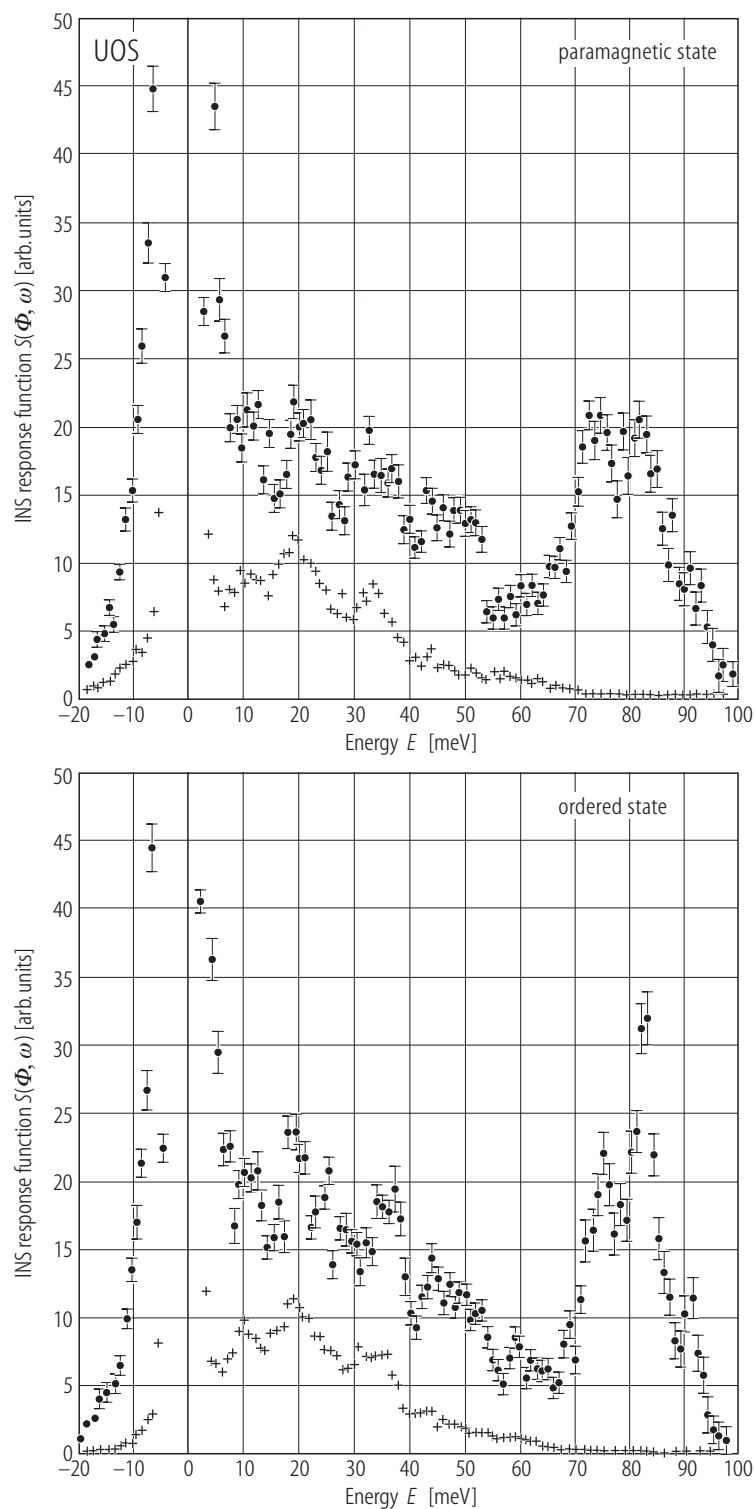


**Fig. 17.** UOS. Inelastic neutron scattering spectra,  $S(\Phi, \omega)$ , measured with incident energy  $E_0 = 110$  meV at an average scattering angle  $\Phi = 5^\circ$  (full circles) and  $136^\circ$  (crosses) [88ABFC, 89ABCF]. Upper panel:  $T = 65$  K (paramagnetic state); lower panel:  $T = 30$  K (antiferromagnetic state). The spectra recorded at  $\Phi = 136^\circ$  give the shape of the phonon density of states. Note two groups of magnetic peaks centered at about 74 and 82 meV, respectively, at 65 K and at about 76 and 84 meV, respectively, at 30 K. Moreover, in the paramagnetic state there is a transition at about 87 meV, which moves to 92 meV at 30 K. Some low intensity features, presumably of vibrational origin, occur in the range 40...55 meV. For detailed discussion of these INS spectra in terms of crystal field excitations see Fig. 20.

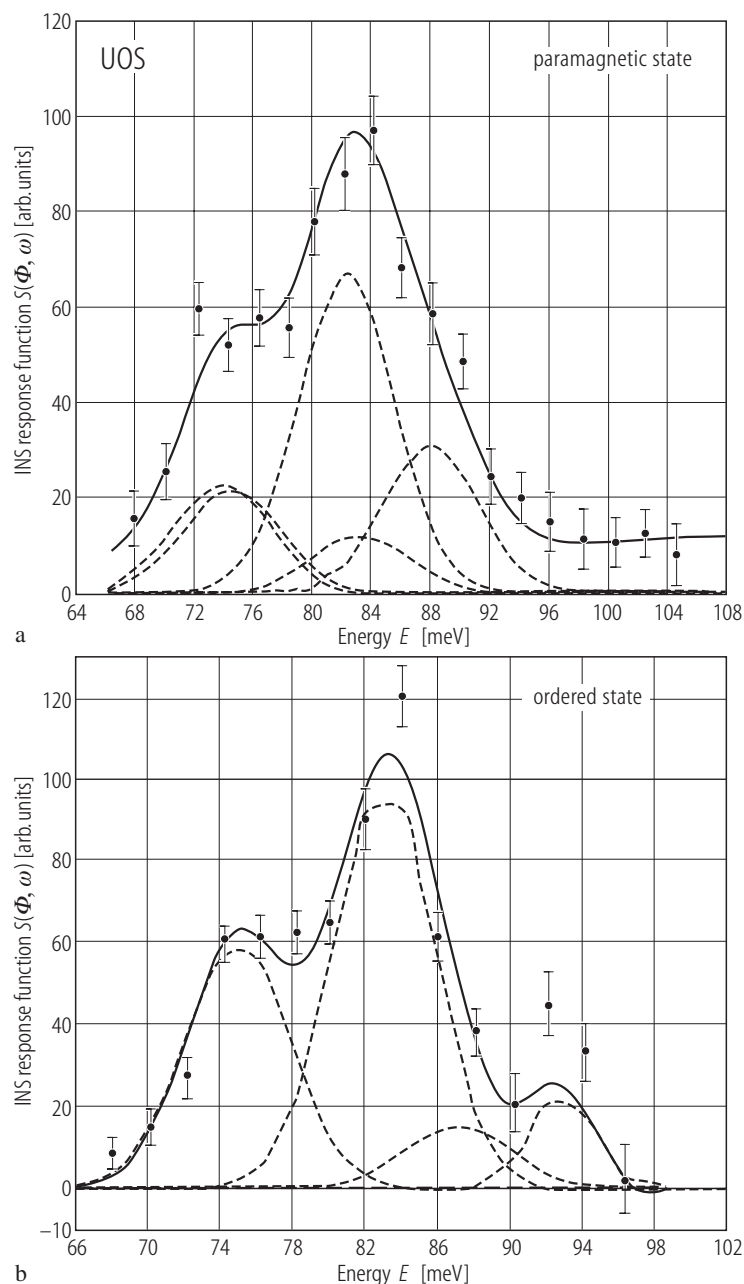


**Fig. 19.** UOS. Magnetic inelastic neutron scattering spectra,  $S(\Phi, \omega)$ , measured with incident energy  $E_0 = 150$  meV at (a)  $T = 65$  K (paramagnetic state) and (b)  $T = 30$  K (antiferromagnetic state) [95ABBC]. The spectra were obtained by subtracting from the scans recorded at an average scattering angle  $\Phi = 5^\circ$  the background and phonon contribution, which were estimated by multiplying the spectrum recorded at  $\Phi = 136^\circ$  by an energy dependent scaling function determined by Monte Carlo simulations. The solid lines represent the theoretical spectra calculated within the crystal field model C specified in Table M (see Fig. 21a). The dashed lines show the particular components of the spectra, i.e. the transitions:  $\Gamma_{15}^{(1)} \rightarrow \Gamma_{12}$ ,  $\Gamma_{15}^{(1)} \rightarrow \Gamma_{15}^{(2)}$ ,  $\Gamma_{15}^{(1)} \rightarrow \Gamma_{14}$ ,  $\Gamma_{15}^{(1)} \rightarrow \Gamma_{15}^{(2)}$  and  $\Gamma_{15}^{(1)} \rightarrow \Gamma_{11}^{(2)}$  from the left to the right, respectively, for  $T = 65$  K, and  $\Gamma_{15}^{(1)} \rightarrow \Gamma_{12}$ ,  $\Gamma_{15}^{(1)} \rightarrow \Gamma_{14}$ ,  $\Gamma_{15}^{(1)} \rightarrow \Gamma_{15}^{(2)}$  and  $\Gamma_{15}^{(1)} \rightarrow \Gamma_{11}^{(2)}$  from the left to the right, respectively, for  $T = 30$  K. For the definitions of the crystal field levels see Table G.

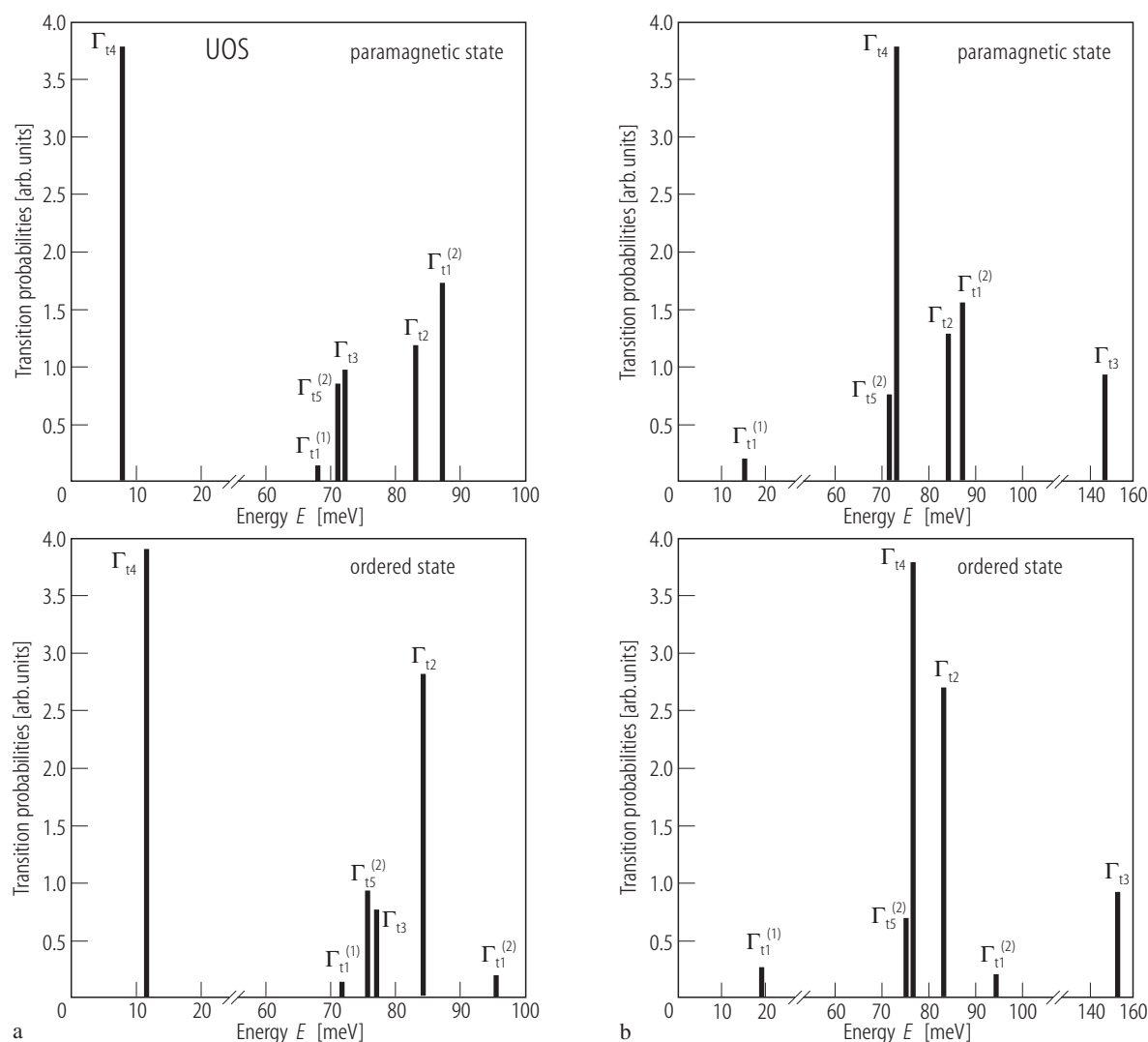


**Fig. 20.** UOS. (a) Energies of the crystal field excitations from the ground state  $\Gamma_{t5}^{(1)}$  and their probabilities calculated for  $T > T_N$  (upper panel) and  $T < T_N$  (lower panel) using the crystal field parameters listed in Table L as model A [89ABCF]. (b) Energies of the crystal field excitations from the ground state  $\Gamma_{t5}^{(1)}$  and their probabilities calculated for  $T > T_N$  (upper panel) and  $T < T_N$  (lower panel) using the crystal field parameters listed in

Table L as model B [89ABCF]. For details on the calculations see the original paper. Note that model A predicts the most intense transition  $\Gamma_{t5}^{(1)} \rightarrow \Gamma_{t4}$  to occur at 8 meV (in the paramagnetic range), which is in clear contradiction to the experimental findings (compare Fig. 18). In turn, model B locates an intense excitation  $\Gamma_{t5}^{(1)} \rightarrow \Gamma_{t3}$  at about 143 meV, i.e. in the energy range where no transition have been observed in INS studies (see Fig. 16).



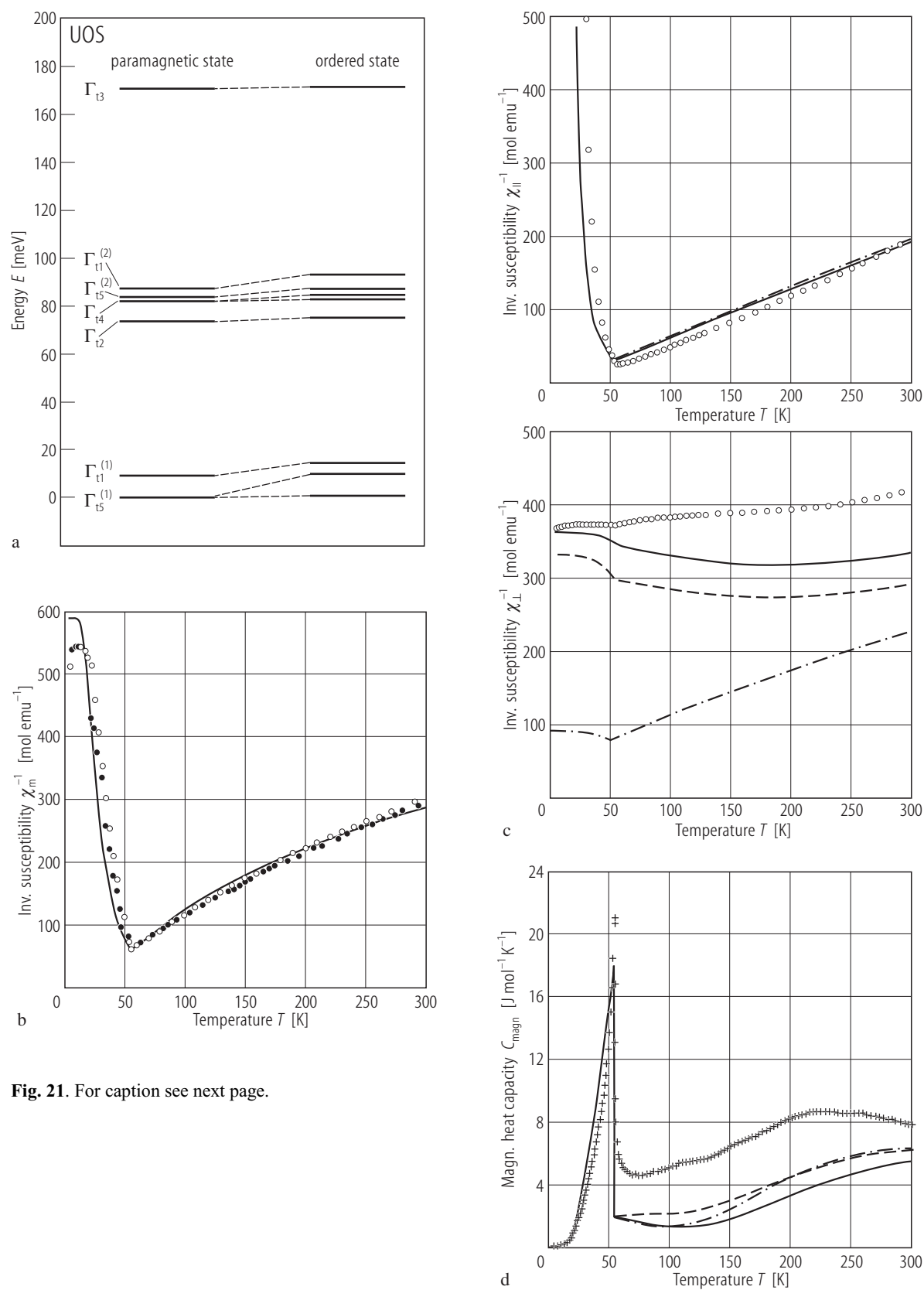


**Fig. 21.** For caption see next page.

←

**Fig. 21.** UOS. (a) Energy level schemes calculated for  $T = 65$  K (paramagnetic state) and  $T = 30$  K (antiferromagnetic state) using the crystal field parameters given in Table M (model C) [95ABBC]. See also Table N for the energy values and the probabilities of crystal field excitations from the ground state. (b) Reciprocal molar magnetic susceptibility,  $\chi_m^{-1}$ , vs. temperature,  $T$ , (solid curve), calculated within the crystal field model C from panel (a) [95ABBC]. For comparison the experimental data (corrected for diamagnetic contribution) are presented. Open circles:  $\chi_m^{-1}(T)$  calculated by averaging the results shown in Fig. 11; full circles: the data after Ref. [87T]. Note a good agreement between the experimental and theoretical results. (c) Reciprocal longitudinal,  $\chi_{||}^{-1}$ , (upper panel) and reciprocal transverse,  $\chi_{\perp}^{-1}$ , (lower panel) molar magnetic susceptibility vs. temperature,  $T$ , (solid curves), calculated within the crystal field model C from panel (a) [95ABBC]. For comparison the experimental data from Fig. 11 are presented, as well as the theoretical curves calculated within the models A (dash-dotted line) and B (dashed line) analyzed in Ref. [89ABCF] (see Fig. 20). (d) Magnetic heat capacity,  $C_{\text{mag}}$ , vs. temperature,  $T$ , (solid curve), calculated within the crystal field model from panel (a) [95ABBC]. For comparison the experimental data from Ref. [84ABCH] (see Fig. 15) are presented (crosses), as well as the theoretical curves calculated within the models A (dash-dotted line) and B (dashed line) analyzed in Ref. [89ABCF].

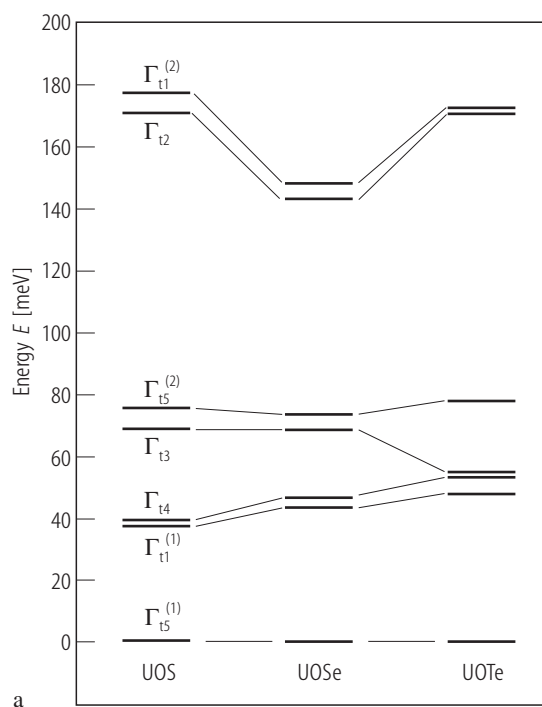


**Fig. 22.** UOY, Y = S, Se, Te. (a) Energy level diagrams derived from the ab initio crystal field parameters given in Table I [00G]. The energies and the wavefunctions of the particular CF levels are listed in Table K. For UOS the results of model I are displayed. (b) Reciprocal longitudinal,  $\chi_{||}^{-1}$ , (upper left-hand side panel) and transversal,  $\chi_{\perp}^{-1}$ , (upper right-hand side panel) molar magnetic susceptibility, Schottky contribution to the heat capacity,  $C_{\text{Sch}}$ , (bottom left-hand side panel), and magnetic entropy,  $S_{\text{mag}}$ , (bottom right-hand side panel) vs. temperature,  $T$ , in the paramagnetic region up to 600 K, calculated from the first principles using the energy level diagrams from panel (a) [00G]. Crosses: UOS; circles: UOSe; squares: UOTe.

For Fig. 22(b) see next page

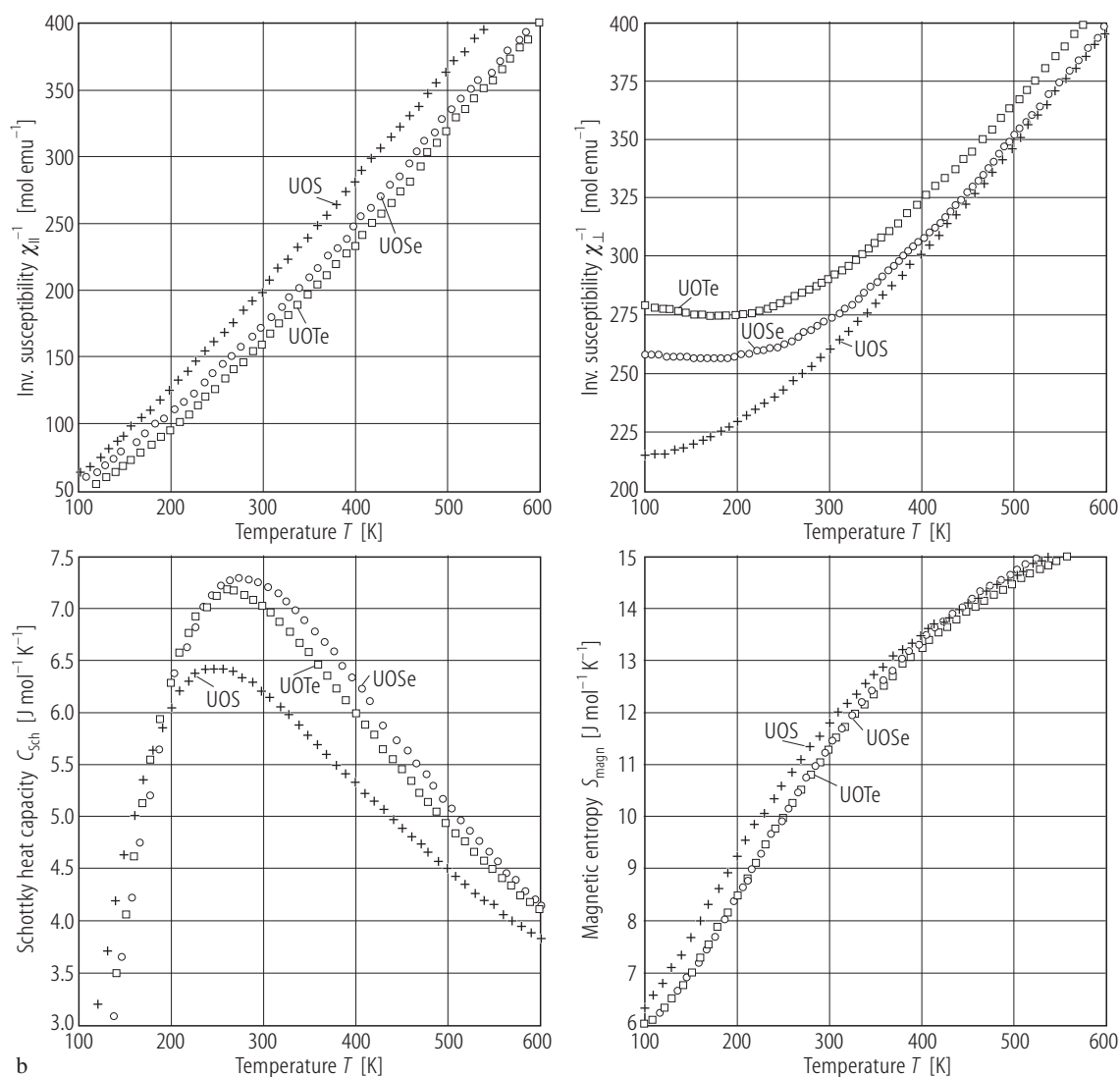


**Fig. 22(b).** For caption see previous page.

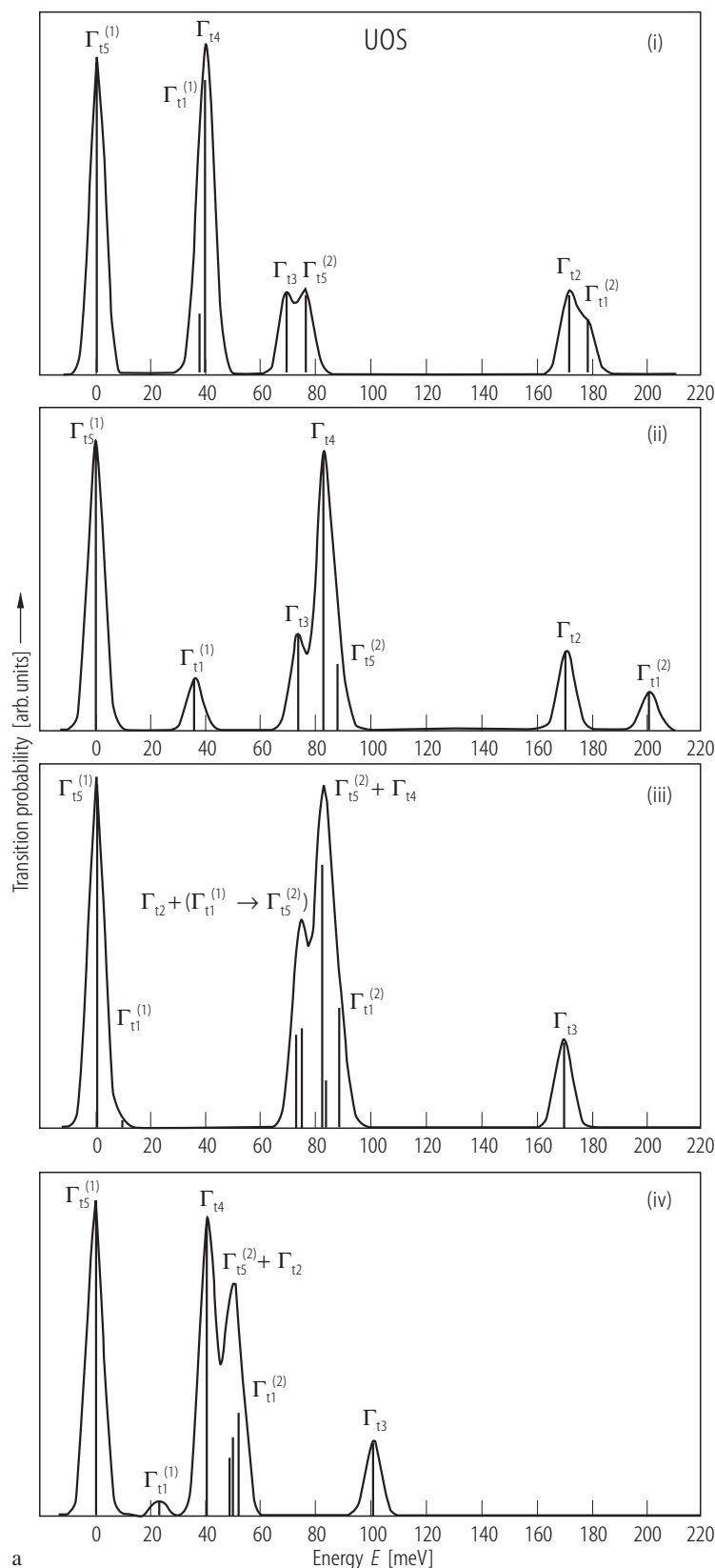


**Fig. 23.** UOS. **(a)** Magnetic excitations spectra simulated in four different crystal field models, which have yielded the CF parameters gathered in Table Q [00G]. (i) *ab initio* calculations – model I; (ii) adjustment of the CF parameters to the inelastic neutron scattering data from Ref. [95ABBC] (see Fig. 19) – model II; (iii) the CF parameters from Ref. [95ABBC] (model C); (iv) same set of the CF parameters as in (iii) but taking into account the mixing of terms effect. For description of the particular CF approaches see the original paper. **(b)** Reciprocal longitudinal,  $\chi_{||}^{-1}$ , (upper left-hand side panel) and transversal,  $\chi_{\perp}^{-1}$ , (upper right-hand side panel) molar magnetic susceptibility, Schottky contribution to the heat capacity,  $C_{\text{Sch}}$ , (bottom left-hand side panel), and magnetic entropy,  $S_{\text{magn}}$ , (bottom right-hand side panel) vs. temperature,  $T$ , in the paramagnetic region up to 1000 K, calculated in the models from panel (a) [00G]. Solid lines: model II; dotted lines: model I; dash-dotted lines: model C. For detailed discussion of the results, mutual comparison of all three CF models considered and their relation to the measured bulk properties of UOS see the original paper. **(c)** Reciprocal average molar magnetic susceptibility,  $\chi_m^{-1}$ , vs. temperature,  $T$ , up to 1000 K, calculated in the models from panel (a) as compared to the experimental data taken from Ref. [87T] (circles) [00G]. Solid curve: model II; dash-dotted curve: model C. Note rather satisfactory agreement between the results of model II with the measured  $\chi_m^{-1}(T)$  variation.

For Fig. 23 (b, c) see next page

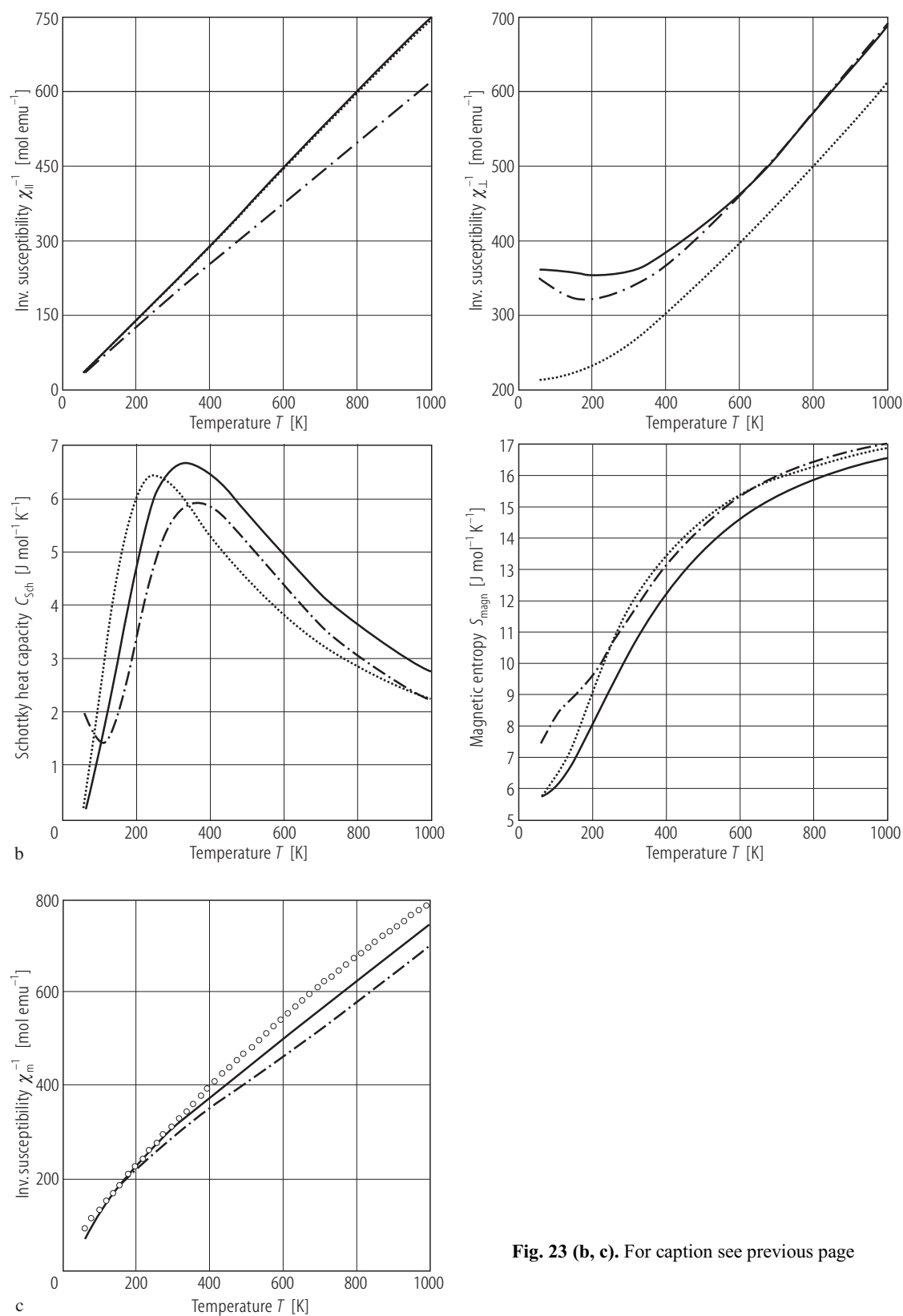
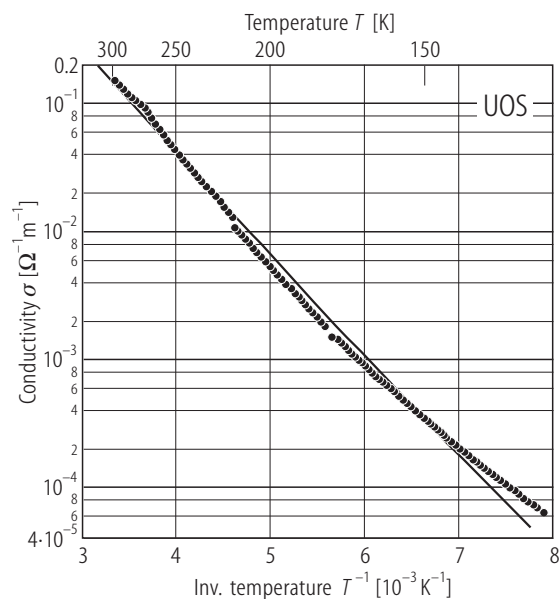
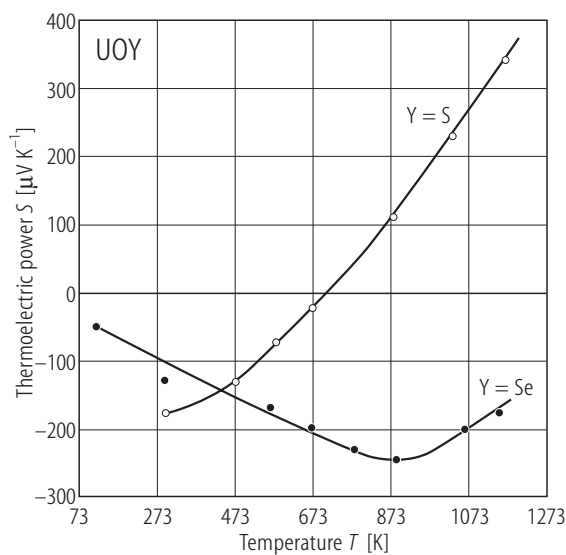


Fig. 23 (b, c). For caption see previous page



**Fig. 24.** UOS. Electrical conductivity,  $\sigma$ , vs. reciprocal temperature,  $1/T$ , in the range 125...300 K [98SMWY]. Note a semiconducting behaviour. The solid line is a fit to the activation law giving the energy gap of 67.5 meV.



**Fig. 25.** UOY, Y = S, Se. Thermoelectric power,  $S$ , vs. temperature,  $T$ , in the range 120...1150 K [64WP]. Open circles: UOS; full circles: UOSe. Note that UOS becomes a p-type material near to 720 K and UOSe remains n-type up to the highest temperature measured.

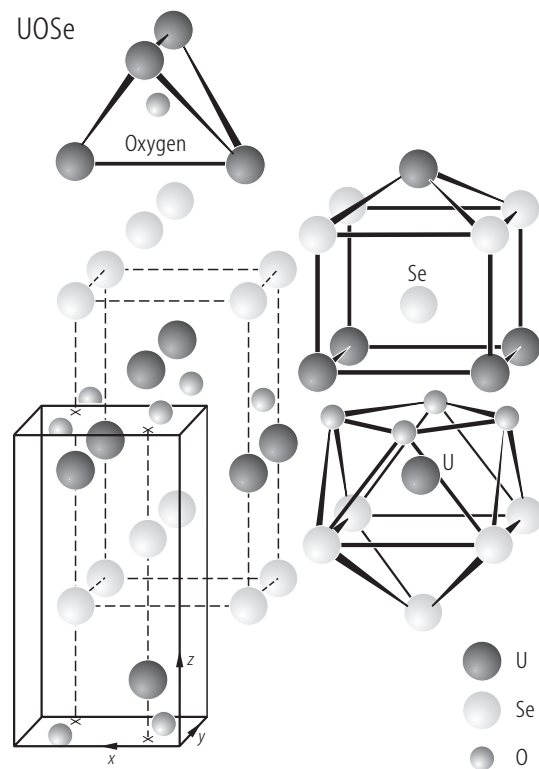


**Fig. 26.** UOSe. Crystal structure and the coordination polyhedra [93KPGZ]. The solid and dashed frames mark two settings of the origin position.

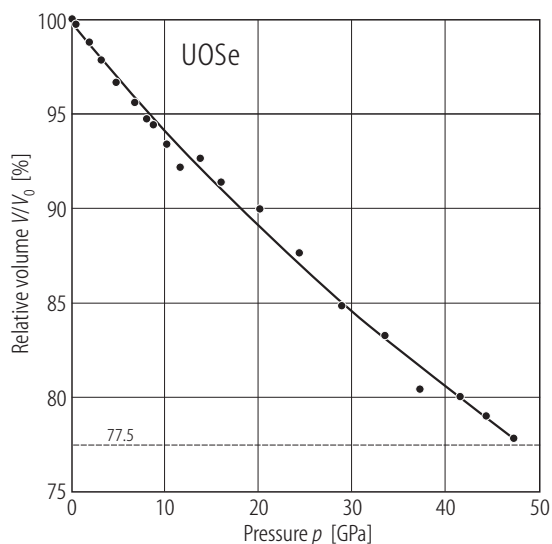


**Fig. 27.** UOSe. Relative volume,  $V/V_0$ , vs. pressure,  $p$ , up to 47.5 GPa [91GGBG]. Note that no phase transformation is observed.  $B_0 = 154$  GPa,  $B'_0 = 1.8$ .

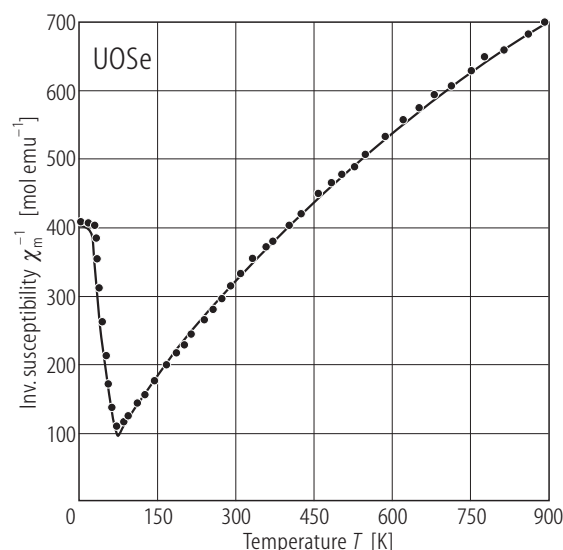


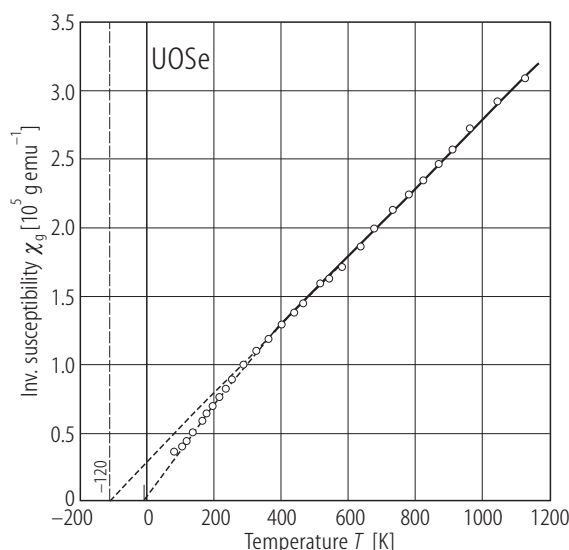
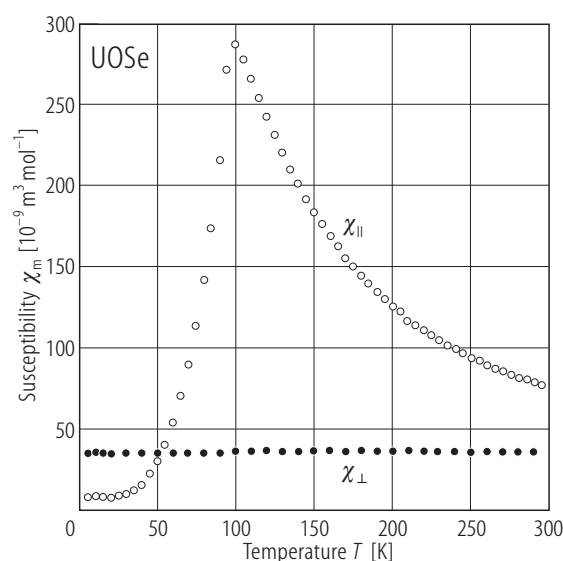
**Fig. 28.** UOSe. Reciprocal molar magnetic susceptibility,  $\chi_m^{-1}$ , vs. temperature,  $T$ , up to 900 K [79TZ]. The compound orders antiferromagnetically below 75 K. The solid lines are fits of the susceptibility to the following

$$\chi_m = \frac{a/T + b - c \exp(-d/T)}{2 + \exp(-d/T)} \quad \text{in the paramagnetic region and}$$

$$\chi_m = \frac{a}{2T} \left( 1 - \langle M_z \rangle^2 \right) + \frac{1}{4} \left[ \frac{d(b+c)}{d + T_N \langle M_z \rangle} + (b-c) \right]$$

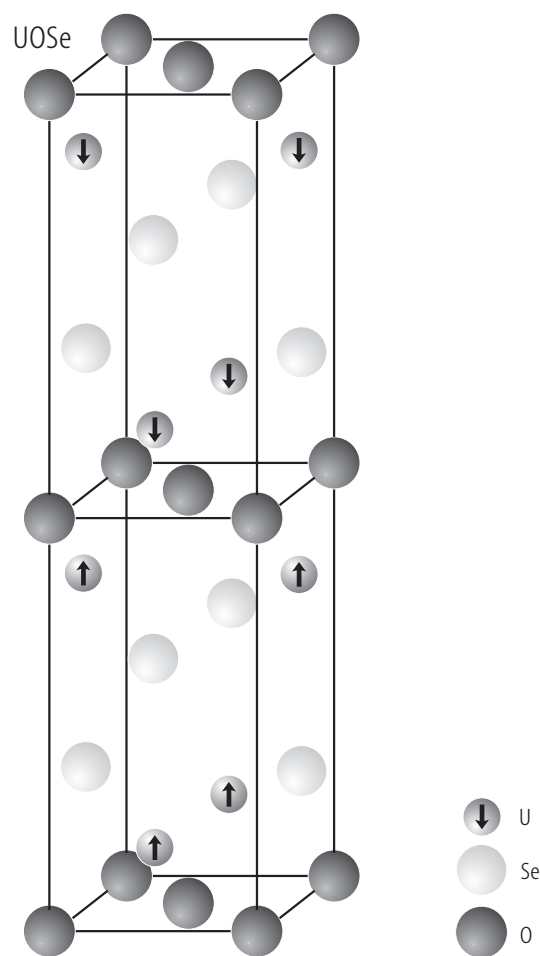
where  $\langle M_z \rangle = \tanh \frac{T_N}{T} \langle M_z \rangle$  in the ordered region,

appropriate for the assumption of a doublet-singlet system of the lowest lying crystal field levels. The fit parameters:  $a = 1.00$  K emu/mol,  $b = 6.0 \cdot 10^{-3}$  emu/mol,  $c = 5.1 \cdot 10^{-3}$  emu/mol,  $d = 320$  K. See also the main magnetic characteristics collected in Table E.

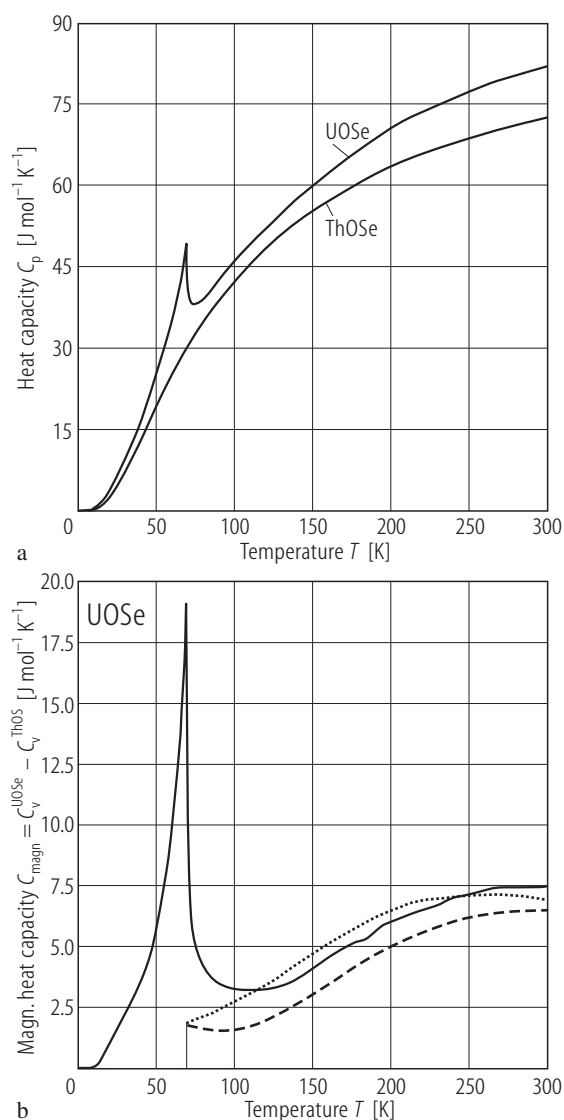


**Fig. 29.** UOSe. Reciprocal mass magnetic susceptibility,  $\chi_g^{-1}$ , vs. temperature,  $T$ , up to 1150 K [68MSTL]. Note a change in the slope of  $\chi_g^{-1}(T)$  at about 300 K. See the Curie-Weiss fit parameters given in Table E.

**Fig. 30.** UOSe. Longitudinal,  $\chi_{||}$ , (open circles) and transverse,  $\chi_{\perp}$ , (filled circles) molar magnetic susceptibility (SI units) vs. temperature,  $T$ , measured on a single crystal having the exact 1:1:1 stoichiometry [93KPGZ]. The compound orders antiferromagnetically at  $T_N = 100(2)$  K. This value of  $T_N$  considerably differs from those determined in powder studies (75 K in [79TZ], 69.8 K in [84ABCH], 90 K in [68MSTL]) presumably because of some deviations from the exact stoichiometry in these other samples (for the discussion on this problem refer to the original paper). Note a huge anisotropy with nearly temperature-independent transverse susceptibility, which unambiguously indicates that the crystal field ground state in this compound is a  $\Gamma_{15}$  doublet, well separated from the excited states. See the crystal field levels scheme shown in Fig. 33.

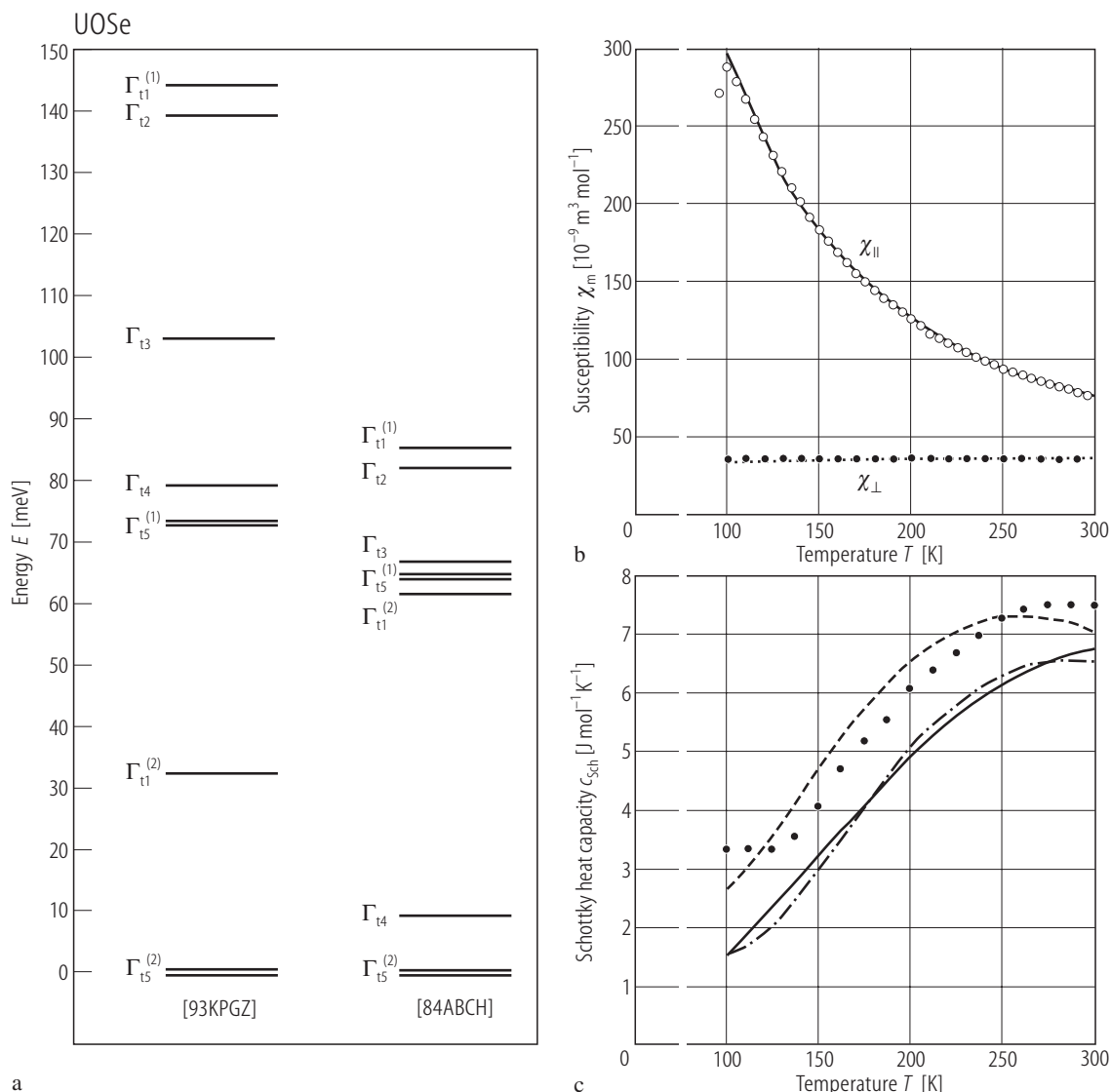


**Fig. 31.** UOSe. Magnetic structure [68MSTL]. The structure is of the AF-II - type. The ordered moment  $p_o$  at 4.2 K amounts to  $2.21(5) \mu_B$ .

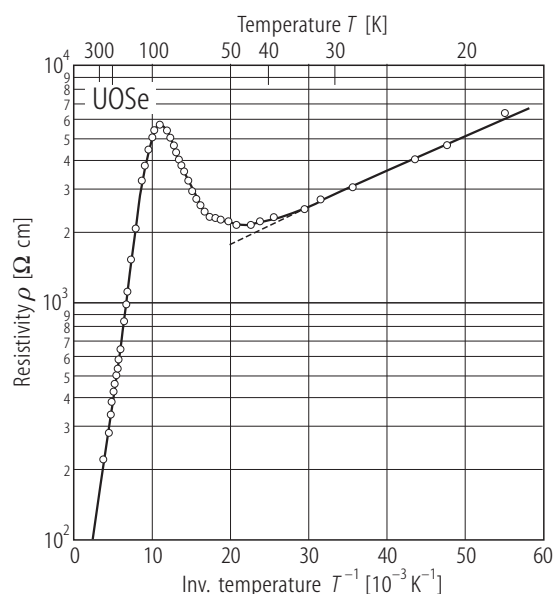


**Fig. 32.** UOSe. (a) Heat capacity,  $C_p$ , vs. temperature,  $T$ , as compared to ThOSe [84ABCH]. A sharp  $\lambda$ -shaped peak with  $C_p(\text{max}) = 49.5$  J/ mol K manifests the anti-ferromagnetic phase transition at  $T_N = 69.80$  K. See the main thermodynamic characteristics given in Table E. (b) Comparison between the experimental  $(C_v^{\text{UOSe}} - C_v^{\text{ThOSe}})(T)$  curve and the calculated Schottky contribution, obtained in the framework of nearest neighbour (NN, dashed line) and lattice sum (LS, dotted line) point-charge models [84ABCH]. Note that better description of the experimental data gives the NN model. For the crystal field parameters see Table G.

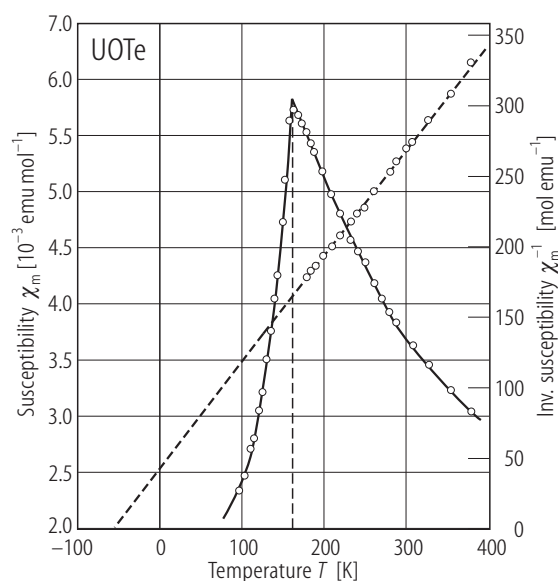




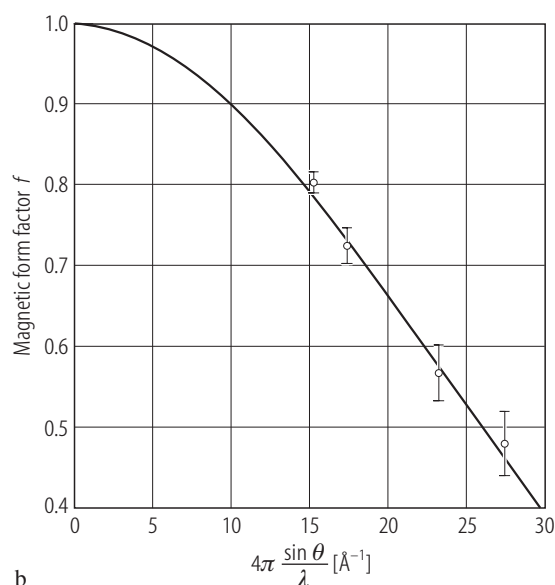
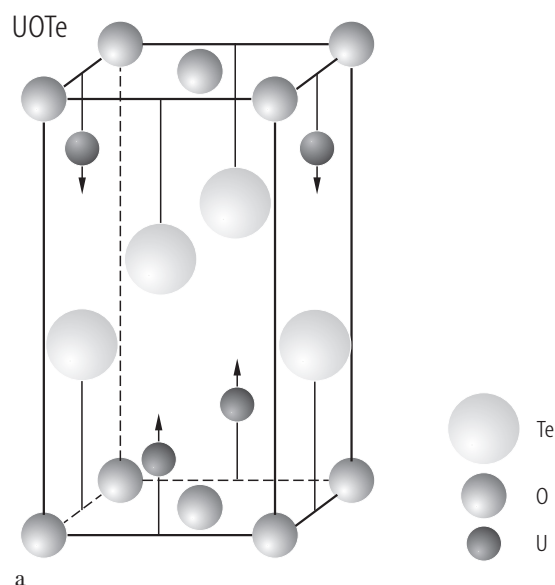
**Fig. 33.** UOSe. (a) Schematic representation of the crystal field splitting of the uranium  $^3H_4$  ground term in a tetragonal crystal field potential of the  $C_{4v}$  symmetry as derived in a perturbative ab initio approach [93KPGZ]. See also the crystal field parameters given in Table P and the coefficients of the wavefunctions of the energy levels listed in Table R. For the description of the calculation method and the detailed analysis of the crystal field parameters see the original paper. For comparison the scheme derived in [84ABCH] is also shown. Note that with respect to [84ABCH] the overall splitting is larger (145 meV against 85 meV), the  $\Gamma_{t4}$  singlet has different position on the energy scale and the  $\Gamma_{t5}^{(2)}$  ground doublet is much better separated from the first excited state. (b) Comparison between the longitudinal,  $\chi_{||}$ , (open circles) and transverse,  $\chi_{\perp}$ , (filled circles) molar magnetic susceptibility measured in the paramagnetic region (the data from Fig. 30) and the corresponding susceptibilities calculated for the crystal field model derived in [93KPGZ] presented in panel (a) (solid and dashed lines for  $\chi_{||}$  and  $\chi_{\perp}$ , respectively). An anisotropy in exchange interactions was accounted for by introducing two different molecular field constants:  $\lambda_{||} = -0.8 \cdot 10^6 \text{ mol/m}^3$  and  $\lambda_{\perp} = 5.3 \cdot 10^6 \text{ mol/m}^3$  for the configurations  $B \parallel c$ -axis and  $B \perp c$ -axis, respectively. Note a very good description of the experimental data. (c) Comparison between the experimental Schottky heat capacity,  $C_{Sch}$ , derived in [84ABCH] (circles; see also Fig. 32) and  $C_{Sch}(T)$  calculated for the crystal field level scheme from [93KPGZ] presented in panel (a) (solid line). For comparison it is shown  $C_{Sch}(T)$  calculated in the framework of the lattice sum (LS, dashed line) and nearest neighbours (NN, dash-dotted line) models considered in [84ABCH] (see Fig. 32 for explanation). Note that the perturbative approach gives a similar agreement with the experimental data as the NN model, which was regarded in [84ABCH] as being more reliable.



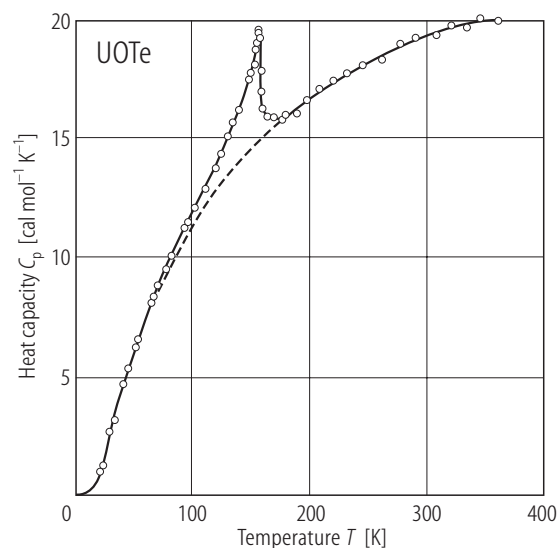
**Fig. 34.** UOSe. Electrical resistivity,  $\rho$ , vs. inverse temperature,  $1/T$  [68MSTL]. The maximum at 90 K was tentatively ascribed by the authors to a magnetic phase transition. Note a semiconducting behaviour reported also in [64WP].



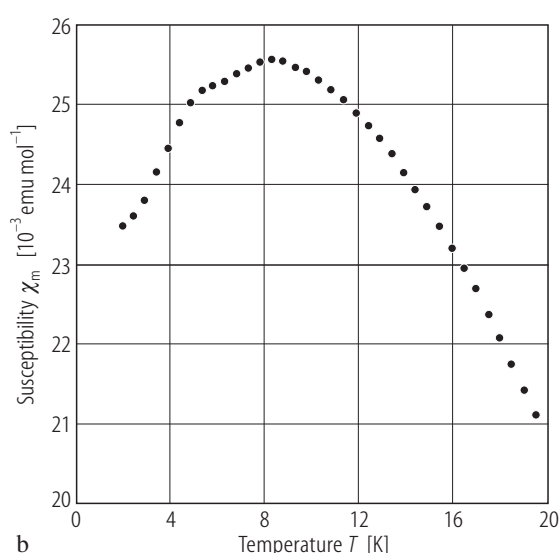
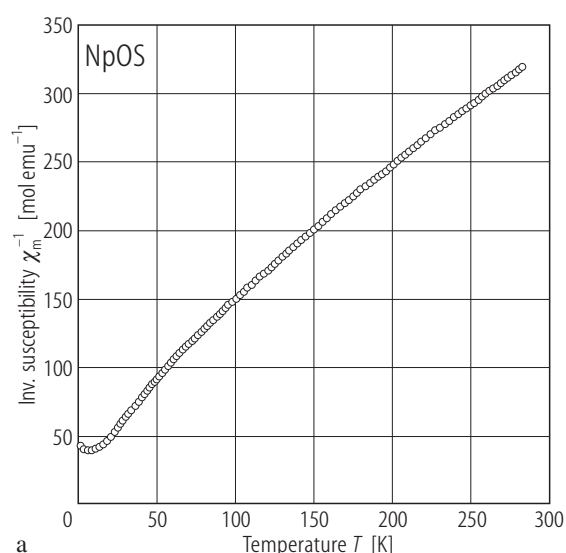
**Fig. 35.** UOTe. Molar magnetic susceptibility,  $\chi_m$ , (left-hand scale) and reciprocal molar magnetic susceptibility,  $\chi_m^{-1}$ , (right-hand scale) vs. temperature,  $T$ , in the range 85...370 K [61TNS]. The dashed line denotes a Curie-Weiss fit with the parameters given in Table B. The compound orders antiferromagnetically at  $T_N = 162$  K.



**Fig. 36.** UOTe. (a) Magnetic structure [65MN]. The structure is of the AF-I - type. The uranium ordered moment  $p_o$  at 4.2 K amounts to  $1.97(5) \mu_B$  [69MSL]. (b) Magnetic form factor for uranium [65MN].

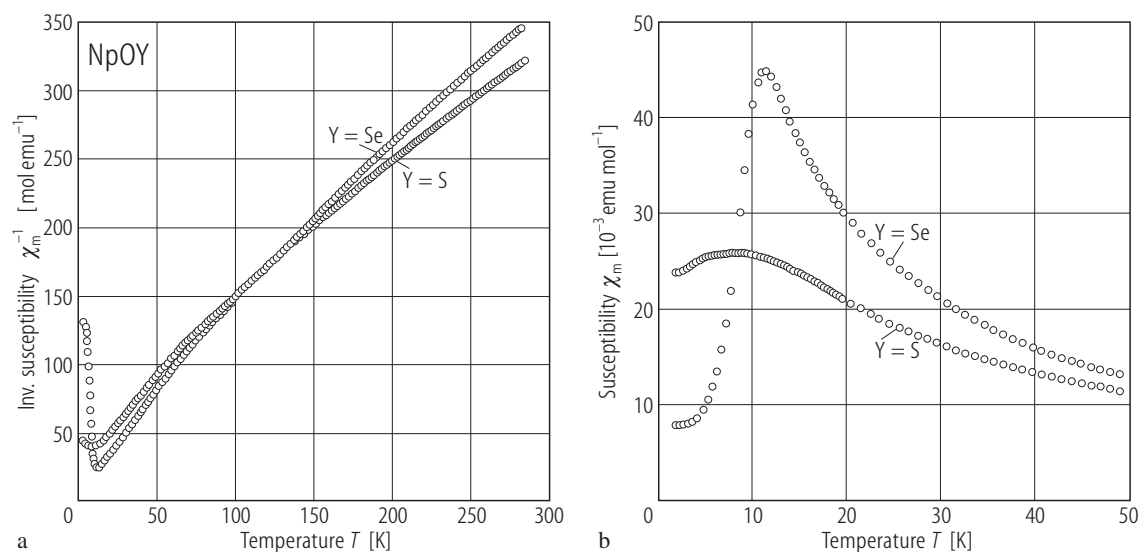


**Fig. 37.** UOTe. Heat capacity,  $C_p$ , vs. temperature,  $T$ , in the range 20...370 K [63SNB]. A sharp  $\lambda$ -shaped peak manifests a second-order antiferromagnetic phase transition at  $T_N = 162$  K. The dashed line represents the lattice contribution,  $C_L$ , calculated using a combination of three Debye functions with the Debye temperatures of 180, 245 and 458 K, respectively (for details see the original paper). The entropy change at the phase transition is  $\Delta S = 1.07$  cal/(mol K), i.e. it is much smaller than the value of 4.4 cal/(mol K) expected for the  $5f^2$  configuration of the  $U^{4+}$  ion and even than the value of 1.38 cal/(mol K) calculated for the lowest spin only moment ( $S = 1/2$ ).



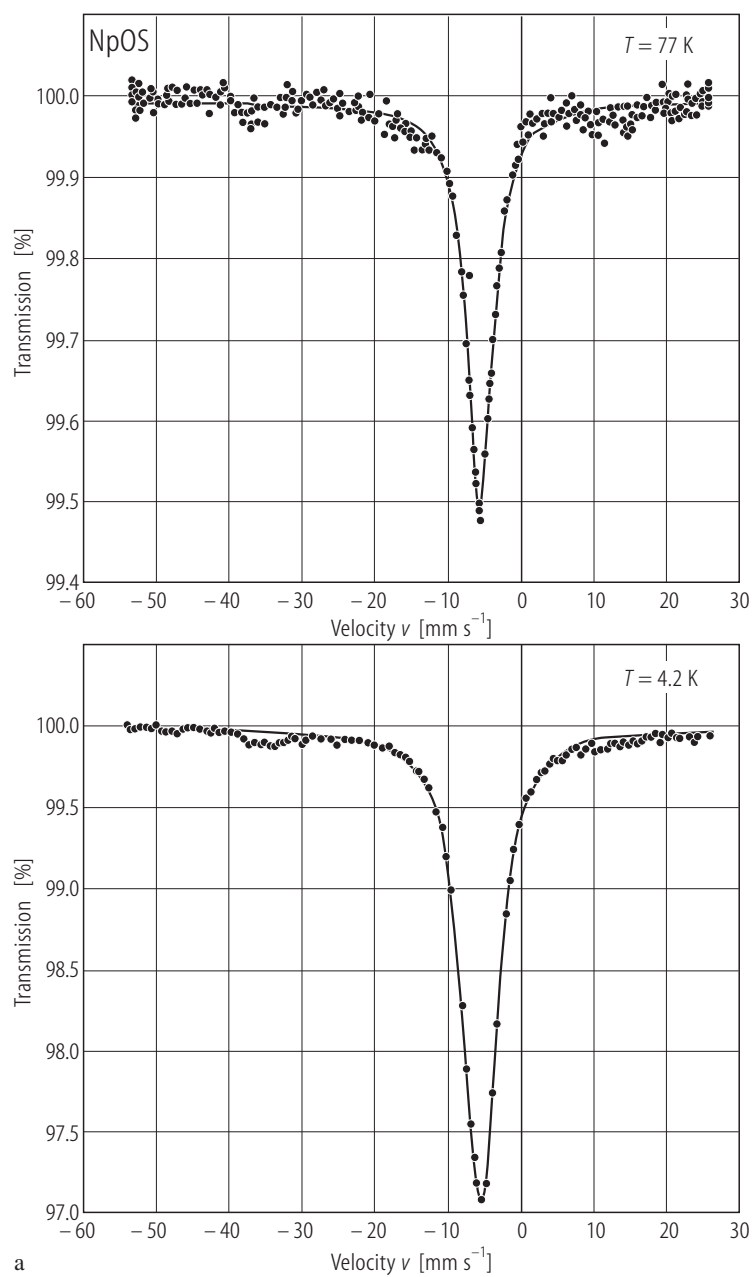
**Fig. 38.** NpOS. (a) Reciprocal molar magnetic susceptibility,  $\chi_m^{-1}$ , vs. temperature,  $T$  [86CBBB]. The compound orders antiferromagnetically at  $T_N = 5$  K. In the range 20...60 K,  $\chi_m^{-1}(T)$  follows a Curie-Weiss law with the parameters given in Table B. Above this range the  $\chi_m^{-1}(T)$  variation is strongly curvilinear, because of crystal field interactions. The effective magnetic moment measured

at 300 K amounts to  $3.37 \mu_B$ , in good agreement with the theoretical value of  $3.62 \mu_B$  for the  $5f^3$  configuration of  $Np^{4+}$  ions. (b) Molar magnetic susceptibility,  $\chi_m$ , vs.  $T$  below 20 K [86CBBB]. Note a rounded maximum around 8 K. The antiferromagnetic phase transition manifests itself as an inflection point below this maximum.

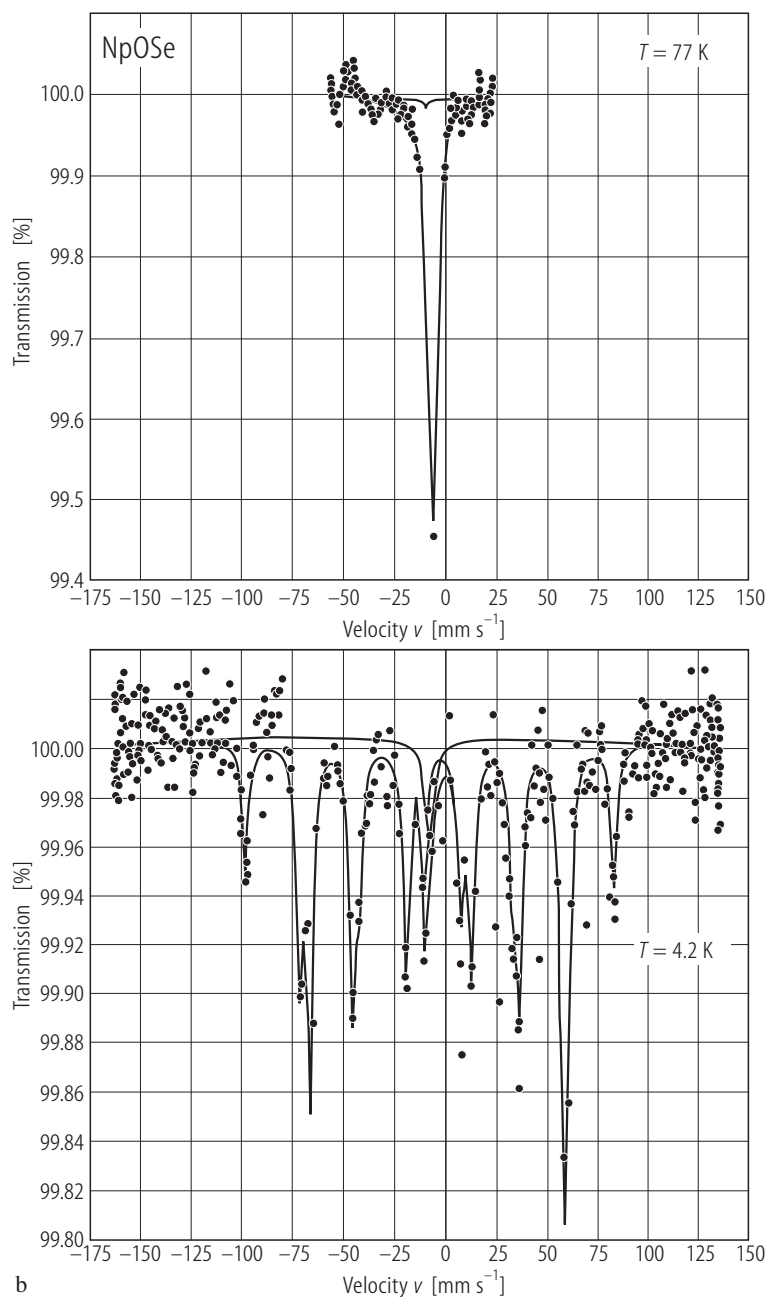


**Fig. 39.** NpOY, Y = S, Se. **(a)** Reciprocal molar magnetic susceptibility,  $\chi_m^{-1}$ , vs. temperature,  $T$  [89ABBB]. The compounds order antiferromagnetically at  $T_N = 4.2$  K and 11 K for NpOS and NpOSe, respectively (see also the Mössbauer data in Fig. 43). Above 50 K,  $\chi_m^{-1}(T)$  for both ternaries are strongly curvilinear. The effective magnetic

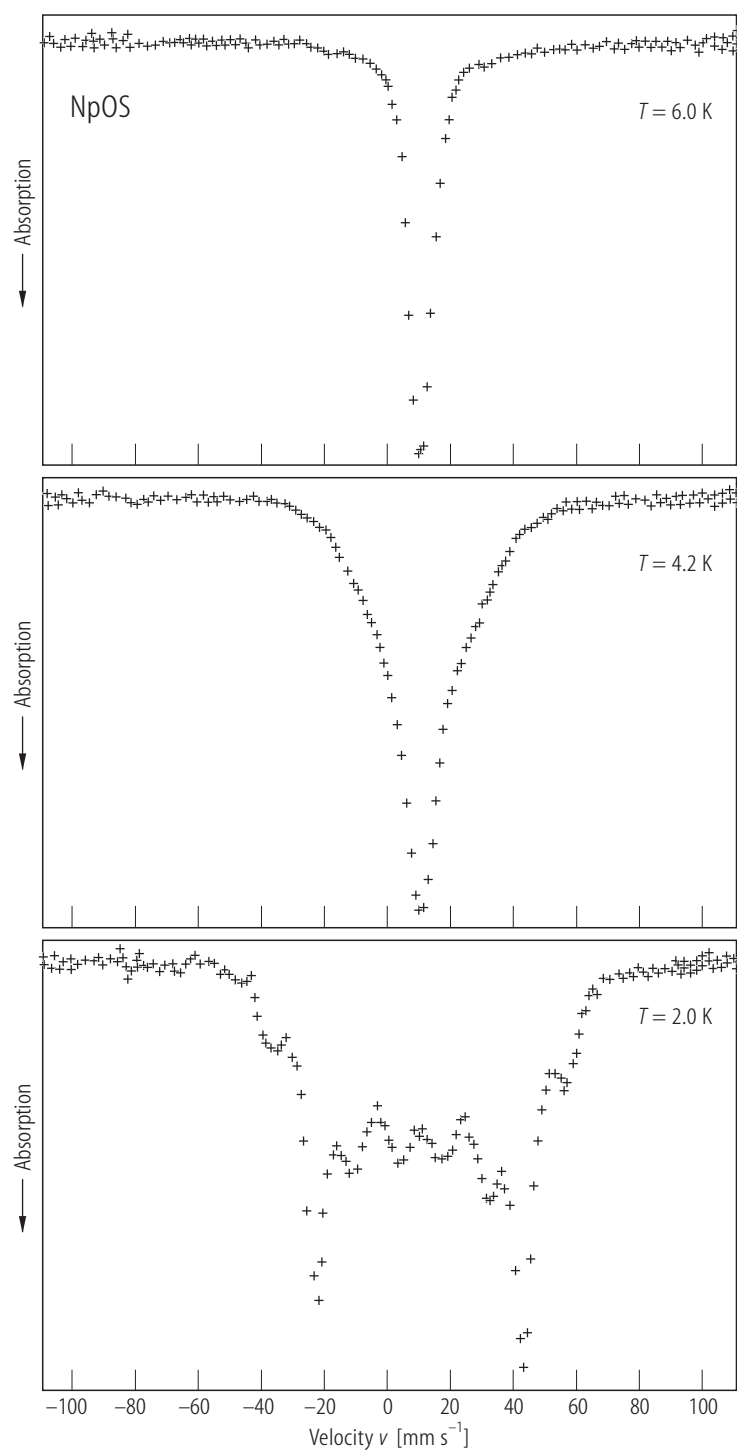
moment calculated at  $T = 300$  K amounts to  $3.1 \mu_B$  and  $2.8 \mu_B$  for the sulphide and the selenide, respectively. **(b)** Molar magnetic susceptibility,  $\chi_m$ , vs.  $T$  below 50 K. Note that the antiferromagnetic phase transition in NpOS manifests itself as an inflection point in  $\chi_m(T)$  at about 4.5 K, while a very rounded maximum in  $\chi_m(T)$  occurs around 8 K.



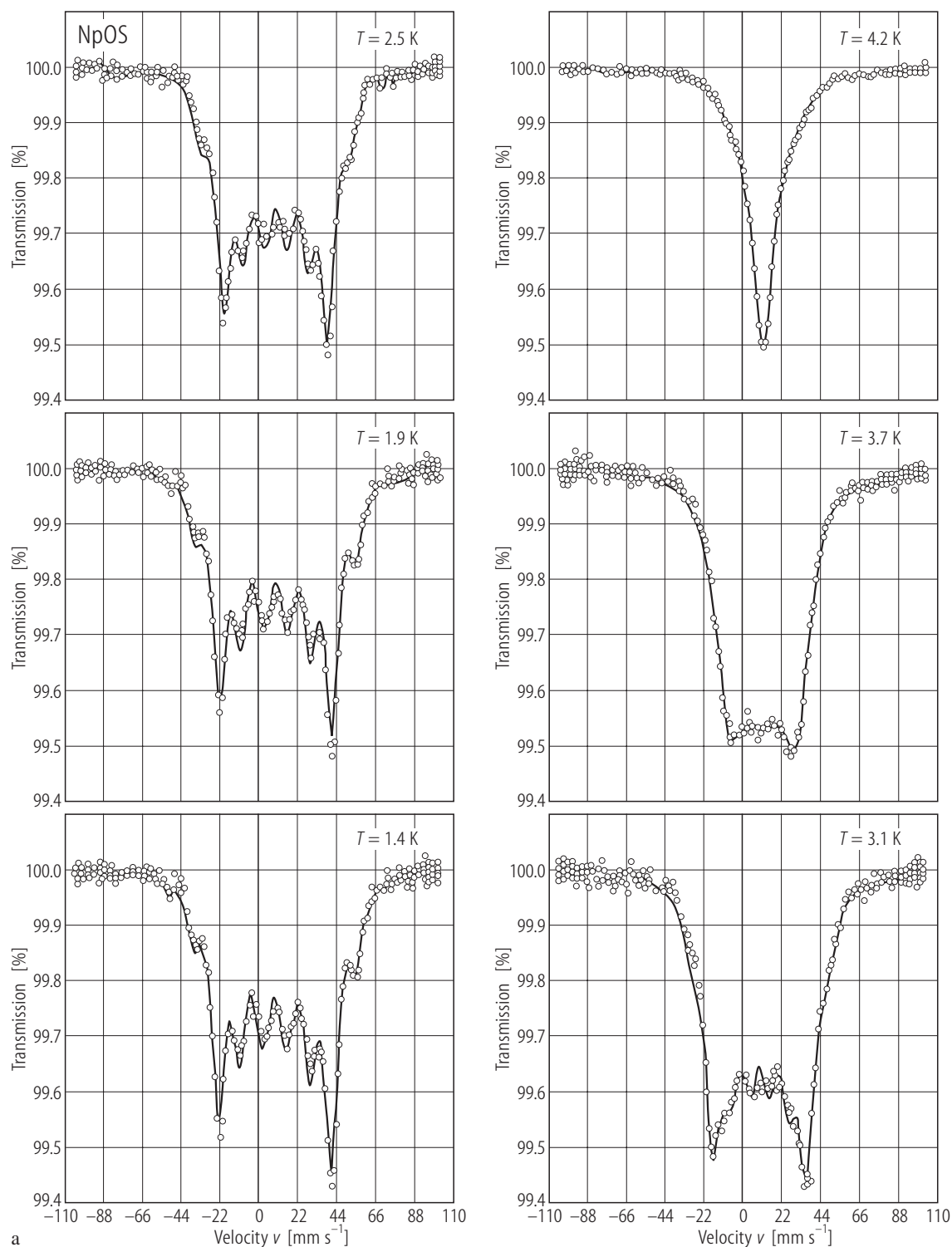
**Fig. 40(a).** For caption see next page



**Fig. 40.**  $\text{NpOY}$ ,  $\text{Y} = \text{S}, \text{Se}$ .  $^{237}\text{Np}$  Mössbauer resonance spectra recorded at 4.2 and 77 K for (a)  $\text{NpOS}$  and (b)  $\text{NpOSe}$ , shown with respect to  $\text{NpAl}_2$  [85TJP1]. At 77 K a single absorption line is observed for both compounds and no evident electrical quadrupolar interaction is present. At 4.2 K  $\text{NpOS}$  remains paramagnetic but  $\text{NpOSe}$  shows a typical magnetic splitting and the spectrum can be fully explained by combined magnetic and electrical interactions. For the hyperfine parameters see Table S. The values of the isomer shifts correspond to a tetravalent state of neptunium in both compounds. The isomer shift increases from the sulphide to the selenide indicating a diminishing participation of the 5f electrons to the chemical bond with the resulting consequence of an increase in the screening of the s-electrons.

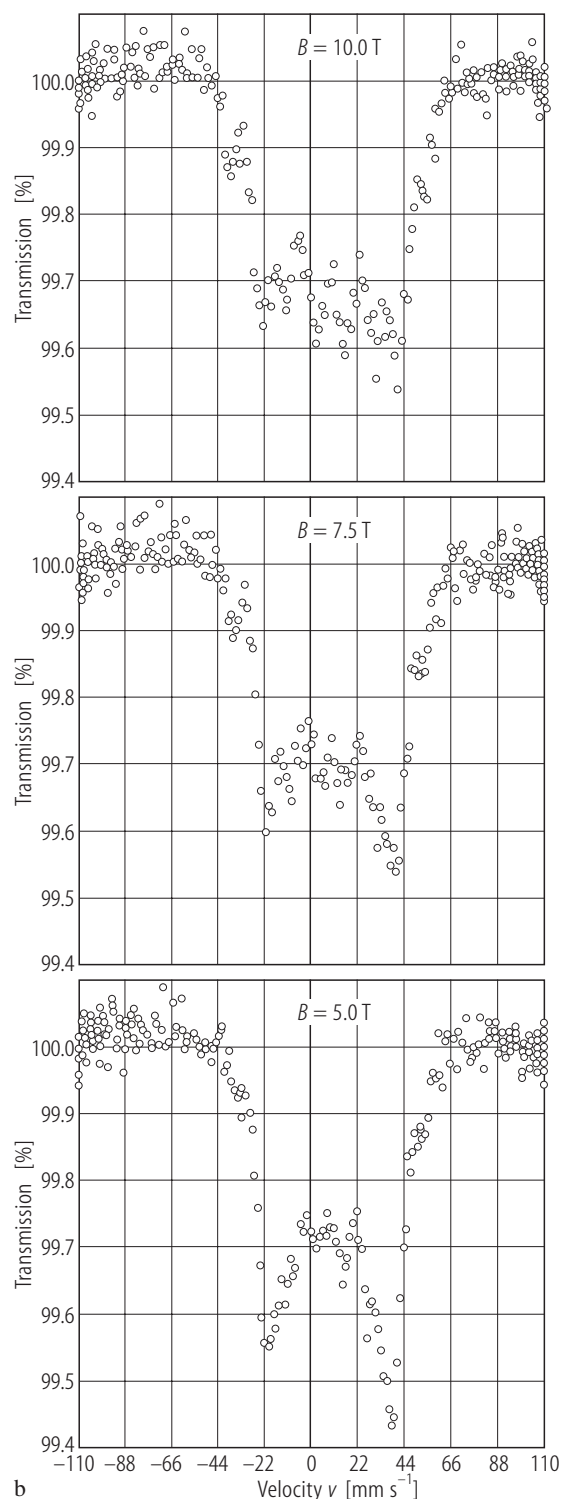


**Fig. 41.** NpOS.  $^{237}\text{Np}$  Mössbauer spectra obtained at 2, 4.2 and 6 K [86CBBB]. The spectrum recorded at 6 K yields an isomer shift of  $-5.2 \text{ mm/s}$  (with respect to  $\text{NpAl}_2$ ), pointing to a  $4^+$  oxidation state for Np ions. The 2 K-spectrum can be described by considering only one Np site with a hyperfine field of 154 T, which corresponds to a magnetic moment of  $0.8 \mu_B$ . The full width at half maximum is  $8.4 \text{ mm/s}$ . For comparison see the hyperfine parameters collected in Table S.

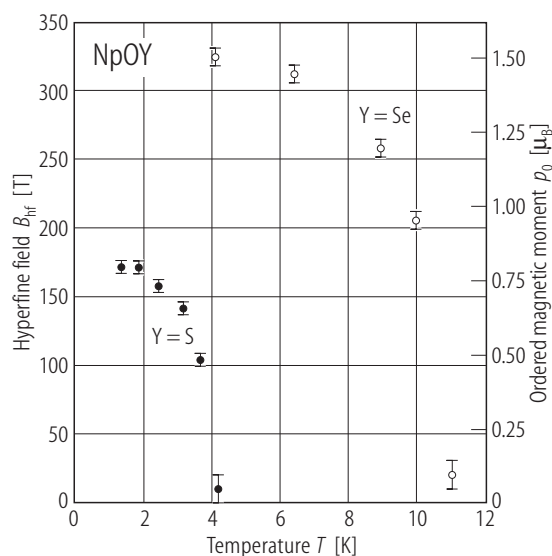


**Fig. 42(a).** For caption see next page.

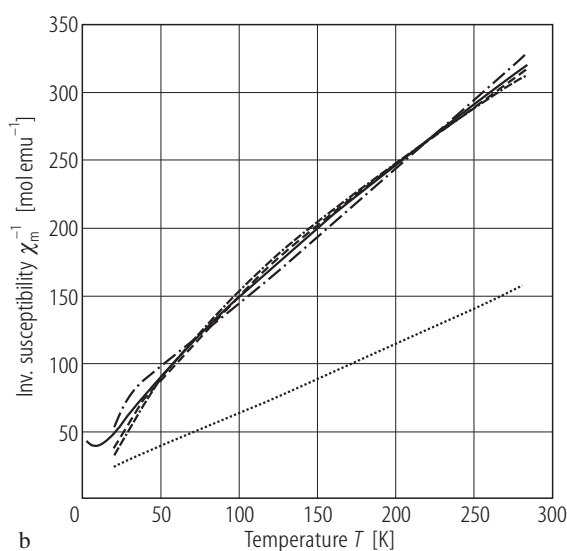
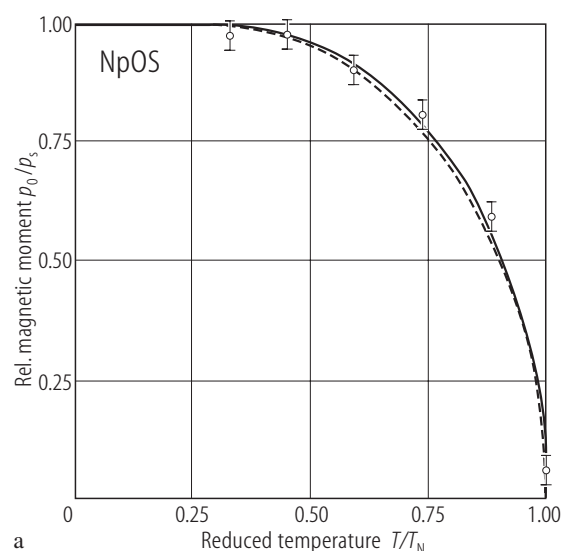




**Fig. 42.** NpOS. (a) <sup>237</sup>Np Mössbauer spectra obtained at several temperatures from 1.4 to 4.2 K in zero external magnetic field [89ABBB]. Note clear hyperfine structures signaling a long-range magnetic order. The isomer shift is  $-5.2(2)$  mm/s (with respect to NpAl<sub>2</sub>), as expected for Np<sup>4+</sup>. The quadrupolar interaction is  $e^2qQ = 0$ . The FWHM parameter (full width at half maximum) is as large as 8.4 mm/s (instead of usually observed 4.5 mm/s). This latter feature the authors interpreted in a dynamic model with two different relaxation frequencies, associated with the magnetic moment components along and perpendicular to the crystallographic  $c$ -axis, respectively. For comparison see the Mössbauer spectra in Fig. 41 and the hyperfine parameters given in Table S. (b) <sup>237</sup>Np Mössbauer spectra obtained at  $T = 2.3$  K in an applied magnetic field of 5, 7.5 and 10 T (from bottom to top, respectively) [89ABBB].

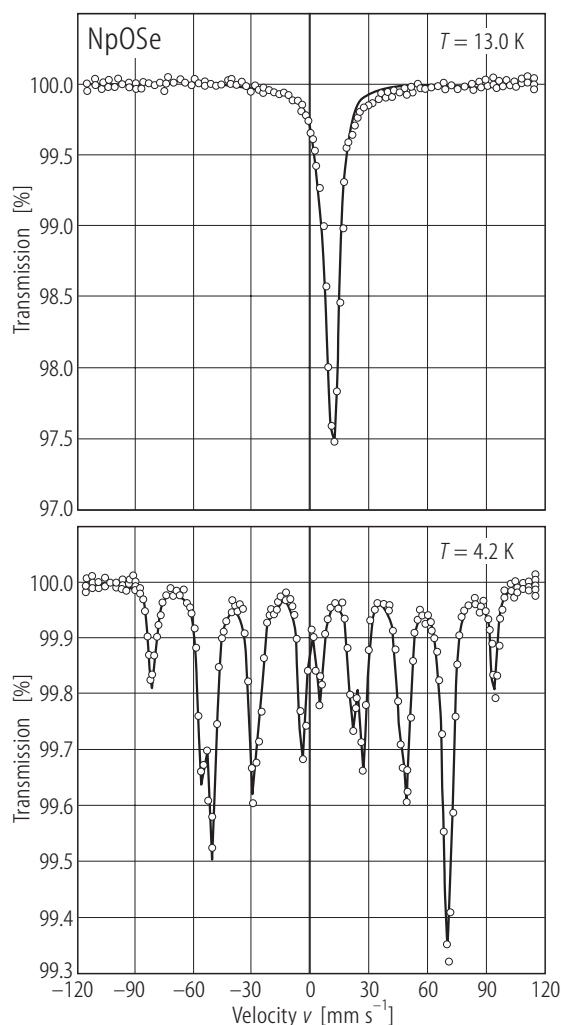


**Fig. 43.** NpOY, Y = S, Se. Hyperfine field,  $B_{\text{hf}}$ , (left-hand side scale) and the corresponding ordered magnetic moment,  $p_o$ , (right-hand side scale) vs. temperature,  $T$  as derived from the  $^{237}\text{Np}$  Mössbauer spectra presented in Fig. 45 [89ABBB]. The ordering temperatures are 4.2 and 11 K, for NpOS and NpOSe, respectively. The neptunium saturation magnetic moments  $p_s$  are 0.82 and 1.64  $\mu_B$ , for NpOS and NpOSe, respectively.



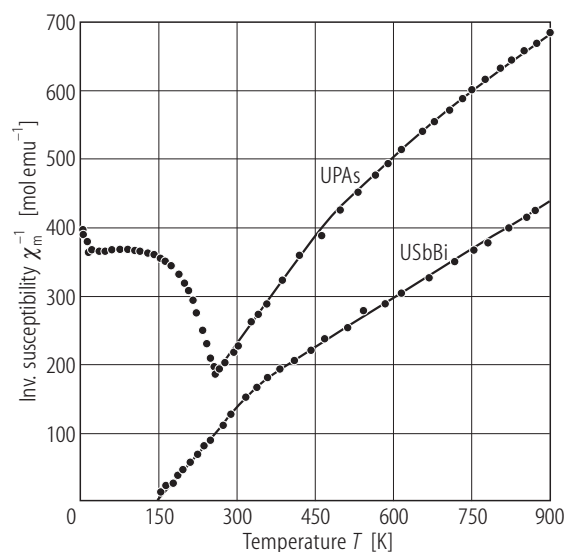
**Fig. 44.** NpOS. (a) Ratio of the neptunium ordered magnetic moment by its saturation value,  $p_o/p_s$ , vs. reduced temperature,  $T/T_N$ , as derived from Mössbauer spectroscopy (circles) and as calculated in the refined crystal field model with the assumption  $p_o \parallel c$ -axis (solid curve) and  $p_o \perp c$ -axis (dashed curve) [89ABBB]. The theoretical results were obtained by solving self-consistently the Brillouin-type problem with the CF parameters listed in Table U. For further details see the original paper. Note that the  $p_o \parallel c$  curve gives a slightly better fitting to the experimental points than the  $p_o \perp c$  curve. (b) Reciprocal molar magnetic

susceptibility,  $\chi_m^{-1}$ , vs. temperature,  $T$ , as measured (solid curve) and calculated in various crystal field models [89ABBB]. Dotted line: point charge model (PCM) with the intermediate coupling scheme and the nearest neighbours approximation (exchange interactions neglected); dashed line: PCM + anisotropic exchange; dash-dotted line: refined model (RM) for  $p_o \parallel c$  + anisotropic exchange; dash-dash-dotted line: RM for  $p_o \perp c$  + anisotropic exchange. The PCM CF parameters are listed in Table T. The CF energy levels in all the models considered are listed in Table V. For discussion see the original paper.



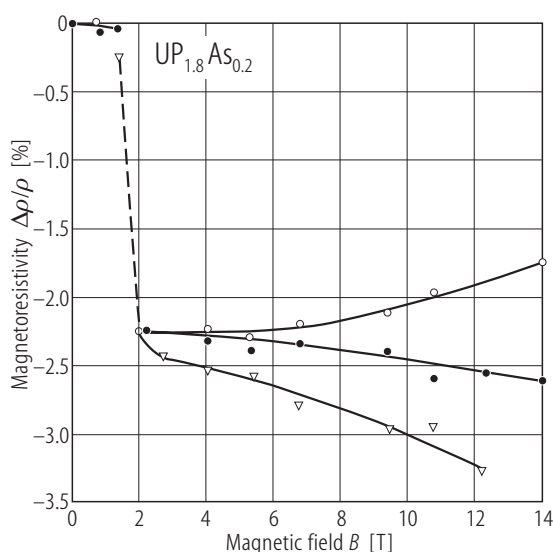
**Fig. 45.** NpOSe.  $^{237}\text{Np}$  Mössbauer spectra obtained at  $T = 4.2$  K and 13 K in zero external magnetic field [89ABBB]. Note clear hyperfine structures signaling a long-range magnetic order. The isomer shift is  $-3.2(2)$  mm/s (with respect to  $\text{NpAl}_2$ ), pointing to a  $4^+$  valency of the Np ions. The quadrupolar interaction is  $e^2qQ = 11.6(3)$  mm/s. For comparison see the Mössbauer spectra in Fig. 40 and the hyperfine parameters in Table S.

**Fig. 49.**  $\text{UP}_{1.8}\text{As}_{0.2}$ . Magnetoresistivity,  $\Delta\rho/\rho$ , vs. magnetic field,  $B$ , up to 14 T, measured at 4.2 K on a single crystal with  $i \parallel a$ -axis (hard magnetization direction) in magnetic field  $B \parallel c$ -axis (open circles),  $B \parallel b$ -axis (open triangles) and  $B \parallel a$ -axis (filled circles) [98HCPF]. Note a step-like change in  $\Delta\rho/\rho$  between 1.6 and 2 T. The magnitude of this jump and the critical field do not depend on the field direction. Thus it cannot be a metamagnetic transition but may rather result from the formation of an isotropic magnetic impurity state in strongly anisotropic  $\text{UP}_2$  matrix when a small part of P atoms are replaced by As atoms.



**Fig. 47.** UPAs, USbBi. Reciprocal molar magnetic susceptibility,  $\chi_m^{-1}$ , vs. temperature,  $T$ , up to 900 K [79TZ]. USbBi orders ferromagnetically below 140 K. UPAs is antiferromagnetic below 264 K. The solid lines are fits of the susceptibility to the formula  $\chi_m^{-1} = \left(\frac{A}{T} + B\right)^{-1} + \lambda$  with the parameters given in Table E.

For Figs. 46, 48 see next page



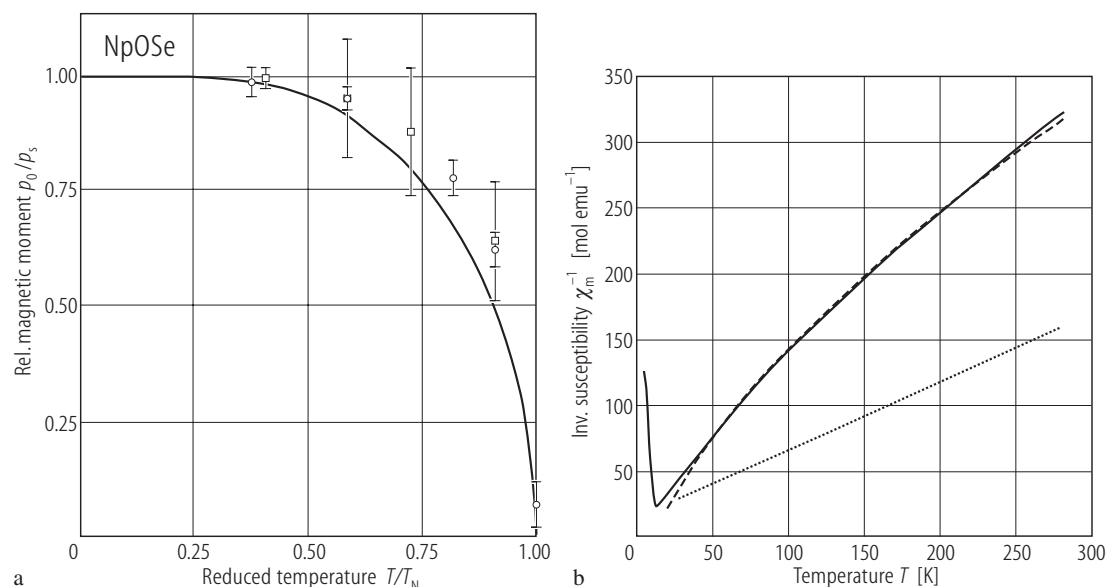


**Fig. 46.** NpOSe. (a) Ratio of the neptunium ordered magnetic moment by its saturation value,  $p_o/p_s$ , vs. reduced temperature,  $T/T_N$ , as derived from Mössbauer spectroscopy (circles), neutron powder diffraction (squares) and as calculated in the refined crystal field model with the assumption  $p_o \parallel c$ -axis (solid curve) [89ABBB]. The theoretical results were obtained by solving self-consistently the Brillouin-type problem with the CF parameters listed in Table U. For further details see the original paper. (b) Reciprocal molar magnetic susceptibility,  $\chi_m^{-1}$ , vs. temperature,  $T$  as measured (solid

curve) and calculated in various crystal field models [89ABBB]. Dotted line: point charge model (PCM) with the intermediate coupling scheme and the nearest neighbours approximation (exchange interactions neglected); dashed line: PCM + anisotropic exchange. The authors mention that the refined CF model gave the  $\chi_m^{-1}(T)$  curve very similar to the dashed one. The PCM CF parameters are listed in Table I. The CF energy levels in all the models considered are listed in Table V. Note a good agreement between the experimental and theoretical results

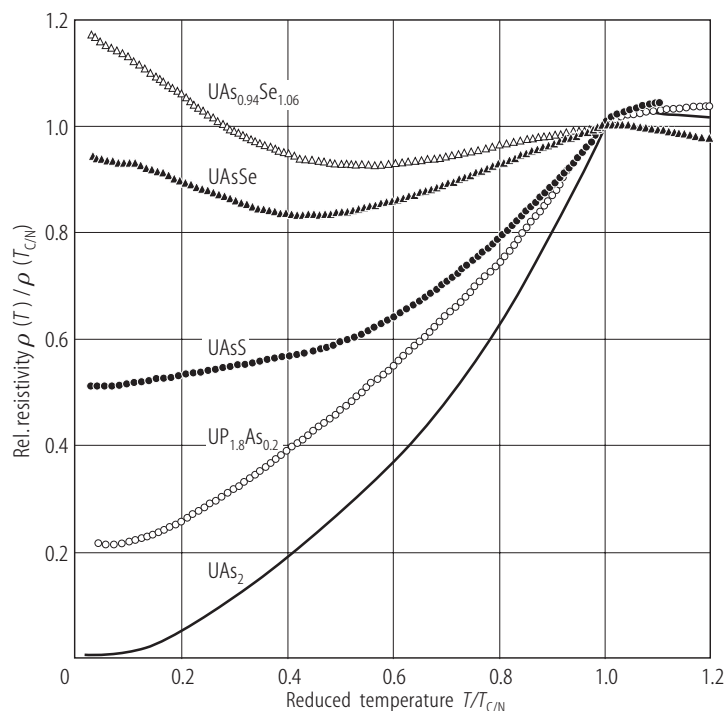


**Fig. 48.** UP<sub>1.8</sub>As<sub>0.2</sub>, UAsS, UAs<sub>0.94</sub>Se<sub>1.06</sub>, UAsSe. Electrical resistivity normalised to its value at the magnetic ordering temperature  $T_{CN}$ ,  $\rho(T)/\rho(T_{CN})$ , vs. normalised temperature,  $T/T_{CN}$ , measured on single crystals with  $i \perp c$ -axis [98HCPF]. Open circles: UP<sub>1.8</sub>As<sub>0.2</sub> ( $T_N = 223$  K); filled circles: UAsS ( $T_C = 117$  K); open triangles: UAs<sub>0.94</sub>Se<sub>1.06</sub> ( $T_C = 102$  K); filled triangles: UAsSe ( $T_C = 108.5$  K). For comparison the resistivity of an isostructural diarsenide UAs<sub>2</sub> ( $T_N = 273$  K) is shown. Note an increase in the residual resistivity on going from UAsSe to UAs<sub>0.94</sub>Se<sub>1.06</sub>, which is presumably due to disordered occupation of the anion positions.

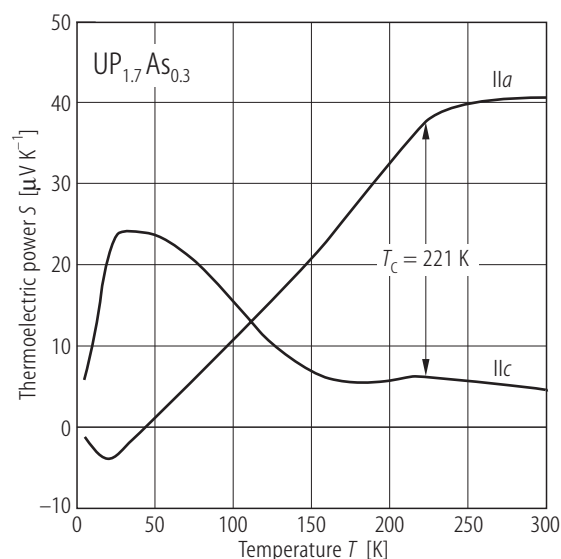


**Fig. 50.**  $\text{UP}_{1.7}\text{As}_{0.3}$ . Thermoelectric power,  $S$ , vs. temperature,  $T$ , measured on a single crystal along the  $a$ - and  $c$ -axes [01HWWK]. The arrows mark the antiferromagnetic phase transition at  $T_N = 221$  K. Note a strong anisotropy.

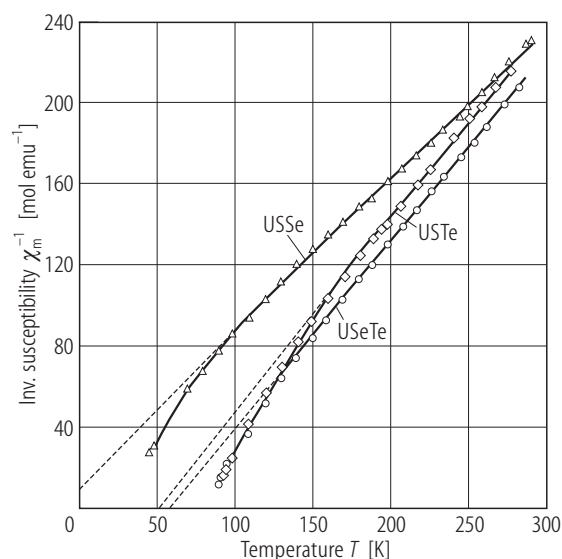


**Fig. 51.**  $\text{UY}'$ ,  $\text{Y}, \text{Y}' = \text{S, Se, Te}$ . Reciprocal molar magnetic susceptibility,  $\chi_m^{-1}$ , vs. temperature,  $T$  for  $\text{USSe}$ ,  $\text{USTe}$ ,  $\text{USeTe}$  [77ZSM]. The dashed lines mark fits of the susceptibility to a Curie-Weiss law with the parameters given in Table B. The deviations from a straight-line behaviour observed for all three compounds at low temperatures the authors attributed to short range magnetic ordering.

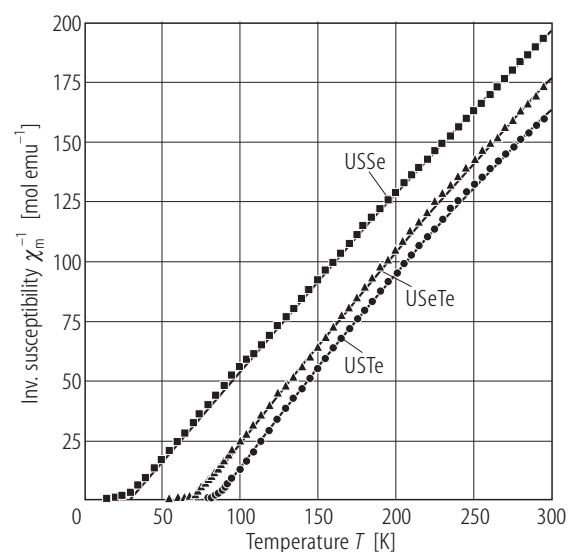


**Fig. 52.**  $\text{UY}'$ ,  $\text{Y}, \text{Y}' = \text{S, Se, Te}$ . Reciprocal molar magnetic susceptibility,  $\chi_m^{-1}$ , vs. temperature,  $T$ , measured along the easy magnetization axis on single crystals of  $\text{USSe}$  (squares),  $\text{USTe}$  (circles),  $\text{USeTe}$  (triangles) [94TKSP]. The solid lines are fits of the susceptibility to a modified Curie-Weiss law with the parameters given in Table B.

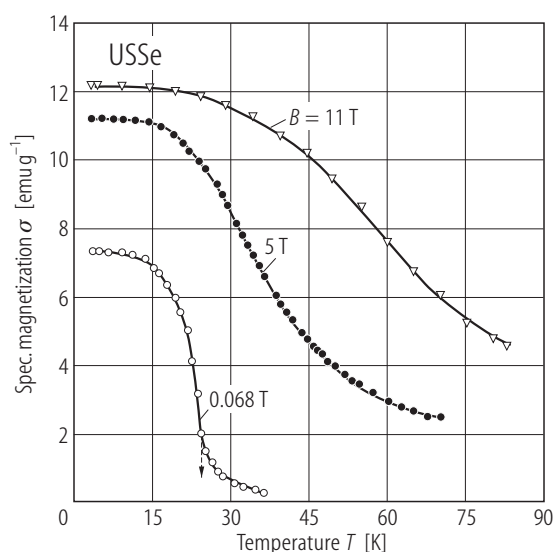


**Fig. 53.**  $\text{USSe}$ . Specific magnetization,  $\sigma$ , vs. temperature,  $T$ , measured in a field of 0.068 T (open circles), 5 T (full circles) and 11 T (triangles) [77ZSM]. The compound orders ferromagnetically at  $T_C = 25$  K.

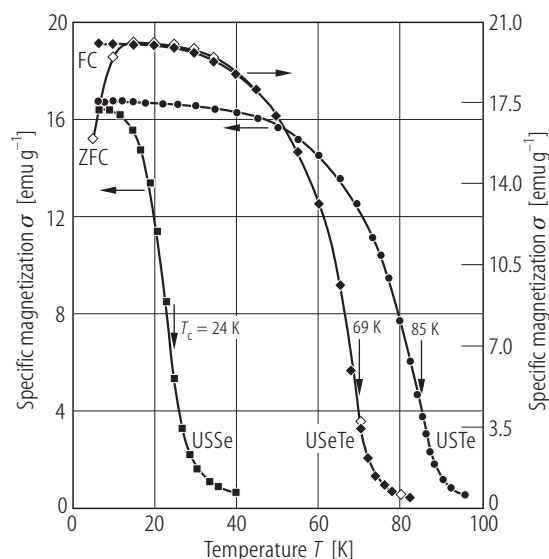


**Fig. 54.** UYY', Y,Y' = S, Se, Te. Specific magnetization,  $\sigma$ , vs. temperature,  $T$ , measured in a field of 0.2 T upon cooling the single-crystalline samples in zero (ZFC, open symbols) and non-zero (FC, filled symbols) magnetic field for USSe (squares), USeTe (circles), USeTe (diamonds) [94TKSP]. Note different vertical scale for USeTe. The compounds order ferromagnetically at  $T_c = 24, 85$  and  $69$  K for USSe, USeTe and USeTe, respectively. Note that  $T_c$  found for USeTe differs from that reported for a powder sample (see Fig. 60), presumably due to different stoichiometry of the two specimens measured (the exact composition of the single crystal was  $\text{USe}_{1.28}\text{Te}_{0.72}$ ).

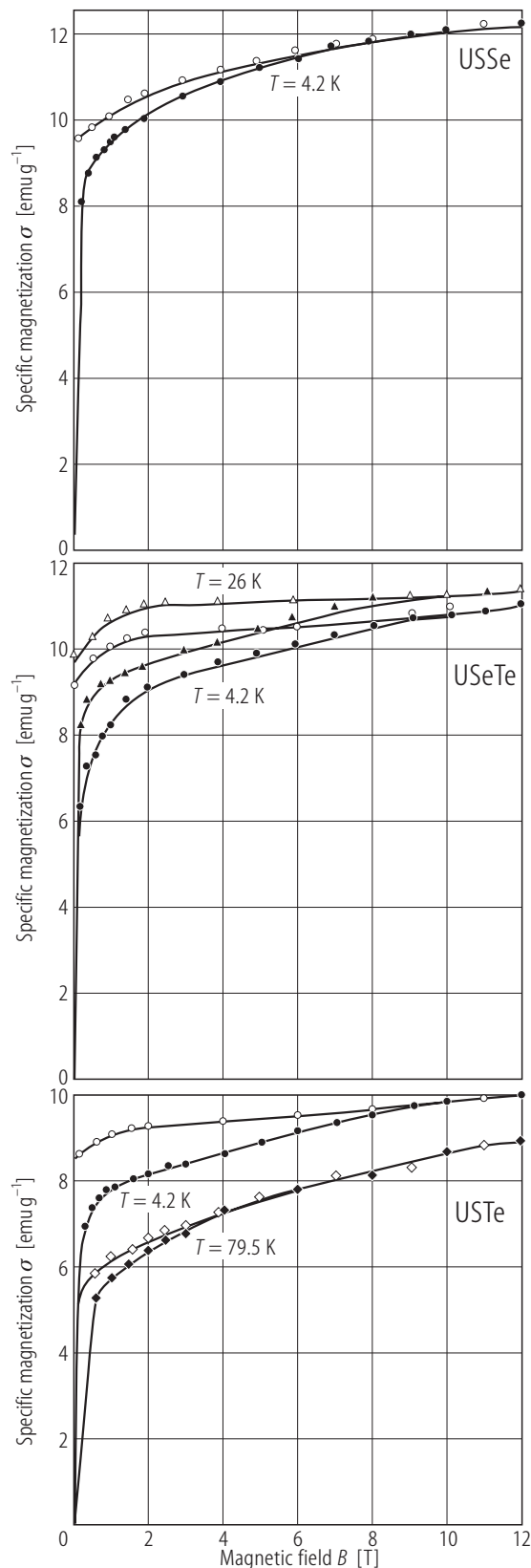


**Fig. 55.** UYY', Y,Y' = S, Se, Te. Specific magnetization,  $\sigma$ , vs. field,  $B$ , taken at  $T = 4.2$  K (circles),  $26$  K (triangles) and  $79.5$  K (diamonds) with increasing (filled symbols) and decreasing (open symbols) magnetic field [77ZSM]. Upper panel: USSe; middle panel: USeTe; bottom panel: UTe. All three compounds are ferromagnets (see also Figs. 53, 59, 60). USSe exhibits the properties characteristic of soft magnetic materials, i.e. rapid initial increase of the magnetization followed by less fast continuous rise with no saturation. The remanence corresponds to ca. 70% of the magnetization obtained in  $B = 12$  T. The two tellurides are harder magnets with the remanence reaching 80-90% of the maximum magnetization, and a clear tendency of  $\sigma(B)$  to saturate in high magnetic fields. This behaviour the authors attributed to uniaxial magnetocrystalline anisotropy. The uranium magnetic moment measured in a field of 12 T was  $1.01, 0.71$  and  $0.91 \mu_B$  for USSe, USeTe and UTe, respectively.

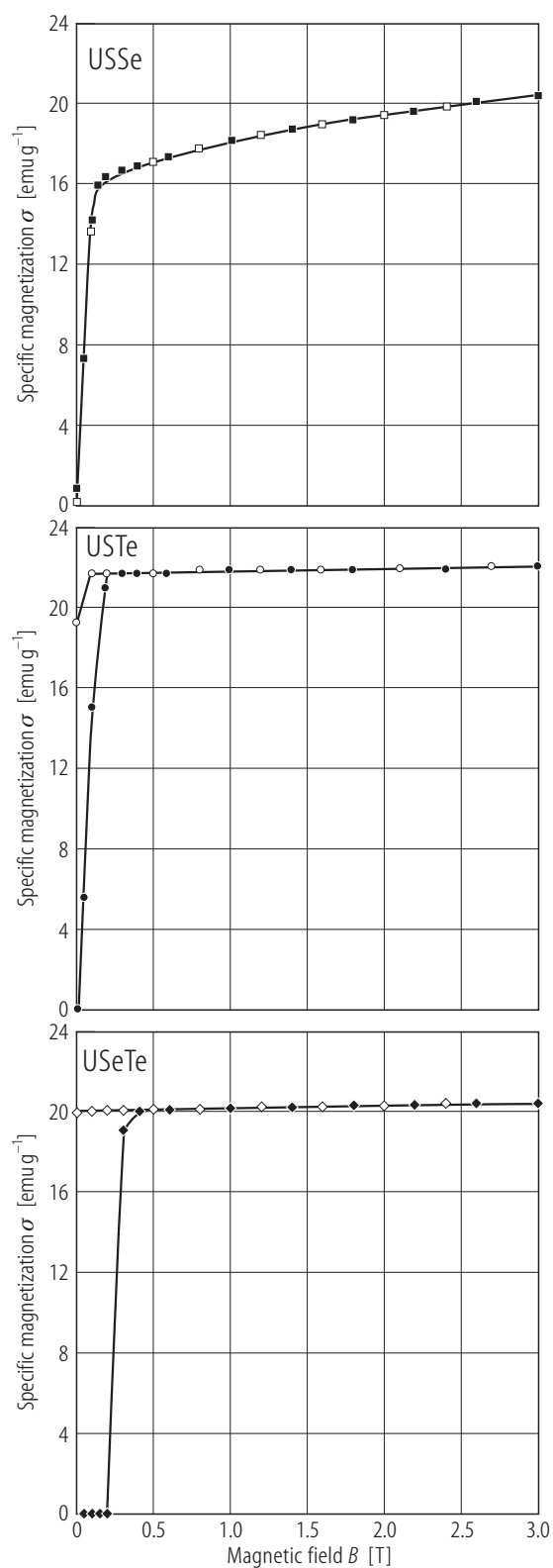


Fig. 56. For caption see next page

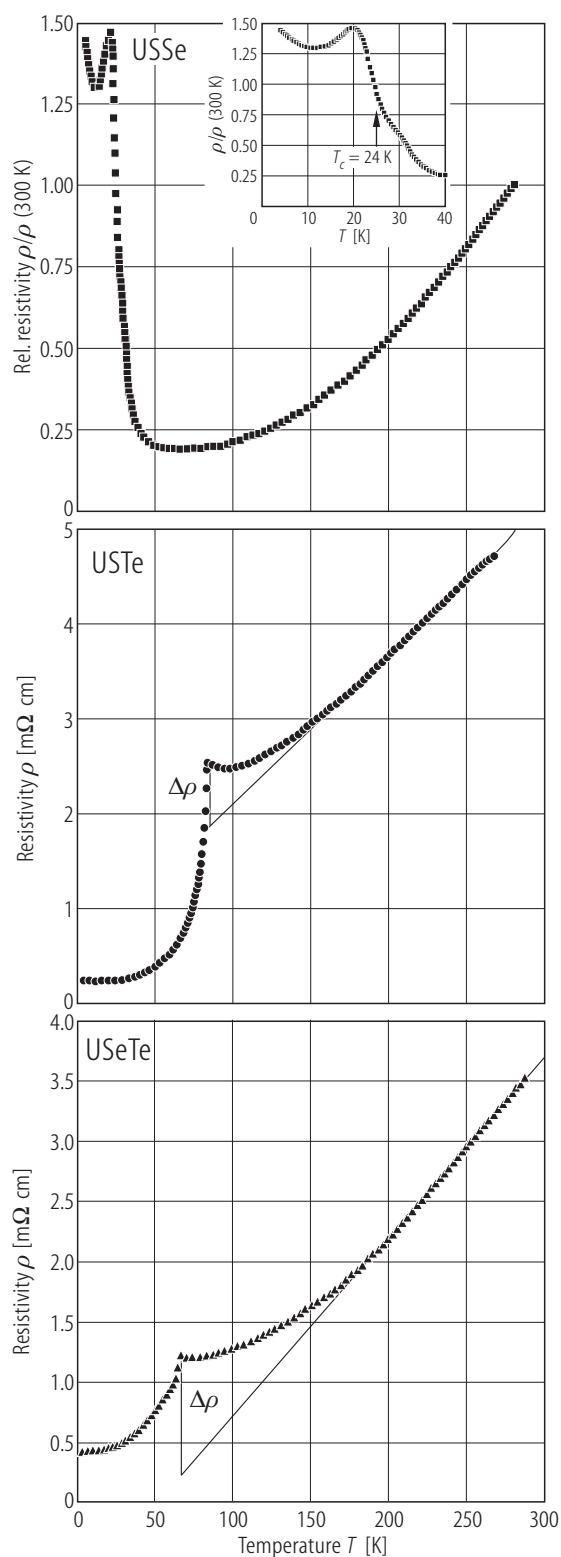
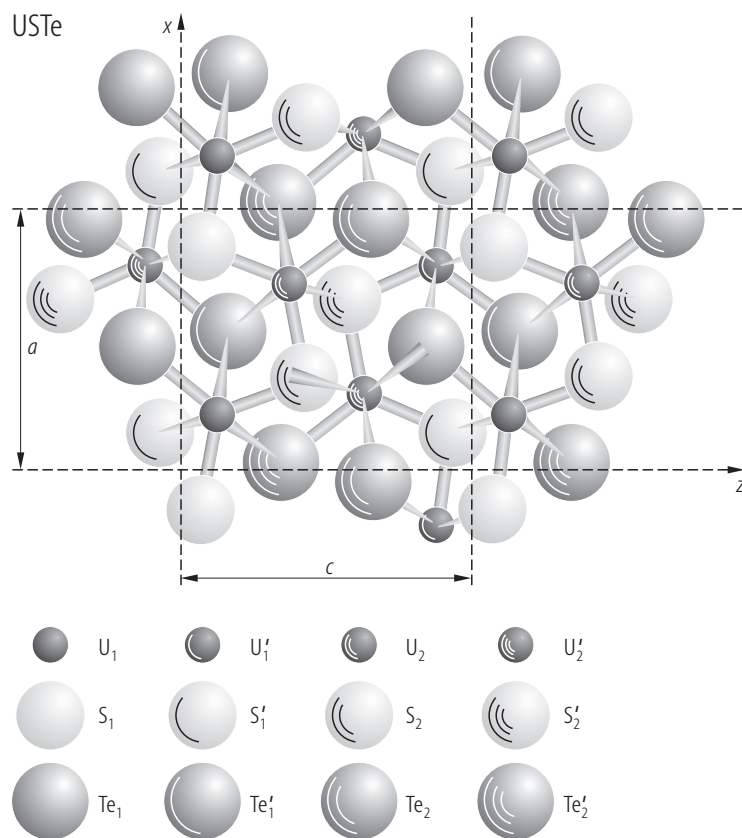


Fig. 57. For caption see next page.

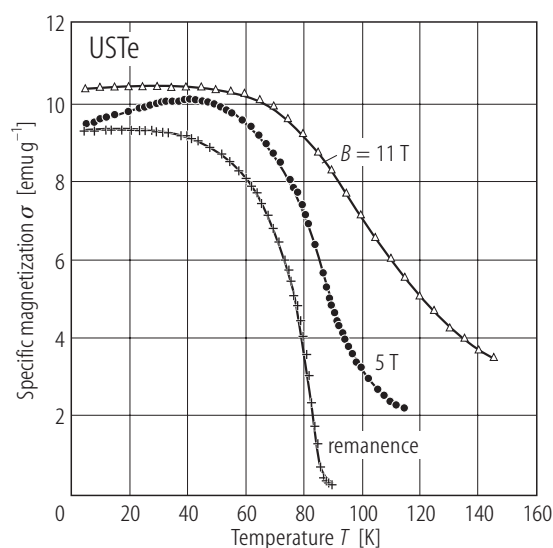
**Fig. 56.**  $UY\text{Y}'$ ,  $Y, Y' = \text{S, Se, Te}$ . Specific magnetization,  $\sigma$ , vs. field,  $B$ , taken at 5 K with increasing (filled symbols) and decreasing (open symbols) magnetic field on single crystals of USSe (squares), USTe (circles) and USeTe (diamonds) freely placed in a sample holder [94TKSP]. It is assumed that these data represent the magnetization along the easy axis. USSe is a soft ferromagnet with no hysteresis effect and lack of saturation up to 3 T. The high field susceptibility ( $B > 0.5$  T) is  $117 \cdot 10^{-6}$  emu/g. The other two compounds are hard magnets with almost 100 % remanence. The saturation magnetic moments amount to  $1.55$  and  $1.62 \mu_B$  in USTe and USeTe, respectively. Note a pronounced domain effect in USeTe.

**Fig. 57.**  $UY\text{Y}'$ ,  $Y, Y' = \text{S, Se, Te}$ . Electrical resistivity,  $\rho$ , vs. temperature,  $T$ , measured on single crystals of USSe (squares), USTe (circles) and USeTe (triangles) with the current flowing along the  $b$ -axis [94TKSP]. For USSe the ratio  $\rho/\rho(300\text{K})$  is presented. Inset: low temperature part of  $\rho(T)$  for USSe. Note a behaviour characteristic of ferromagnetic semiconductors with cusp-like anomalies in the resistivity of USTe and USeTe at the ferromagnetic phase transitions (see Fig. 54). The solid lines mark a linear behaviour of the resistivity at high temperatures and define the  $\Delta\rho$  values which can be considered as a measure of the number of free carriers. From the observed increase in  $\Delta\rho/\rho(T_C)$  on going from USTe to USeTe (28% and 76%, respectively) the authors deduced a strong reduction in the number of carriers. Below 50 K the resistivity of both compounds can be fitted by the formula:  $\rho(T) = a + c_m T^2 \exp(-\Delta/T)$ , appropriate for scattering processes on spin wave excitations over the gap  $\Delta$ , with the following fit parameters:  $a = 228 \mu\Omega\text{cm}$ ,  $c_m = 0.124 \mu\Omega\text{cm/K}^2$  and  $\Delta = 60$  K for USTe and :  $a = 408 \mu\Omega\text{cm}$ ,  $c_m = 0.286 \mu\Omega\text{cm/K}^2$  and  $\Delta = 36$  K for USeTe. In the case of USSe the ferromagnetic phase transition manifests itself as a small kink on the  $\rho(T)$  curve. The complex resistivity behaviour below  $T_C$  was interpreted by the authors as a result of gradual closing the energy gap with lowering the temperature, which is caused by the onset of magnetic order, yet with leaving a remanent gap, responsible for a sharp increase of the resistivity at the lowest temperatures. The semiconducting gap was estimated to decrease from about 430 K just above  $T_C$  to about 1.5 K below 7 K.

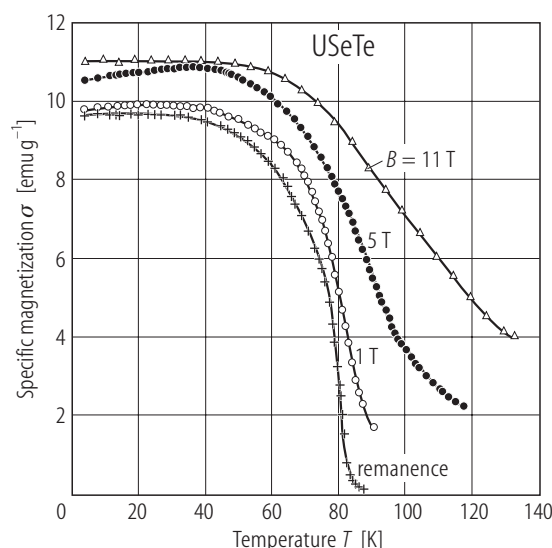


**Fig. 58.** USTe. Crystal structure [73RN].

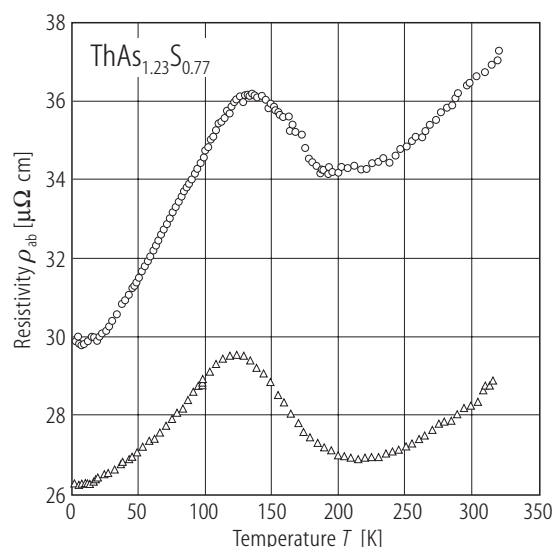




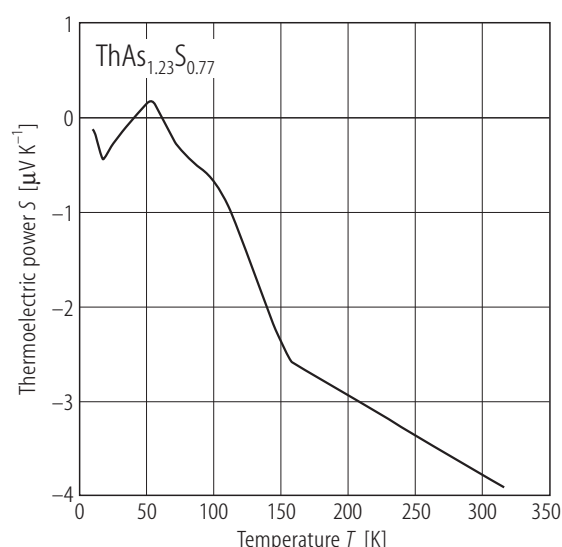
**Fig. 59.** UTe. Specific magnetization,  $\sigma$ , vs. temperature,  $T$ , measured in a field of 5 T (full circles) and 11 T (triangles) as well as in remanent field (crosses) [77ZSM]. The compound orders ferromagnetically at  $T_C = 87$  K. Note a broad maximum in  $\sigma(T)$  taken in  $B = 5$  T, signaling a large magnetocrystalline anisotropy.



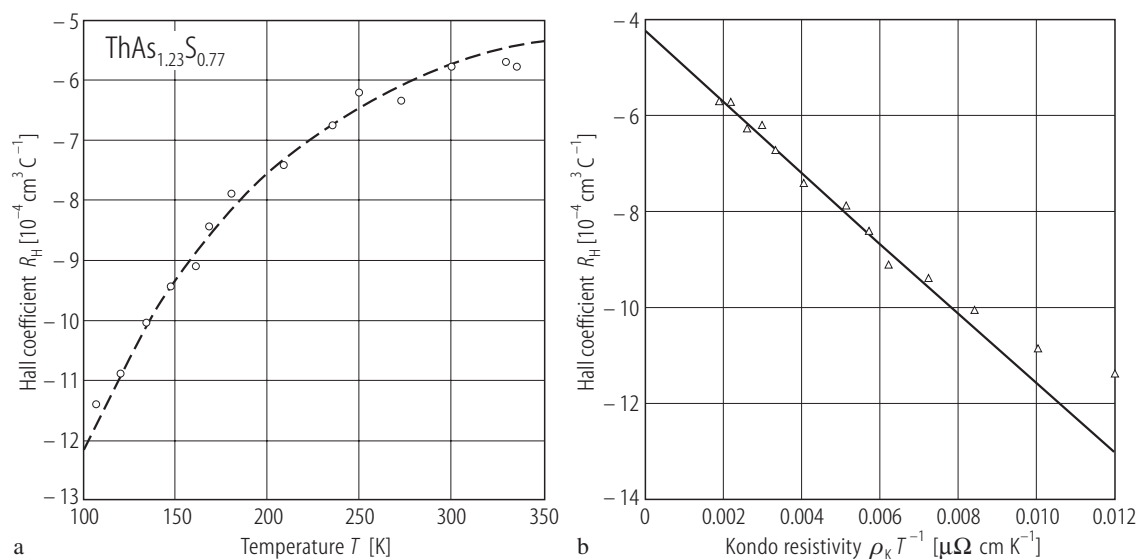
**Fig. 60.** USeTe. Specific magnetization,  $\sigma$ , vs. temperature,  $T$ , measured in a field of 1 T (open circles), 5 T (full circles) and 11 T (triangles) as well as in remanent field (crosses) [77ZSM]. The compound orders ferromagnetically at  $T_C = 83$  K. Note a broad maximum in  $\sigma(T)$  taken in  $B = 1$  T and  $B = 5$  T, signaling a large magnetocrystalline anisotropy.



**Fig. 61.**  $\text{ThAs}_{1.23}\text{S}_{0.77}$ . Electrical resistivity,  $\rho_{ab}$ , vs. temperature,  $T$ , in the range 2...320 K measured on two different single crystals with  $i \perp c$ -axis [01WWMC,02HW]. A broad shallow minimum around 200 K is reminiscent of single-ion Kondo effect. Kondo-like features are seen also in the thermopower and the Hall coefficient of  $\text{ThAs}_{1.23}\text{S}_{0.77}$  (see Figs. 62 and 63, respectively). Yet, this behaviour has not a magnetic nature because the compound is diamagnetic. Instead, a non-magnetic two-level system scenario has been proposed as for UPS and UAsSe (compare Figs. 70 and 119, respectively), which arises due to off-stoichiometry of these compounds.



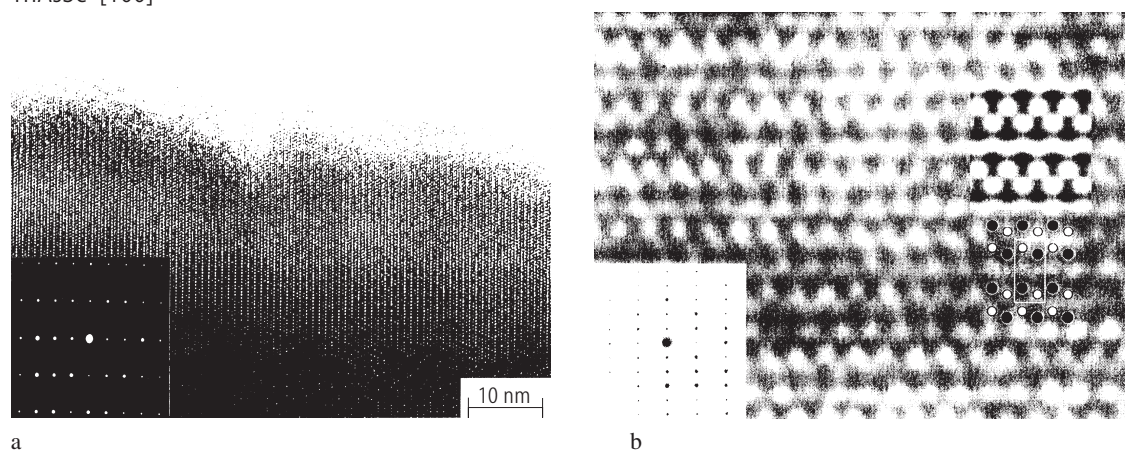
**Fig. 62.**  $\text{ThAs}_{1.23}\text{S}_{0.77}$ . Thermoelectric power,  $S$ , vs. temperature,  $T$ , in the range 2...320 K measured on a single crystal along the  $a$ -axis [01WWMC,02HW]. Note a low-temperature maximum in  $S(T)$  that is considered as a characteristic feature of Kondo systems.



**Fig. 63.**  $\text{ThAs}_{1.23}\text{S}_{0.77}$ . (a) Hall coefficient,  $R_H$ , vs. temperature,  $T$ , in the range 107...336 K, measured on a single crystal in a magnetic field of 1.25 T applied along the  $c$ -axis [02HW]. The observed temperature dependence of  $R_H$  is reminiscent of Kondo systems. (b) Hall coefficient,  $R_H$ , vs. Kondo resistivity over temperature,  $\rho_K/T$ , measured as in panel (a) [01WWMC,02HW]. The Kondo resistivity was derived from the data presented in Fig. 61, assuming

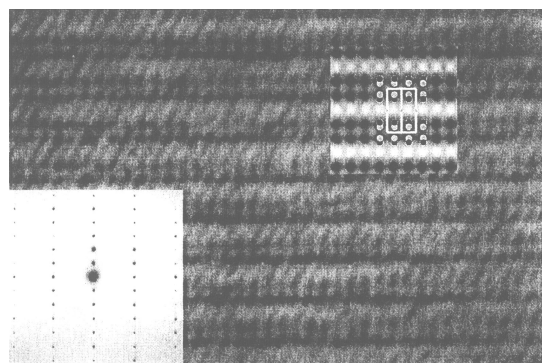
$T_K = 22 \text{ K}$ . The solid line marks a linear behaviour at high temperatures, which possibly indicates the presence of an anomalous contribution to the Hall coefficient due to a Kondo-like scattering mechanism. The linear extrapolation gives the ordinary Hall coefficient  $R_0 = -4.3 \cdot 10^{-4} \text{ cm}^3/\text{C}$  that corresponds in a one band model to the carrier density of  $1.45 \cdot 10^{22} \text{ e/cm}^3$  (1 electron per formula unit) and the Hall mobility of  $13 \text{ cm}^2/\text{Vs}$ .

#### ThAsSe [100]



**Fig. 64.**  $\text{ThAsSe}$ . (a) High resolution transmission electron microscopy (HRTEM) image of a wedge crystal in [100] orientation [01HPWK]. Inset: selected area electron diffraction (SAED) pattern. Note that the crystal studied exhibits a well ordered structure over long distances (at least 400 Å) with no signature of ordering defects or microtwins. At the edge of the crystal there is an amorphous layer resulting from surface oxidation and carbon contamination in the microscope. Changes in the

thickness of the crystal along the normal direction to its edge are visualized by the contrast changes. (b) Magnified portion of the image from panel (a) (the thinnest one close to the edge) after digitalization. Inset: the same image after application of the crystallographic image processing (CIP) procedure, the SAED pattern and a model of the crystal structure with the black dots marking the positions of the Th atoms and the open circles showing the position of both As and Se atoms.

ThAsSe  $[1\bar{1}0]$ 

**Fig. 65.** ThAsSe. High resolution transmission electron microscopy (HRTEM) image of a wedge crystal in  $[1\bar{1}0]$  orientation [01HPWK]. Insets: selected area electron diffraction (SAED) pattern, the image analyzed by the crystallographic image processing (CIP) procedure and a model of the crystal structure with the black dots marking the positions of the Th atoms and the open circles showing the position of both As and Se atoms. Note a good correspondence between the image and the crystal structure model.

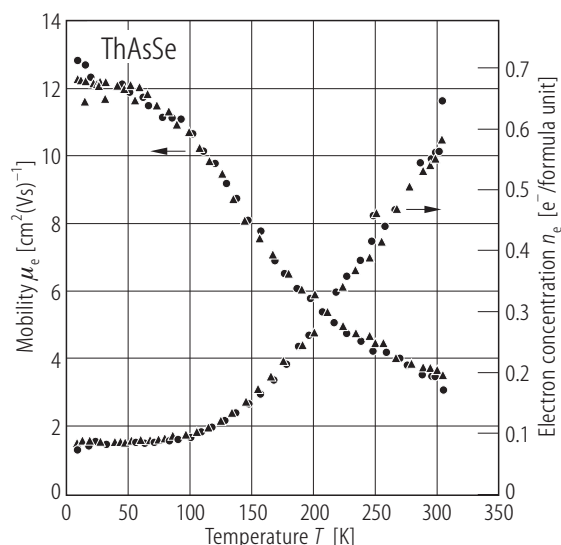
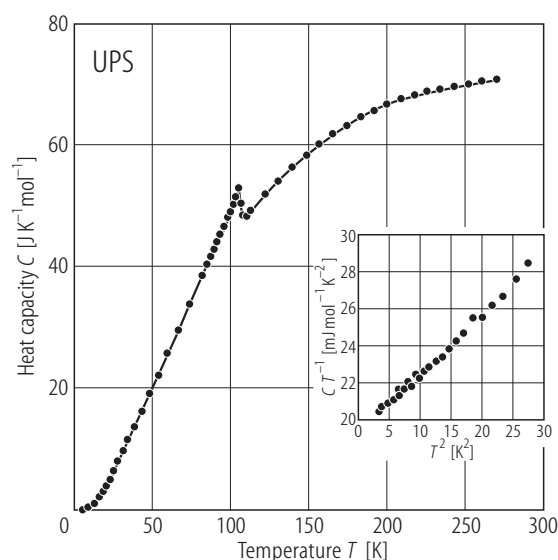


**Fig. 66.** ThAsSe. Free-electron mobility,  $\mu_e$ , (left-hand scale) and free-electron density per formula unit,  $n_e$ , (right-hand scale), vs. temperature,  $T$ , as derived from the Hall effect data, obtained on a single crystal with  $i \perp c$ -axis in a field of 5 T (triangles) and 10 T (circles) applied along the  $c$ -axis [88SBH]. To derive  $n_e$  a one-band model was assumed,  $\mu_e(T)$  was computed from  $n_e(T)$  and the resistivity data shown in Fig. 117. Note a strong reduction in the carrier concentration with decreasing temperature from 0.6 e/f.u. at 300 K to 0.08 e/f.u. below 100 K. Simultaneously the mobility increases with decreasing temperature from 3.5  $\text{cm}^2/\text{Vs}$  at 300 K to 12  $\text{cm}^2/\text{Vs}$  at 2 K. This rather low mobility in a diamagnetic material with light masses ( $m^* \approx 0.2 m_e$ ) indicates strong electron-phonon scattering.

For Fig. 67 see next page.

**Fig. 68.** UPS. Heat capacity,  $C$ , vs. temperature,  $T$ , measured on a single crystal [02WCWH]. The lambda-shaped peak manifests a ferromagnetic phase transition. Inset: low-temperature  $C/T$  vs.  $T^2$ .  $\gamma(0) = 19.3 \text{ mJ/K}^2 \text{ mol}$ ,  $\Theta_D = 264 \text{ K}$ .

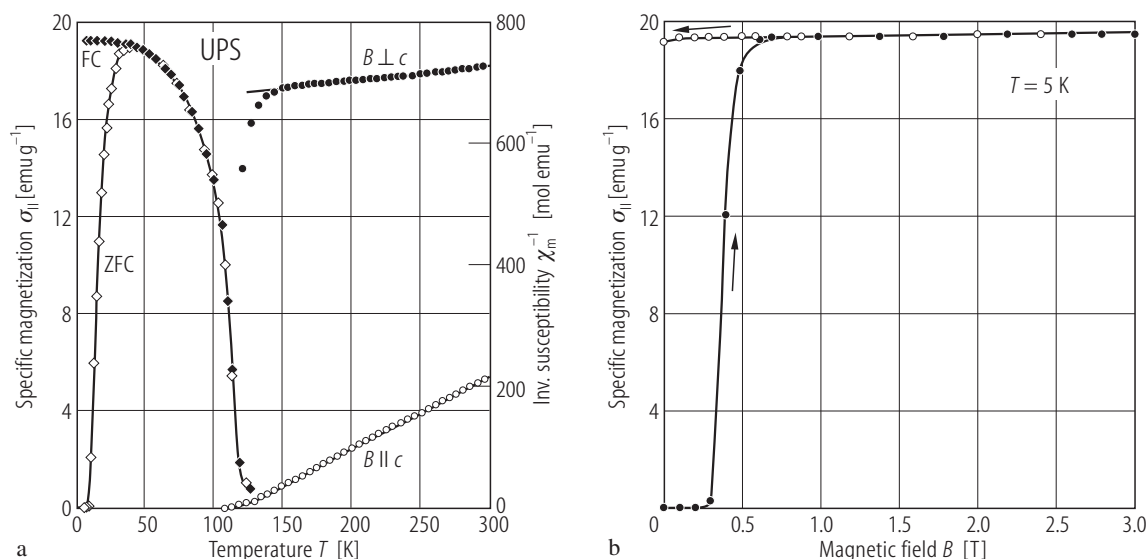


**Fig. 67.** UPS. (a) Specific magnetization,  $\sigma_{||}$ , measured along the  $c$ -axis in a field of 0.2 T with cooling the sample with (FC, full diamonds) and without (ZFC, open diamonds) an applied magnetic field (left-hand scale) and reciprocal longitudinal,  $\chi_{||}^{-1}$ , (open circles), and transversal,  $\chi_{\perp}^{-1}$ , (full circles) molar magnetic susceptibility, measured along and perpendicular to the  $c$ -axis, respectively (right-hand scale) vs. temperature,  $T$  [94KNPZ]. The compound orders ferromagnetically at  $T_C = 118$  K. The solid lines are

Curie-Weiss fits with the parameters given in Table B. Note a pronounced domain effect at low temperatures and strongly anisotropic behaviour of the susceptibility caused mainly by crystal field interactions. (b) Specific magnetization,  $\sigma_{||}$ , vs. magnetic field,  $B$ , taken at 5 K with increasing (full circles) and decreasing (open circles) magnetic field. The saturation uranium magnetic moment is  $1.06 \mu_B$ . Note a salient domain effect.

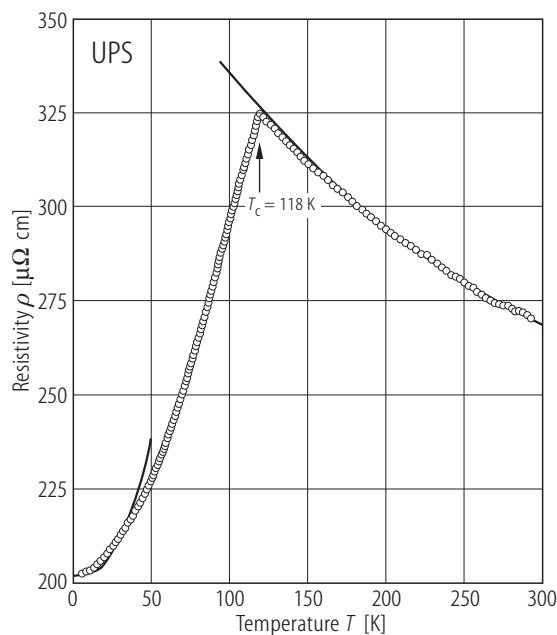


**Fig. 69.** UPS. Electrical resistivity,  $\rho$ , vs. temperature,  $T$ , measured on a single crystal with  $i \perp c$ -axis [94KNPZ]. The arrow marks a ferromagnetic phase transition at  $T_C = 118$  K. Note a strongly negative slope in  $\rho(T)$  in the paramagnetic region. The solid curves are least-squares fits of the resistivity to the functions:  $\rho(T) = \rho_0 + c_m T^2$  (for  $T < 20$

K) and  $\rho(T) = \rho_0 + \rho_0^{\infty} - c_K \ln T$  (for  $T > 120$  K) with the following parameters:  $\rho_0 = 202 \mu\Omega \text{ cm}$ ,  $c_m = 0.014 \mu\Omega \text{ cm/K}^2$ ,  $\rho_0^{\infty} = 429 \mu\Omega \text{ cm}$  and  $c_K = 63.6 \mu\Omega \text{ cm}$  (for the meaning of all the terms see the original paper).

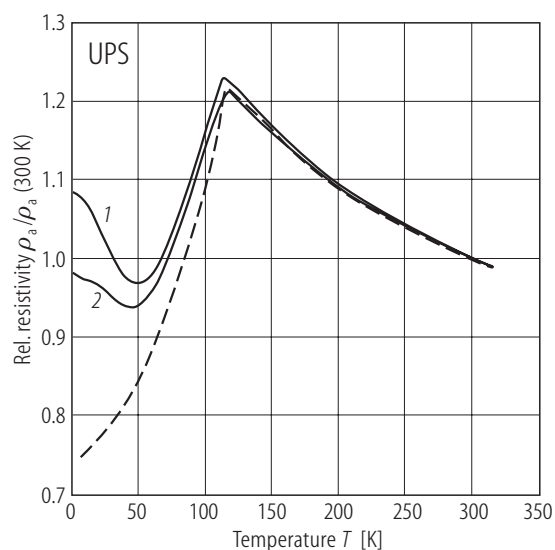


**Fig. 70.** UPS. Reduced electrical resistivity,  $\rho_a/\rho_a(300\text{ K})$ , vs. temperature,  $T$ , in the range 2...320 K measured on two different single crystals with  $i \parallel a$ -axis [01WWH]. The room temperature resistivity  $\rho_a(300\text{ K})$  is ca.  $240\text{ }\mu\Omega\text{cm}$ . The two crystals studied had slightly different Curie temperatures: (1)  $T_C = 113.8\text{ K}$  and (2)  $T_C = 114.6\text{ K}$ . The dashed curve represents for comparison the data taken from [94KNPZ] for a crystal with  $T_C = 118\text{ K}$  (see Fig. 69). Note the low-temperature resistivity upturn, which markedly increases with decreasing  $T_C$ . This feature is tentatively ascribed to non-magnetic Kondo effect involving TLS scattering centers, as in the case of UAsSe (see Fig. 119).

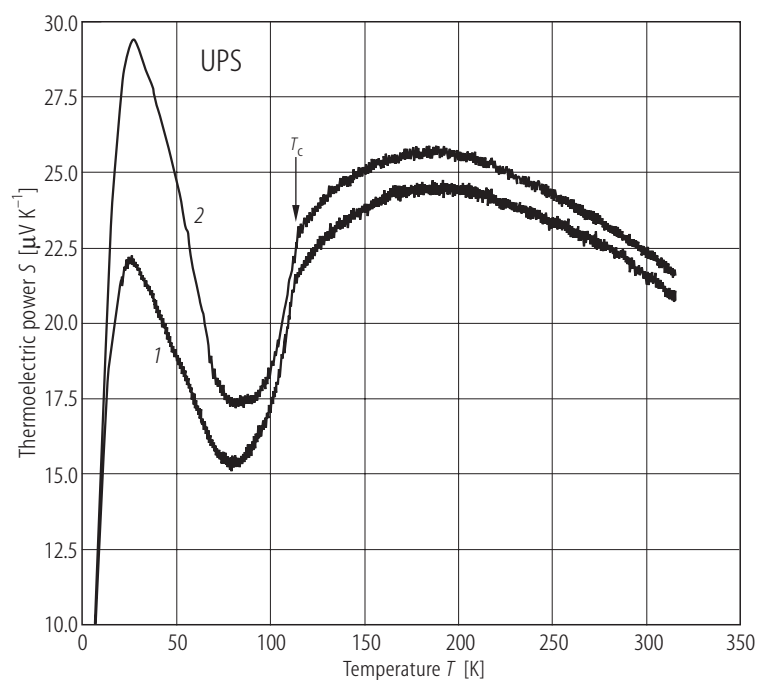


**Fig. 71.** UPS. Thermoelectric power,  $S$ , vs. temperature,  $T$ , measured on two different single crystals with  $\nabla T \perp c$ -axis [01WWH]. The arrow marks the ferromagnetic phase transition. The crystals had slightly different Curie temperatures: (1)  $T_C = 113.8\text{ K}$  and (2)  $T_C = 114.6\text{ K}$ , probably because of tiny differences in the stoichiometry. The peak in  $S(T)$  at about 25 K was interpreted as a hallmark of Kondo effect. Note that the magnitude of this anomaly increases with increasing  $T_C$ .

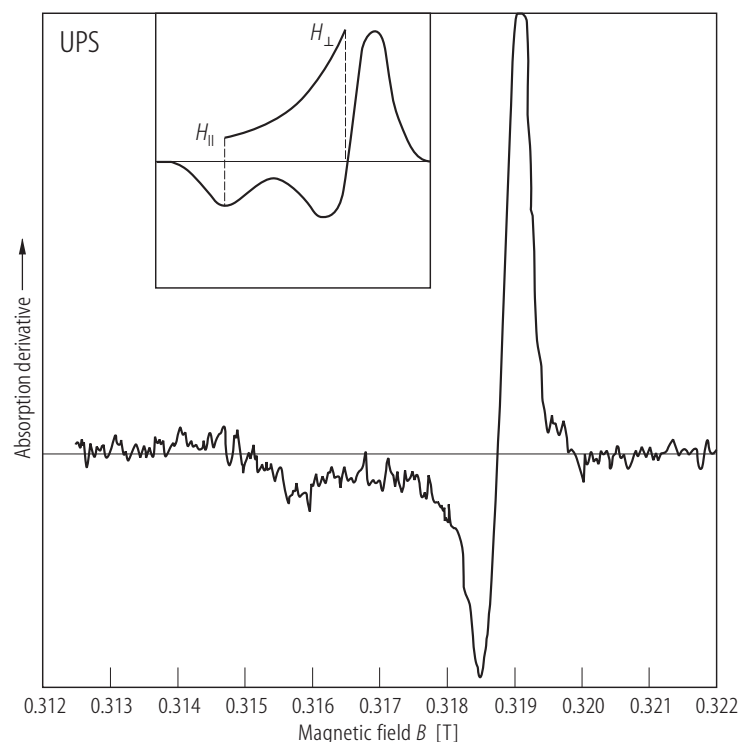


**Fig. 72.** UPS. Powder  $^{31}\text{P}$  NMR spectrum (absorption derivative) taken at a nominal resonance frequency of 5.5244 MHz [82ZZ]. Note the asymmetric line shape characteristic of axial Knight shift anisotropy (the local symmetry at the P site is  $D_{2d}$ ). The inset shows schematically the positions of the two components of the Knight shift. The measured Knight shift parameters:  $K_x = K_y = 0.45(3) \%$ ,  $K_z = 1.45(3) \%$ .

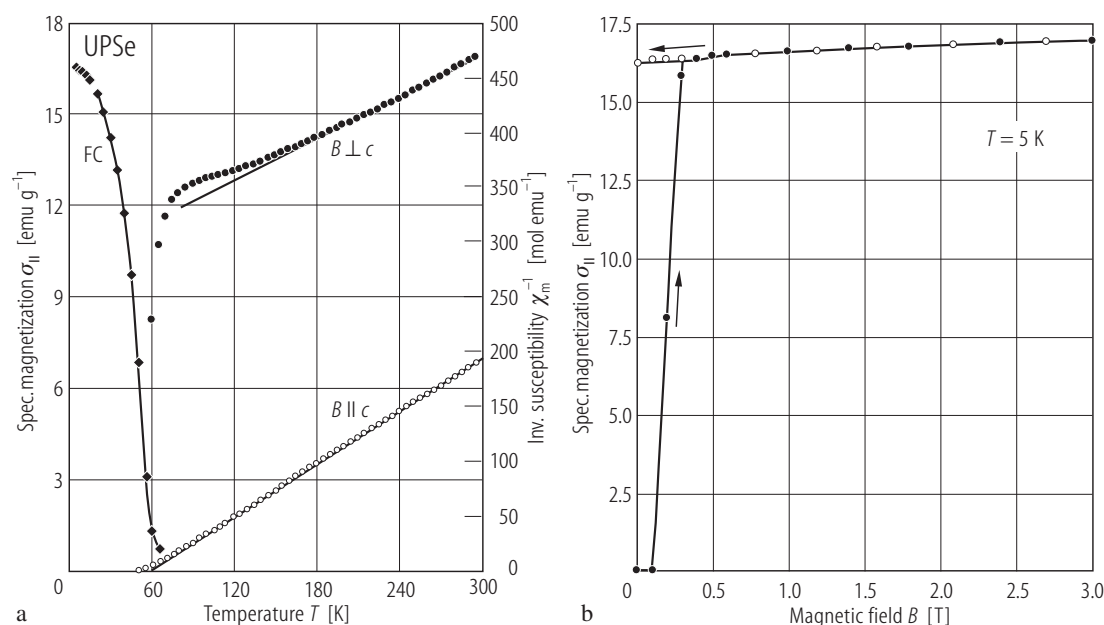


**Fig. 73.** UPS. (a) Specific magnetization,  $\sigma_{\parallel}$ , measured along the  $c$ -axis in a field of 0.2 T with cooling the sample with an applied magnetic field (FC, full diamonds, left-hand scale) and reciprocal longitudinal,  $\chi_{\parallel}^{-1}$ , (open circles), and transversal,  $\chi_{\perp}^{-1}$ , (full circles) molar magnetic susceptibility, measured along and perpendicular to the  $c$ -axis, respectively (right-hand scale) vs. temperature,  $T$  [95KNZ]. The compound orders ferromagnetically at  $T_C = 55$  K. Note that this  $T_C$  of the compound crystallizing with

the UGeTe-type crystal structure is two times lower than  $T_C$  reported for its ZrSiS-type counterpart (see Table B). The solid lines are Curie-Weiss fits with the parameters given in Table B. Note a strongly anisotropic behaviour of the susceptibility caused mainly by crystal field interactions. (b) Specific magnetization,  $\sigma_{\parallel}$ , vs. magnetic field,  $B$ , taken at 5 K with increasing (full circles) and decreasing (open circles) magnetic field. The saturation uranium magnetic moment is  $1.07(2) \mu_B$ .

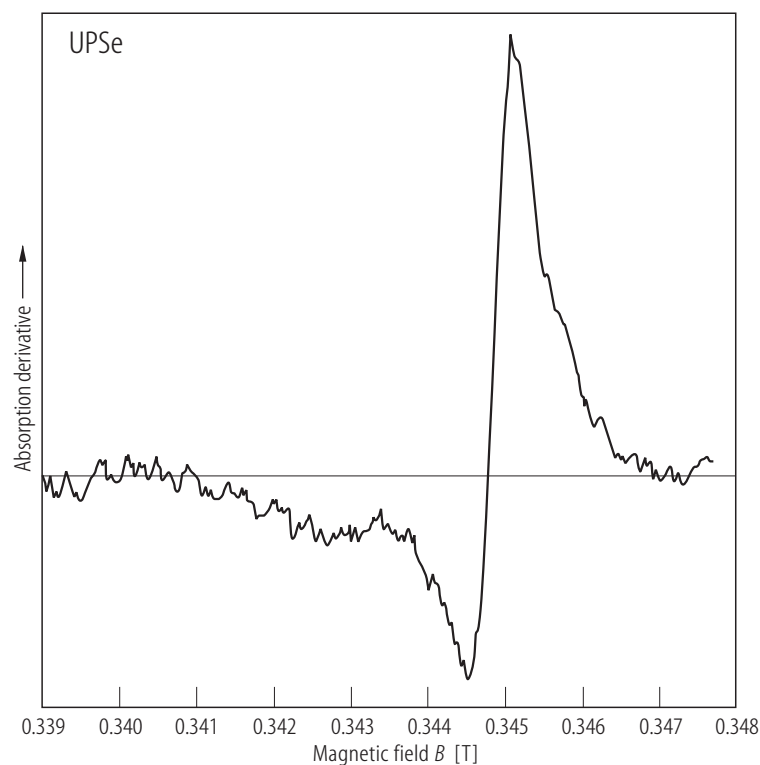


**Fig. 74.** UPSe. Powder  $^{31}\text{P}$  NMR spectrum (absorption derivative) taken at a nominal resonance frequency of 5.985 MHz [82ZZ]. The measured Knight shift has three components which suggest that the local symmetry at the P site is lower than axial (see also the single crystals results given in Fig. 75).

For Fig. 75 see next page

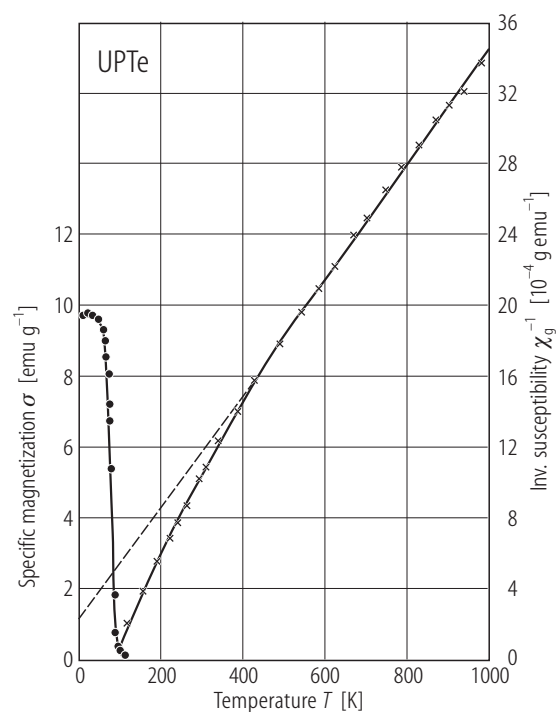


**Fig. 76.** UPTe. Specific magnetization,  $\sigma$ , vs. temperature,  $T$ , taken in a field of 0.4 T (left-hand scale) and reciprocal mass magnetic susceptibility,  $\chi_g^{-1}$ , vs. temperature,  $T$ , up to 1000 K (right-hand scale) [73ZC]. The dashed line is a Curie-Weiss fit with the parameters given in Table B. The compound orders ferromagnetically at  $T_C = 85$  K. See also the single crystal results in Fig. 79.

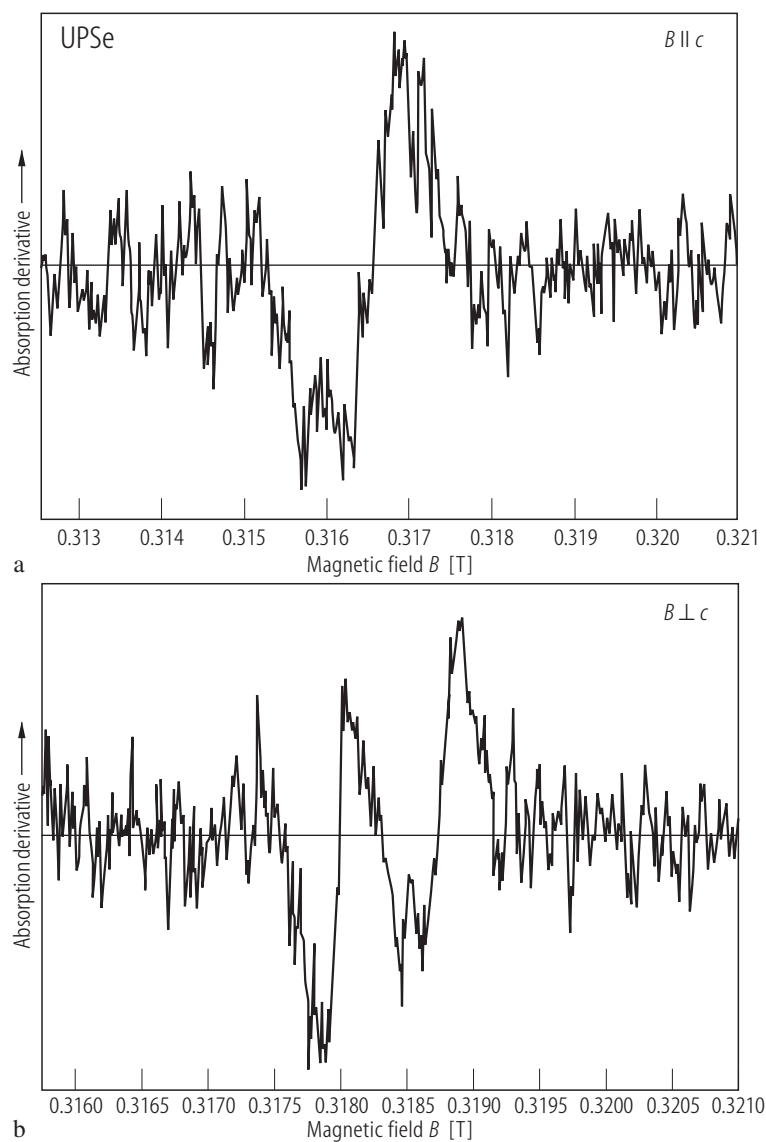


**Fig. 75.** UPSe.  $^{31}\text{P}$  NMR spectrum (absorption derivative) taken on a stack of single crystals with: (a)  $B \parallel c$ -axis at a frequency of 5.5246 MHz; (b)  $B \perp c$ -axis at a frequency of 5.5207 MHz [82ZZ]. Note that for  $B \parallel c$  only one resonance line is seen, while for  $B \perp c$  two resonance lines are observed. The measured Knight shift parameters:  $K_x = 0.48(3) \%$ ,  $K_y = 0.71(3) \%$ ,  $K_z = 1.26(3) \%$ .



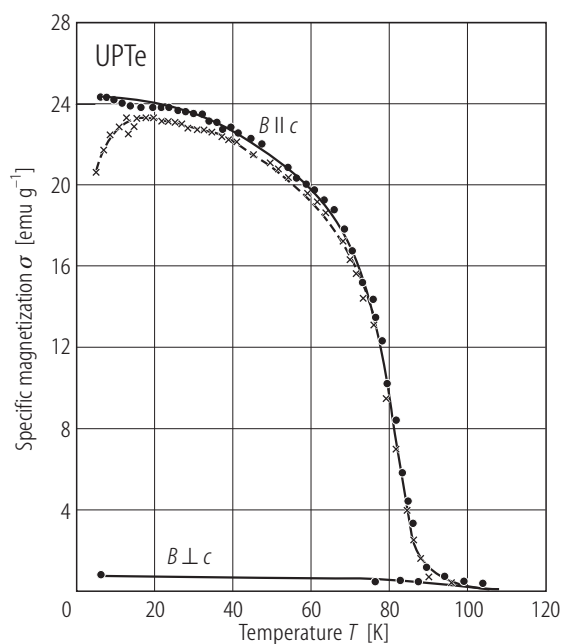


**Fig. 77.** UPTe. Specific magnetization,  $\sigma$ , vs. temperature,  $T$ , measured in a field of 0.64 T (circles) and 0.25 T (crosses) on a single crystal with  $B \parallel c$ -axis and  $B \perp c$ -axis [73ZC]. The solid lines are guides for the eye. The compound orders ferromagnetically at  $T_C = 85$  K with the magnetic moments pointing along the  $c$ -axis. A strong magnetocrystalline anisotropy results from uniaxial character of the crystal field potential.

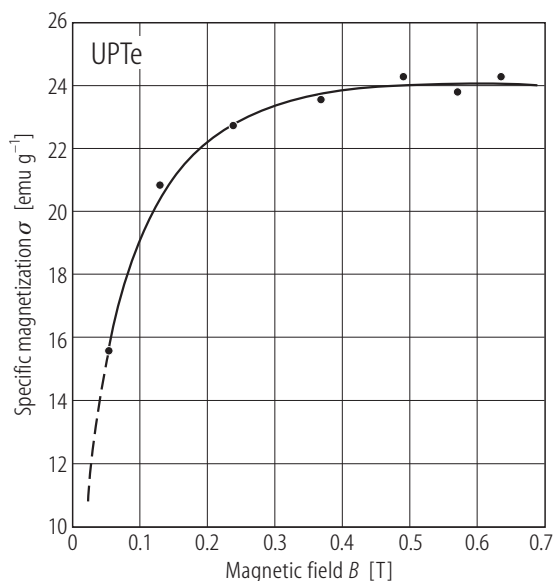


**Fig. 78.** UPTe. Specific magnetization,  $\sigma$ , vs. magnetic field,  $B$ , measured at 4.2 K on a single crystal with  $B \parallel c$ -axis [73ZC]. The compound is a ferromagnet with the uranium magnetic moments aligned along the  $c$ -axis (see Fig. 80). The saturation magnetic moment amounts to  $1.74 \mu_B$ . The magnetization at 4.2 K taken in the direction  $B \perp c$ -axis is about 50 times smaller than that for  $B \parallel c$  (not shown).

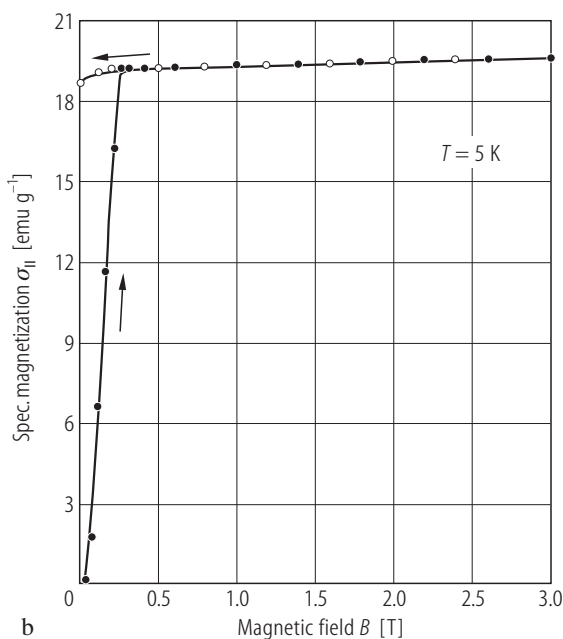
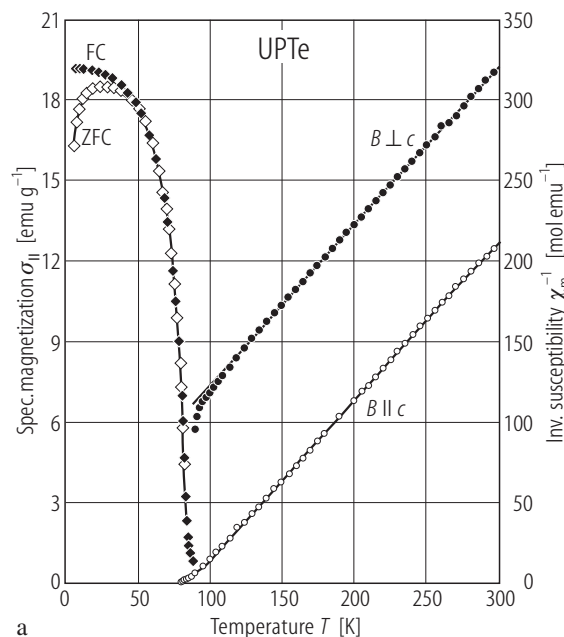


**Fig. 79.** For caption see next page.

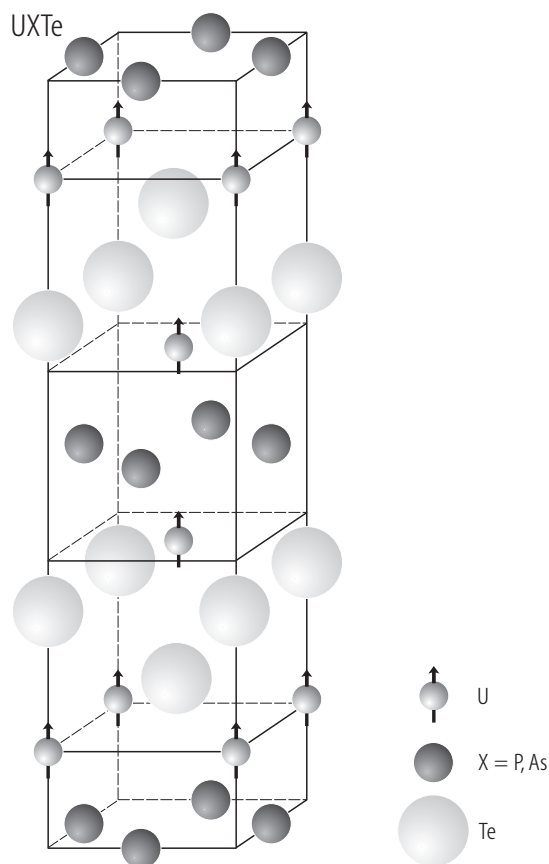


**Fig. 80.** UXTe, X = P, As. Crystal and magnetic structure [74ZMLL]. Both compounds order ferromagnetically at low temperatures with the uranium magnetic moments aligned along the tetragonal  $c$ -axis. The Curie temperature is 85 and 66 K for UPTe and UAsTe, respectively. The ordered magnetic moment  $p_o$  is 1.44(15) and 1.59(15)  $\mu_B$  for UPTe and UAsTe, respectively.

←

**Fig. 79.** UPTe. (a) Specific magnetization,  $\sigma_{||}$ , measured along the  $c$ -axis in a field of 0.2 T with cooling the sample with (FC, full diamonds) and without (ZFC, open diamonds) an applied magnetic field (left-hand scale) and reciprocal longitudinal,  $\chi_{||}^{-1}$ , (open circles), and transversal,  $\chi_{\perp}^{-1}$ , (full circles) molar magnetic susceptibility, measured along and perpendicular to the  $c$ -axis, respectively (right-hand scale) vs. temperature,  $T$  [95KNZ]. The compound orders ferromagnetically at  $T_C = 85$  K. The solid lines are Curie-Weiss fits with the parameters given in Table B. Note a strongly anisotropic behaviour of the susceptibility caused mainly by crystal field interactions. (b) Specific magnetization,  $\sigma_{||}$ , vs. magnetic field,  $B$ , taken at 5 K with increasing (full circles) and decreasing (open circles) magnetic field. The saturation uranium magnetic moment is 1.40(2)  $\mu_B$ . The uniaxial magnetic anisotropy constant  $K_1$  was estimated to be of the order of  $10^7$  erg/g.

UXTe

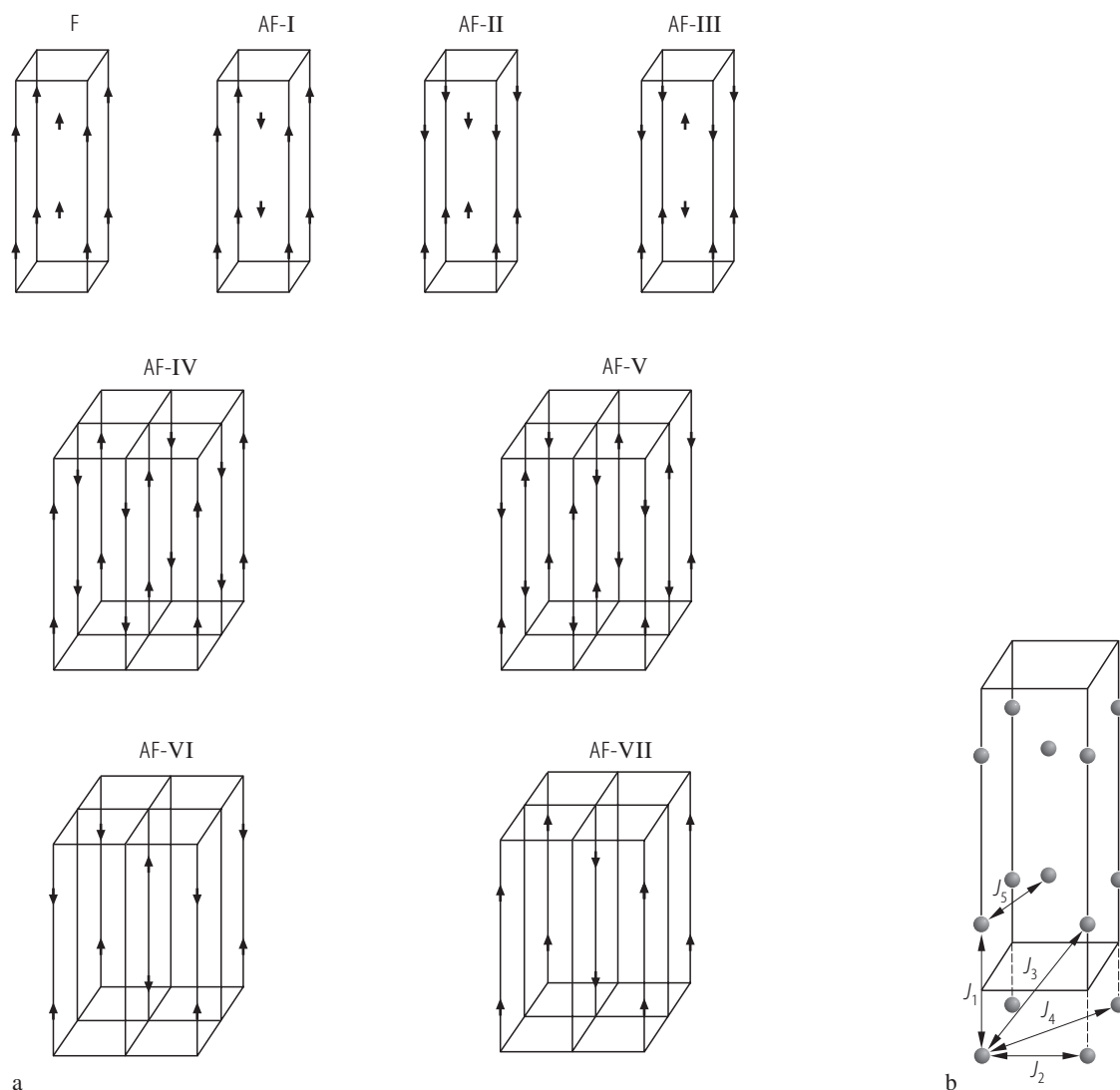
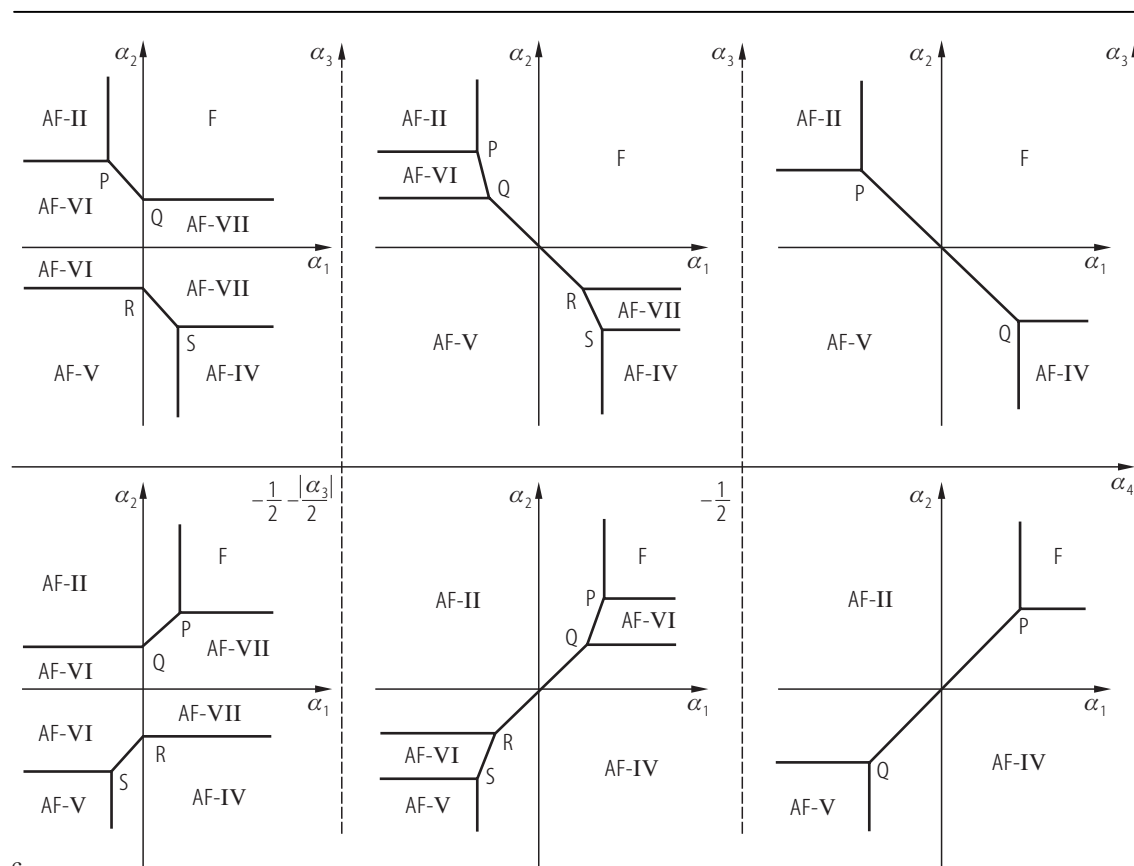


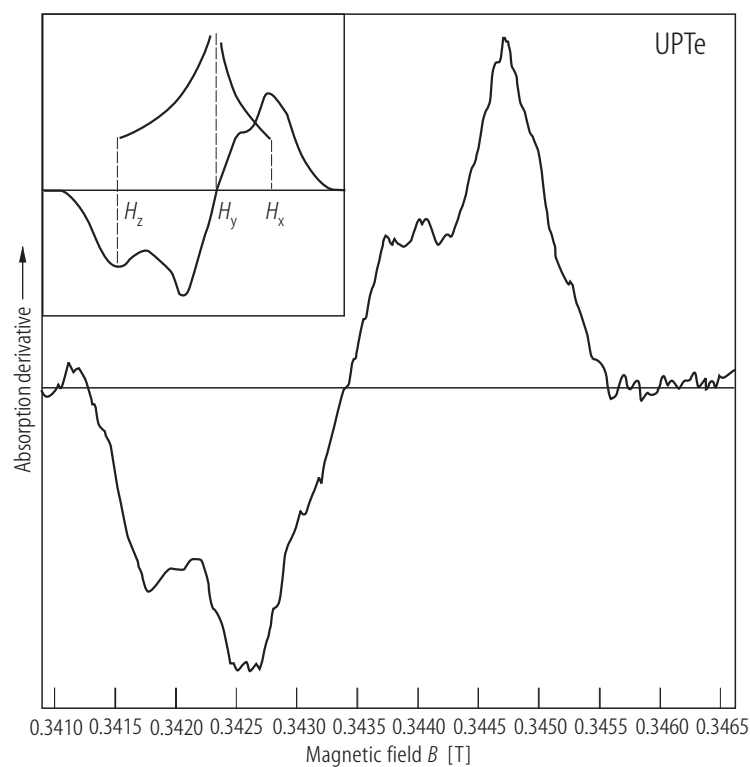
**Fig. 81.** UPTe, UAsTe, UGeTe. (a) Possible magnetic structures of the uranium compounds crystallizing with the tetragonal UGeTe-type crystal structure (s.g.  $I4/mmm$ ), calculated by the Smart's method within the molecular field approximation [74LPZ]. The five different exchange integrals considered are shown schematically in panel (b). The structures F, AF-I, AF-II and AF-III are invariant with respect to the magnetic space group  $I4/mmm$  and are completely determined by considering only isotropic

interactions in the crystal. The other four structures: AF-IV – AF-VII cannot be completely determined by the isotropic Heisenberg model. Note that the only structure which has been observed experimentally is F. (c) Stability diagram of the structures presented in panel (a), obtained assuming that the stable structure is the one with the highest critical temperature.  $\alpha_1 = 8J_1/|J_5|$ ,  $\alpha_2 = 1 + 2J_2/|J_5|$ ,  $\alpha_3 = 2J_3/|J_5|$ ,  $\alpha_4 = 2J_4/|J_5|$ ,  $\alpha_5 = J_5$ . For the details see the original paper.

For Fig. 81(c) see next page.



c

**Fig. 81(c).** For caption see previous page.**Fig. 82.** UPTe. Powder  $^{31}\text{P}$  NMR spectrum (absorption derivative) taken at a nominal resonance frequency of 5.9848 MHz [82ZZ]. The local symmetry at the P site is lower than axial ( $D_{2h}$ ) and therefore the Knight shift has three components, shown schematically in the inset. The measured Knight shift parameters:  $K_x = 0.73(3) \%$ ,  $K_y = 1.09(3) \%$ ,  $K_z = 1.56(3) \%$ .

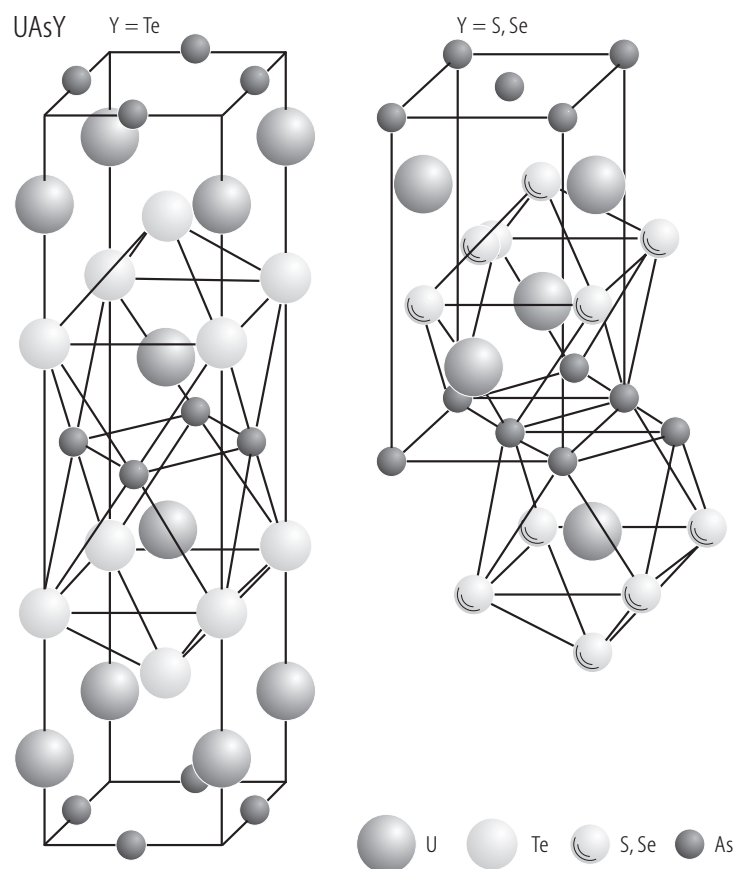


**Fig. 83.** UAsY, Y = S, Se, Te. Crystal structures with coordination polyhedra of uranium atom [75PL].

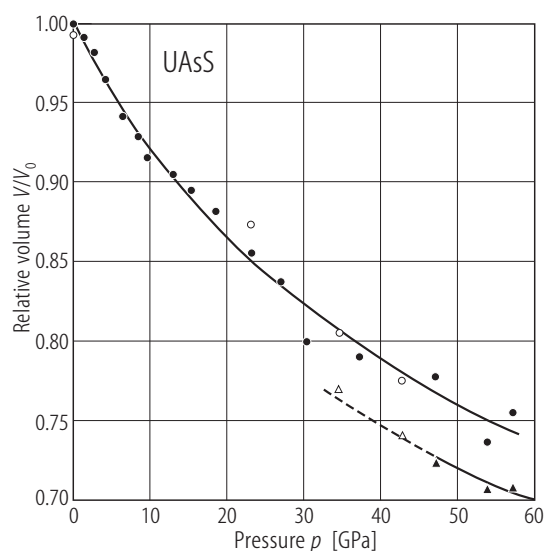


**Fig. 84.** UAsS. Relative volume,  $V/V_0$ , vs. pressure,  $p$ , up to 60 GPa [90GSBD]. Circles: tetragonal phase; triangles: orthorhombic phase. Filled symbols: increasing pressure; open symbols: decreasing pressure). A first-order tetragonal-to-orthorhombic phase transformation takes place at about 46 GPa with a 7 % volume collapse.  $B_0 = 105(7)$  GPa,  $B_0' = 3.7(5)$ .

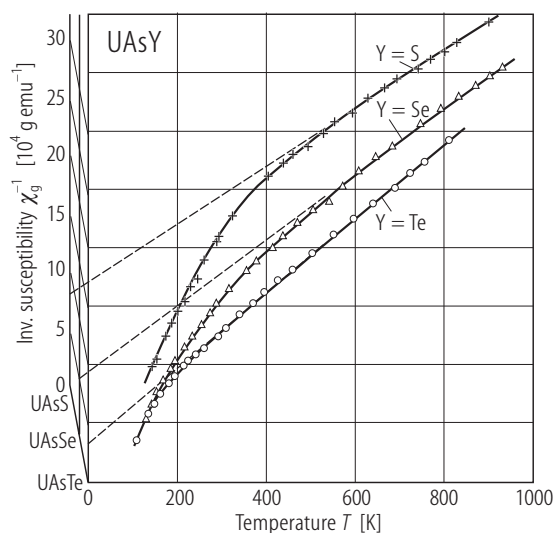


**Fig. 85.** UAsY, Y = S, Se, Te. Reciprocal mass magnetic susceptibility,  $\chi_g^{-1}$ , vs. temperature,  $T$ , in the paramagnetic region up to 950 K [72ZD]. Crosses: UAsS; triangles: UAsSe; circles: UAsTe. The dashed lines are Curie-Weiss fits with the parameters given in Table B. Strongly curvilinear character of  $\chi_g^{-1}(T)$  the authors ascribed to crystal field interactions.

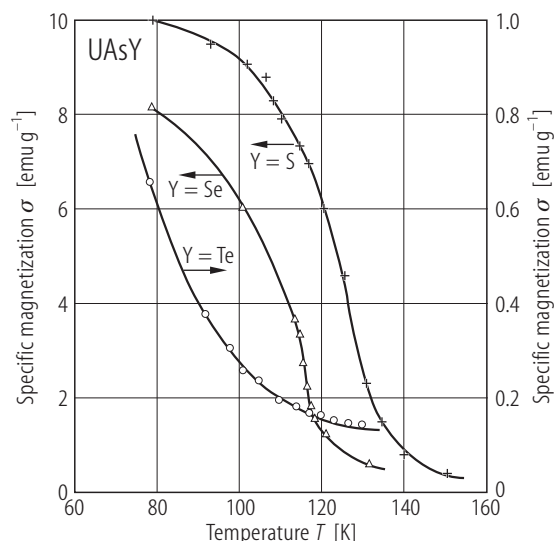


**Fig. 86.** UAsY, Y = S, Se, Te. Specific magnetization,  $\sigma$ , vs. temperature,  $T$ , taken in a field of 0.6 T [72ZD]. Crosses: UAsS; triangles: UAsSe; circles: UAsTe. Note the right-hand scale for UAsTe. UAsS and UAsSe order ferromagnetically at  $T_C = 128$  and 118 K. The Curie temperature for UAsTe is 66 K (see Fig. 144) and was not reached in the experiment presented. See also the single crystal results in Figs. 87 and 109.

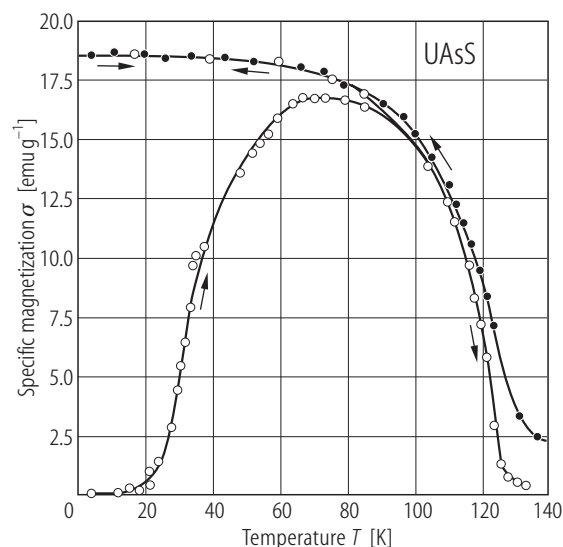


**Fig. 87.** UAsS. Specific magnetization,  $\sigma$ , vs. temperature,  $T$ , taken on a single crystal in a field of 0.1 (open circles) and 1 T (filled circles) oriented along the  $c$ -axis [72BZ]. The arrows indicate increasing and decreasing temperature. The Curie temperature is 124 K. A characteristic maximum in  $\sigma(T)$  obtained with increasing temperature in 0.1 T manifests strongly anisotropic character of the compound which exhibits at low temperatures a compensated 180° domain structure (see also in Fig. 92 a sudden increase of the magnetization at 4.2 K above 0.4 T).

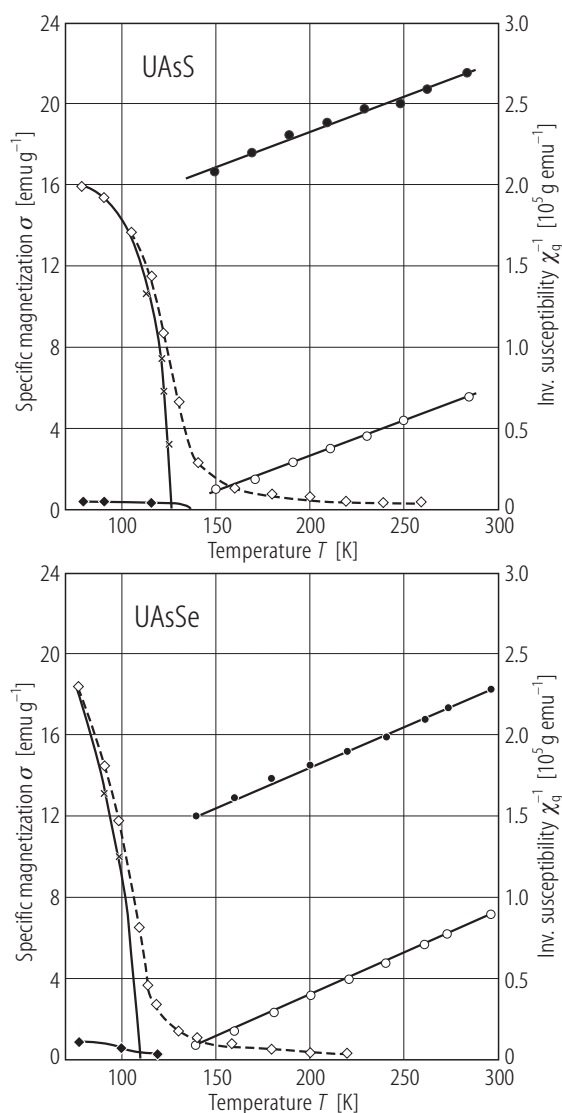


**Fig. 88.** UAsY, Y = S, Se. Specific magnetization,  $\sigma_{\parallel}$  and  $\sigma_{\perp}$ , measured along (open diamonds) and perpendicular (full diamonds) to the  $c$ -axis in a field of 1.2 T (left-hand scale) and reciprocal longitudinal,  $\chi_{\parallel}^{-1}$ , (open circles), and transversal,  $\chi_{\perp}^{-1}$ , (full circles) mass magnetic susceptibility, measured along and perpendicular to the  $c$ -axis, respectively (right-hand scale) vs. temperature,  $T$  [73BDZL]. The crosses mark the spontaneous magnetization,  $\sigma_s$ , along the  $c$ -axis. The lines are guides to the eye.

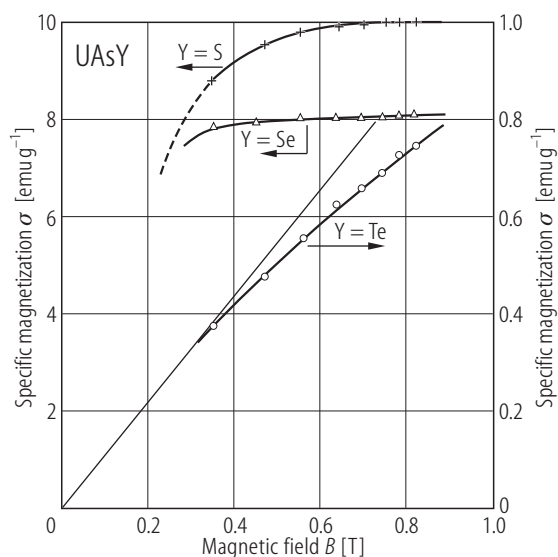


**Fig. 89.** UAsY, Y = S, Se, Te. Specific magnetization,  $\sigma$ , vs. magnetic field,  $B$ , measured at 77 K [72ZD]. Crosses: UAsS; triangles: UAsSe; circles: UAsTe. Note the right-hand scale for UAsTe. The compounds order ferromagnetically at low temperatures (see Fig. 86). For UAsS compare the single crystal data shown in Fig. 90.

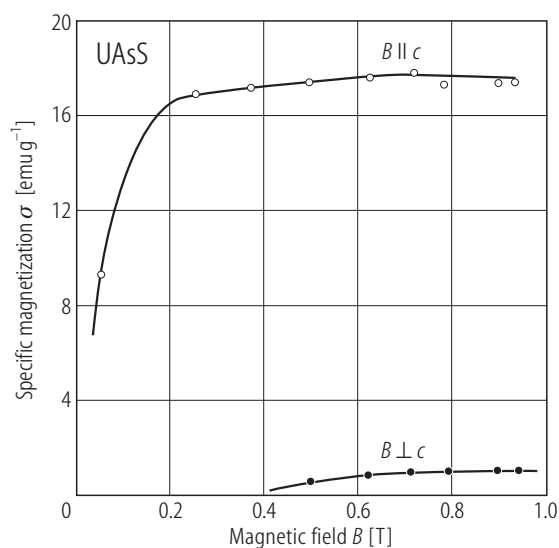


**Fig. 90.** UAsS. Specific magnetization,  $\sigma$ , vs. magnetic field,  $B$ , measured at 77 K on a single crystal with  $B \parallel c$ -axis (open circles) and  $B \perp c$ -axis (filled circles) [72ZD]. The compounds orders ferromagnetically at low temperatures with the magnetic moments pointing along the  $c$ -axis. The strong magnetic anisotropy constant of the order of  $10^7$  erg/cm<sup>3</sup> [72BZ] may result from the strongly uniaxial character of the crystal field potential. See also the low-temperature results presented in Fig. 92.

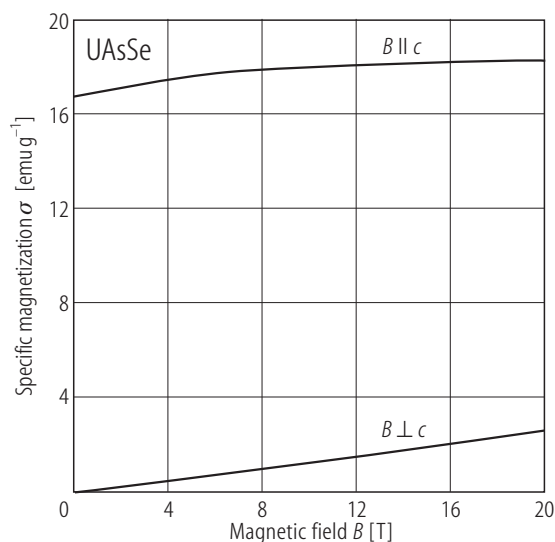
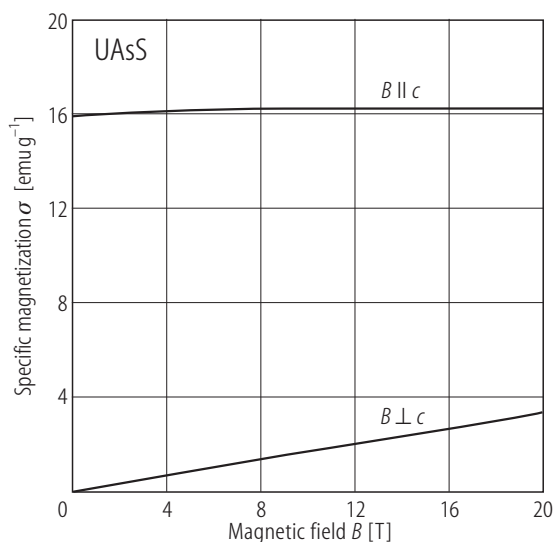


**Fig. 91.** UAsY, Y = S, Se. Specific magnetization,  $\sigma$ , vs. magnetic field,  $B$ , measured at 78 K in pulsed magnetic fields up to 20 T on single crystals with  $B \parallel c$ -axis and  $B \perp c$ -axis [73BDZL]. Note a huge magnetic anisotropy in both compounds being of the order of 80...130 T. The anisotropy constants estimated from the anisotropy field:  $K \approx 6...10 \cdot 10^6$  erg/g.

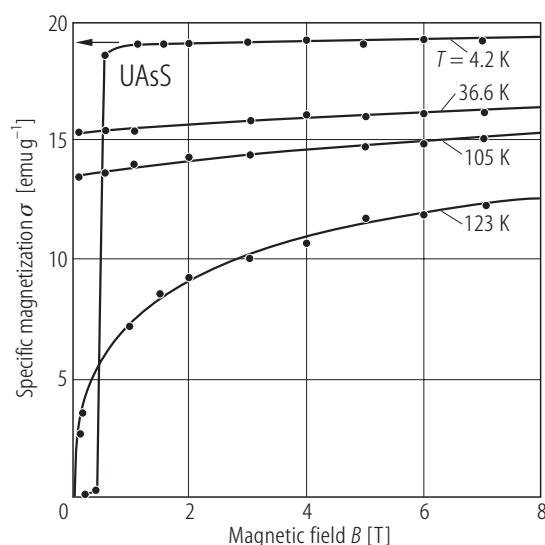


**Fig. 92.** UAsS. Specific magnetization,  $\sigma$ , vs. magnetic field,  $B$ , measured at several temperatures below  $T_C = 124$  K on a single crystal with  $B \parallel c$ -axis [72BZ]. The compound is a uniaxial ferromagnet with the moments aligned along the  $c$ -axis (see Fig. 90). The arrow marks the remanent magnetization which reaches about 98% of the saturation value at 4.2 K ( $p_s = 1.14 \mu_B$ ). The coercive field at 4.2 K is 0.4 T.

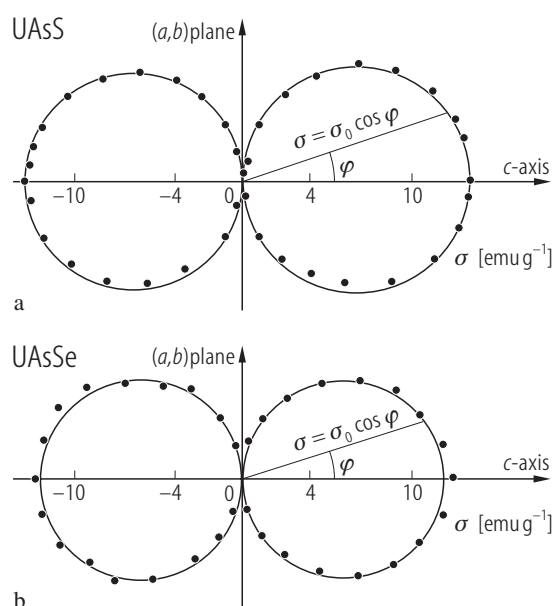


**Fig. 93.** UAsY, Y = S, Se. Specific magnetization,  $\sigma$ , vs. angle,  $\varphi$ , between magnetic field direction and the tetragonal  $c$ -axis, measured at 105 K in magnetic field of 1.22 T on a single crystal of (a) UAsS and (b) UAsSe [73BDZL]. Points: experimental data; solid circles: theoretical results obtained assuming that the magnetic moment stays always confined to the  $c$ -axis.

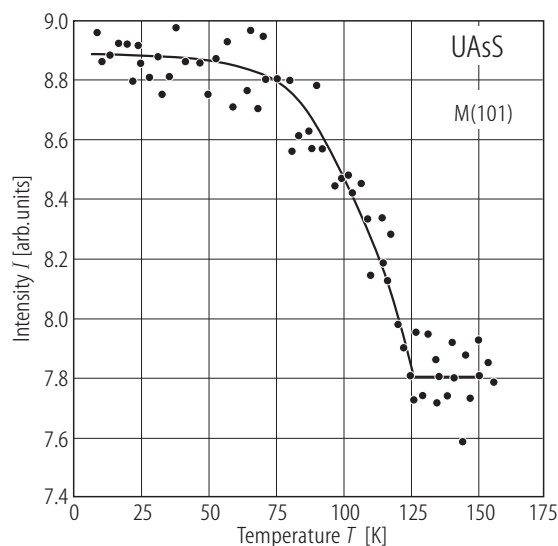


**Fig. 94.** UAsS. Neutron diffraction intensity of the magnetic reflection (101),  $I$ , vs. temperature,  $T$  [74ZLPL]. The compound orders ferromagnetically at  $T_C = 125(3)$  K with the uranium moments aligned along the tetragonal  $c$ -axis (see Fig. 90). The ordered moment  $p_0$  at 4 K amounts to  $1.24(1) \mu_B$ .



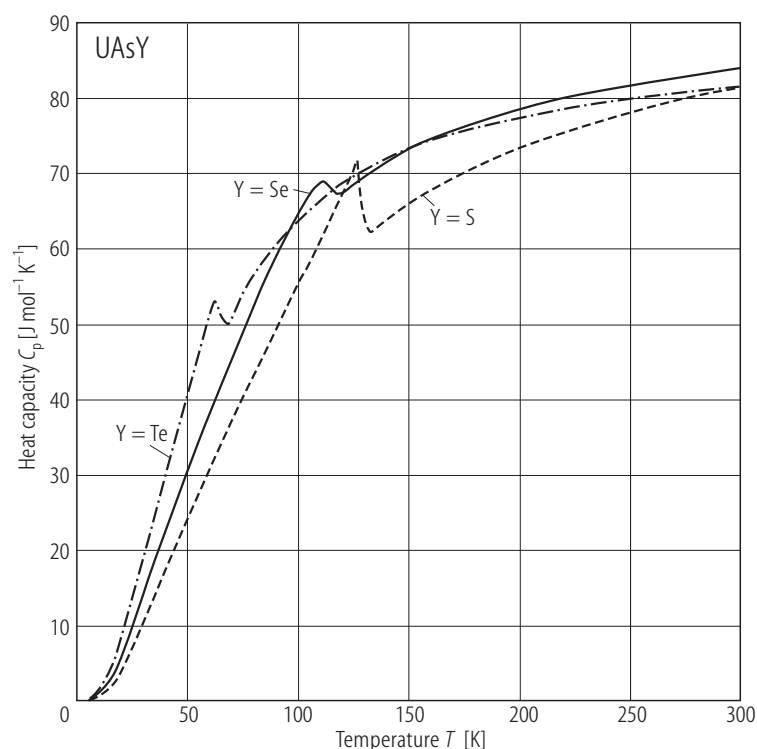


**Fig. 95.** UAsY, Y = S, Se, Te. Heat capacity,  $C_p$ , vs. temperature,  $T$  [80BLWZ]. The  $\lambda$ -shaped peaks superimposed on classical sigmoid curves manifest ferromagnetic phase transitions occurring at  $T_C = 125.8$ ,  $108.8$  and  $62.8$  K for UAsS (dashed line), UAsSe (solid line) and UAsTe (dash-dotted), respectively. See the main thermodynamic characteristics gathered in Table W. Small magnetic entropy (well below  $R\ln 2$ ) and relatively high electronic heat capacity coefficient ( $23\ldots 56$  mJ/mol K<sup>2</sup>) found for all three compounds suggest a tendency of 5f electrons to be itinerant.

For Figs. 96, 97 see next pages

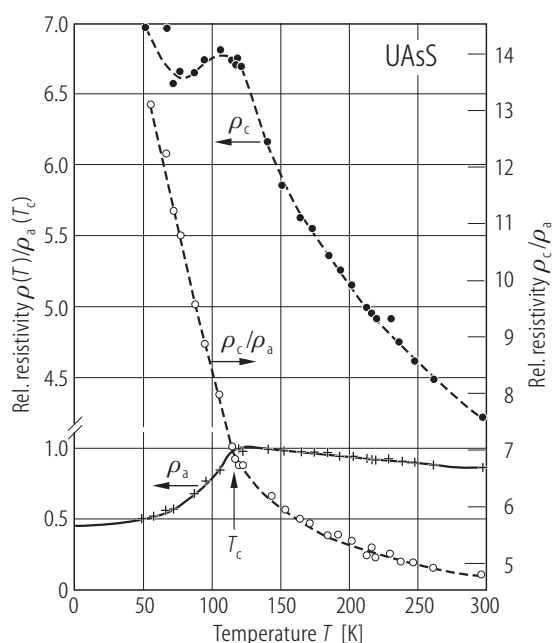


**Fig. 98.** UAsS. Electrical resistivity of single crystals measured with  $i \parallel c$ -axis,  $\rho_c$ , (full circles) and  $i \parallel a$ -axis,  $\rho_a$ , (crosses and solid line), normalised to the value of  $\rho_a$  at the Curie temperature  $T_C = 119$  K (left-hand side scale), and the resistivity ratio,  $\rho_c/\rho_a$ , (open circles; right-hand side scale) vs. temperature,  $T$  [87WMHL]. The broken line is a guide to the eye. The solid curve represents  $\rho_a(T)$  measured by conventional four point dc method. Crosses and full circles represent the data obtained by Montgomery modification of the van der Pauw method. Note a good agreement between the results of different measurement techniques.  $\rho_a(T_C) = 315 \mu\Omega\text{cm}$ . The negative temperature coefficient of the resistivity in the paramagnetic region the authors attributed to dense Kondo effect or, alternatively, to scattering of the conduction electrons by collective excitations associated with a singlet crystal field ground state. Note that the anisotropy of the resistivity, measured by  $\rho_c/\rho_a$ , increases with decreasing temperature and  $\rho_c/\rho_a(T)$  rapidly changes its slope at  $T_C$ , which indicates that it is mainly governed by strongly anisotropic magnetic exchange interactions.

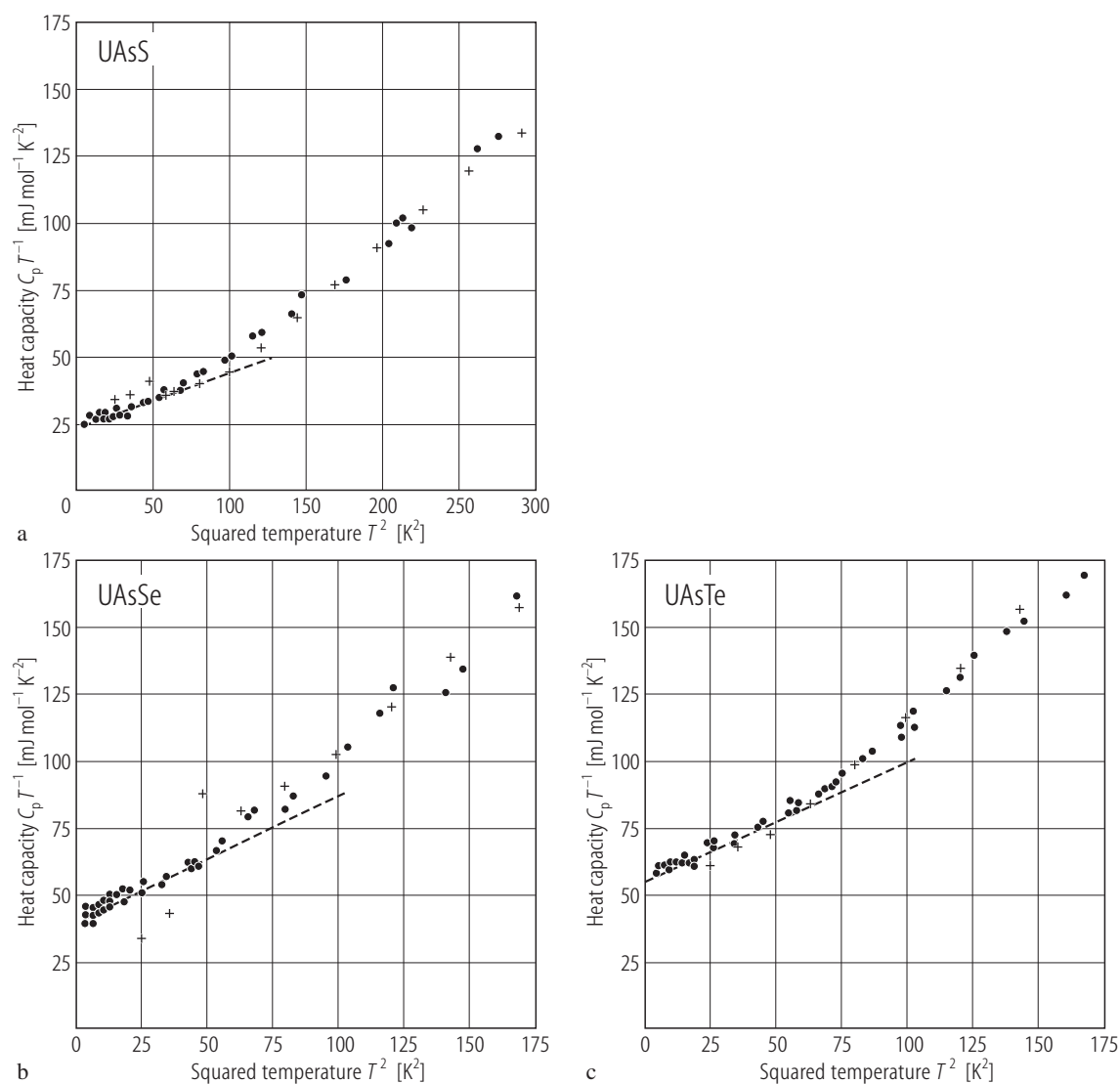


**Fig. 96.** UAsY, Y = S, Se, Te. Low temperature heat capacity in the form  $C_p/T$  vs.  $T^2$  measured using transient (circles) and adiabatic (crosses) methods for (a) UAsS, (b) UAsSe and (c) UAsTe [80BLWZ]. The dashed lines mark the regions where  $C_p = \gamma T + \beta T^3$  (see Table W).

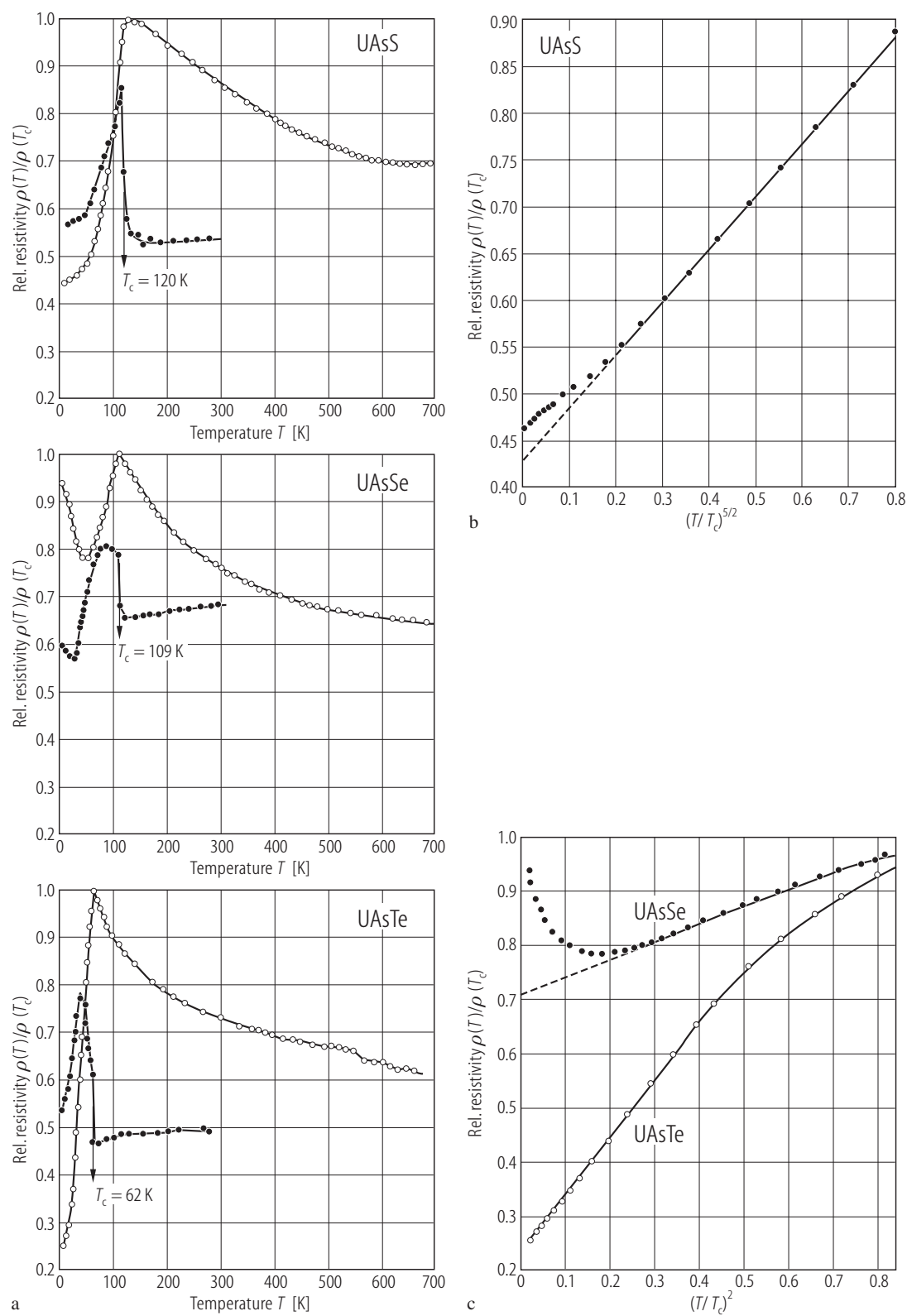
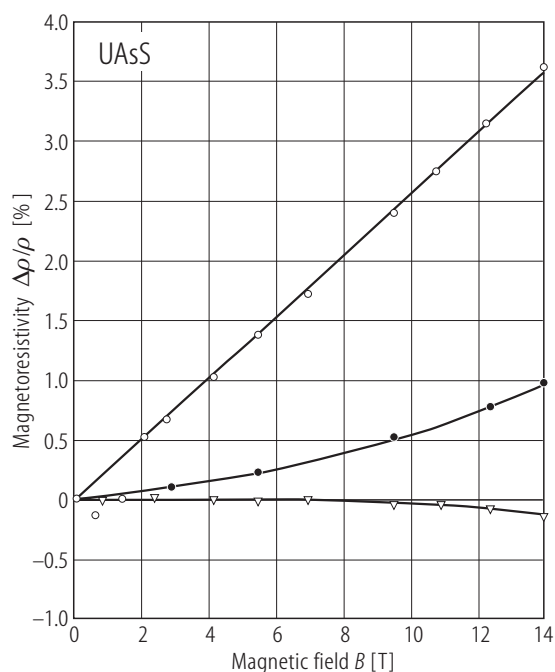
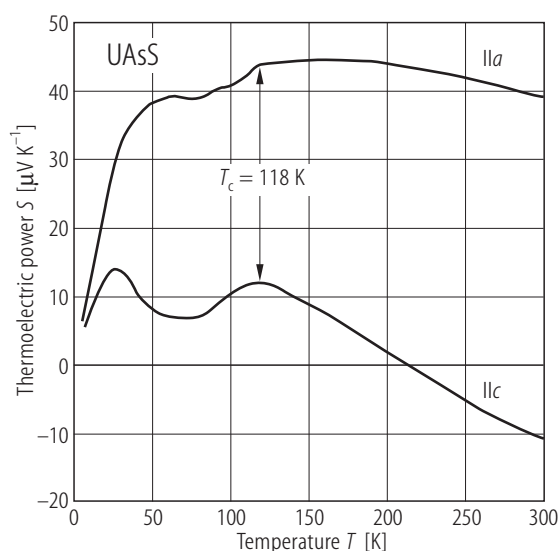


Fig. 97. For caption see next page

**Fig. 97.** UAsY, Y = S, Se, Te. **(a)** Electrical resistivity normalised to its value at the corresponding Curie temperature  $T_C$ ,  $\rho/\rho(T_C)$ , vs. temperature,  $T$ , up to 700 K, measured on single crystals with  $i \perp c$ -axis [72WHK]. The room temperature resistivity was 270(20), 280(20) and 270(20)  $\mu\Omega\text{cm}$  for UAsS, UAsSe and UAsTe, respectively. The closed circles are the temperature derivatives of the resistivity,  $d\rho/dT$ . All three compounds order ferromagnetically at low temperatures. The ordering temperature determined from  $d\rho/dT(T)$  is  $T_C = 120$ , 109 and 62 K for UAsS, UAsSe and UAsTe, respectively. On the basis of the shape of  $d\rho/dT(T)$  for  $T$  approaching  $T_C$  from the paramagnetic region, the authors suggested that in UAsS the critical behaviour is dominated by short-range spin fluctuations, while the contribution of long-range spin fluctuations gradually rises when passing to Se and then to Te. Note a negative temperature coefficient of the resistivity in the paramagnetic region for all compounds, and additionally below 45 K for UAsSe. **(b)** Low-temperature  $\rho/\rho(T_C)$ , vs.  $(T/T_C)^{5/2}$  for UAsS. Note that only at the lowest temperatures a deviation from a linear behaviour occurs, which was attributed by the authors to magnetic domain effects. **(c)** Low-temperature  $\rho/\rho(T_C)$ , vs.  $(T/T_C)^2$  for UAsSe (closed circles) and UAsTe (open circles). A  $T^2$  dependence of the resistivity may manifest scattering of the conduction electrons on spin-wave excitations. The pronounced deviation from a linear behaviour observed for UAsSe at the lowest temperatures the authors ascribed to magnetic domain effects.



**Fig. 99.** UAsS. Magnetoresistivity,  $\Delta\rho/\rho$ , vs. magnetic field,  $B$ , up to 14 T, measured at 4.2 K on a single crystal with  $i \parallel a$ -axis (hard magnetization direction) in magnetic field  $B \parallel c$ -axis (open circles),  $B \parallel b$ -axis (open triangles) and  $B \parallel a$ -axis (filled circles) [98HCPE]. Note a linear-in- $B$  behaviour of the transverse magnetoresistivity taken with the field aligned along the easy magnetization axis ( $c$ -axis), which was ascribed by the authors to the Kondo impurity component of the resistivity (see Fig. 98). Note also that for the magnetic field directed perpendicular to the easy magnetization axis  $\Delta\rho/\rho$  is much lower than for  $B \parallel c$ -axis, varies non-linearly with  $B$  and is negative for the transverse and positive for the longitudinal field direction.



**Fig. 100.** UAsS. Thermoelectric power,  $S$ , vs. temperature,  $T$ , measured on a single crystal in the  $ab$ -plane (upper curve) and along the  $c$ -axis (lower curve) [02HWWK]. The arrows mark the ferromagnetic phase transition at  $T_C = 118$  K. Note a strong anisotropy.

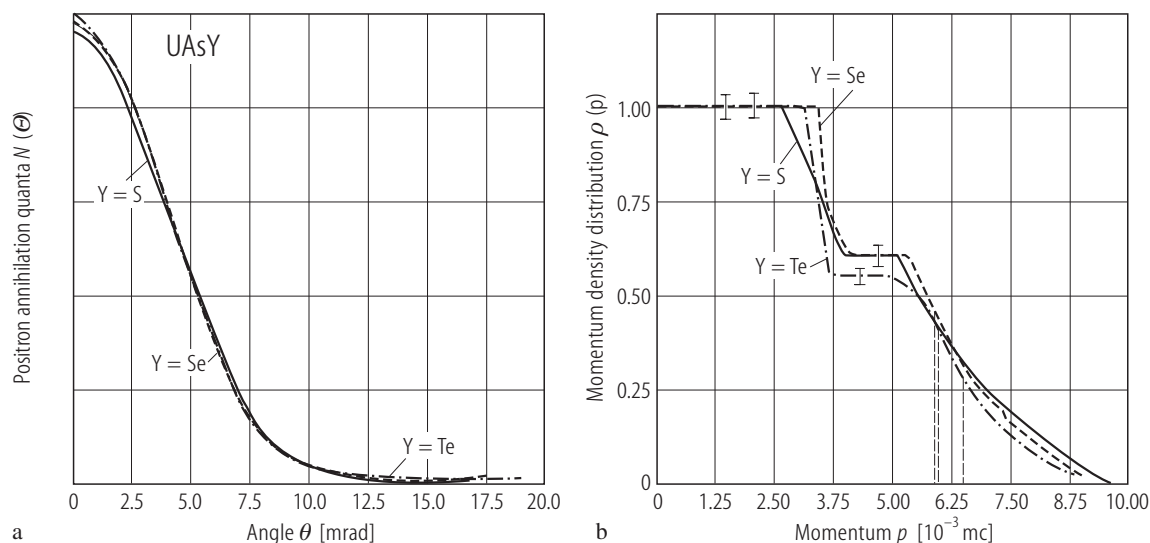


**Fig. 101.**  $\text{UAsY}$ ,  $Y = \text{S}, \text{Se}, \text{Te}$ . (a) Angular distribution of positron annihilation quanta,  $N(\theta)$ , normalised to the same area [77RDHW]. (b) Momentum density distribution,  $\rho(p)$ , obtained from the data shown in panel (a) after subtraction core annihilation. According to the authors, all valence electrons ( $Z_v$ ) with the maximum momentum  $p_v$  can be divided into a group of electrons ( $Z_c$ ) with smaller maximum momenta  $p_c$ , which are responsible for metallic-type electrical conductivity, and a group of electrons, which participate in chemical bonding of covalent or ionic

character. The values derived from the  $\rho(p)$  curves in the framework of the free electron model approximation:  $Z_v = 10.3(4)$ ,  $p_v = 6.60(13) \cdot 10^{-3} \text{ mc}$ ,  $Z_c = 1.3(4)$  and  $p_c = 3.3(4) \cdot 10^{-3} \text{ mc}$  for  $\text{UAsS}$ ,  $Z_v = 10.1(4)$ ,  $p_v = 6.40(13) \cdot 10^{-3} \text{ mc}$ ,  $Z_c = 1.6(4)$  and  $p_c = 3.4(4) \cdot 10^{-3} \text{ mc}$  for  $\text{UAsSe}$ ,  $Z_v = 11.7(4)$ ,  $p_v = 6.46(13) \cdot 10^{-3} \text{ mc}$ ,  $Z_c = 1.5(4)$  and  $p_c = 3.3(4) \cdot 10^{-3} \text{ mc}$  for  $\text{UAsTe}$ . Note that the so-derived numbers of valence electrons is for all three compounds smaller than the sum of valence electrons of constituent elements.

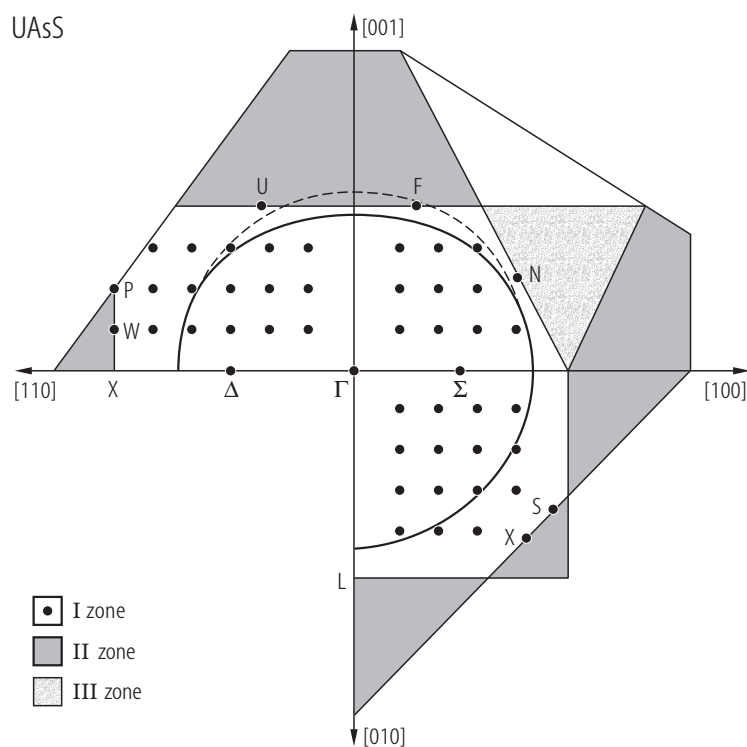


**Fig. 102.**  $\text{UAsS}$ . Cross-sections through the Brillouin zones and Fermi surface as derived from the calculated electron momentum density distributions on the basis of the results of the positron annihilation experiments presented in Fig. 101 [80DR]. Note an ellipsoidal shape of the Fermi surface, which is in line with the observed anisotropy of the electrical conductivity (see Fig. 98).

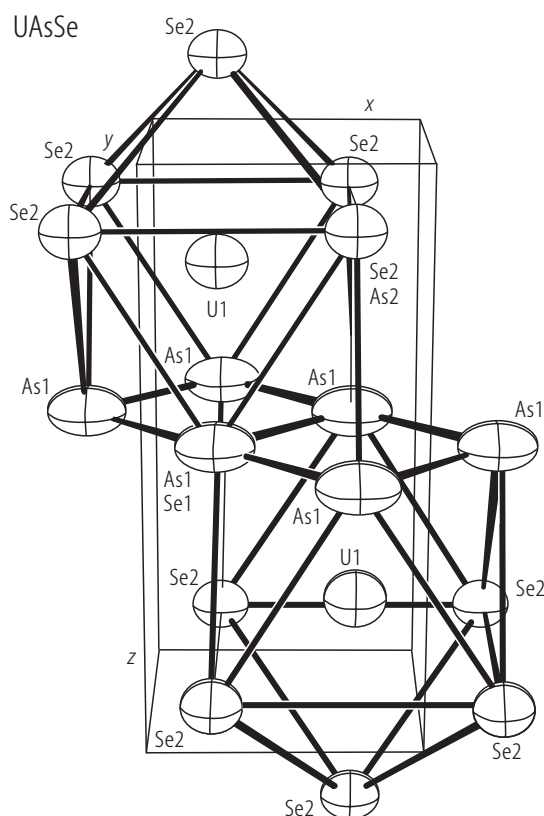


**Fig. 103.** UAsSe. Crystallographic unit cell with emphasised nearest neighbour coordination sphere of uranium atoms, i.e.  $[\text{UAs}_4\text{Se}_5]$  polyhedrons [98HCPF]. The ellipsoids visualize the anisotropic thermal atom displacement parameters. Note a very large anisotropy in the Debye-Waller factor of arsenic ions. The crystal structure refinements have revealed a possible partial occupation (less than 20 %) of Se atoms at As sites, postulated in order to interpret the electrical transport properties (see Fig. 141).

For Fig. 104 see next page

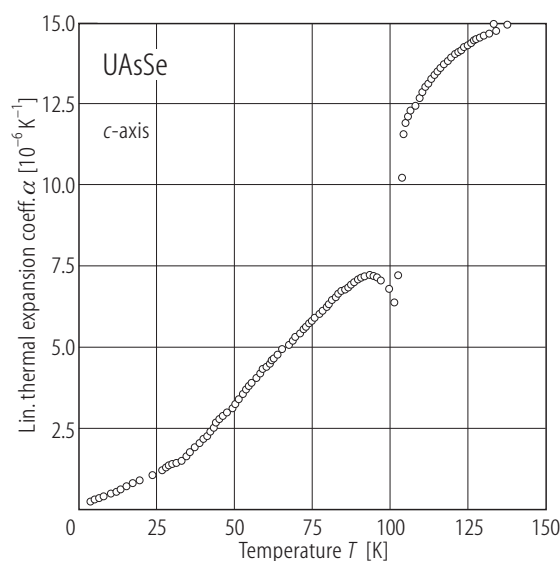


**Fig. 105.** UAsSe. Thermal expansion coefficient,  $\alpha$ , vs. temperature in the range 5...140 K, measured using a capacitive dilatometer on a single crystal along the  $c$ -axis [01CMKM]. The sharp anomaly at  $T_C = 101.5$  K manifests a ferromagnetic phase transition. Note that no other features are observed in the ordered region, thus proving that such phenomena as structural phase transitions or charge density wave formation cannot be responsible for unusual electrical transport properties of this compound (see Fig. 119).

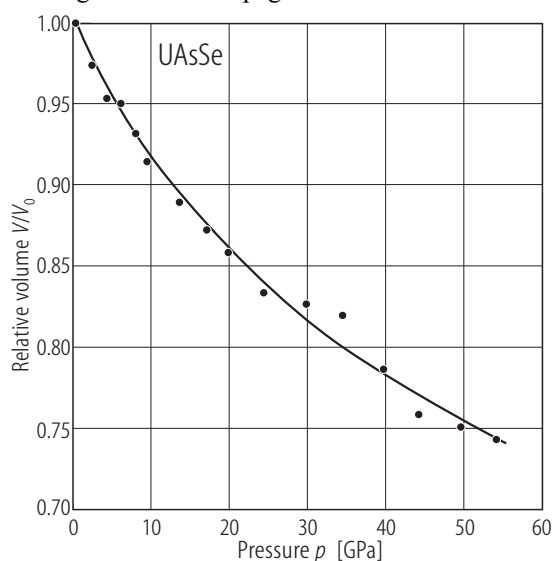
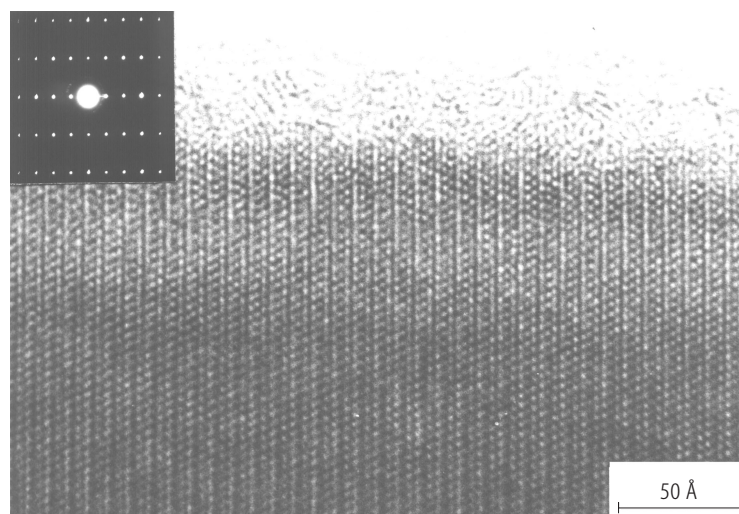
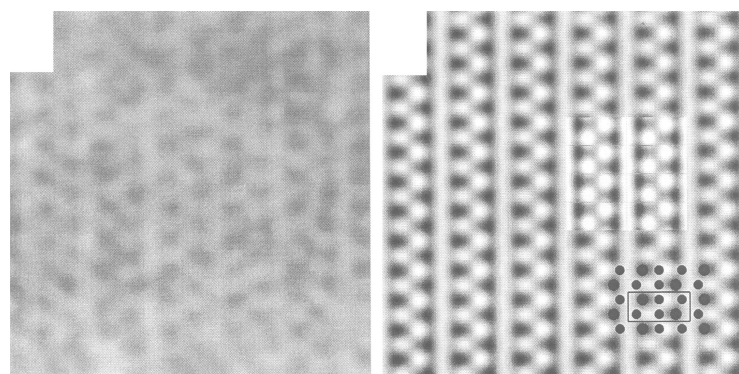


**Fig. 106.** UAsSe. Relative volume,  $V/V_0$ , vs. pressure,  $p$ , up to 55 GPa [90GSBD]. In contrast to UAsS (see Fig. 84) no phase transformation is observed.  $B_0 = 99(6)$  GPa,  $B'_0 = 3.8(5)$ .

UAsSe [010]



a



b

c

**Fig. 104.** UAsSe. (a) High resolution transmission electron microscopy (HRTEM) image of a wedge crystal in [010] orientation [98HCPF]. Inset: selected area electron diffraction pattern (SAED). Note that the crystal studied exhibits a well ordered structure over long distances (at least 400 Å) with no signature of ordering defects or microtwins. At the edge of the crystal there is an amorphous layer resulting from surface oxidation and carbon contamination in the microscope. Changes in the thickness of the crystal along the normal direction to its edge are visualized by the contrast changes. (b) Magnified portion of the image from panel (a) (the thinnest one close to the edge) upon digitalization. (c) The same image as in panel (b) after application of the crystallographic image processing procedure. Superimposed are a simulated HRTEM image (upper inset) and a model of the structure with the black dots marking the positions of the uranium atoms (lower inset). The positions of As and Se could not be derived due to limited resolution of the microscope.

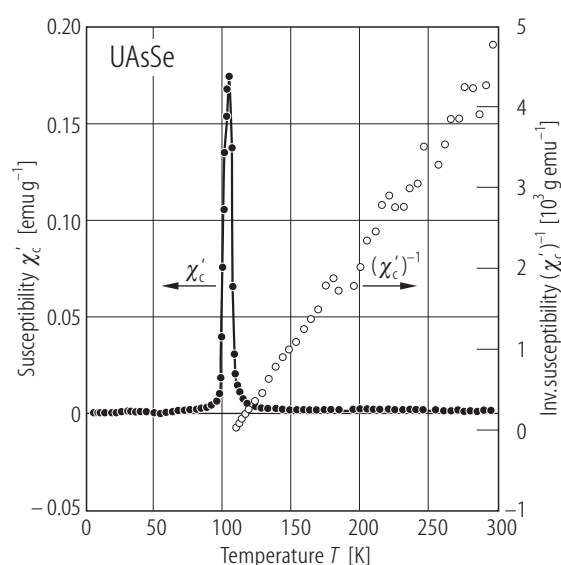


**Fig. 107.** UAsSe. Real component of the ac magnetic susceptibility,  $\chi'$ , (filled circles, left-hand scale) and its inverse,  $(\chi')^{-1}$ , (open circles, right-hand scale) vs. temperature,  $T$ , measured in an alternating magnetic field  $B = 10$  Oe with the frequency 400 Hz on a single crystal with  $B \parallel c$ -axis [95HFWZ]. In the paramagnetic region  $(\chi')^{-1}(T)$  follows roughly a Curie-Weiss law with the effective magnetic moment of  $3.48 \mu_B$  (determined from the range 108...125 K) and the paramagnetic Curie temperature of 108.3 K. A sharp-peak behaviour of  $\chi'(T)$  in the vicinity of  $T_C$  indicates a huge magnetic anisotropy (see also the captions of Figs. 109 and 91).



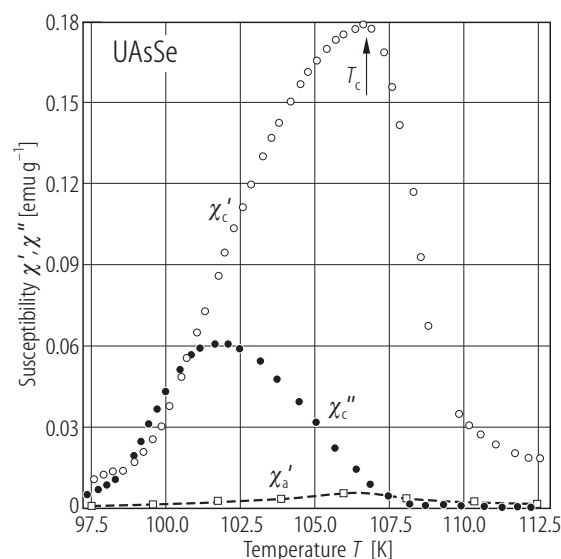


**Fig. 108.** UAsSe. Real,  $\chi'_c$ , (open circles) and imaginary,  $\chi''_c$ , (filled circles) components of the ac magnetic susceptibility, measured on a single crystal with  $B \parallel c$ -axis, as well as real component,  $\chi'_a$ , (open squares) of the ac magnetic susceptibility, measured on a single crystal with  $B \parallel a$ -axis, vs. temperature,  $T$ , in the vicinity of  $T_C = 107$  K [95HFWZ]. The experimental conditions of the measurements were as specified in the caption of Fig. 107. Note a strong anisotropy in the susceptibility (at  $T_C$ :  $\chi'_c/\chi'_a = 33$ ).

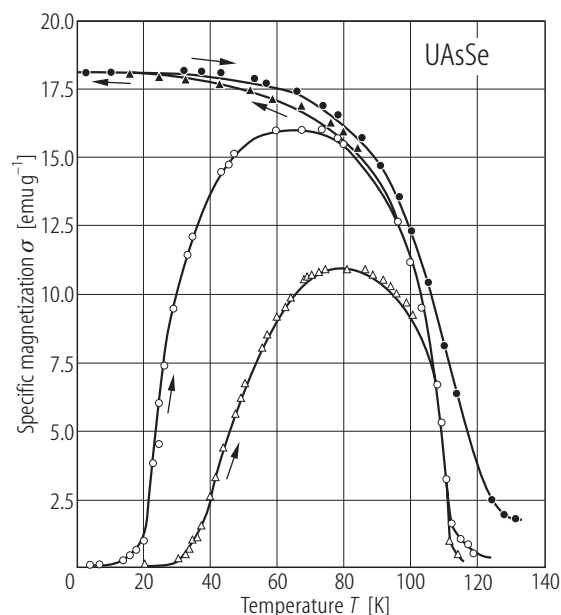


**Fig. 109.** UAsSe. Specific magnetization,  $\sigma$ , vs. temperature,  $T$ , taken on a single crystal in a field of 0.05 (triangles), 0.1 (open circles) and 1 T (filled circles) oriented along the  $c$ -axis [72BZ]. The arrows indicate increasing and decreasing temperature during measurement at 0.1 T. The Curie temperature is 113 K. A characteristic maximum in  $\sigma(T)$  obtained with increasing temperature in 0.1 T manifests strongly anisotropic character of the compound which exhibits at low temperatures a compensated  $180^\circ$  domain structure (see also in Fig. 110 a sudden increase of the magnetization at 4.2 K above 0.38 T).

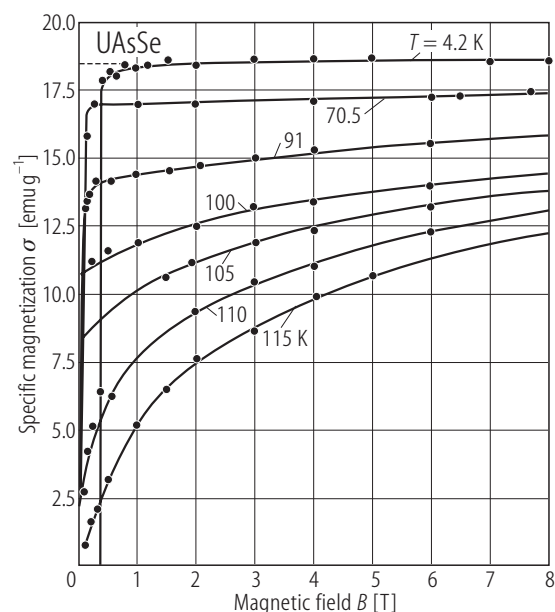


**Fig. 110.** UAsSe. Specific magnetization,  $\sigma$ , vs. magnetic field,  $B$ , measured at several temperatures below  $T_C = 113$  K and at 115 K on a single crystal with  $B \parallel c$ -axis [72BZ]. The compound is a uniaxial ferromagnet with the moments aligned along the  $c$ -axis. The dashed line marks the remanent magnetization which reaches about 98% of the saturation value at 4.2 K ( $p_s = 1.36 \mu_B$ ). The coercive field at 4.2 K is 0.38 T.



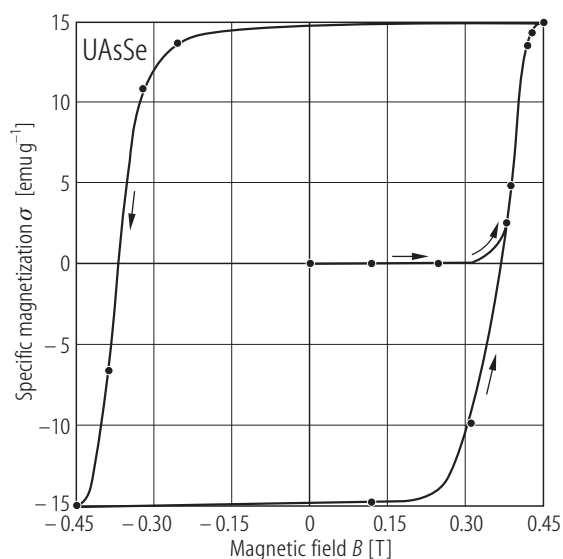


**Fig. 111.** UAsSe. Hysteresis loop, i.e. specific magnetization,  $\sigma$ , vs. magnetic field,  $B$ , taken at 4.2 K on a single crystal with  $B \parallel c$ -axis [72BZ]. Note a nearly rectangular form of the loop. The coercive field is 0.38 T.

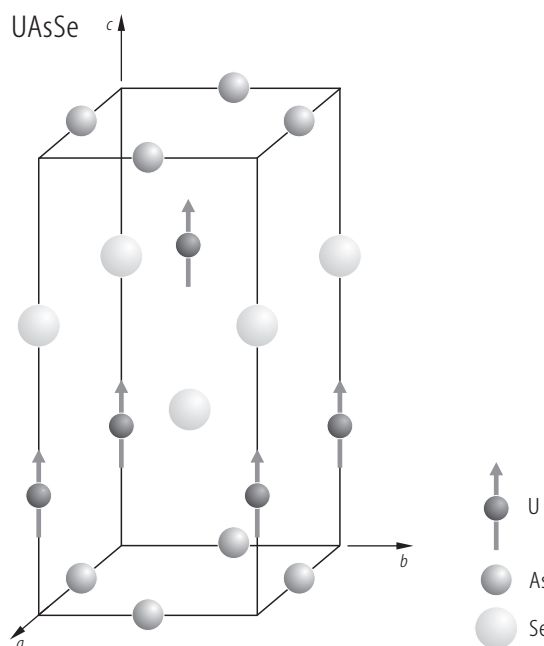


**Fig. 112.** UAsSe. Crystal and magnetic structure [99WGHW].

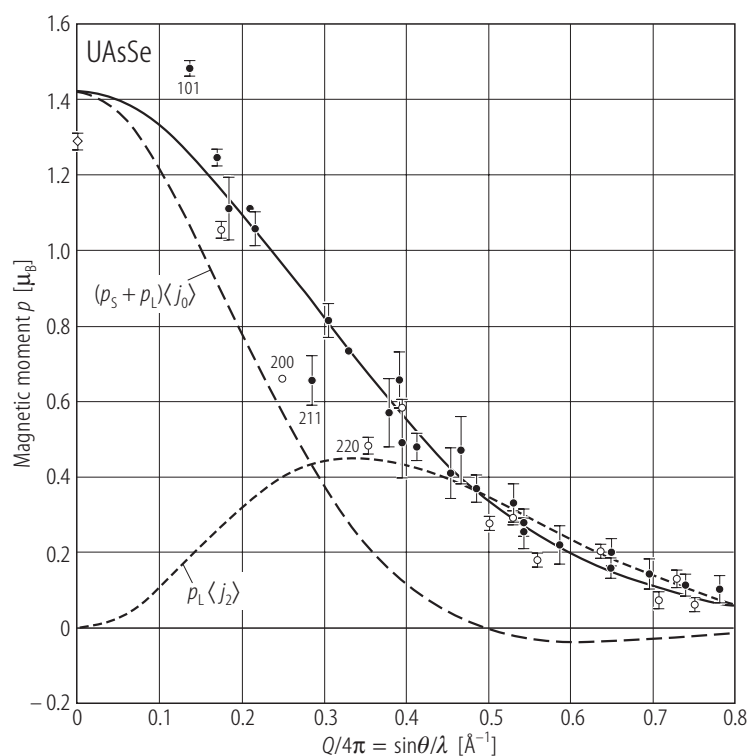


**Fig. 113.** UAsSe. Magnetic amplitude of uranium ions measured on a single crystal by polarised neutron diffraction at 5 K with a vertical magnetic field of 2 T applied parallel to the  $c$ -axis [99WGHW]. Open and full circles represent in-plane and off-plane reflections, respectively. The solid line is the magnetic amplitude calculated with the  $U^{4+}$  form factor taken in the dipole approximation. The dashed lines denote magnetic moment components proportional to  $p_L$  and  $(p_S + p_L)$ . The separation of the two contributions yields the orbital moment of  $2.07(5) \mu_B$  and the spin moment of  $-0.65(9) \mu_B$ . The total uranium magnetic moment is  $1.42(4) \mu_B$ . For comparison the ordered magnetic moment obtained from bulk magnetization measurements ( $p_o = 1.29(2) \mu_B$ ) is shown by a diamond. The resulting ratio  $-p_L/p_S$  amounts to  $3.2(4)$  indicating rather weak hybridisation of 5f electron states with conduction band states (the  $U^{4+}$  free ion value for this ratio is 3). This finding does not support the idea of a strong anisotropy in the delocalisation of 5f electrons proposed in [96OBAK] (see the caption of Fig. 136). Note also a deviation of the reflections (101), (200), (211) and (220) from a smooth form factor curve which may be due to neglecting the f-p hybridisation in the analysis.

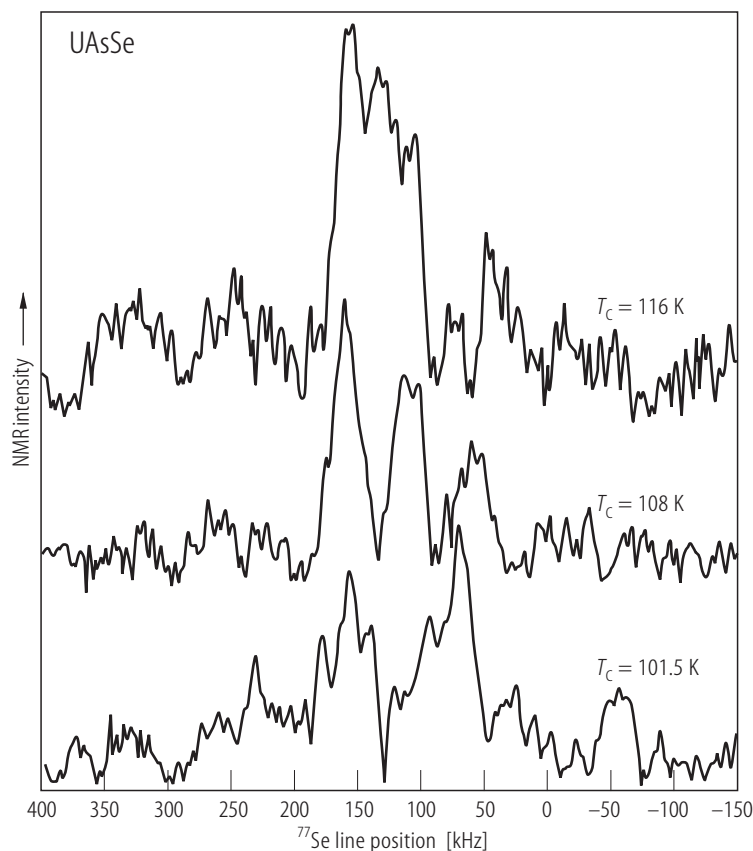


**Fig. 114.** UAsSe.  $^{77}\text{Se}$  NMR spin-echo spectra taken at room temperature in a fixed field of 7 T for three different single crystals characterized by the Curie temperature  $T_C$  of 101.5, 108 and 116 K [01CMKM]. The signal-to-noise ratio is poor, yet clearly more than one resonance line is observed indicating that there is more than one position for Se atoms in the unit cell, i.e. the structure is somewhat disordered. With decreasing  $T_C$  both the separation of NMR lines and their linewidth increase thus pointing to enhanced disorder. This finding supports the assumptions of two-level system model developed for UAsSe in order to explain its anomalous low-temperature resistivity (see Fig. 119).

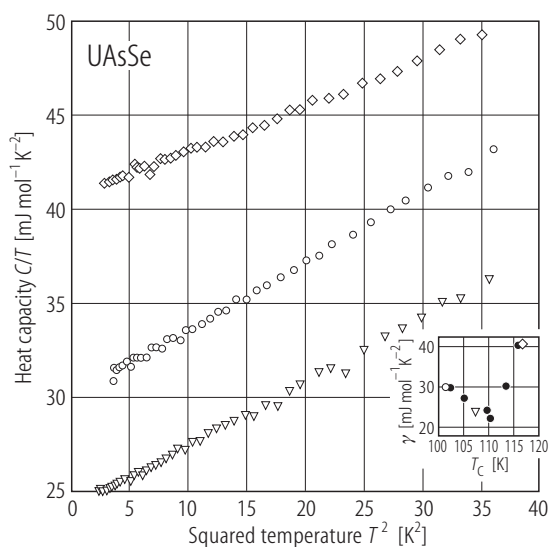


**Fig. 115.** UAsSe. Heat capacity over temperature,  $C_p/T$ , vs. squared temperature,  $T^2$ , measured on three single crystals obtained from different syntheses and characterized by the Curie temperature  $T_C$  of 101.5 K (circles), 107.5 K (triangles) and 117 K (diamonds) [01CHGL]. Inset: electronic heat capacity,  $\gamma = C_p/T(T \rightarrow 0)$ , vs.  $T_C$  for several single crystals. The enhancement of  $\gamma$  with decreasing  $T_C$  below 111 K the authors attributed to an increase of the concentration of two-level scattering centers responsible for non-magnetic Kondo effect (see the original paper for explanation). The subsequent rise of  $\gamma$  observed for  $T_C > 111$  K is unclear as yet.

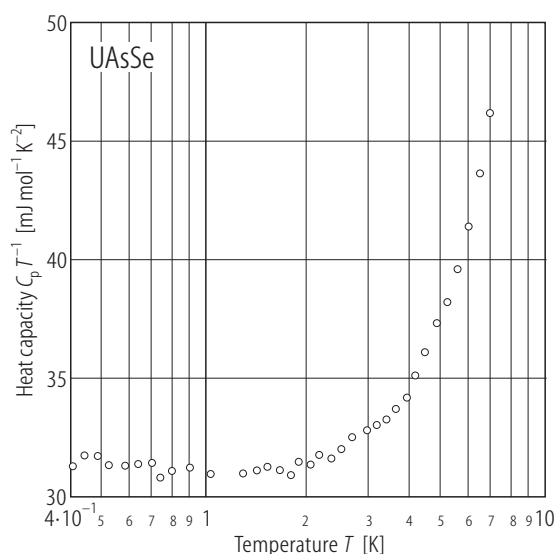


**Fig. 116.** UAsSe. Low temperature heat capacity over temperature,  $C_p/T$ , vs. temperature,  $T$ , in the range 0.4...7 K measured on a single crystal [02CHWP]. Note a small upturn below 1 K that possibly results from nuclear hyperfine field of As nuclei or/and electron-assisted tunneling in a system with structural disorder (for discussion see the original paper).

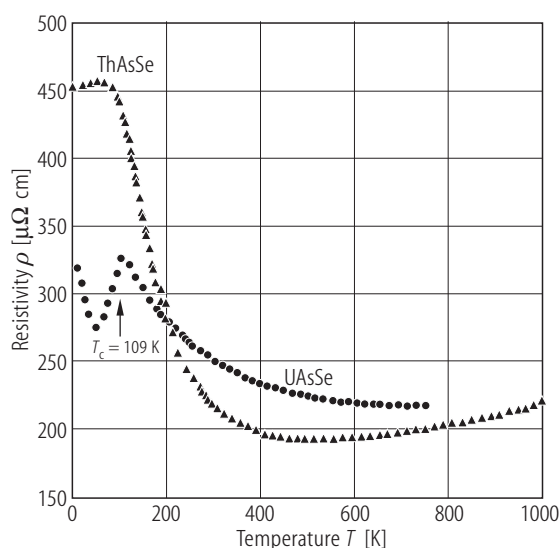


**Fig. 117.** ThAsSe, UAsSe. Electrical resistivity,  $\rho$ , vs. temperature,  $T$ , measured on single crystals with  $i \perp c$ -axis [88SBH]. The arrow marks a ferromagnetic phase transition in UAsSe at  $T_c = 109$  K. Note negative temperature coefficients of the resistivity of UAsSe between 2 and 50 K and above  $T_c$  (compare Fig. 97). The authors stress that this feature cannot be related to Kondo effect or any other mechanism of magnetic origin because a negative  $d\rho/dT$  characterizes also diamagnetic ThAsSe. Instead they suggest that the low temperature increase of the resistivity of both compounds is due to a reduction of the carrier concentration (see Fig. 66).

For Fig. 118 see next page

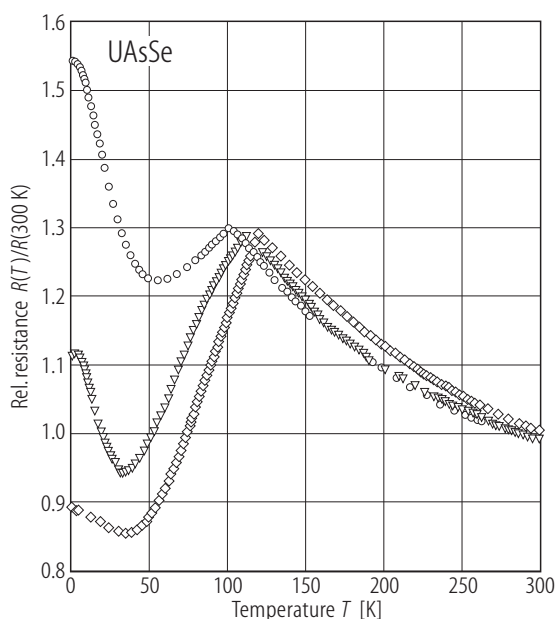


**Fig. 119.** UAsSe. Electrical resistance normalized to its room temperature value,  $R(T)/R(300\text{K})$ , vs. temperature,  $T$ , measured with the current flowing within the crystallographic  $ab$  plane on three different single crystals characterized by the Curie temperature  $T_c$  of 101.5 K (circles), 110.5 K (triangles) and 117 K (diamonds) [01CHGL]. Note that in the paramagnetic region the resistivity is hardly sample dependent but distinct differences occur in the ordered state where the anomalous low-temperature upturn monotonically increases with decreasing  $T_c$ . The observed behaviour the authors attributed to a non-magnetic Kondo effect arising from the presence of two-level system scattering centers, the concentration of which decreases with rising  $T_c$  (for explanation see the original paper).

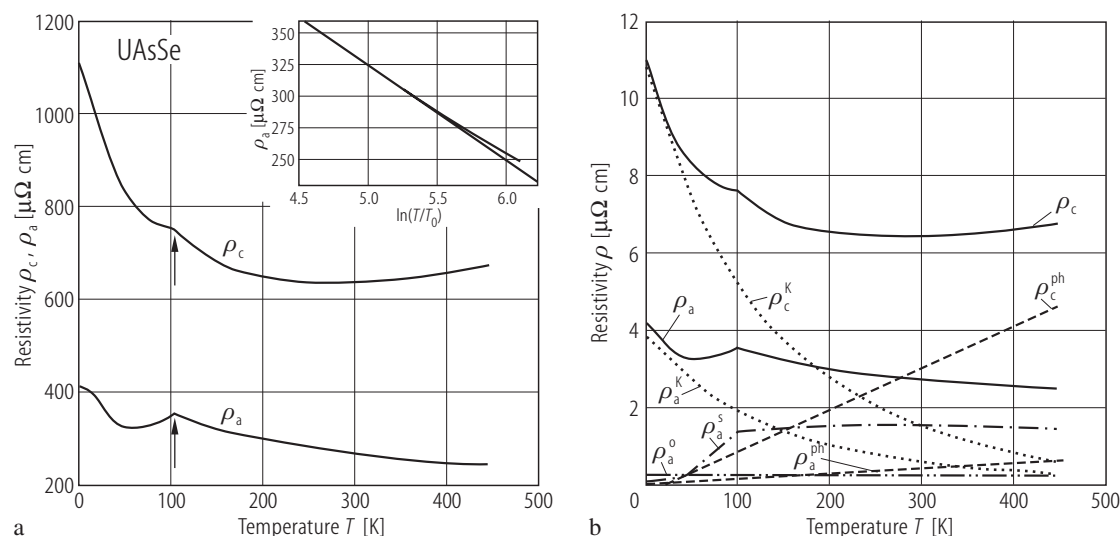


**Fig. 118.** UAsSe. (a) Electrical resistivity,  $\rho_c$  and  $\rho_a$ , vs. temperature,  $T$ , in the range 2...450 K measured on a single crystal with  $i \parallel c$ -axis and  $i \parallel a$ -axis, respectively [94HFW]. The arrows mark a ferromagnetic phase transition occurring at  $T_C = 102.0(5)$  K. Inset:  $\rho_a(T)$  on a semi-logarithmic scale in the paramagnetic region ( $T_0 = 1$  K). The solid line marks a linear in  $-\ln T$  variation of  $\rho_a$ , ascribed by the authors to magnetic scattering in contrast to the discussion given in [88SBH] (see Fig. 117). In  $\rho_c(T)$  no  $\ln T$  dependence was observed above  $T_C$ . Note that at low temperatures there is a

negative temperature coefficient in both  $\rho_a(T)$  and  $\rho_c(T)$  with neither saturation nor activation behaviour down to 2 K. (b) Decomposition of the experimental  $\rho_c(T)$  and  $\rho_a(T)$  curves from panel (a) into the components: residual  $\rho^0$  (dot-dot-dashed line), spin disorder  $\rho^s(T)$  (dot-dashed line), phonon  $\rho^{ph}(T)$  (dashed line) and Kondo  $\rho^K(T)$  (dotted line) [95HFW]. For the description of the method of the decomposition refer to the original paper. Note that the authors assumed that the only anisotropic components to the total resistivity of UAsSe are  $\rho^{ph}(T)$  and  $\rho^K(T)$

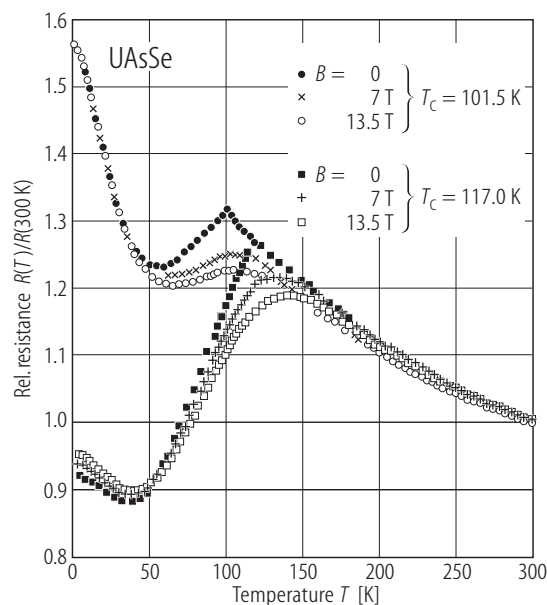


**Fig. 120.** UAsSe. Electrical resistance normalized to its room temperature value,  $R(T)/R(300\text{ K})$ , vs. temperature,  $T$ , measured on single crystals with  $i \perp c$ -axis and magnetic field of 0, 7 T and 13.5 T applied along the  $c$ -axis [02CHWP]. Two different single crystals were studied, characterized by the Curie temperature  $T_C$  of 101.5 K and 117 K. Note that in the region of low-temperature upturns of the resistance the effect of magnetic field is very small implying non-magnetic origin of this behaviour.

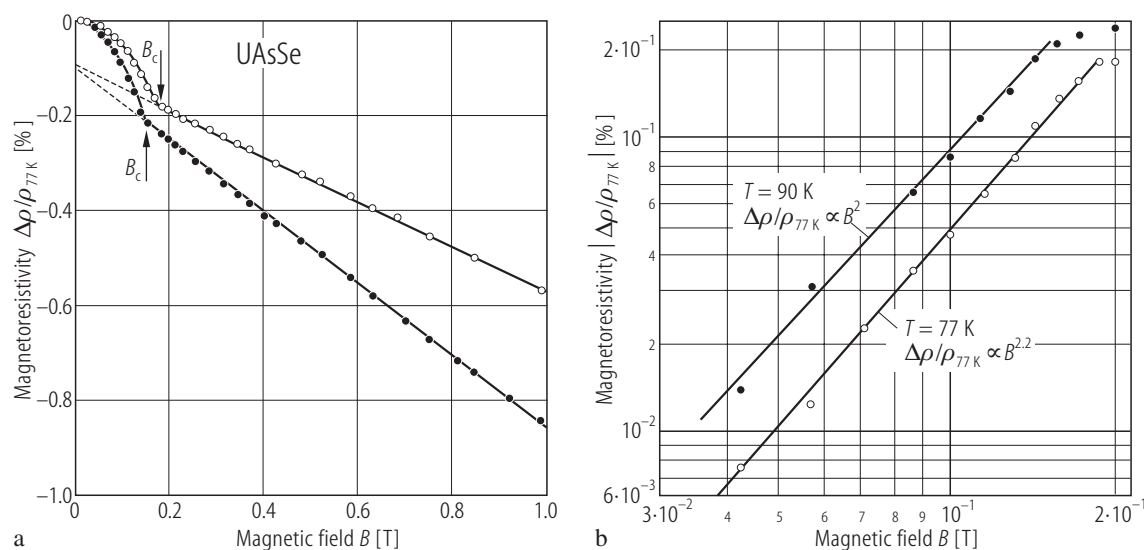


**Fig. 121.** UAsSe. (a) Transverse magnetoresistivity,  $\Delta\rho/\rho_{77K} = [\rho(T, B) - \rho(T, 0)]/\rho(77\text{ K}, 0)$ , vs. magnetic field,  $B$ , up to 1 T, measured at 77 K (open circles) and 90 K (full circles) on a single crystal with  $i \parallel a$ -axis and  $B \parallel c$ -axis (easy magnetization direction) [77WH]. Note that  $\Delta\rho/\rho_{77K}$

is negative and above a certain value of magnetic field  $B_c$  depends linearly on  $B$ . (b) The data from panel (a) for  $B < B_c$ , plotted with a double logarithmic scale [77WH]. Note that in this range  $\Delta\rho/\rho_{77K}$  vs.  $B$  obeys approximately a  $B^2$  law.

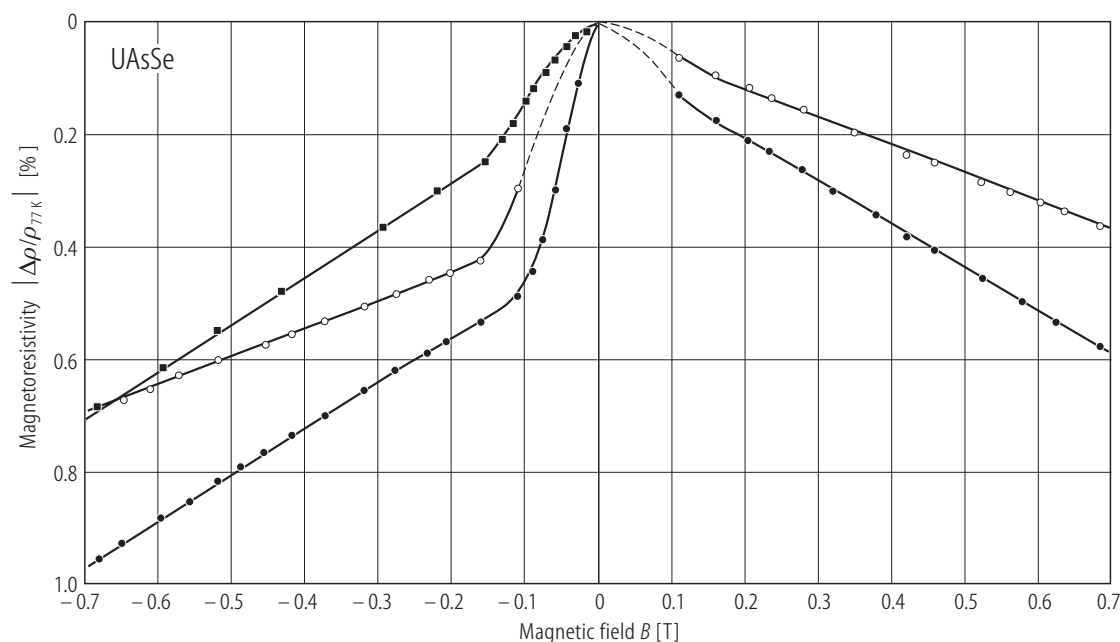


**Fig. 122.** UAsSe. Transverse magnetoresistivity,  $\Delta\rho/\rho_{77K} = [\rho(T, B) - \rho(T, 0)]/\rho(77\text{ K}, 0)$ , vs. magnetic field,  $B$ , measured at 77 K (open symbols) and 90 K (full symbols) on two different single crystals (circles and squares, respectively) with  $i \parallel a$ -axis and  $B \parallel c$ -axis [77WH]. The magnetic field was applied in two opposite directions (left- and right-hand side panels, respectively). Note that the slope of the linear parts of  $\Delta\rho/\rho_{77K}$  vs.  $B$  at a fixed

temperature is identical for both samples and for opposite directions of  $B$ . Thus, the effect can be ascribed to suppression of the spin fluctuations by magnetic field. Note also that  $\Delta\rho/\rho_{77K}$  exhibits considerably different values for different field directions over the whole magnetic field range. This asymmetry in  $\Delta\rho/\rho_{77K}$  vs.  $B$  the authors associated with domain effects.

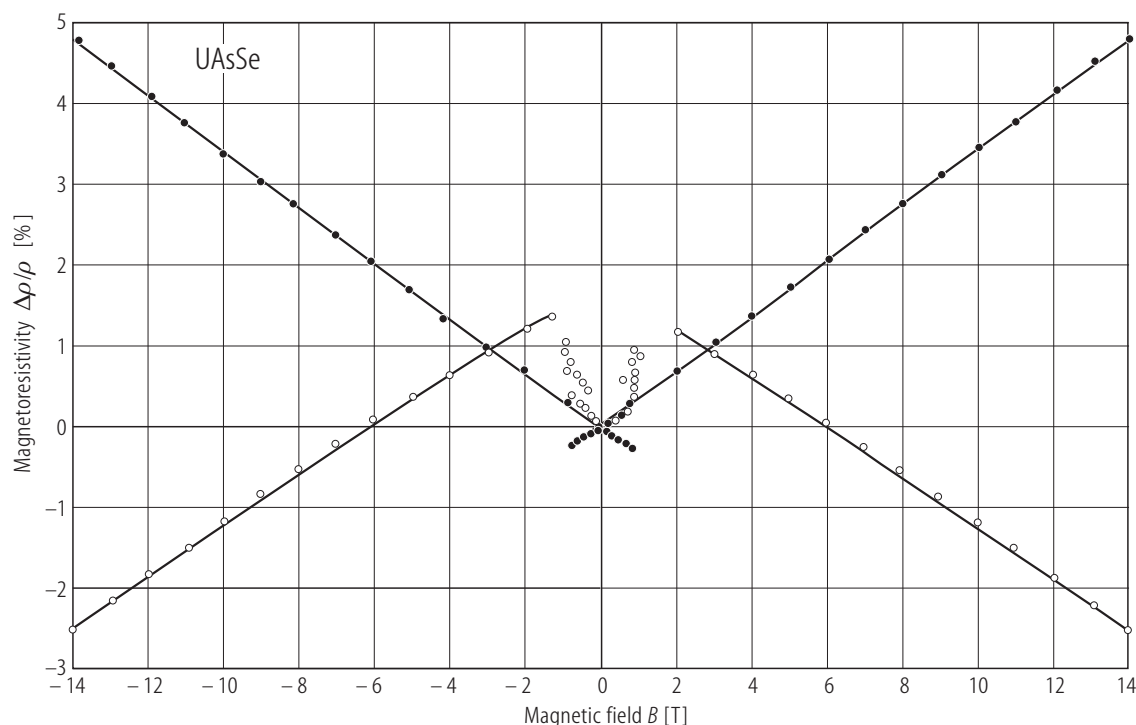


**Fig. 123.** UAsSe. Transverse ( $i \perp c$ -axis, filled circles) and longitudinal ( $i \parallel c$ -axis, open circles) magnetoresistivity,  $\Delta\rho/\rho$ , vs. magnetic field,  $B$ , in the range  $\pm 14$  T, measured at 4.2 K on a single crystal with  $B \parallel c$ -axis (easy magnetization direction) [00HCFW]. The hysteresis below 1 T the authors ascribed to domain effects (see Fig. 132). Note different signs of the longitudinal and transverse magnetoresistivity. For  $B \parallel a$ -axis (not shown)  $\Delta\rho/\rho$  is an order of magnitude lower but also positive for  $i \perp c$ -axis and

negative for  $i \parallel c$ -axis. This behaviour contradicts the hypothesis about usual Kondo scattering on magnetic impurities (see Fig. 118). Instead the authors suggested that the magnetoresistivity of UAsSe reflects the magnetic properties of the conduction electron channels and the compound is a novel-type Kondo system describable within the two-level Kondo model. The mechanism leading to the formation in UAsSe of two levels may be disorder in the As and Se sublattices (see Fig. 103).

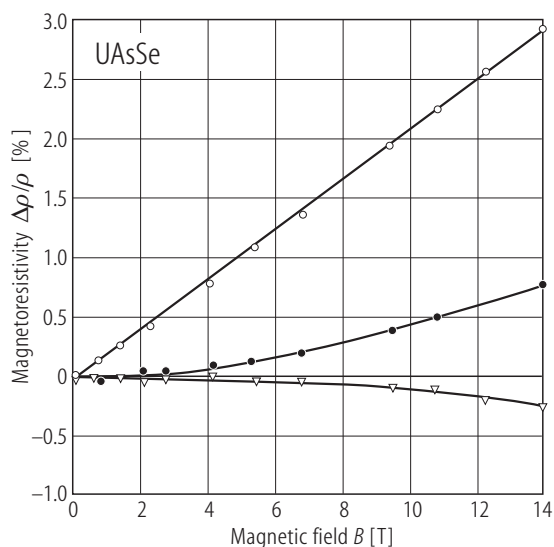


**Fig. 124.** UAsSe. Magnetoresistivity,  $\Delta\rho/\rho$ , vs. magnetic field,  $B$ , up to 14 T, measured at 4.2 K on a single crystal with  $i \parallel a$ -axis (hard magnetization direction) in magnetic field  $B \parallel c$ -axis (open circles),  $B \parallel b$ -axis (open triangles) and  $B \parallel a$ -axis (filled circles) [98HCPF]. Note a linear-in- $B$  behaviour of the transverse magnetoresistivity taken with the field aligned along the easy magnetization axis ( $c$ -axis), which was ascribed by the authors to the Kondo impurity component of the resistivity (see Fig. 118). Note also that for the magnetic field directed perpendicular to the easy magnetization axis  $\Delta\rho/\rho$  is much lower than for  $B \parallel c$ -axis, varies non-linearly with  $B$  and is negative for the transverse and positive for the longitudinal field direction.

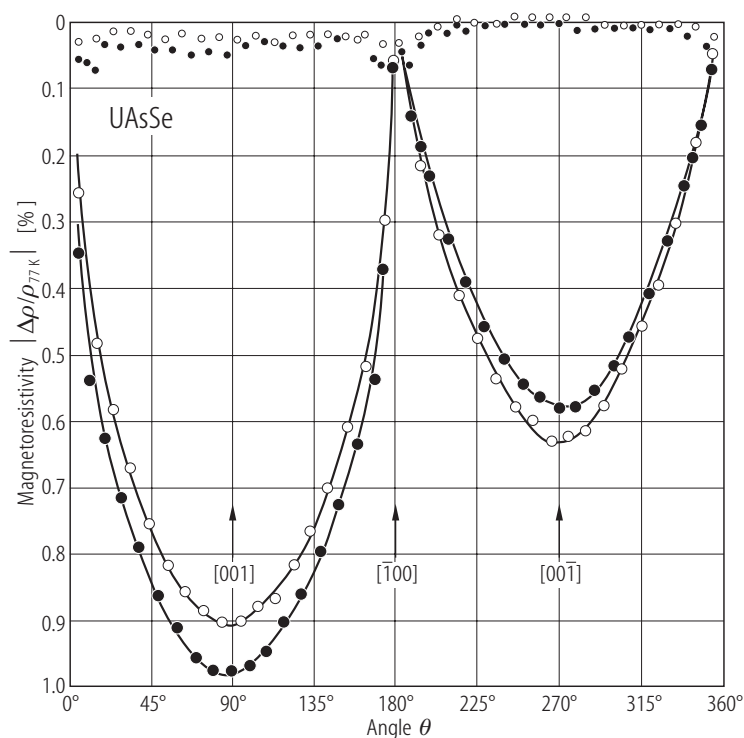


**Fig. 125.** UAsSe. Transverse magnetoresistivity,  $\Delta\rho/\rho_{77\text{K}} = [\rho(T, B) - \rho(T, 0)]/\rho(77\text{K}, 0)$ , vs. angle,  $\theta$ , between the magnetic field vector and the [010] direction in the (100) plane [77WH]. The measurements were done at  $T = 90\text{ K}$  in a magnetic field of  $0.69\text{ T}$  on two different single crystalline samples (open and full symbols, respectively) with  $i \parallel a$ -axis. Small circles show the residual magnetoresistivity. Note that  $\Delta\rho/\rho_{77\text{K}}$  is strongly anisotropic reaching its maximum when  $B$  is parallel to the easy magnetization [001] axis and a minimum being close to zero if  $B$  is perpendicular to this direction. The residual magnetoresistivity is also anisotropic and exhibits a rather large dispersion. Note also that the magnetoresistivity effect is asymmetrical. The latter feature is independent of the manner of cooling the sample and was attributed by the authors to the effect of presence of crystal lattice defects in the samples studied (for explanation see the original paper).

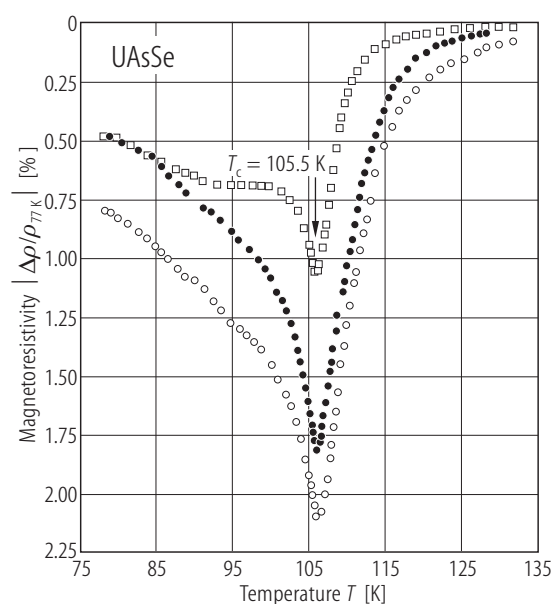


**Fig. 126.** UAsSe. Transverse magnetoresistivity,  $\Delta\rho/\rho_{77\text{K}} = [\rho(T, B) - \rho(T, 0)]/\rho(77\text{K}, 0)$ , vs. temperature,  $T$ , in the range  $77 \dots 135\text{ K}$ , measured in a constant field of  $0.923\text{ T}$  (circles) and  $0.295\text{ T}$  (squares) on a single crystal with  $i \parallel a$ -axis and  $B \parallel c$ -axis (easy magnetization direction) [77WH]. Open and filled symbols represent the data taken with two opposite directions of the field. Note a negative minimum at the ferromagnetic phase transition at  $T_c = 105.5\text{ K}$ . The anomaly around  $90\text{ K}$  the authors attributed to domain processes.

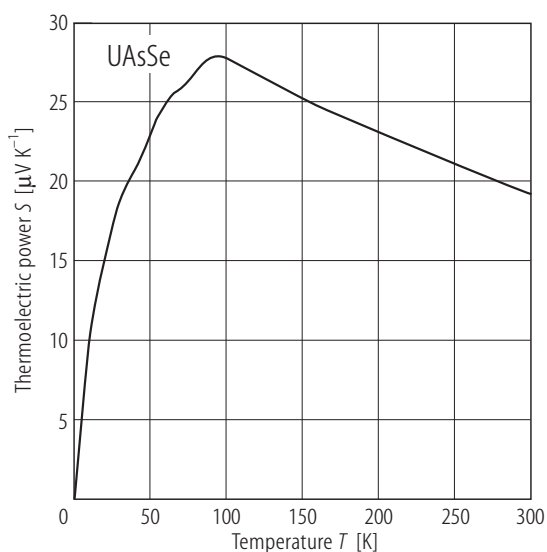


**Fig. 127.** UAsSe. Thermoelectric power,  $S$ , vs. temperature,  $T$ , measured on a single crystal in the  $ab$ -plane [94HFW]. Note that  $S$  is positive but rather high as for a normal metal. The ferromagnetic phase transition manifests itself as a maximum in  $S(T)$  at  $95\text{ K}$ . At the lowest temperatures the slope in  $S(T)$  is as high as  $1.1\text{ μV/K}$ .

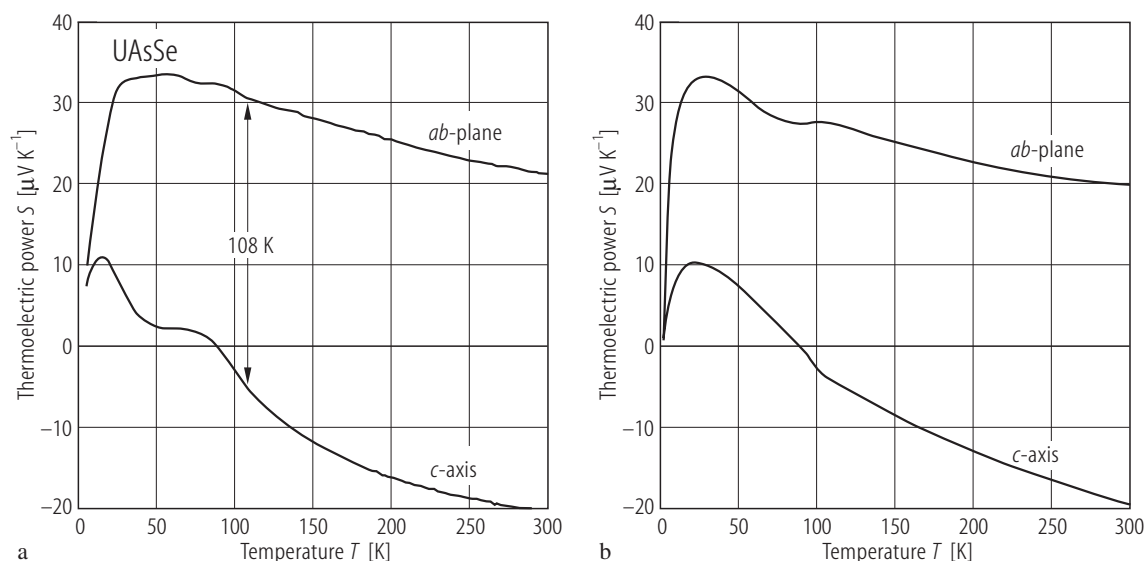


**Fig. 128.** UAsSe. (a) Thermoelectric power,  $S$ , vs. temperature,  $T$ , measured on a single crystal in the  $ab$ -plane (upper curve) and along the  $c$ -axis (lower curve) [00HCFW]. The arrows mark the ferromagnetic phase transition at  $T_C = 108$  K. Note a strong anisotropy. (b) Calculated  $S(T)$  in the  $ab$ -plane (upper curve) and along the

$c$ -axis (lower curve). The total thermopower was considered as a weighted sum of a ferromagnetic metal contribution and a Kondo contribution. For details of the analysis refer to the original paper. Note a similarity between the calculated and measured dependencies, which argues for the presence of Kondo effect in UAsSe (compare Fig. 117).

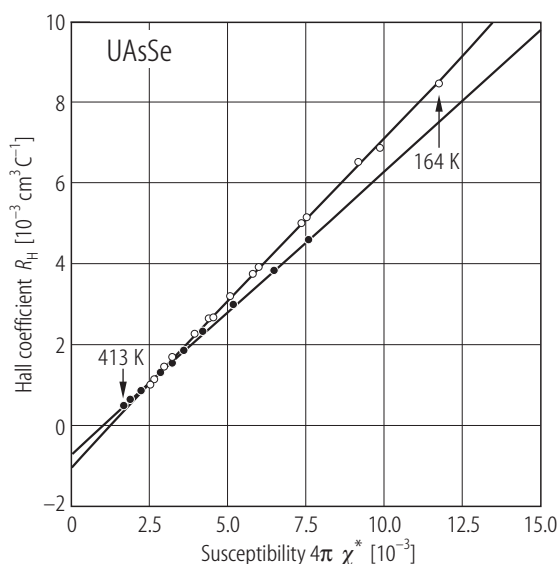


**Fig. 129.** UAsSe. Effective Hall coefficient,  $R_H$ , measured on two single crystals with  $T_C = 107.0$  K (open circles) and  $T_C = 104.8$  K (filled circles), respectively, in the configuration  $i \perp c$ -axis and  $B \parallel c$ -axis, vs. effective magnetic susceptibility,  $\chi^* = \frac{C}{T - (\Theta - 4\pi NC)}$ , [94HFW].

The values (not given in the paper) of the Curie constant,  $C$ , the paramagnetic Curie temperature,  $\Theta$ , and the demagnetization factor,  $N$ , were fitted in order to get a linear dependence of  $R_H = R_0 + 4\pi R_s \chi^*$ . For the sample with  $T_C = 107.0$  K:  $R_0 = -1 \cdot 10^{-3} \text{ cm}^3/\text{C}$  and  $R_s = 0.81 \text{ cm}^3/\text{C}$ . For the sample with  $T_C = 104.8$  K:  $R_0 = -7 \cdot 10^{-4} \text{ cm}^3/\text{C}$  and  $R_s = 0.70 \text{ cm}^3/\text{C}$ . These values of  $R_0$  correspond in a single-band model to the carrier concentration of 0.41...0.58 e/f.u. Yet, the positive sign of the thermopower (see Fig. 127) accompanying the negative sign of the normal Hall coefficient suggest that UAsSe is not a single-band system.



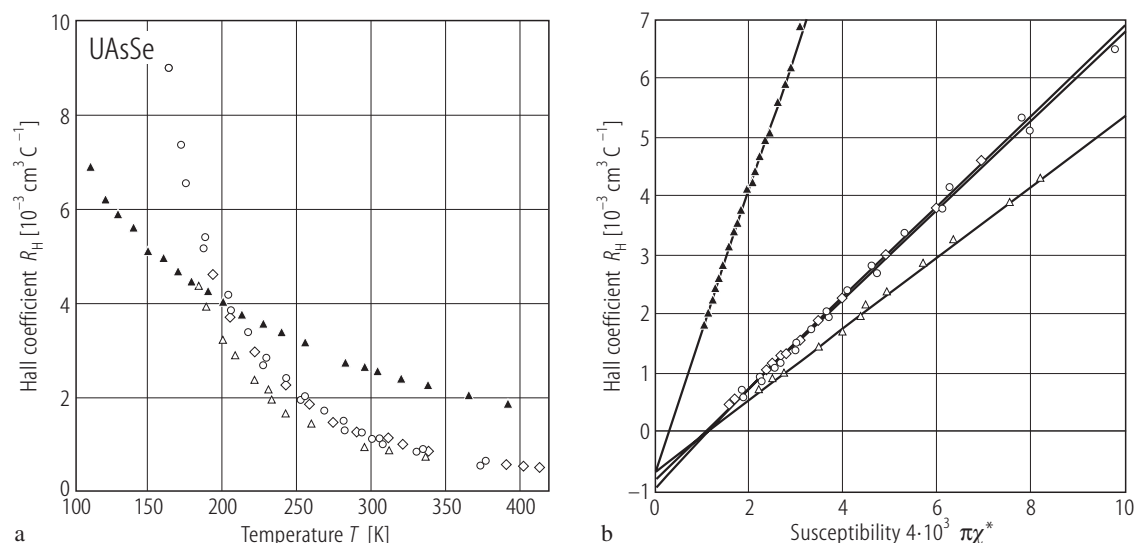


**Fig. 130.** UAsSe. (a) Effective Hall coefficient,  $R_H$ , measured on selected single crystals with  $T_C = 107.0$  K (circles), 104.8 K (diamonds) and 106.0 K (triangles) in the two configurations:  $i \parallel b$ -axis and  $B \parallel c$ -axis (open symbols) or  $i \parallel c$ -axis and  $B \parallel b$ -axis (filled symbols), vs. temperature,  $T$ , in the range  $T_C \dots 430$  K [95HFW]. Note a similar behaviour of  $R_H(T)$  of the samples with different  $T_C$ , measured in the same configuration. (b) Hall effect data from panel (a) vs. effective magnetic susceptibility,

$$\chi^* = \frac{C}{T - (\Theta - 4\pi NC)}$$

the paramagnetic Curie temperature,  $\Theta$ , and the demagnetization factor,  $N$ , were fitted in order to get a

linear dependence of  $R_H = R_0 + 4\pi R_s \chi^*$  (marked by the solid lines). Note a good agreement between the data obtained with  $B \parallel c$ -axis for the samples with  $T_C = 107.0$  K and  $T_C = 104.8$  K. Another slope got in this configuration for the sample with  $T_C = 106.0$  K the authors attributed to some inaccuracy in the thickness measurement. The normal Hall coefficient,  $R_0$ , is isotropic and equal to  $-8.8 \cdot 10^{-4} \text{ cm}^3/\text{C}$ , which corresponds in a single-band model to the carrier concentration of 0.47 e/f.u. The spontaneous Hall coefficient,  $R_s$ , is strongly anisotropic and equal to 0.78  $\text{cm}^3/\text{C}$  and 3.0  $\text{cm}^3/\text{C}$  for  $B \parallel c$ -axis and  $B \parallel b$ -axis, respectively. Compare the values given in the caption to Fig. 129.

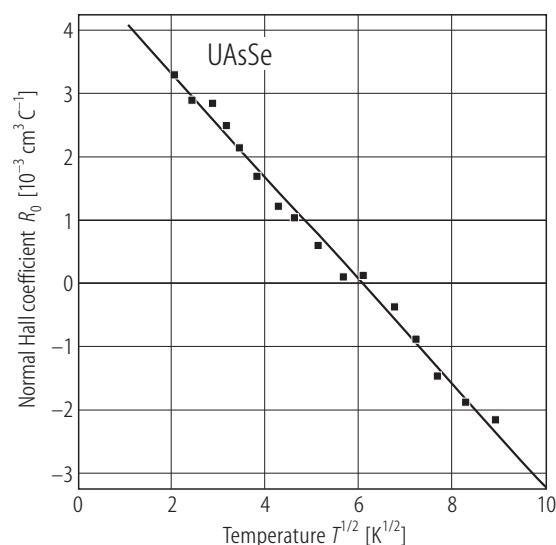


**Fig. 131.** UAsSe. Normal Hall coefficient,  $R_0$ , vs. square root of temperature,  $T^{1/2}$ , below  $T_C = 106$  K [00HCFW]. Note an anomalous behaviour of  $R_0$  previously observed for metallic glasses and amorphous metals. The spontaneous Hall coefficient of UAsSe (not shown) behaves typically for ferromagnets: it decreases monotonously from 2.16  $\text{cm}^3/\text{C}$  at  $T_C$  down to 0.06  $\text{cm}^3/\text{C}$  at 4.2 K.

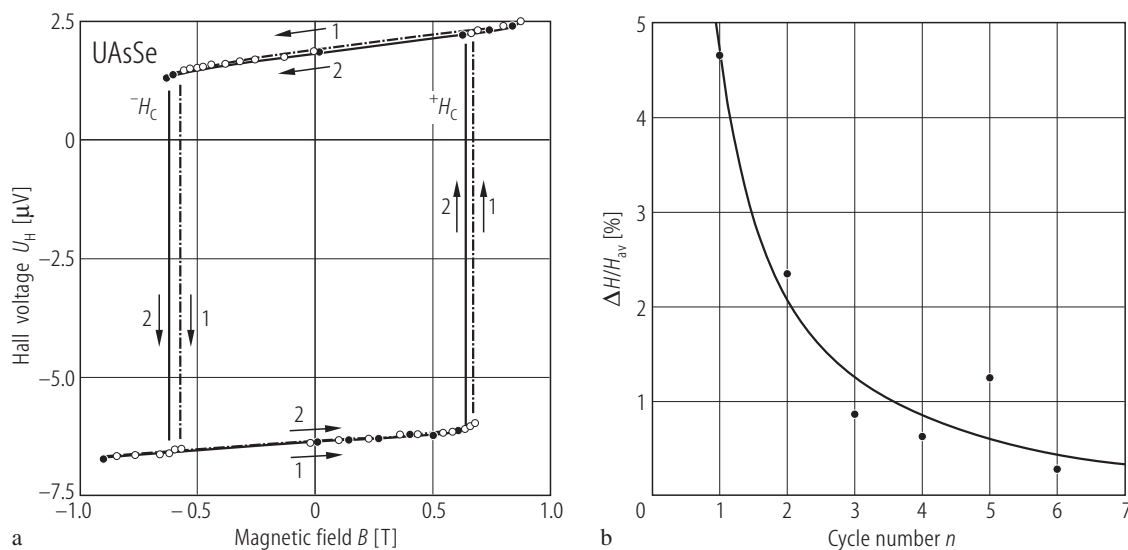


**Fig. 132.** UAsSe. (a) Hall voltage hysteresis loop,  $U_H(B)$ , taken at 4.26 K on a single crystal cooled in zero field with  $i \perp c$ -axis and  $B \parallel c$ -axis [98HCPF]. The arrows indicate increasing and decreasing magnetic field. Two cycles (labeled 1 and 2) are shown (open and filled circles, respectively, connected by dashed and solid lines, respectively). At the critical field  $H_c$  there occurs a 180°-domain wall reconstruction. Note that this latter feature is not symmetric.

(b) Asymmetry ratio,  $\Delta H/H_{av} = \frac{|+H_c| - |-H_c|}{H_{average}}$ , of the

critical field  $H_c$ , vs. number of cycles,  $n$ , of magnetic field change (see panel (a)). The solid line is a guide for the eye. The rapid decrease of  $\Delta H/H_{av}$  with increasing  $n$  the authors interpreted as an indication of the presence of magnetic impurities (for the arguments refer to the original paper).

For Figs. 133, 134 see next pages

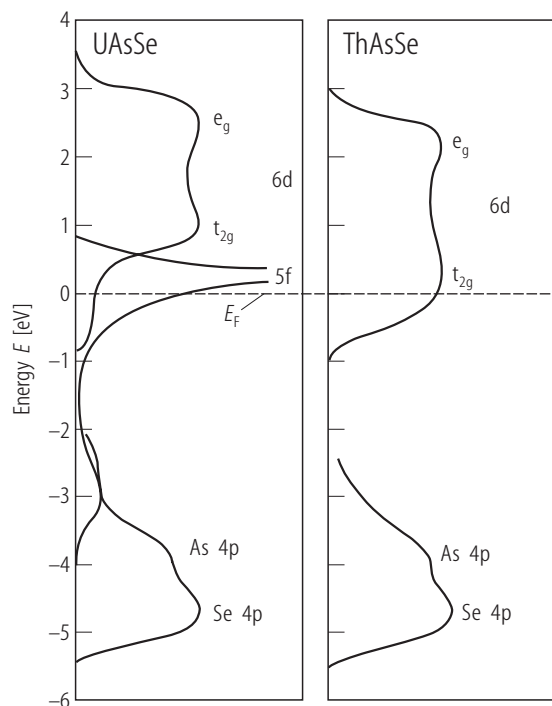


**Fig. 135.** ThAsSe, UAsSe. Empirical energy level schemes as derived from optical and magneto-optical studies [86R]. The 5f electrons in UAsSe form a band at the Fermi energy, which is occupied by nearly 3 electrons. In spite of relatively high density of d-states at  $E_F$ , ThAsSe is diamagnetic because of strong diamagnetism of the inner shell, exceeding the Pauli paramagnetism due to d electrons. Note that the d band in UAsSe exhibits no exchange splitting, as evidenced by the same energy of  $f \rightarrow d$  transition seen in  $\sigma_{xx}$  and  $\sigma_{xy}$  (see Figs. 133 and 134, respectively).

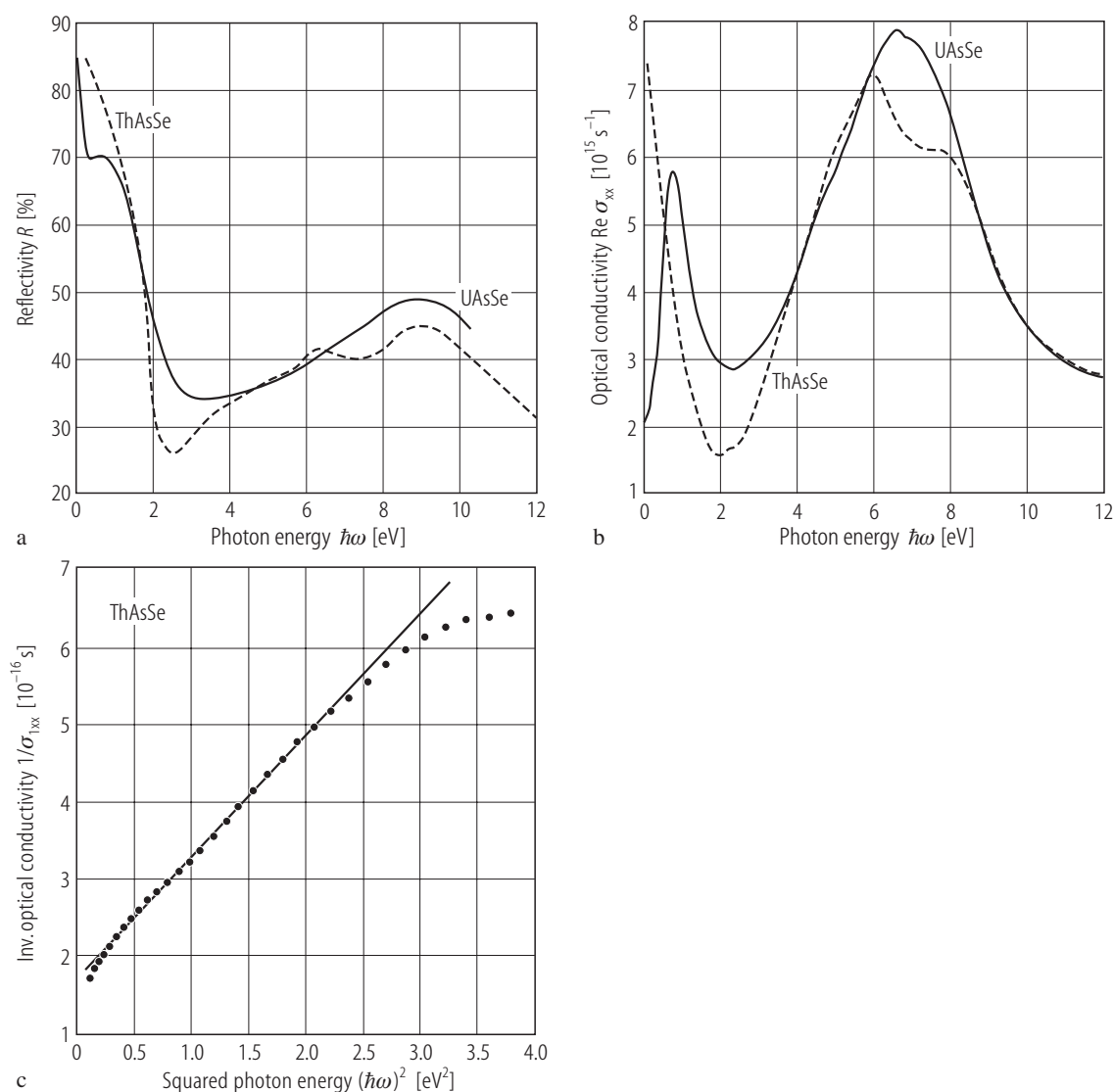


**Fig. 133.** ThAsSe, UAsSe. **(a)** Near normal incidence reflectivity,  $R$ , vs. photon energy,  $\hbar\omega$ , in the energy range 0.03...12 eV, measured on cleaved single crystals at room temperature [86R]. Note pronounced differences below 4 eV, i.e. a Drude behaviour for ThAsSe (dashed curve) and a strong interband transition around 1 eV for UAsSe (solid curve). **(b)** Absorptive diagonal conductivity,  $\text{Re } \sigma_{xx}$ , vs.  $\hbar\omega$  as derived from a Kramers-Kronig inversion of the reflectivity shown in panel (a) [86R]. The broad absorption band, centered at 6.9 eV, is assigned to the charge transfer transition of p valence electrons of As and Se into empty d states of Th or U. Note that no crystal field splitting is resolved in UAsSe (solid curve), which is the case for

ThAsSe (dashed curve). The sharp maximum seen for UAsSe at 0.73 eV is an  $f \rightarrow d$  excitation, absent in the low-energy spectrum of ThAsSe, which is dominated by the conduction electrons (see panel (c)). The number of charge carriers in UAsSe is estimated to be less than 0.3 electrons per formula unit. **(c)** Drude fit,  $1/\sigma_{xx}$  vs.  $(\hbar\omega)^2$ , of the optical conductivity of ThAsSe, shown in panel (b) [86R]. The parameters of the fit in the range 0.25...1.5 eV:  $\hbar\omega_p = 7.15$  eV and  $\hbar\gamma = 1.0$  eV ( $\gamma$ : interband electron relaxation time parameter). The concentration of conduction electrons is calculated to be  $3.7 \cdot 10^{22} \text{ cm}^{-3}$ , i.e. about 2.6 free electrons per formula unit.

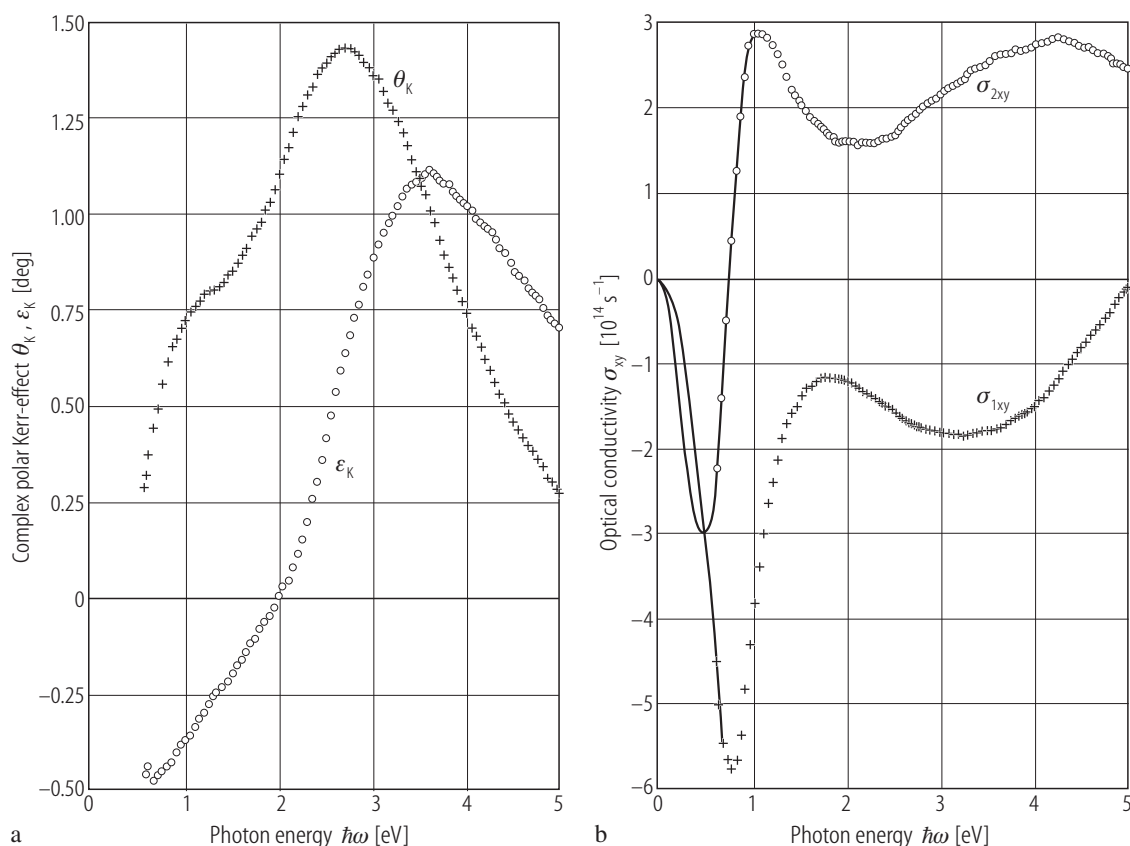


**Fig. 134.** UAsSe. (a) Polar Kerr rotation,  $\theta_K$ , and polar Kerr ellipticity,  $\varepsilon_K$ , vs. photon energy,  $\hbar\omega$ , in the range 0.5...5 eV, measured on cleaved single crystals at magnetic saturation, i.e. at  $T = 10$  K in a field of 5 T oriented parallel to the easy-magnetization  $c$ -axis [86R]. (b) Complex off-diagonal conductivity at magnetic saturation as calculated from the polar magneto-optical Kerr effect displayed in panel (a) and the optical constants [86R]. The extrapolation for  $\hbar\omega < 0.5$  eV has been estimated by Kramers-Kronig transformation. The peak in  $\sigma_{xy}$  at 4.3 eV is assigned to the excitation of bonding pd-electrons from the top of the valence band (note a weak shoulder in  $\sigma_{xx}$  shown in Fig.

133) into spin-polarised f states. The well pronounced "diamagnetic" line-shaped structure at 0.73 eV corresponds to the sharp maximum in  $\sigma_{xx}$  at the same energy (see Fig. 133) and is assigned to an  $f \rightarrow d$  transition. The absence of any fine structure in this signal and its high oscillator strength are indicative of the itinerant character of the 5f electrons, which form a narrow f-band at  $E_F$  with a correlation energy smaller than the band width and an occupation close to 3 electrons per U atom. Note that contradictory conclusions about the character of f electrons in UAsSe have been drawn from XPS measurements (compare Fig. 138).

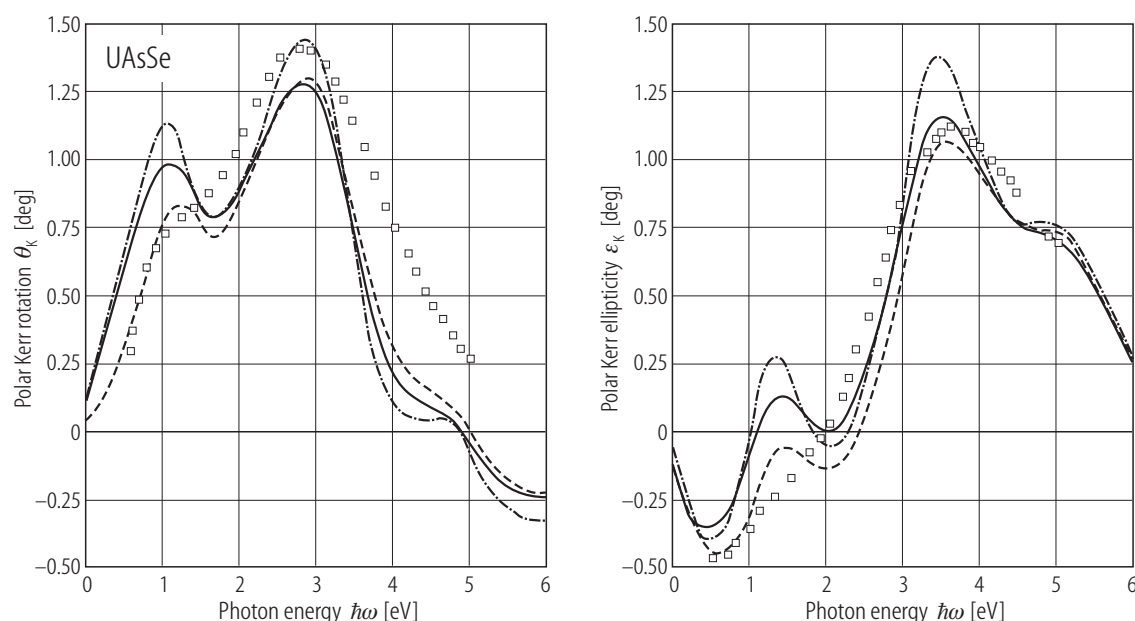


**Fig. 136.** UAsSe. Polar Kerr rotation,  $\theta_K$ , and polar Kerr ellipticity,  $\varepsilon_K$ , vs. photon energy,  $\hbar\omega$ , calculated on the basis of density functional theory in the local spin-density approximation (for further details see the original paper), as compared to the experimental data (squares) taken from [86R] (see also Fig. 134) [96OBAK]. The relaxation-time broadening parameter applied was 0.03 Ry (dashed-dotted lines) and 0.04 Ry (solid lines). The dashed curves are the spectra calculated for the broadening of 0.04 Ry with taking into account an intraband Drude-type contribution to the conductivity with the parameters:  $\sigma_D = 3 \cdot 10^{15} \text{ s}^{-1}$  and  $\tau_D^{-1} = 0.02 \text{ Ry}$ . Note a very good agreement between LSDA

band theory and experiment, strongly suggesting that the 5f electrons in UAsSe are at least partially itinerant. As the magnetization and magnetic susceptibility behaviour (see Figs. 85-89) and the photoemission data (see Fig. 138) support rather a well localised picture of the magnetism in this compound, the authors proposed that delocalisation of the 5f electrons is strongly anisotropic, i.e. the 5f electrons are itinerant in the uranium atoms planes (which are selectively probed by the polar magneto-optical spectroscopy) but more localised perpendicular to these planes.

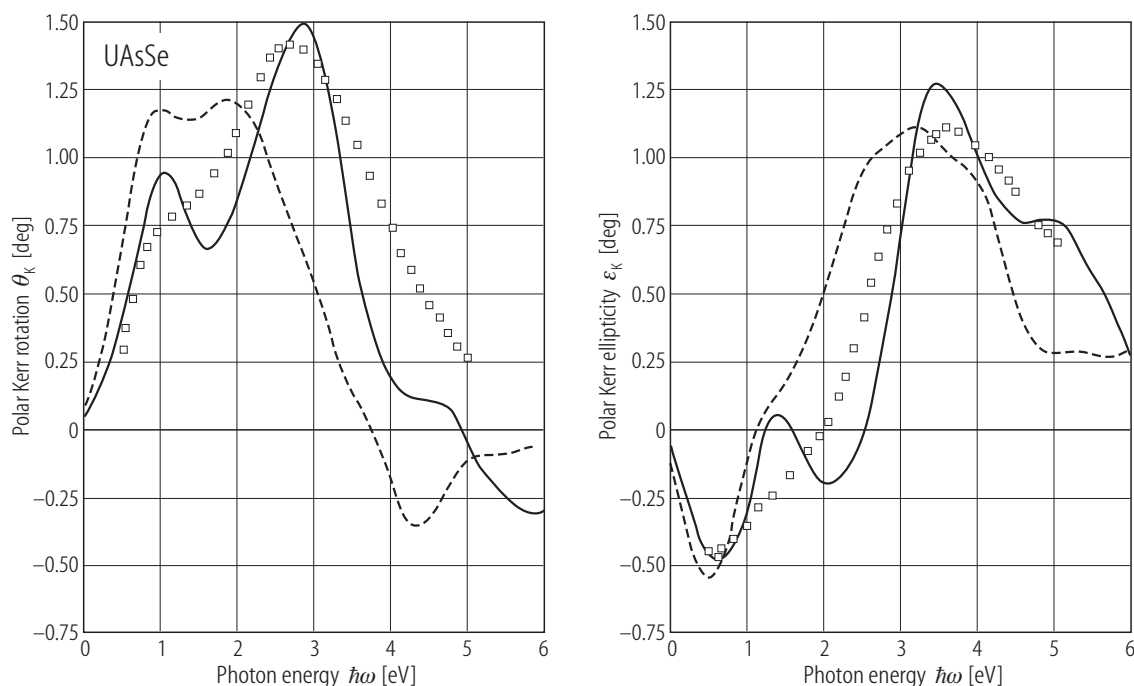


**Fig. 137.** UAsSe. Polar Kerr rotation,  $\theta_K$ , and polar Kerr ellipticity,  $\varepsilon_K$ , vs. photon energy,  $\hbar\omega$ , calculated as described in the caption of Fig. 136 for the incident light along the  $c$ -axis (solid lines) and along the  $a$ -axis (dashed lines) [96OBAK]. The relaxation-time broadening.

parameter applied was 0.03 Ry and a Drude conductivity was taken into account. For comparison the experimental spectra taken from [86R] are shown (squares). Note a pronounced anisotropy in the calculated magneto-optical spectra

For Fig. 138 see next page

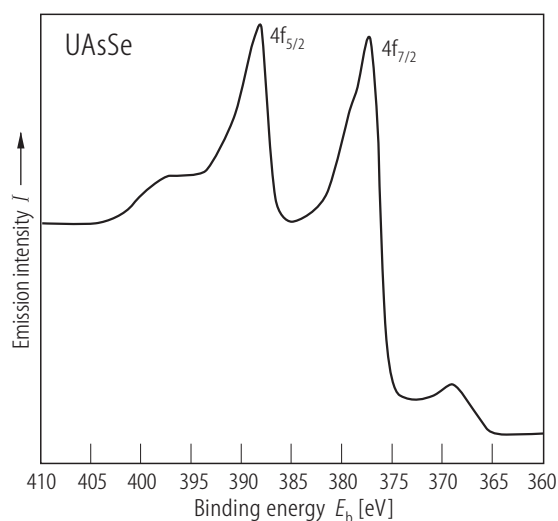


**Fig. 139.** UAsSe. 4f core level spectrum obtained on a single crystal cleaved *in situ* perpendicular to the [001] axis [81BEH]. The line shape indicates the existence of uranium in one single valence state. The satellite at about 7 eV above the  $4f_{5/2}$  line is assigned to a final state excitation in the form of a shake-up. The shoulder on the higher energy side of the  $4f_{7/2}$  component is due to the X-ray satellite contribution from the  $4f_{5/2}$  line. Large asymmetry of the 4f lines is indicative for the high density of states at the Fermi level (see also Fig. 138).

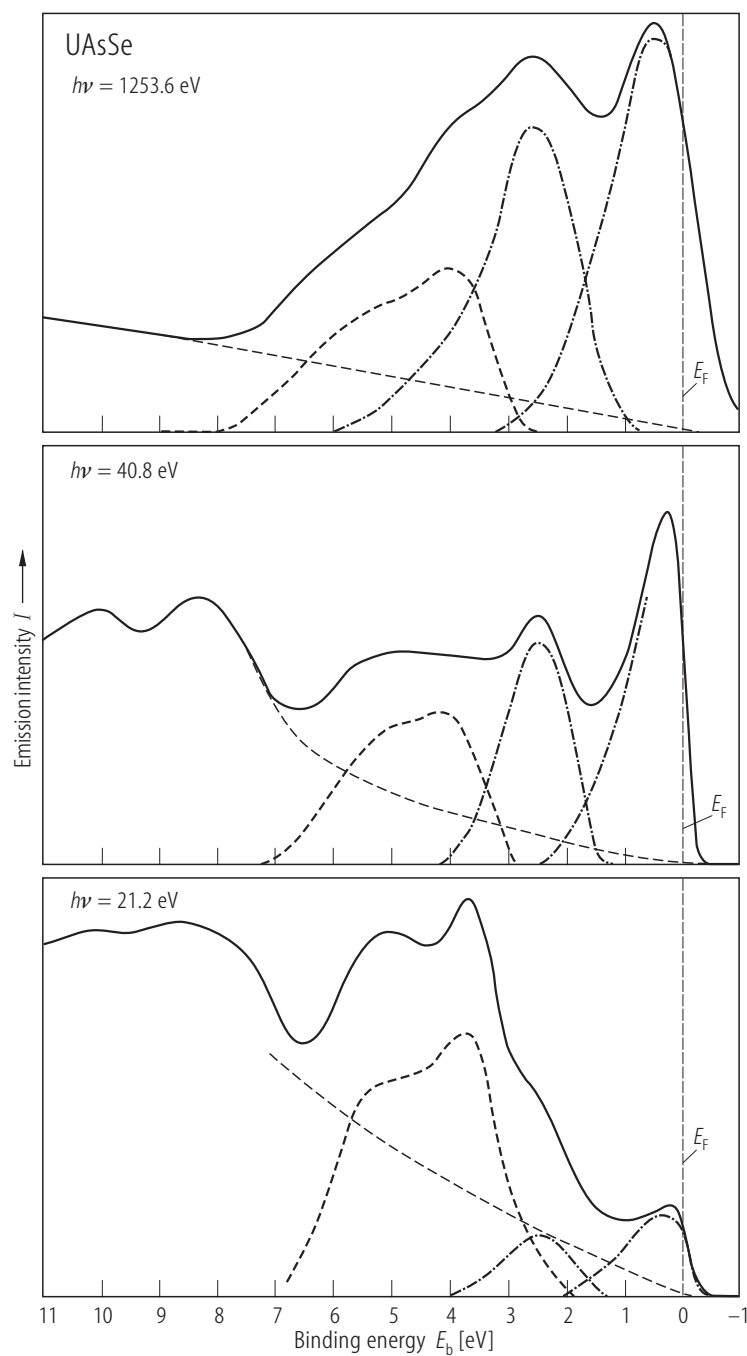


**Fig. 138.** UAsSe. Photoemission energy distribution curves at the photon energies  $h\nu = 21.2$ ,  $40.8$  and  $1253.6$  eV (panels from the bottom to the top, respectively), taken on single crystals cleaved *in situ* perpendicular to the  $[001]$  axis [81BEH]. Zero binding energy is the Fermi level. The dashed curves correspond to the contribution of the valence electrons. The dashed-dotted curves denote the contribution of the  $5f$  electrons. The valence band peaks at  $3.7$  and  $5.2$  eV are due to arsenic  $4p$  and selenium  $4p$  electrons, respectively. Note the presence of two structures with  $f$ -character: the one at  $E_F$  corresponds to the ground state location, the other at  $2.6$  eV is due to splitting on the uranium  $5f$ -shell left behind by the photoemission process. This observation is a strong indication for the localized character of the  $5f$  electrons in UAsSe, and thus contradicts the itinerant picture derived in magneto-optical studies (see Fig. 134).

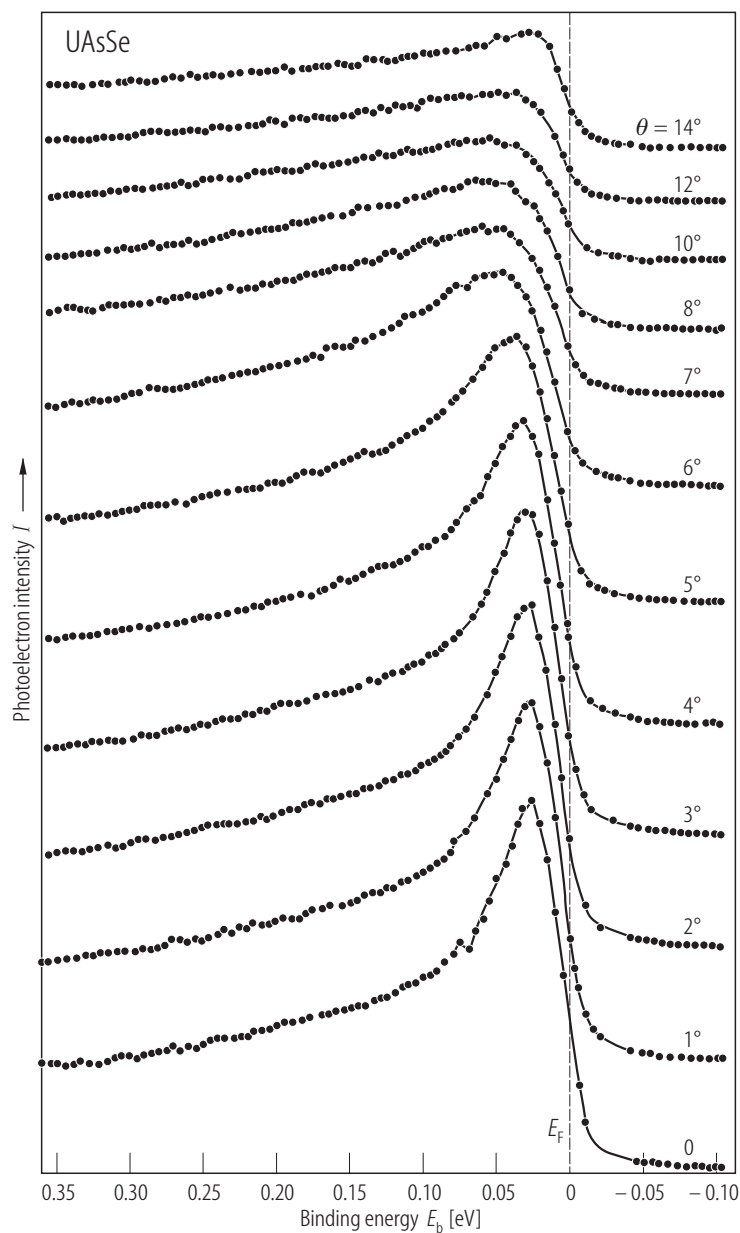


**Fig. 140.** UAsSe. Angle resolved photoemission spectra measured on a single crystal at 20 K and photon energy of 40 eV with angles  $\theta$  given in the figure (measured from the sample normal  $\Gamma$ ) [99AJST]. The intense peak near  $\Gamma$  has a 5f character. Note that this feature diminishes rapidly in intensity as it disperses away from  $E_F$  (about 30 meV of dispersion are evident) in accord with predictions of the periodic Anderson model (for discussion see the original paper).



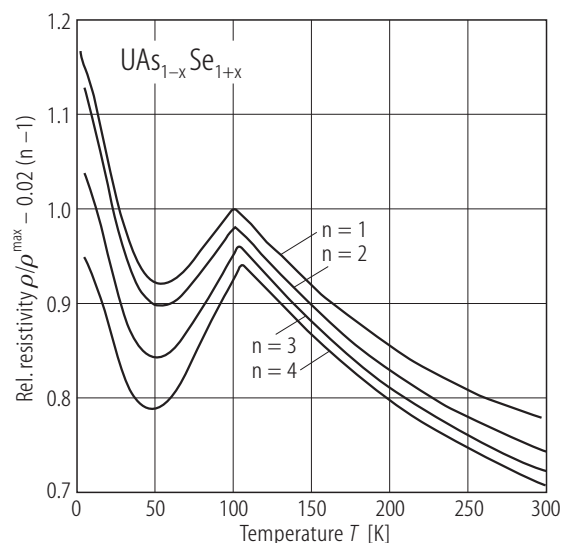


**Fig. 141.**  $\text{UAs}_{1-x}\text{Se}_{1+x}$ . Electrical resistivity normalised to its peak value,  $\rho/\rho^{\max}$ , vs. temperature,  $T$ , measured with  $i \perp c$ -axis on four selected single crystals with different  $x$  [95HFWZ]. For clarity the curves were shifted downwards by  $0.02(n-1)$ , where  $n$  is a sample-label. The low temperature upturn in the resistivity the authors attributed to incoherent Kondo effect (in the presence of ferromagnetic order) and fitted by the Fermi liquid formula

$$\rho \propto \left(1 - \frac{T}{T_K}\right)^2.$$

It appeared that the temperature range where this relation holds is more extended for samples having lower absolute resistivity.

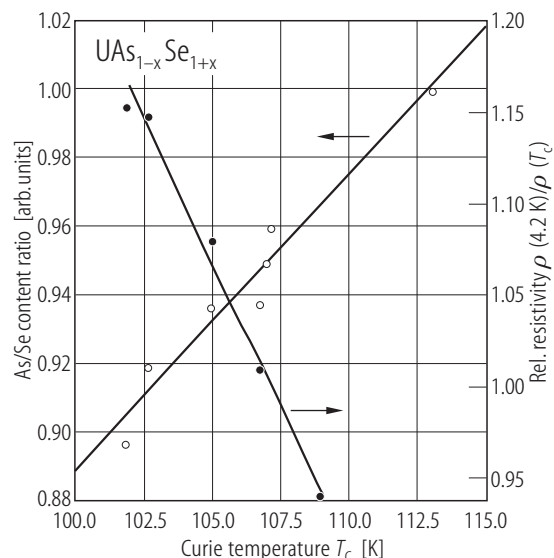


**Fig. 142.**  $\text{UAs}_{1-x}\text{Se}_{1+x}$ . Correlation of the As/Se content ratio, as determined by EDAX measurement (open circles) and the normalised residual resistivity,  $\rho(4.2 \text{ K})/\rho(T_C)$ , (filled circles) with the Curie temperature,  $T_C$  [95HFWZ]. The solid lines are guides to the eye. The authors concluded that the decrease in the As/Se content ratio implicates lowering of  $T_C$  and leads to considerable enhancement in incoherent Kondo scattering at the lowest temperatures (see also Fig. 119).

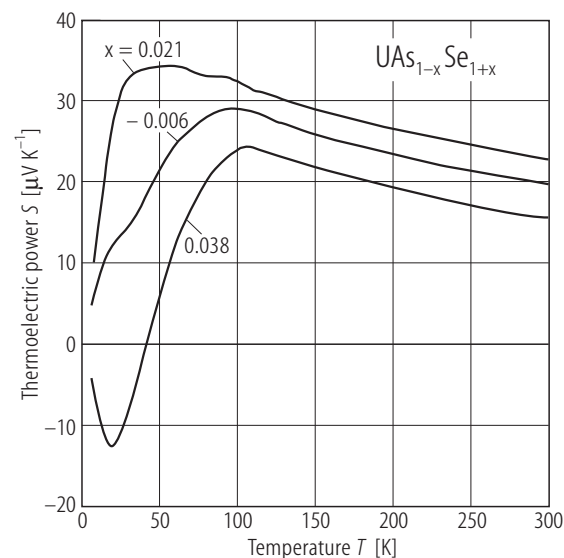


**Fig. 143.**  $\text{UAs}_{1-x}\text{Se}_{1+x}$ . Thermoelectric power,  $S$ , vs. temperature,  $T$ , measured along the  $a$ -axis on three single crystals with different stoichiometry [01HWWK]. The crystals studied had distinctly different Curie temperatures:  $T_C = 104 \text{ K}$  for  $x = 0.038$ ,  $T_C = 108 \text{ K}$  for  $x = 0.021$  and  $T_C = 114 \text{ K}$  for  $x = -0.006$ . Note that the peak in  $S(T)$  observed for  $x = 0.021$ , which is considered as a manifestation of the Kondo effect (see Fig. 128) disappears when  $x$  either decreases or increases. This finding seems incompatible with a gradual decrease of the Kondo effect with decreasing  $x$  derived from the resistivity data (compare Figs. 119 and 142).

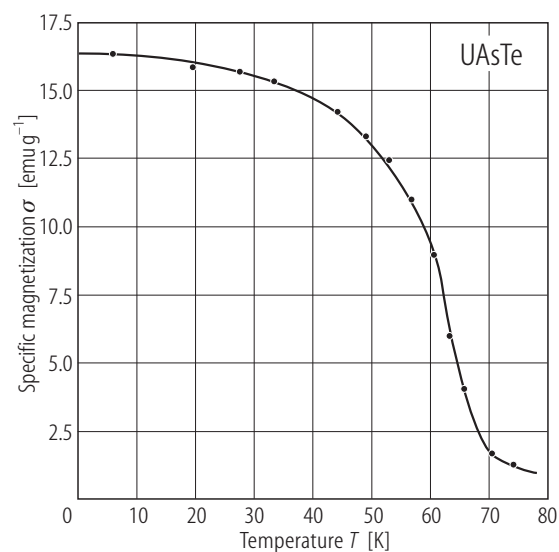


**Fig. 144.** UAsTe. Specific magnetization,  $\sigma$ , vs. temperature,  $T$ , taken in a field of 0.3 T [72BZ]. The compound orders ferromagnetically at  $T_C = 66$  K.

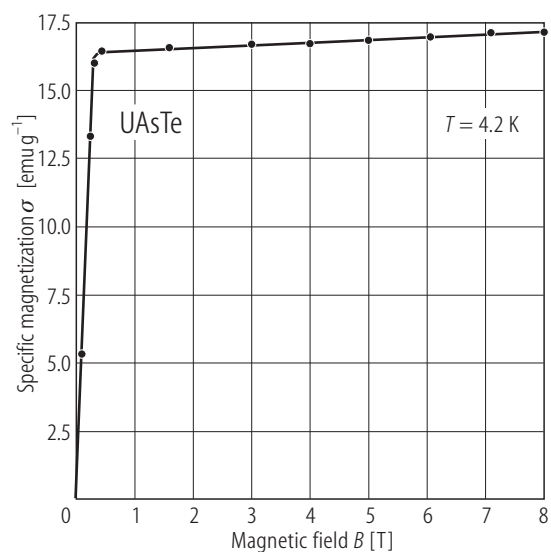


**Fig. 145.** UAsTe. Specific magnetization,  $\sigma$ , vs. magnetic field,  $B$ , measured at 4.2 K [72BZ]. The compound is ferromagnetic at low temperatures (see Fig. 144). The magnetic moment in a field of 8 T is  $1.29 \mu_B$ .

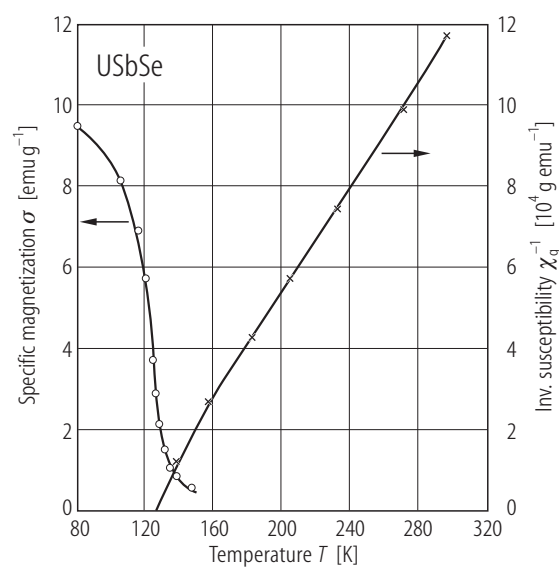


**Fig. 146.** USbSe. Specific magnetization,  $\sigma$ , (left-hand scale) and reciprocal mass magnetic susceptibility,  $\chi_g^{-1}$ , (right-hand scale) vs. temperature,  $T$ , measured in a field of 0.78 T [72LZ]. The compound orders ferromagnetically at  $T_C = 127$  K. See the Curie-Weiss fit parameters given in Table B.

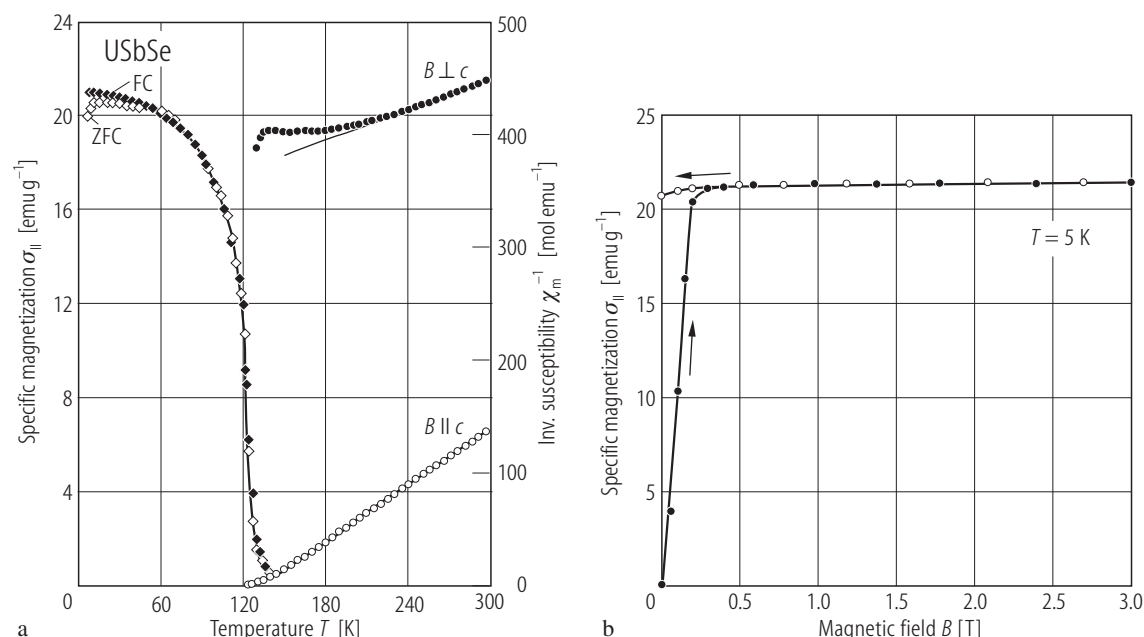


**Fig. 147.** USbSe. **(a)** Specific magnetization,  $\sigma_{||}$ , measured along the  $c$ -axis in a field of 0.2 T with cooling the sample with (FC, full diamonds) and without (ZFC, open diamonds) an applied magnetic field (left-hand scale) and reciprocal longitudinal,  $\chi_{||}^{-1}$ , (open circles), and transversal,  $\chi_{\perp}^{-1}$ , (full circles) molar magnetic susceptibility, measured along and perpendicular to the  $c$ -axis, respectively (right-hand scale) vs. temperature,  $T$  [95KNZ]. The compound

orders ferromagnetically at  $T_C = 128$  K. The solid lines are Curie-Weiss fits with the parameters given in Table B. Note a strongly anisotropic behaviour of the susceptibility caused mainly by crystal field interactions. **(b)** Specific magnetization,  $\sigma_{||}$ , vs. magnetic field,  $B$ , taken at 5 K with increasing (full circles) and decreasing (open circles) magnetic field. The saturation uranium magnetic moment is  $1.68(2) \mu_B$ .

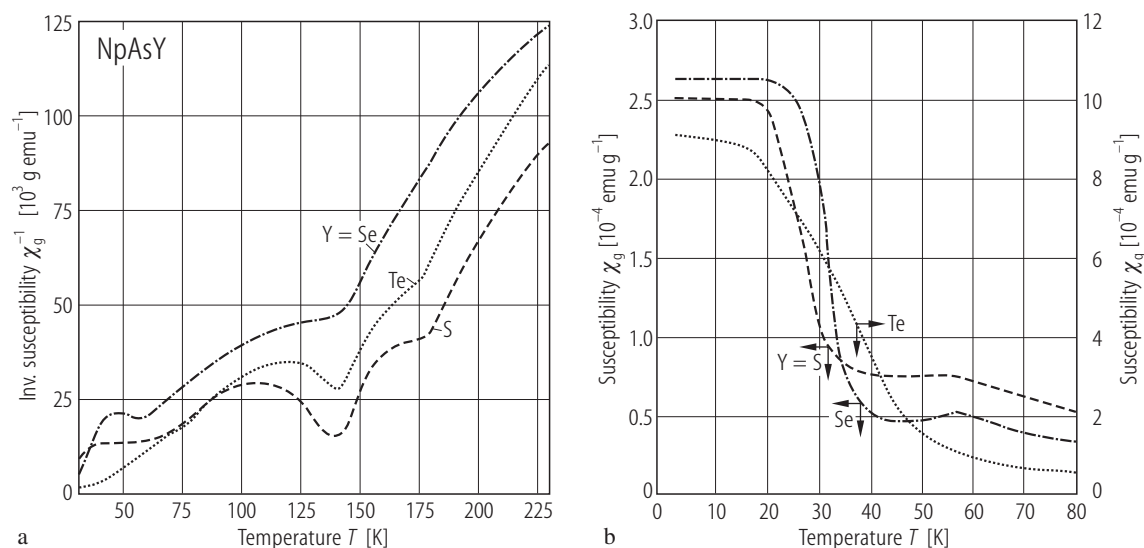


**Fig. 149.** NpAsY, Y = S, Se, Te. **(a)** Reciprocal mass magnetic susceptibility,  $\chi_g^{-1}$ , vs. temperature,  $T$ , measured in a field of 1 T [77BCSW]. Note unusual behaviour of the susceptibility with notable anomalies around 60, 140 and 180 K. **(b)** Mass magnetic susceptibility,  $\chi_g$ , vs.  $T$  below 80

K, taken in a field of 1 T [77BCSW]. Note a different (right-hand side) vertical scale for NpAsTe. At low temperatures all three compounds show ferromagnetic-like properties with  $T_C = 30, 35$  and  $40$  K for NpAsS, NpAsSe and NpAsTe, respectively.

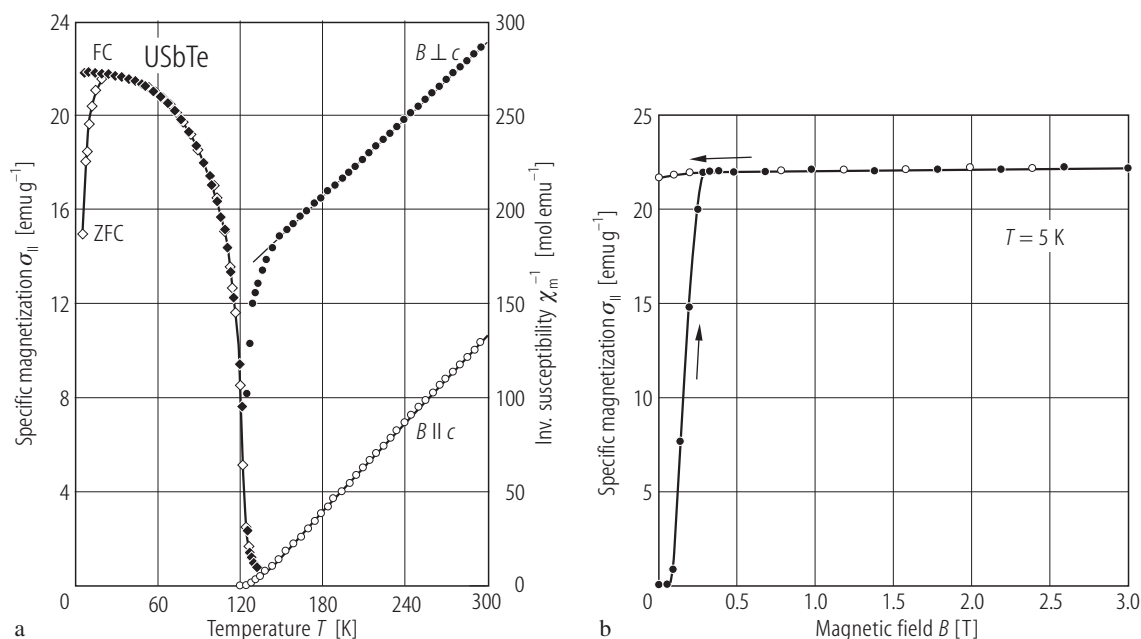


**Fig. 148.** USbTe. (a) Specific magnetization,  $\sigma_{||}$ , measured along the  $c$ -axis in a field of 0.2 T with cooling the sample with (FC, full diamonds) and without (ZFC, open diamonds) an applied magnetic field (left-hand scale) and reciprocal longitudinal,  $\chi_{||}^{-1}$ , (open circles), and transversal,  $\chi_{\perp}^{-1}$ , (full circles) molar magnetic susceptibility, measured along and perpendicular to the  $c$ -axis, respectively (right-hand scale) vs. temperature,  $T$  [95KNZ]. The compound

orders ferromagnetically at  $T_C = 127$  K. The solid lines are Curie-Weiss fits with the parameters given in Table B. Note a strongly anisotropic behaviour of the susceptibility caused mainly by crystal field interactions. (b) Specific magnetization,  $\sigma_{||}$ , vs. magnetic field,  $B$ , taken at 5 K with increasing (full circles) and decreasing (open circles) magnetic field. The saturation uranium magnetic moment is  $1.93(2) \mu_B$ .

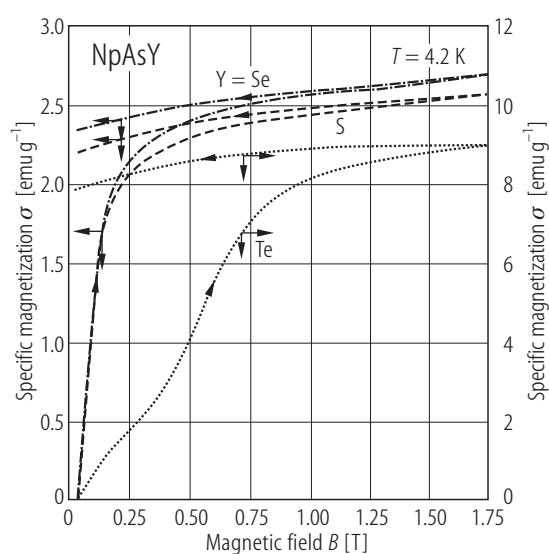


**Fig. 150.** NpAsY, Y = S, Se, Te. Specific magnetization,  $\sigma$ , vs. magnetic field,  $B$ , measured at 4.2 K with increasing and decreasing (marked by the arrows) magnetic field [77BCSW]. Note a different (right-hand side) vertical scale for NpAsTe. The neptunium ordered magnetic moment, obtained by extrapolation to zero field, amounts to 0.15, 0.17 and  $0.65 \mu_B$  for NpAsS, NpAsSe and NpAsTe, respectively. Note that the  $\sigma(B)$  curves do not saturate even in the highest fields applied.

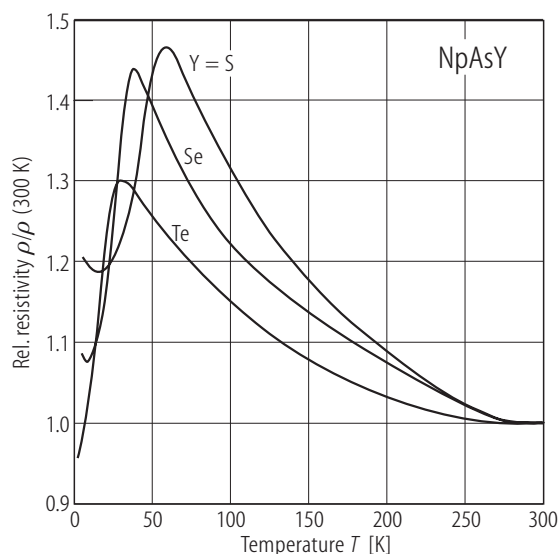


**Fig. 151.** NpAsY, Y = S, Se, Te. Normalised electrical resistivity,  $\rho/\rho(300\text{ K})$ , vs. temperature,  $T$ , [85W]. The maxima at 63, 40 and 32 K for NpAsS, NpAsSe and NpAsTe, respectively, manifest the ferromagnetic transitions reported in [77BCSW] and [84BCFC]. Note a semimetallic behaviour and a negative temperature coefficient in the paramagnetic regions. See also Fig. 154.

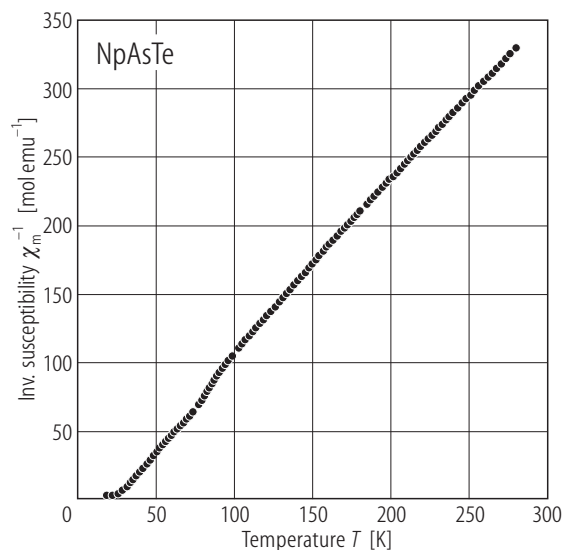


**Fig. 152.** NpAsTe. Reciprocal molar magnetic susceptibility,  $\chi_m^{-1}$ , vs. temperature,  $T$  [84BCFC]. The compound orders ferromagnetically at  $T_C = 25\text{ K}$  (see Fig. 153). A small anomaly at about 80 K is due to 0.25% mass. of  $\text{Np}_3\text{As}_4$  present in the sample. The effective magnetic moment above 250 K is close to that expected for a free  $\text{Np}^{3+}$  ion ( $2.68\ \mu_B$ ). The effective moment below 50 K is  $2.35\ \mu_B$  being in good agreement with the value calculated in [83ABF]. See the Curie-Weiss fit parameters given in Table B.

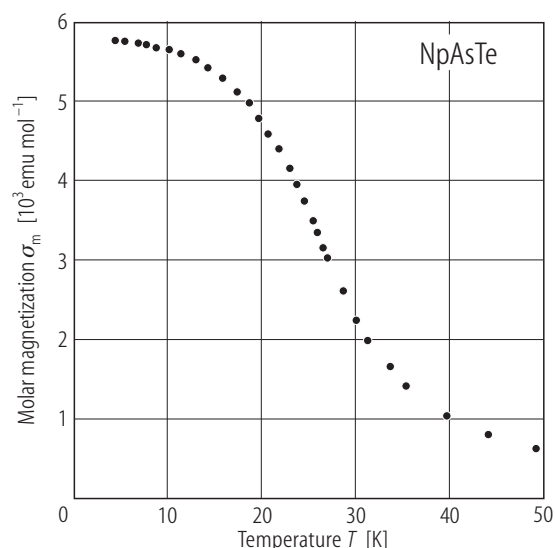


**Fig. 153.** NpAsTe. Molar magnetization,  $\sigma_m$ , vs. temperature,  $T$ , measured in a field of 2 T [84BCFC]. The compound orders ferromagnetically at  $T_C = 25\text{ K}$ . The magnetization measured at 4 K does not saturate in fields up to 4 T reaching  $1.07\ \mu_B$  (not shown).

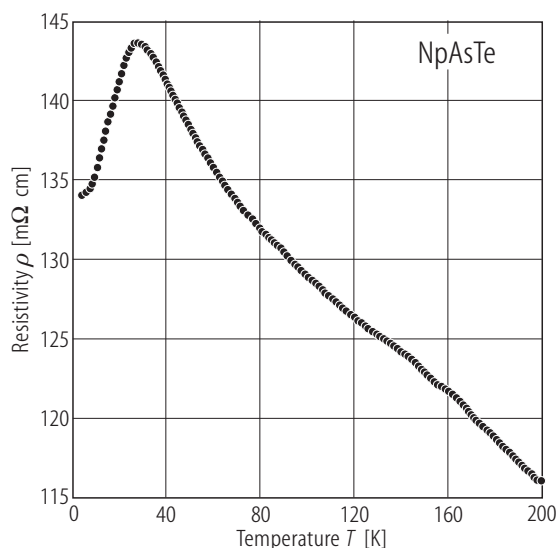


**Fig. 154.** NpAsTe. Electrical resistivity,  $\rho$ , vs. temperature,  $T$ , [84BCFC]. The maximum at 29 K corresponds to the ferromagnetic transitions at  $T_C = 25\text{ K}$  (see Fig. 153). Compare also Fig. 151.

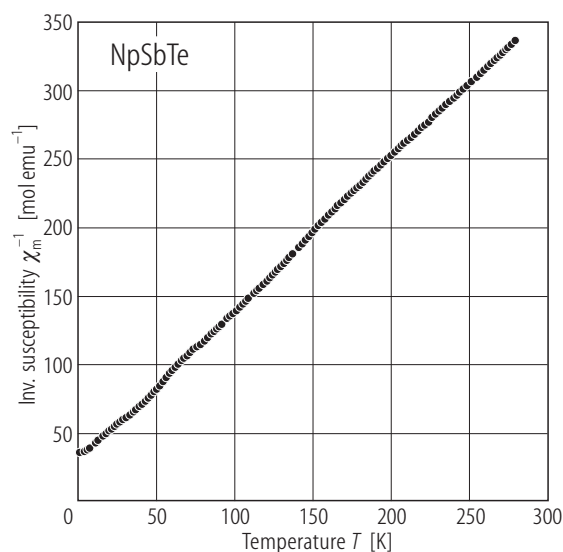


**Fig. 155.** NpSbTe. Reciprocal molar magnetic susceptibility,  $\chi_m^{-1}$ , vs. temperature,  $T$  [84BCFC]. The compound remains paramagnetic down to 1.8 K. The effective magnetic moment is equal to that expected for a free  $\text{Np}^{3+}$  ion ( $2.68 \mu_B$ ). See the Curie-Weiss fit parameters given in Table B.

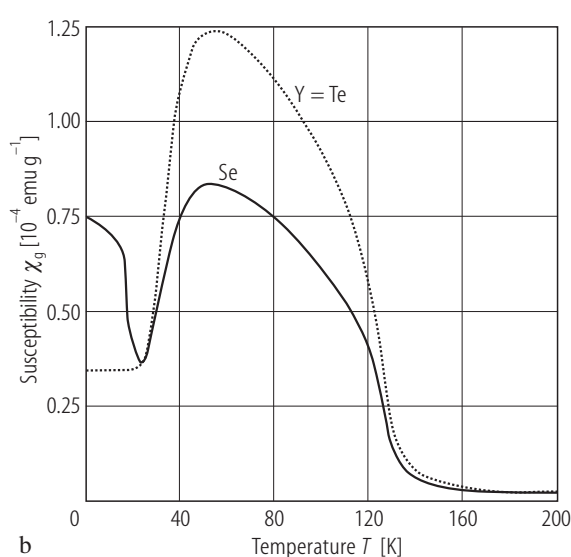
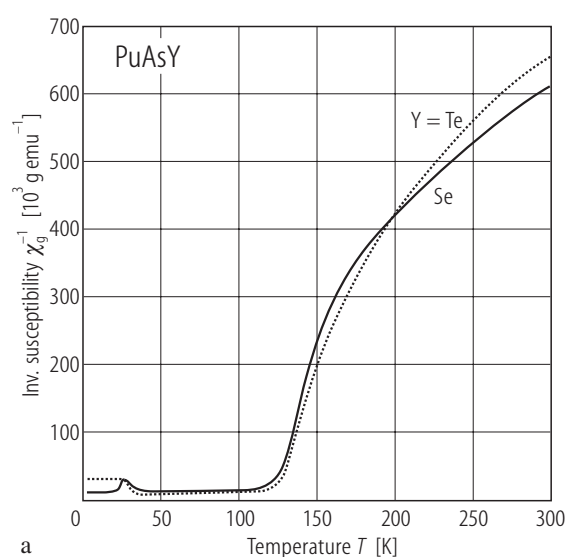


**Fig. 156.** PuAsY, Y = Se, Te. (a) Reciprocal mass magnetic susceptibility,  $\chi_g^{-1}$ , vs. temperature,  $T$ , measured in a field of 1 T [77BCSW]. The two compounds order ferromagnetically below  $T_C = 126$  and 125 K for PuAsSe and PuAsTe, respectively. In the paramagnetic region the

$\chi_g^{-1}(T)$  variations are strongly curved and follow a modified Curie-Weiss law with the parameters given in Table B. (b) Mass magnetic susceptibility,  $\chi_g$ , vs.  $T$  below 200 K, taken in a field of 1 T [77BCSW]. Note unusual features in the ferromagnetic state.

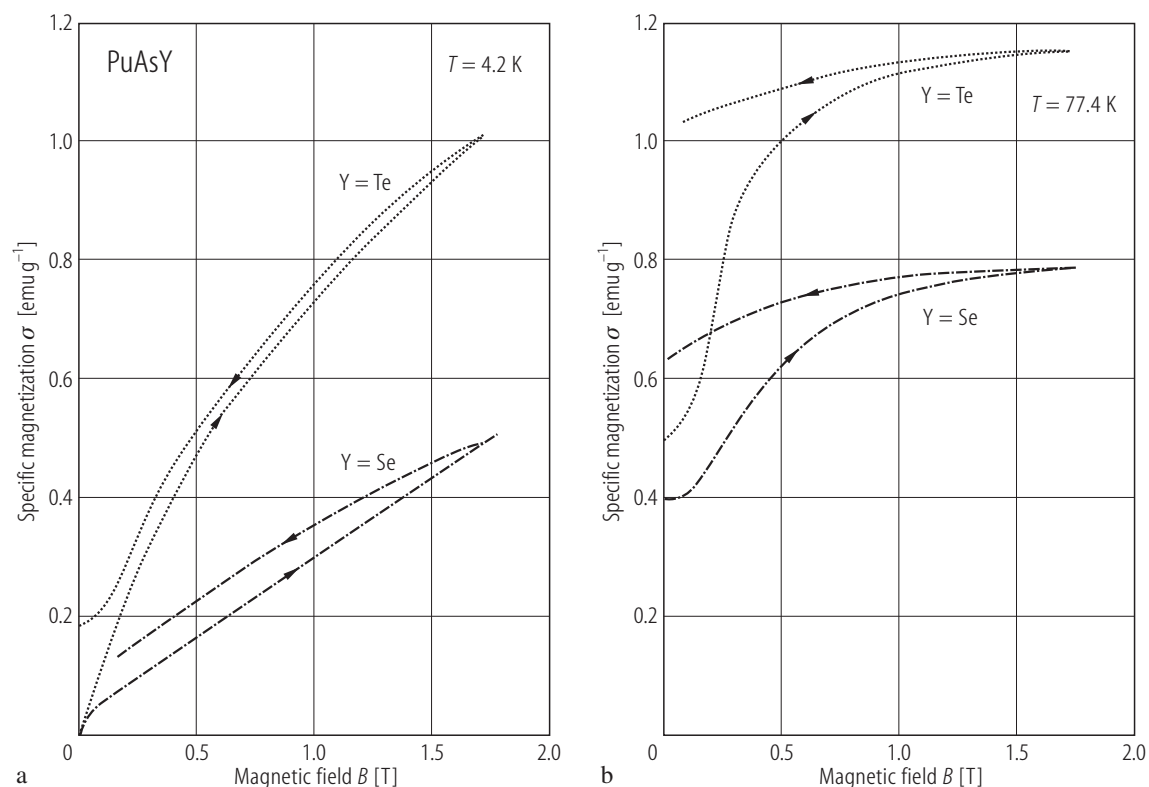


**Fig. 157.**  $\text{PuAsY}$ ,  $Y = \text{Se, Te}$ . Specific magnetization,  $\sigma$ , vs. magnetic field,  $B$ , measured at  $T = 4.2 \text{ K}$  (a) and  $T = 77.4 \text{ K}$  (b) with increasing and decreasing (marked by the arrows) magnetic field [77BCSW]. At  $77.4 \text{ K}$ , the  $\sigma(B)$  curves are

nearly saturated, with very small values of the ordered moment ( $0.05$  and  $0.09 \mu_{\text{B}}$  for  $\text{PuAsSe}$  and  $\text{PuAsTe}$ , respectively), while at  $4.2 \text{ K}$  they do not show any tendency to saturation, even in the highest fields applied.

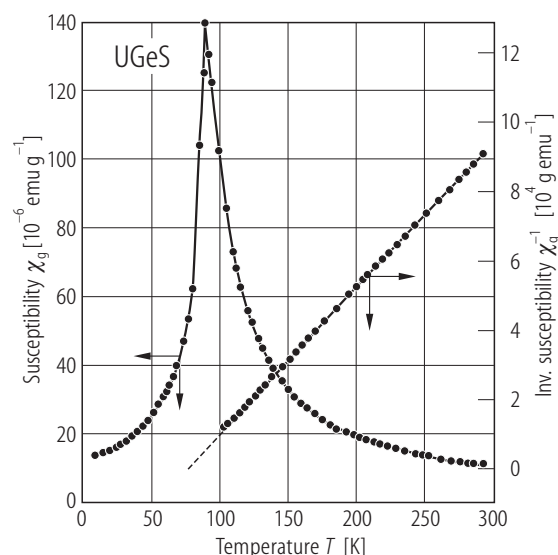


**Fig. 158.**  $\text{UGeS}$ . Mass magnetic susceptibility,  $\chi_{\text{g}}$ , (left-hand scale) and reciprocal mass magnetic susceptibility,  $\chi_{\text{g}}^{-1}$ , vs. temperature,  $T$ , measured in a field of  $0.4 \text{ T}$  [77Z]. The compound orders antiferromagnetically at  $T_{\text{N}} = 88 \text{ K}$ . See the neutron powder diffraction results in Fig. 160. The Curie-Weiss fit parameters are given in Table B. The author presents in the original paper a crystal field levels scheme obtained within the point charge model of splitting the ground  $^3\text{H}_4$  term of  $\text{U}^{4+}$  ion placed in a tetragonal potential of the  $\text{C}_{4v}$  symmetry, which however does not reproduce the experimental  $\chi_{\text{g}}(T)$ .

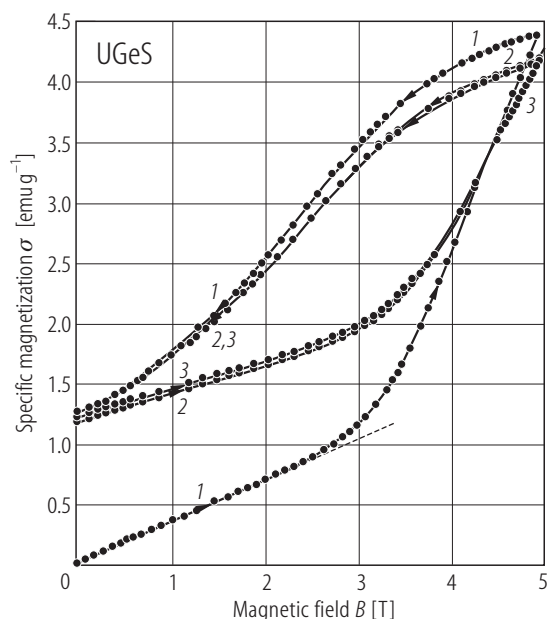


**Fig. 159.** UGeS. Specific magnetization,  $\sigma$ , vs. magnetic field,  $B$ , taken at 4.2 K [77Z]. The arrows indicate measurements taken with increasing and decreasing field. The numbers correspond to subsequent field cycles. The compound is antiferromagnetic at low temperatures (see Fig. 158). Note a pronounced metamagnetic transition at 2.5 T.

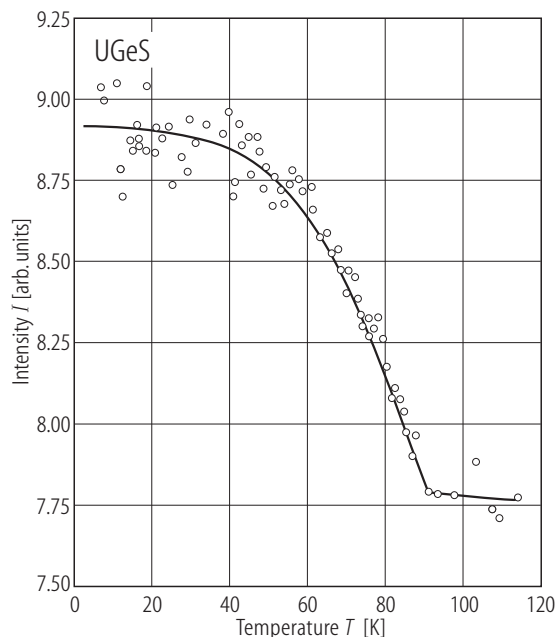


**Fig. 160.** UGeS. Neutron diffraction intensity of the magnetic reflection ( $10\frac{1}{2}$ ),  $I$ , vs. temperature,  $T$  [78PLZ]. The compound orders antiferromagnetically at  $T_N = 88$  K with the AF-II - type magnetic structure (see Fig. 161). The ordered moment  $p_o$  at 4 K amounts to  $1.28(9) \mu_B$ .

For Fig. 161 see next page

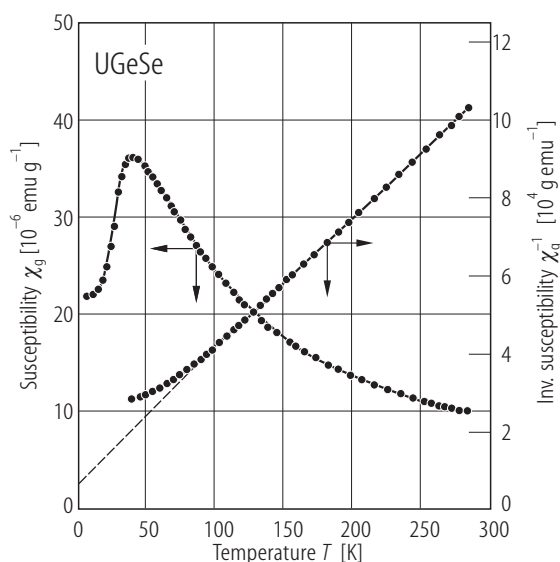


**Fig. 162.** UGeSe. Mass magnetic susceptibility,  $\chi_g$ , (left-hand scale) and reciprocal mass magnetic susceptibility,  $\chi_g^{-1}$ , vs. temperature,  $T$ , measured in a field of 0.4 T [77Z]. The compound orders antiferromagnetically at  $T_N = 40$  K. The Curie-Weiss fit parameters are given in Table B.

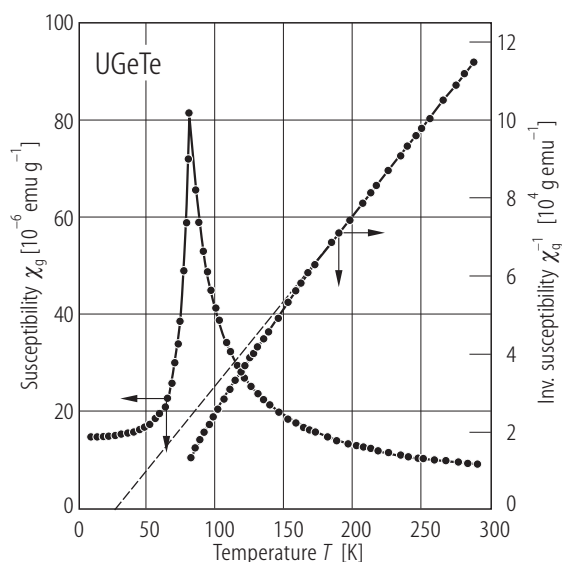


**Fig. 163.** UGeTe. Mass magnetic susceptibility,  $\chi_g$ , (left-hand scale) and reciprocal mass magnetic susceptibility,  $\chi_g^{-1}$ , vs. temperature,  $T$ , measured in a field of 0.4 T [77Z]. The compound orders antiferromagnetically at  $T_N = 73$  K. See the neutron powder diffraction results in Fig. 165. The Curie-Weiss fit parameters are given in Table B.



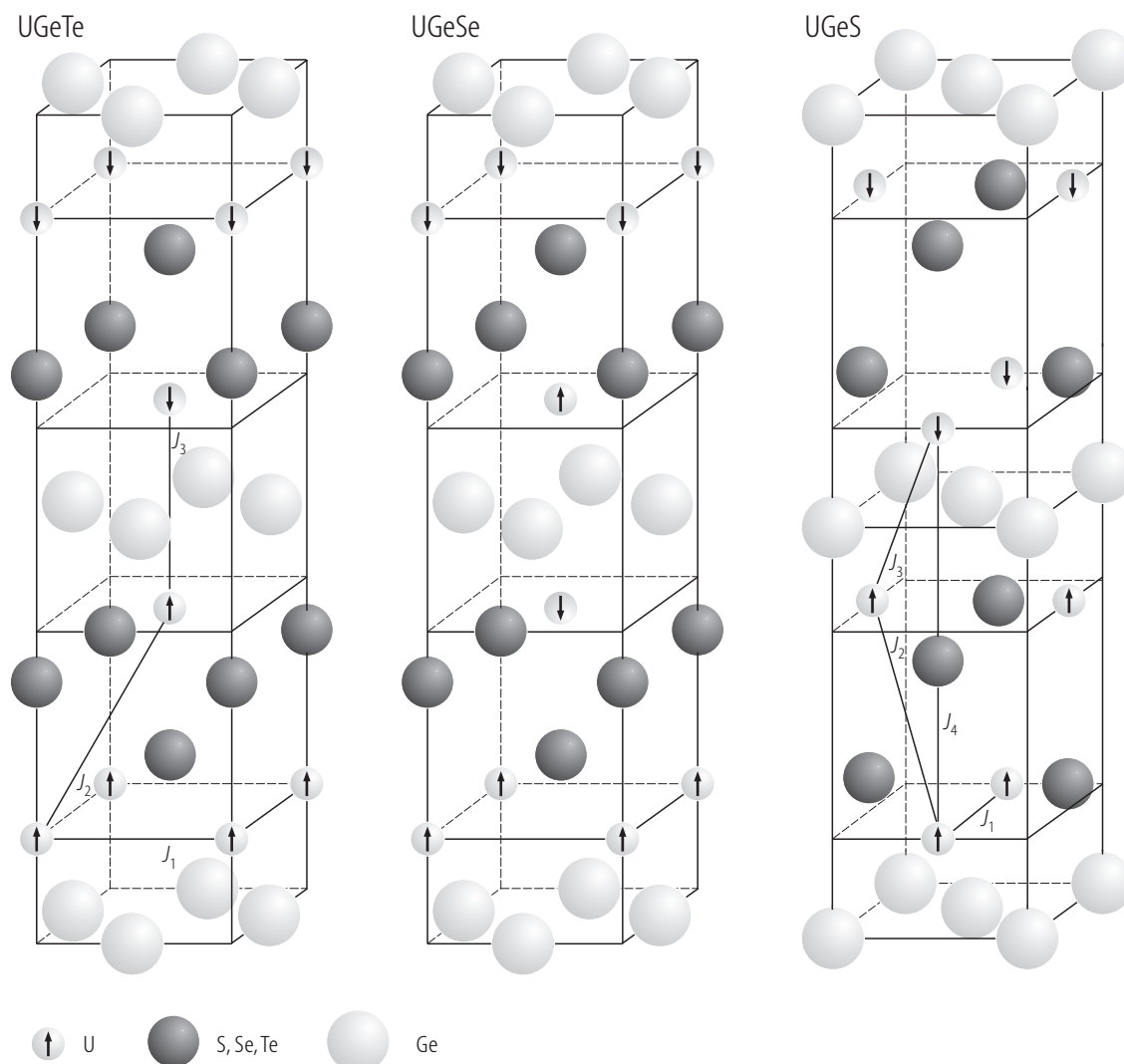


**Fig. 161.** UGeY, Y = S, Se, Te. Magnetic structures [78PLZ]. The principal exchange interactions between uranium atoms are marked. See the original paper for the analysis of the exchange integrals within the molecular field approximation.

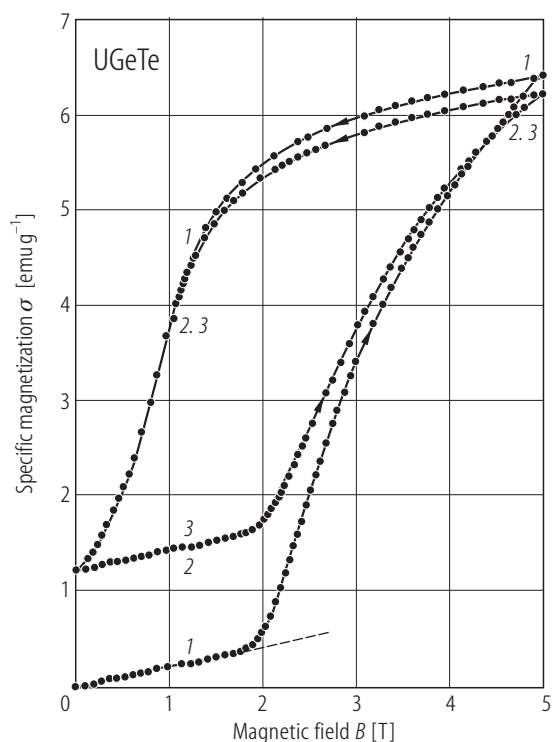


**Fig. 164.** UGeTe. Specific magnetization,  $\sigma$ , vs. magnetic field,  $B$ , taken at 4.2 K [77Z]. The arrows indicate measurements taken with increasing and decreasing field. The numbers correspond to subsequent field cycles. The compound is antiferromagnetic at low temperatures (see Fig. 163). Note a pronounced metamagnetic transition at 1.7 T.

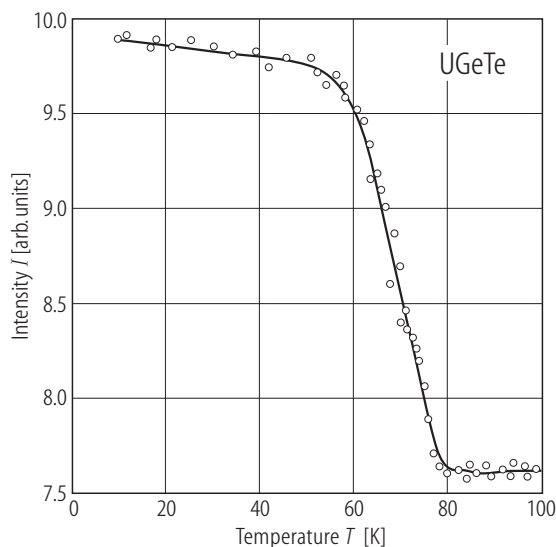


**Fig. 165.** UGeTe. Neutron diffraction intensity of the magnetic reflection (102),  $I$ , vs. temperature,  $T$  [78PLZ]. The compound orders antiferromagnetically at  $T_N = 73$  K with the AF-II - type magnetic structure (see Fig. 161). The ordered moment  $p_o$  at 4 K amounts to  $1.50(5) \mu_B$ .

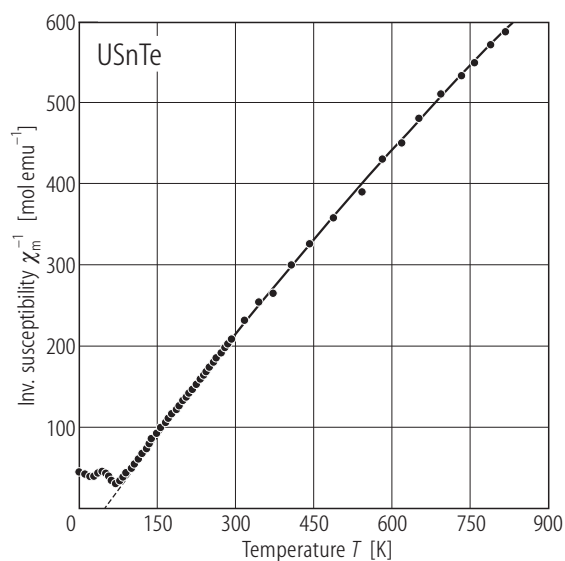


**Fig. 166.** USnTe. Reciprocal molar magnetic susceptibility,  $\chi_m^{-1}$ , vs. temperature,  $T$ , up to 800 K [87T]. The compound orders antiferromagnetically below ca. 80 K (see Fig. 167).

The solid line is a fit to the formula  $\chi_m^{-1} = \left( \frac{A}{T} + B \right)^{-1} + \lambda$  with the parameters given in Table E.

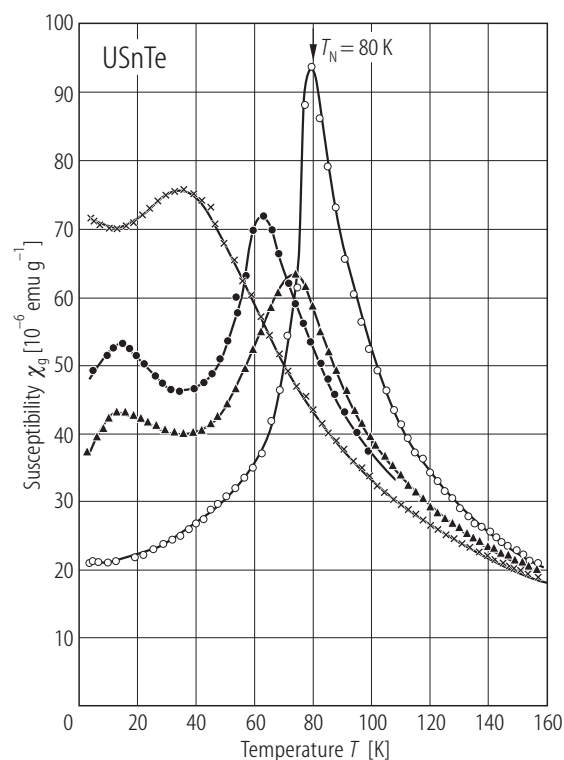


**Fig. 167.** USnTe. Mass magnetic susceptibility,  $\chi_g$ , vs. temperature,  $T$ , up to 150 K, measured on four different samples showing some variation in the lattice parameters [87T]. Note the occurrence of two maxima in  $\chi_g(T)$ , which shift towards lower temperatures with an increase in the  $c/a$  ratio. The observed behaviour the author attributed to slight differences in the stoichiometry of the samples measured.

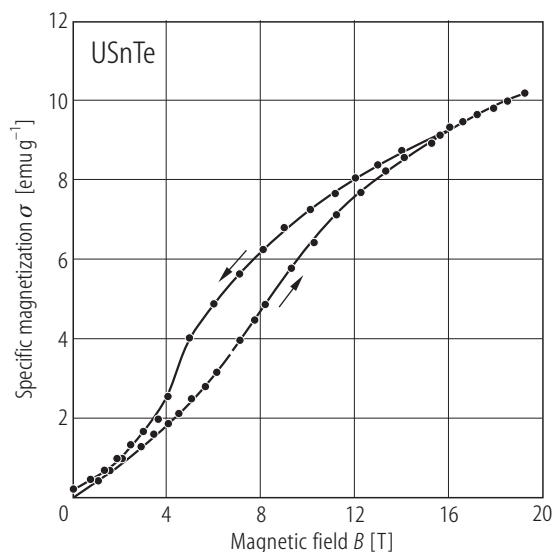
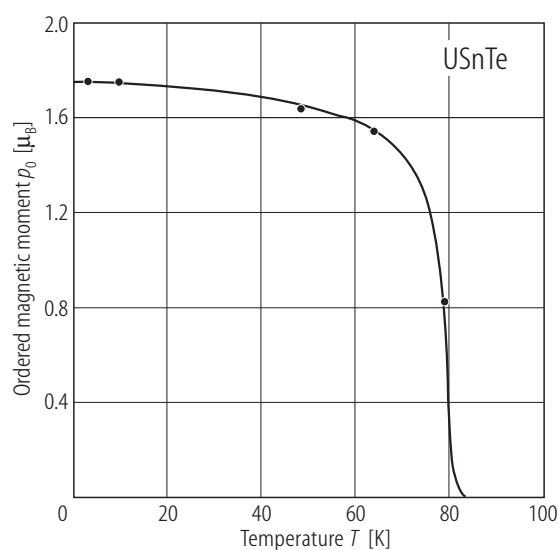


**Fig. 168.** USnTe. Specific magnetization,  $\sigma$ , vs. magnetic field,  $B$ , up to 20 T, measured at  $T = 4.2$  K [87T]. The arrows indicate measurements taken with increasing and decreasing field. Note a pronounced metamagnetic transition, which corroborates an antiferromagnetic ground state (see Fig. 167). However, no saturation was reached up to the highest fields applied.

**Fig. 169.** USnTe. Ordered magnetic moment,  $p_0$ , vs. temperature,  $T$ , as determined by neutron diffraction [87T]. The compound orders antiferromagnetically below  $T_N = 80$  K.

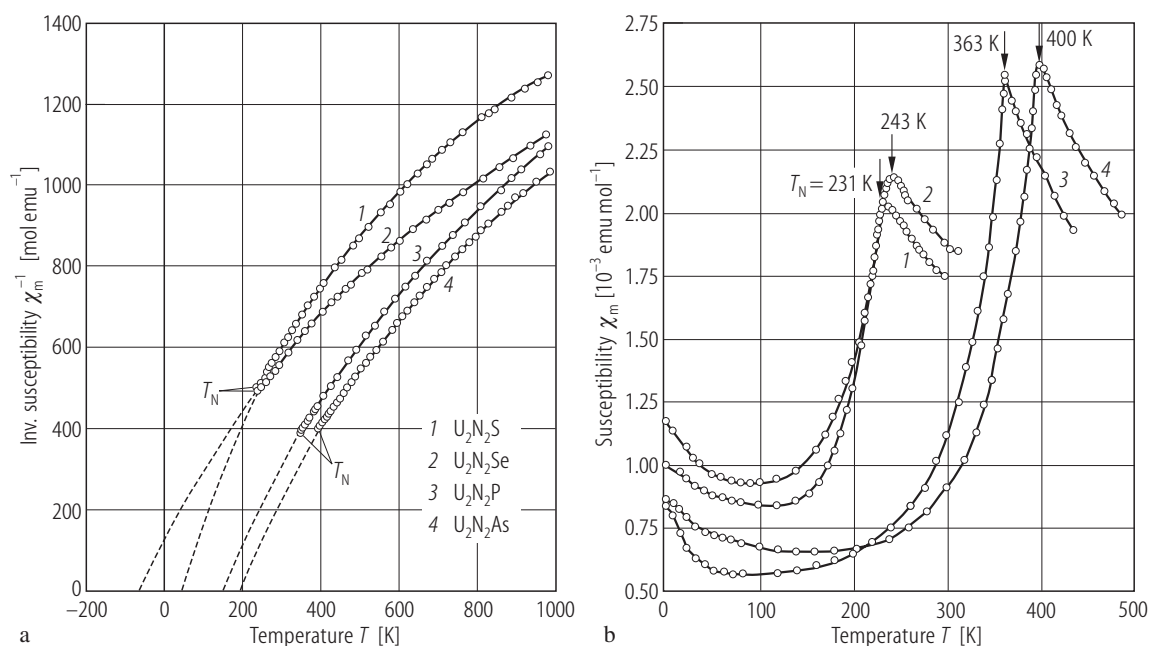


**Fig. 170.**  $U_2N_2X$ ,  $U_2N_2Y$ ,  $X = P, As$ ,  $Y = S, Se$ . **(a)** Reciprocal molar magnetic susceptibility,  $\chi_m^{-1}$ , vs. temperature,  $T$ , up to 1000 K [76ZT]. The solid lines are fits of the susceptibility to the formula

$$\chi_m^{-1} = \left( \frac{A}{T} + B \right)^{-1} + \lambda \quad \text{with the parameters given in Table$$

**Y.** Note a strongly curvilinear character of  $\chi_m^{-1}(T)$  up to the highest temperatures studied, interpreted by the authors as a signature of strong crystal field interactions. It is suggested that the ground state is a strongly anisotropic  $\Gamma_{3T}$  doublet

consisting of either  $(|\pm 4\rangle, |\mp 2\rangle)$  or  $(|\pm 4\rangle, |\pm 1\rangle)$  components and being well separated from the excited crystal field levels. For the crystal field calculations in the framework of perturbative and non-perturbative point charge model refer to the original paper. **(b)** Molar magnetic susceptibility,  $\chi_m$ , vs.  $T$  [76ZT]. The compounds order antiferromagnetically below  $T_N = 363, 400, 231$  and  $243$  K for  $X = P, As$  and  $Y = S, Se$ , respectively, with the magnetic structures presented in Fig. 172. Note exceptionally high values of the Néel temperature. The tails in  $\chi_m(T)$  observed at the lowest temperatures have unclear origin.

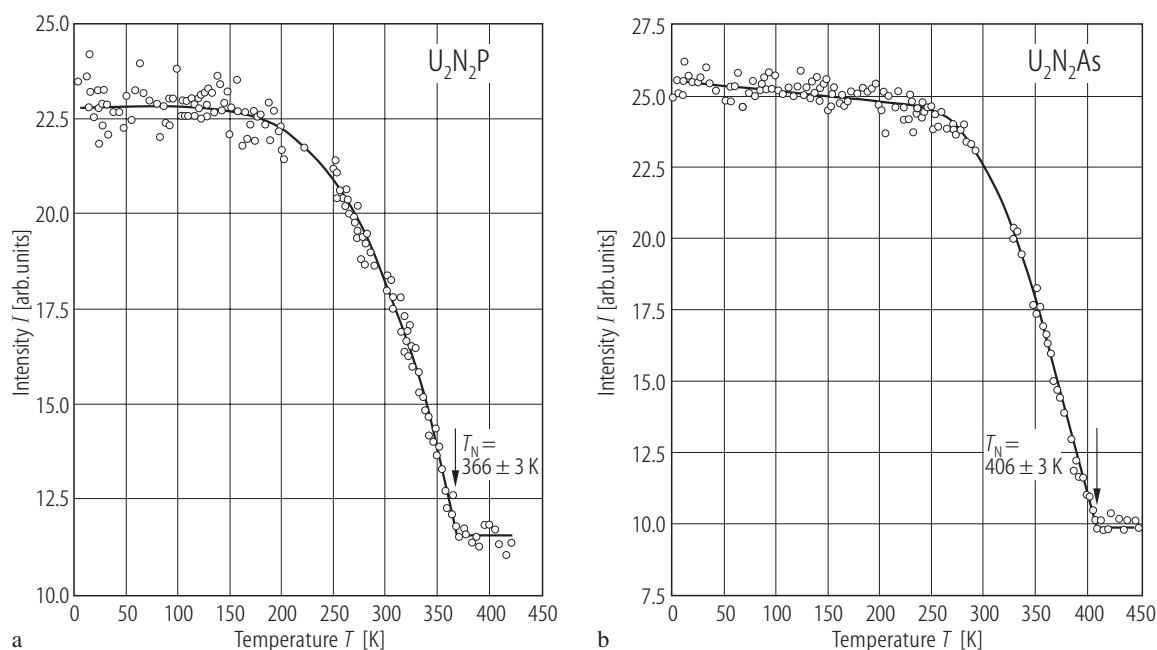


**Fig. 171.**  $\text{U}_2\text{N}_2\text{X}$ ,  $\text{X} = \text{P}, \text{As}$ . Neutron diffraction intensity of the magnetic reflection ( $10\frac{1}{2}$ ),  $I$ , vs. temperature,  $T$ , for (a)  $\text{U}_2\text{N}_2\text{P}$  and (b)  $\text{U}_2\text{N}_2\text{As}$  [75LZLT]. The compounds order antiferromagnetically at  $T_N = 366(3) \text{ K}$  and  $406(3) \text{ K}$ ,

respectively, with the magnetic structure shown in Fig. 172b. At 4 K the ordered magnetic moments  $p_0$  amount to 1.7 and 1.6  $\mu_B$  for the phosphide and the arsenide, respectively.

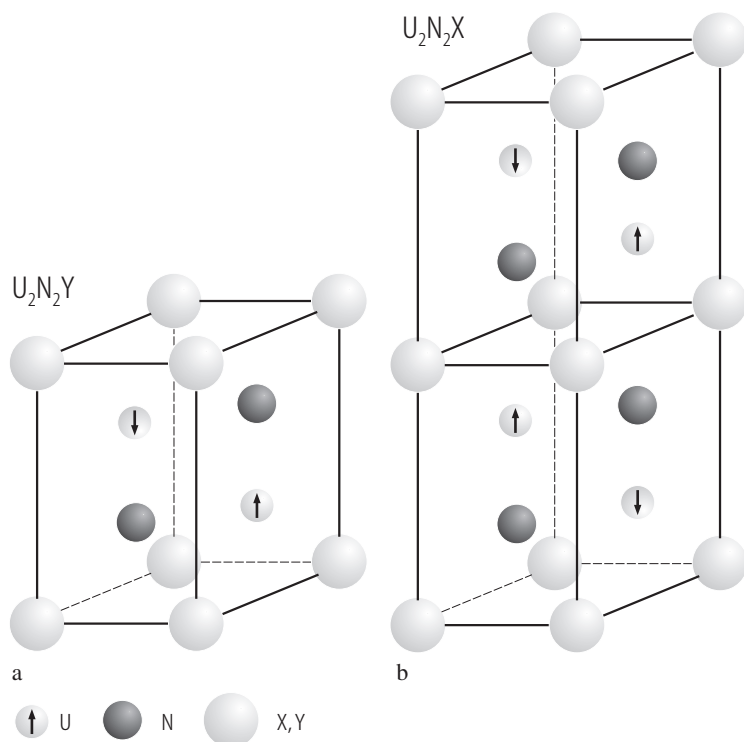


**Fig. 172.**  $\text{U}_2\text{N}_2\text{X}$ ,  $\text{U}_2\text{N}_2\text{Y}$ ,  $\text{X} = \text{P}, \text{As}$ ,  $\text{Y} = \text{S}, \text{Se}$ . Magnetic structures of (a)  $\text{U}_2\text{N}_2\text{Y}$  and (b)  $\text{U}_2\text{N}_2\text{X}$  [75LZLT]. Note doubling of the chemical unit cell along the  $c$ -axis in the case of  $\text{U}_2\text{N}_2\text{X}$  compounds. The uranium magnetic moments point along the hexagonal axis and at 4 K they amount to 1.4, 1.7, 1.6 and 2.3  $\mu_B$  for  $\text{U}_2\text{N}_2\text{S}$ ,  $\text{U}_2\text{N}_2\text{P}$ ,  $\text{U}_2\text{N}_2\text{As}$  and  $\text{U}_2\text{N}_2\text{Se}$ , respectively.

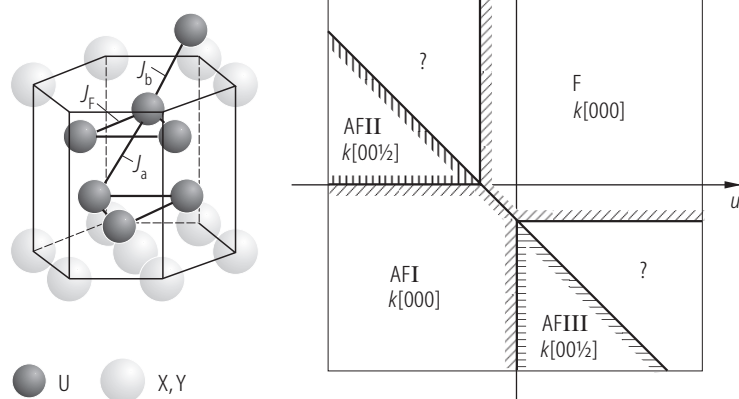
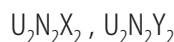


**Fig. 173.**  $\text{U}_2\text{N}_2\text{X}$ ,  $\text{U}_2\text{N}_2\text{Y}$ ,  $\text{X} = \text{P}, \text{As}$ ,  $\text{Y} = \text{S}, \text{Se}$ . Stability diagram of the magnetic phases [76ZT]. Possible magnetic moment configurations in a hexagonal structure of the  $\text{Ce}_2\text{O}_2\text{S}$ -type, characteristic of all the compounds considered, were analyzed in the framework of the Bertaut's matrix method. The three main exchange integrals,  $J_a$ ,  $J_b$  and  $J_F$ , which were used in the calculations ( $u = J_a/J_F$  and  $v = J_b/J_F$ ) are shown on a schematic view of the crystal

structure. There are four simple ordering schemes denoted by AFI, AFII, AFIII and F that are characterized by the propagation vectors given in the figure. The regions marked by the symbol ? correspond to some other magnetic structures, which show up by taking into account more than three exchange integrals. The experimentally observed magnetic structures (see Fig. 172):  $\text{U}_2\text{N}_2\text{S}$  and  $\text{U}_2\text{N}_2\text{Se}$  – AFI;  $\text{U}_2\text{N}_2\text{P}$  and  $\text{U}_2\text{N}_2\text{As}$  – AFII,  $\text{U}_2\text{N}_2\text{N}$  – F.

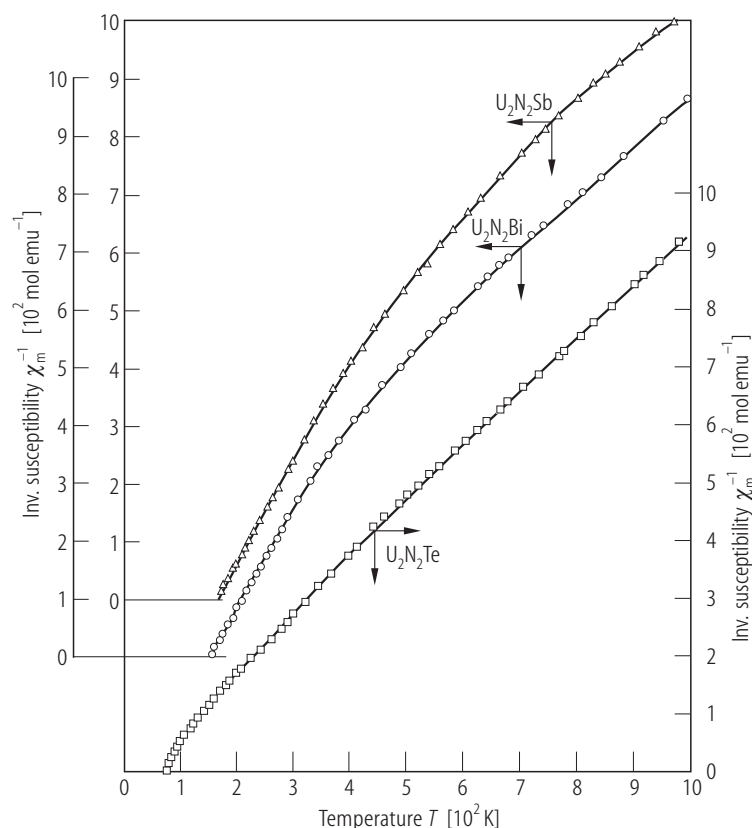


**Fig. 174.**  $\text{U}_2\text{N}_2\text{X}$ ,  $\text{U}_2\text{N}_2\text{Te}$ ,  $\text{X} = \text{Sb}, \text{Bi}$ . Reciprocal molar magnetic susceptibility,  $\chi_m^{-1}$ , vs. temperature,  $T$ , up to 1000 K, measured at 0.6 T for  $\text{U}_2\text{N}_2\text{Sb}$  (triangles),  $\text{U}_2\text{N}_2\text{Bi}$  (circles) and  $\text{U}_2\text{N}_2\text{Te}$  (squares) [78ZT]. Note shifts on the vertical left-hand scale constructed for the pnictides and the other right-hand scale constructed for  $\text{U}_2\text{N}_2\text{Te}$ . The compounds are ferromagnets with  $T_C = 166, 154$  and  $71$  K for  $\text{X} = \text{Sb}, \text{Bi}$  and  $\text{U}_2\text{N}_2\text{Te}$ , respectively. The solid lines are fits of the susceptibility

to the formula  $\chi_m^{-1} = \left( \frac{A}{T} + B \right)^{-1} + \lambda$

with the parameters given in Table Y. Note a strongly curvilinear character of  $\chi_m^{-1}(T)$  of  $\text{U}_2\text{N}_2\text{Sb}$  and  $\text{U}_2\text{N}_2\text{Bi}$  up to the highest temperatures studied and an almost linear behaviour of  $\chi_m^{-1}(T)$  of  $\text{U}_2\text{N}_2\text{Te}$  above 400 K, which indicate quite different crystal field levels schemes in the pnictides and the telluride. For the crystal field models see Fig. 178.

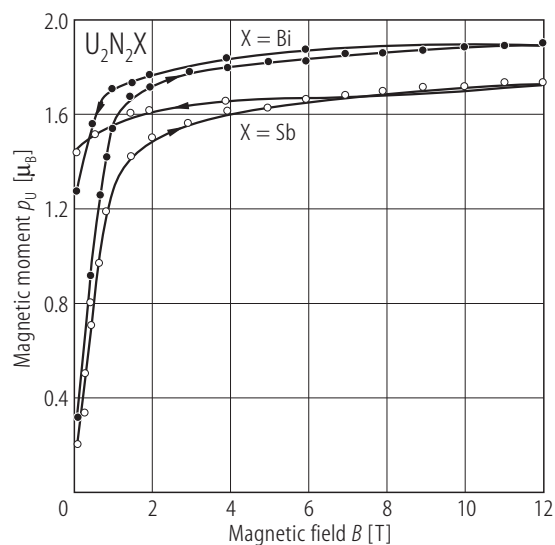


**Fig. 175.**  $\text{U}_2\text{N}_2\text{X}$ ,  $\text{X} = \text{Sb, Bi}$ . Magnetic moment per U atom,  $p_{\text{U}}$ , vs. field,  $B$ , measured at 4.2 K with increasing and decreasing magnetic field as indicated by the arrows [78ZT]. Open circles:  $\text{U}_2\text{N}_2\text{Sb}$ ; filled circles:  $\text{U}_2\text{N}_2\text{Bi}$ . Note that at low fields the magnetization increases rapidly and then saturates, which indicates rather weak magnetocrystalline anisotropy. The remanent magnetization is quite large being about 84 % and 67 % of the magnetization at 12 T for  $\text{U}_2\text{N}_2\text{Sb}$  ( $1.72 \mu_{\text{B}}$ ) and  $\text{U}_2\text{N}_2\text{Bi}$  ( $1.88 \mu_{\text{B}}$ ), respectively.

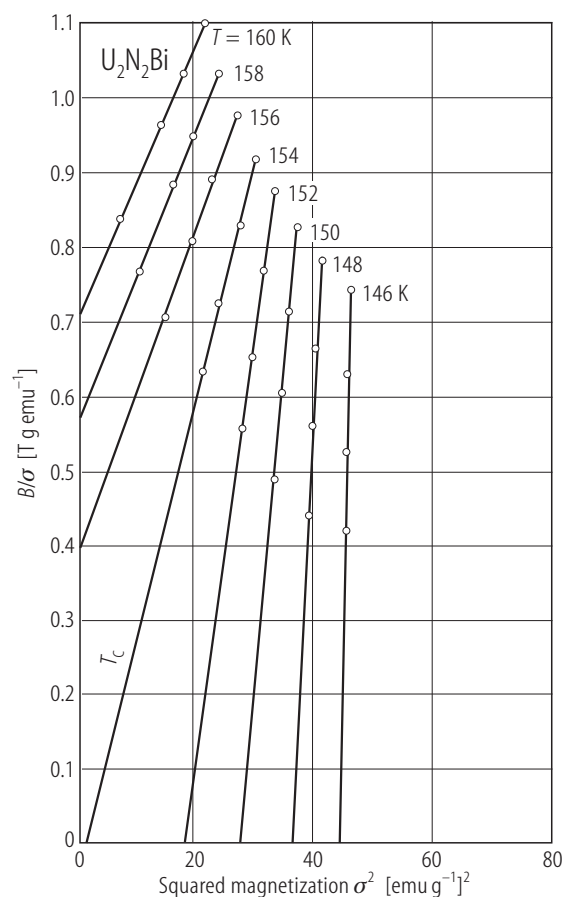
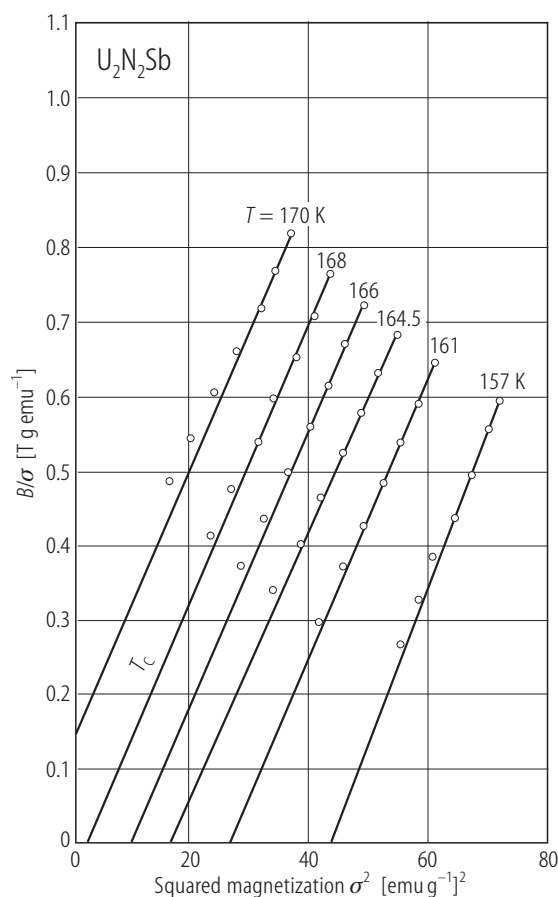


**Fig. 176.**  $\text{U}_2\text{N}_2\text{X}$ ,  $\text{X} = \text{Sb, Bi}$ . Arrott's plots,  $B/\sigma$  vs.  $\sigma^2$ , for several temperatures near the Curie temperature [78ZT]. Left-hand panel:  $\text{U}_2\text{N}_2\text{Sb}$ ; right-hand panel:  $\text{U}_2\text{N}_2\text{Bi}$ . The saturation uranium magnetic moment derived from these plots amounts to  $1.80$  and  $1.95 \mu_{\text{B}}$  in  $\text{U}_2\text{N}_2\text{Sb}$  and  $\text{U}_2\text{N}_2\text{Bi}$ , respectively. The Curie temperature is  $168$  and  $154$  K, respectively.

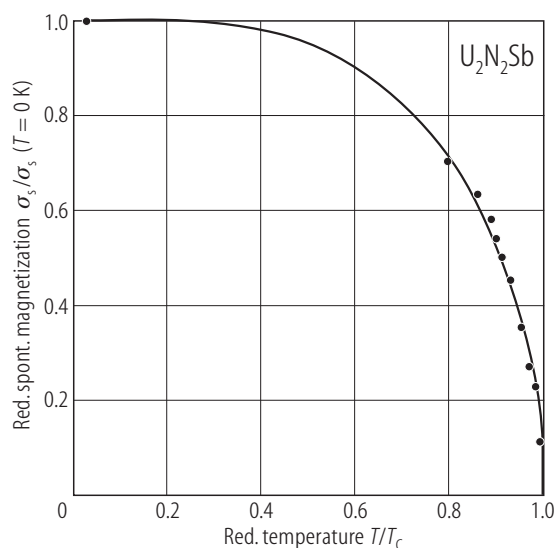


**Fig. 177.**  $U_2N_2Sb$ . Reduced spontaneous magnetization,  $\sigma_s/\sigma_s(T = 0\text{ K})$  vs. reduced temperature,  $T/T_C$ , as derived from Arrot's plots presented in Fig. 176 [78ZT]. The solid line is the theoretical function calculated for an isolated doublet (see Fig. 178). Note a good agreement between the experimental and theoretical results.

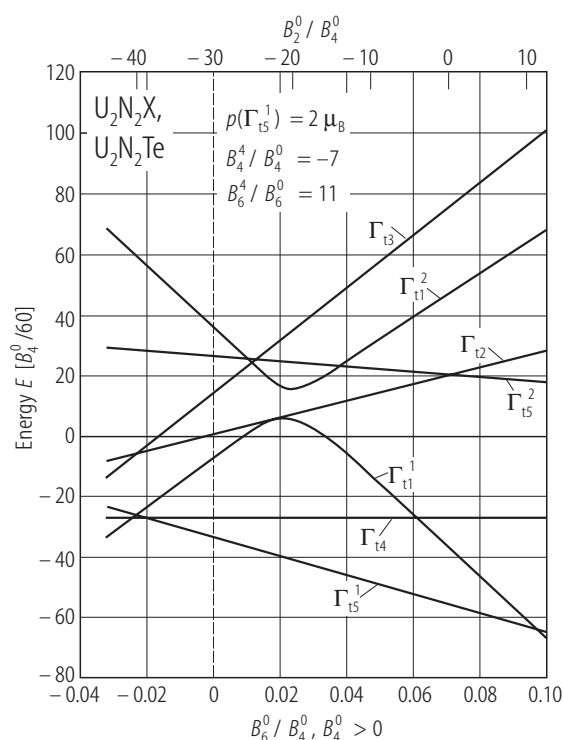


**Fig. 178.**  $U_2N_2X$ ,  $U_2N_2Te$ ,  $X = Sb, Bi$ . Energy diagram (in  $B_4^0$  units) of the crystal field levels resulting from the  $^3H_4$  ground multiplet of  $U^{4+}$  ion placed in a tetragonal crystal field potential [78ZT]. For the method used to construct the diagram and its detailed description refer to the original paper. The magnetic properties of  $U_2N_2Sb$  and  $U_2N_2Bi$  indicate that their CF ground state is the  $\Gamma_{t5}^1$  doublet, quite well separated from the excited levels. The authors deduced that the first excited level in both compounds is the  $\Gamma_{t1}^1$  singlet, i.e. the ratio  $B_6^0/B_4^0$  is larger than 0.06 (see the diagram). For  $U_2N_2Te$  the authors concluded that the  $\Gamma_{t5}^1$  doublet cannot be the ground state and instead one deals with a set of very closely spaced CF levels:  $\Gamma_{t1}^2 + \Gamma_{t3} + \Gamma_{t5}^2$ , with the singlet  $\Gamma_{t1}^2$  having the lowest energy (upper crossing in the diagram). This model accounts for the direction of the magnetic moment, which does not coincide with the  $c$ -axis (see Fig. 183), its magnitude, which is larger than expected for a  $\Gamma_{t5}$  doublet (see Fig. 182), the reduced Curie temperature (see Fig. 174) and complex magnetization behaviour (see Fig. 180). However in [81BMTZ] another CF model is presented with the  $\Gamma_{t5}$  ground state,  $\Gamma_{t1}$  as the first excited level being 100 K above  $\Gamma_{t5}$  and the second excited level  $\Gamma_{t3}$  being 300 K above  $\Gamma_{t5}$ . The latter CF model explains well not only the magnetic behaviour but also the heat capacity data. For further details refer to [81BMTZ].



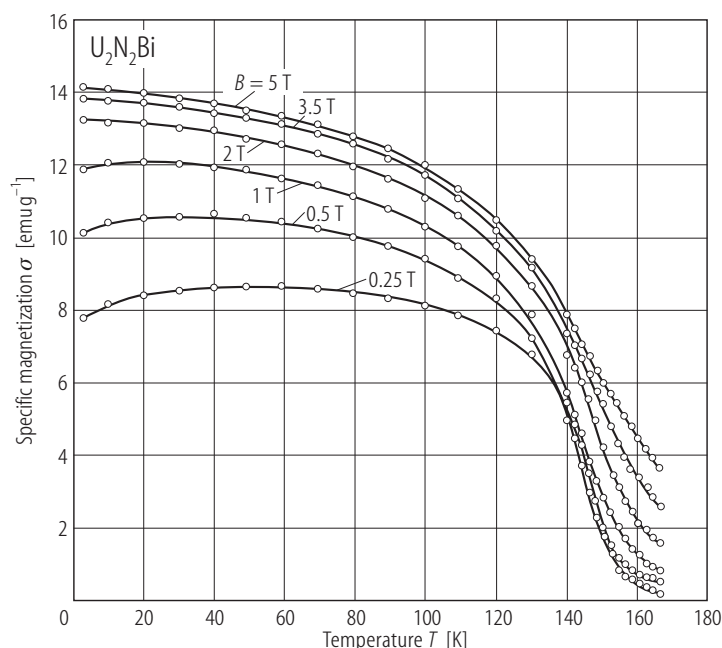


**Fig. 179.**  $\text{U}_2\text{N}_2\text{Bi}$ . Isofield magnetization,  $\sigma$ , vs. temperature,  $T$ , taken in various magnetic fields, specified in the figure, upon cooling the sample in zero field [78ZT]. Note that no maxima in  $\sigma(T)$ , characteristic of strongly anisotropic ferromagnets, are observed (see also Fig. 175).

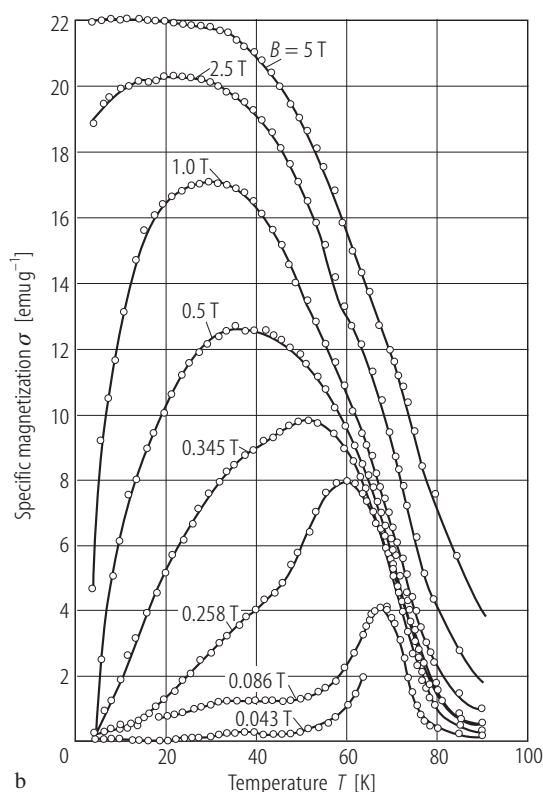
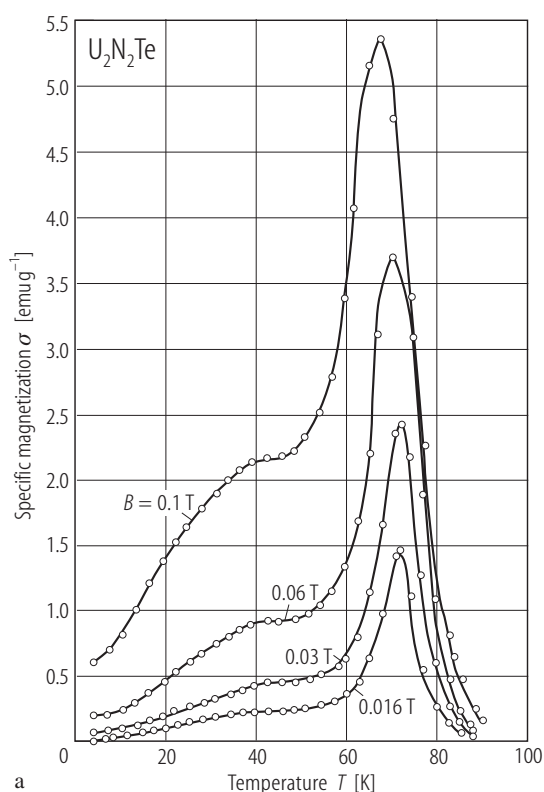


**Fig. 180.**  $\text{U}_2\text{N}_2\text{Te}$ . Isofield specific magnetization,  $\sigma$ , vs. temperature,  $T$ , taken in various magnetic fields from (a) 0.016 to 0.1 T and (b) 0.043 to 5 T, upon cooling the sample in zero field [78ZT]. Two distinct maxima in  $\sigma(T)$  occur in fields up to 0.5 T, whose shape and position with respect to the temperature axis strongly depend on the applied field strength. This

unusual behaviour of the magnetization the authors attributed to the formation of a specific ferromagnetic structure with the uranium magnetic moments tilted by about  $20^\circ$  from the basal plane (see Fig. 183). The features observed at low temperatures in weak magnetic fields may be associated with the presence of a compensated narrow-wall domain structure.

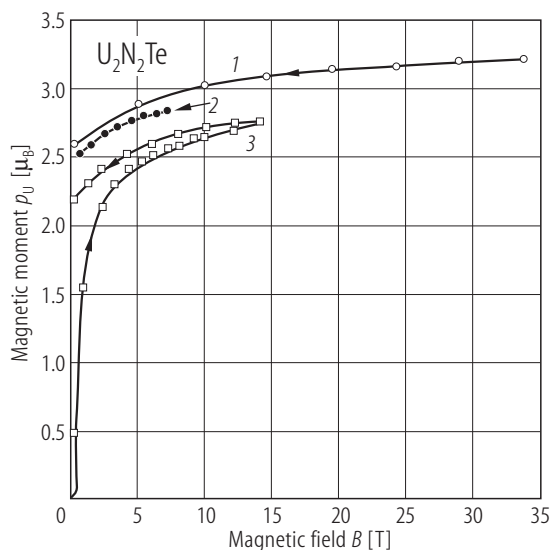


**Fig. 181.**  $\text{U}_2\text{N}_2\text{Te}$ . Magnetic moment per U atom,  $p_{\text{U}}$ , vs. magnetic field,  $B$ , up to 33 T [78SZT]. Curves (1) and (2): semicontinuous measurement on free powder; curve (3): Bitter coil data. The arrows indicate measurements taken with increasing and decreasing field. At 33 T  $p_{\text{s}} = 3.18 \mu_{\text{B}}$ , i.e. it is close to the maximum possible value for a  $\text{U}^{4+}$  ion ( $3.18 \mu_{\text{B}}$ ). The differences between the curves are ascribed by the authors to a field induced preferential orientation of the crystallites.

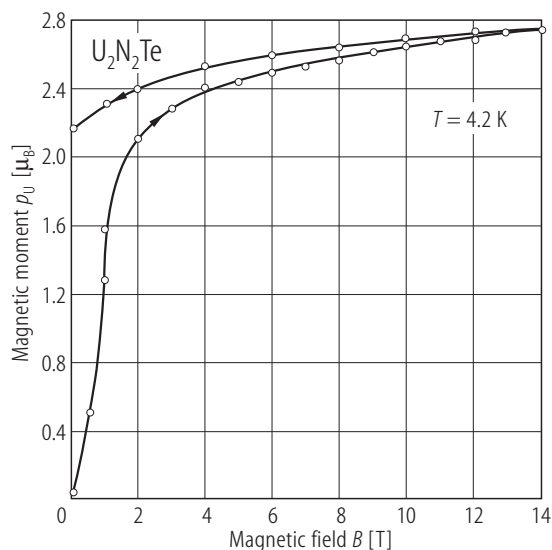


**Fig. 182.**  $\text{U}_2\text{N}_2\text{Te}$ . Magnetic moment per U atom,  $p_{\text{U}}$ , vs. field,  $B$ , measured at 4.2 K with increasing and decreasing magnetic field as indicated by the arrows [78ZT]. At low fields the magnetization increases rather slowly and it is almost linear in  $B$  and reversible up to 0.45 T. At 14 T the magnetic moment reaches as high value as  $2.78 \mu_{\text{B}}$  being yet still far from saturation. Note that this behaviour is quite different from that characteristic of isostructural pnictides  $\text{U}_2\text{N}_2\text{Sb}$  and  $\text{U}_2\text{N}_2\text{Bi}$  (compare Fig. 175). A reason for that may be different crystal field splitting (see Fig. 178).

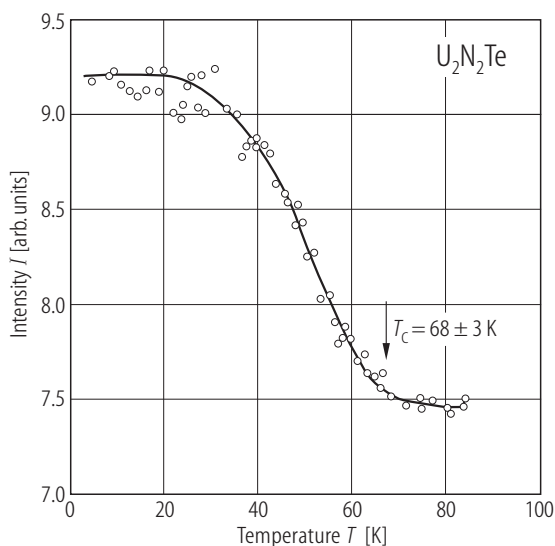


**Fig. 183.**  $\text{U}_2\text{N}_2\text{Te}$ . Neutron diffraction intensity of the magnetic reflection (101),  $I$ , vs. temperature,  $T$  [77LZT]. The compound orders ferromagnetically at  $T_{\text{C}} = 68(3)$  K with the magnetic moments forming an angle  $70(5)^\circ$  to the tetragonal axis. This unusual magnetic structure can be understood in terms of a peculiar scheme of low-lying crystal field levels (see Fig. 178). At 4 K the ordered magnetic moment  $p_{\text{o}}$  amounts to  $2.50(5) \mu_{\text{B}}$ .

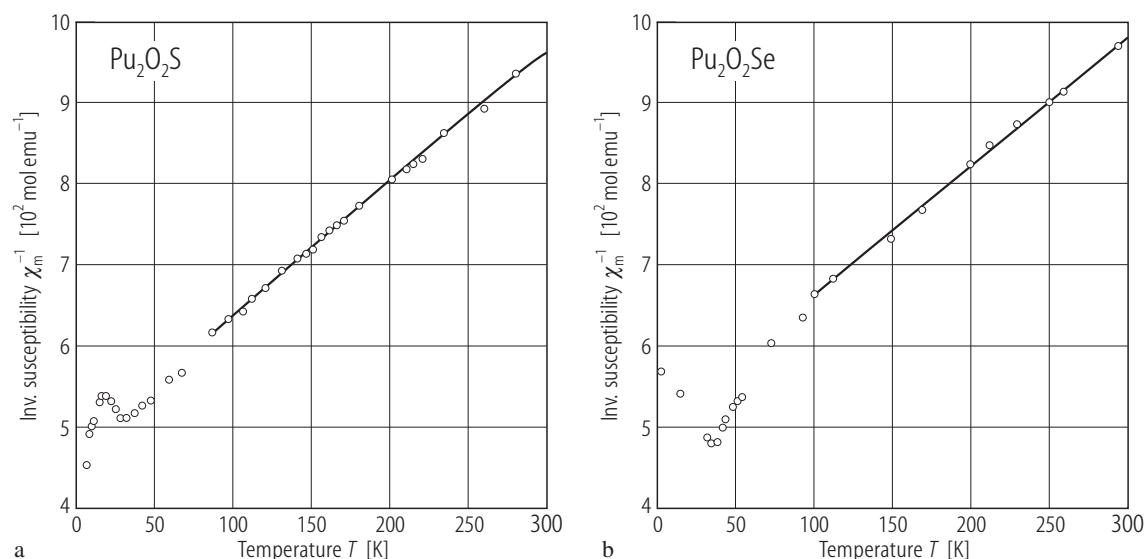


**Fig. 184.**  $\text{Pu}_2\text{O}_2\text{Y}$ ,  $\text{Y} = \text{S}, \text{Se}$ . Reciprocal molar magnetic susceptibility,  $\chi_m^{-1}$ , vs. temperature,  $T$  for (a)  $\text{Y} = \text{S}$ , (b)  $\text{Y} = \text{Se}$  [83CDDDB1]. The compounds order antiferromagnetically at  $T_N = 28$  and  $34$  K, for  $\text{Pu}_2\text{O}_2\text{S}$  and  $\text{Pu}_2\text{O}_2\text{Se}$ , respectively. The Curie-Weiss fit (solid lines) parameters are given in Table B. The magnetic behaviour of

these materials the authors interpreted in terms of superexchange coupling interactions via nonmetal p orbitals (f-p mixing). On going from  $\text{Y} = \text{S}$  to  $\text{Y} = \text{Se}$  the 5f-p covalency is enhanced as the chalcogen electronegativity decreases and the p radial extent increases. As a consequence the Néel temperature rises.

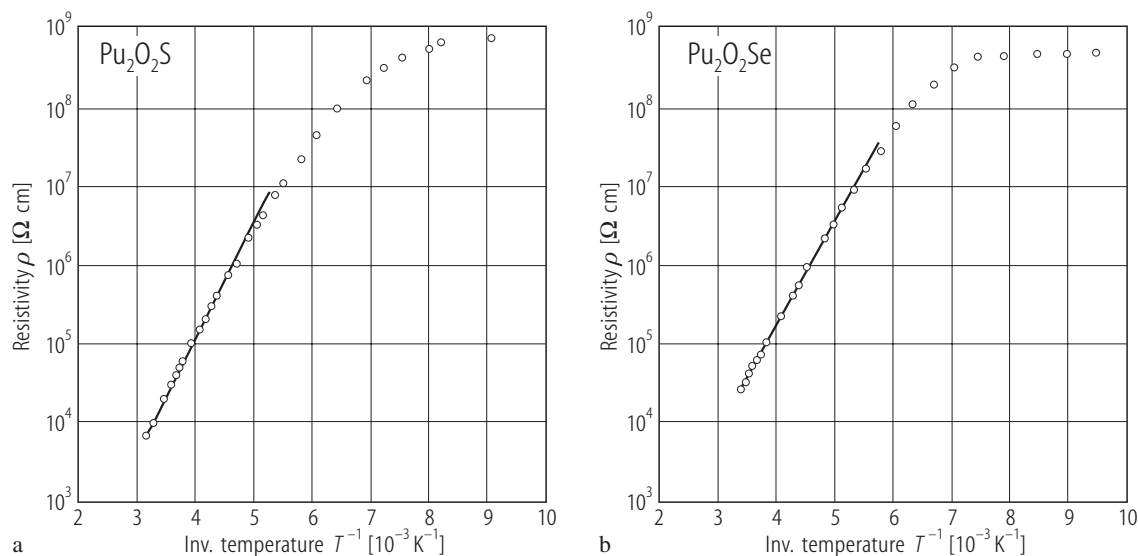


**Fig. 185.**  $\text{Pu}_2\text{O}_2\text{Y}$ ,  $\text{Y} = \text{S}, \text{Se}$ . Electrical resistivity,  $\rho$ , vs. reciprocal temperature,  $1/T$ , for (a)  $\text{Y} = \text{S}$ , (b)  $\text{Y} = \text{Se}$  [83CDDDB1]. Note a semiconducting behaviour of both compounds, marked by solid lines. From the linear part of  $\rho(1/T)$  an intrinsic energy gap of  $0.55$  and  $0.54$  eV is

deduced, for  $\text{Pu}_2\text{O}_2\text{S}$  and  $\text{Pu}_2\text{O}_2\text{Se}$ , respectively. This gap is ascribed by the authors to the energy difference between the chalcogen p valence band and the 6d-7s conduction band. The 5f localised states are considered to overlap the bottom of the chalcogen p band.

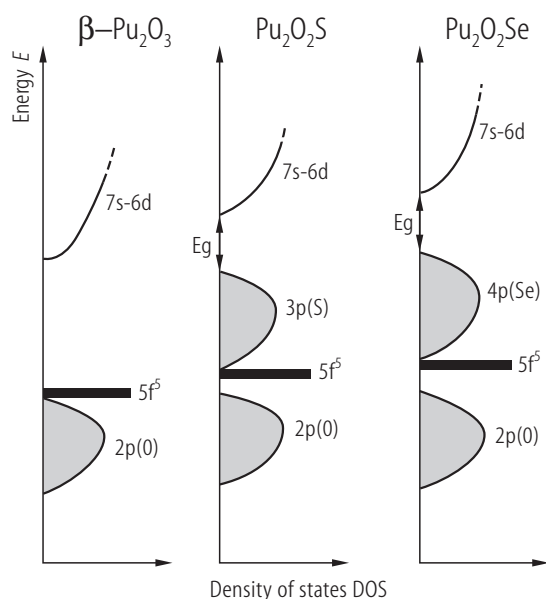


**Fig. 186.**  $\text{Pu}_2\text{O}_2\text{Y}$ ,  $\text{Y} = \text{S}, \text{Se}$ . Schematic band model accounting for the magnetic and electrical properties of the two antiferromagnetic semiconductors (see Figs. 184 and 185) [83CDDb1]. For comparison the band model is given for isostructural  $\beta\text{-Pu}_2\text{O}_3$ , which is an antiferromagnetic insulator.

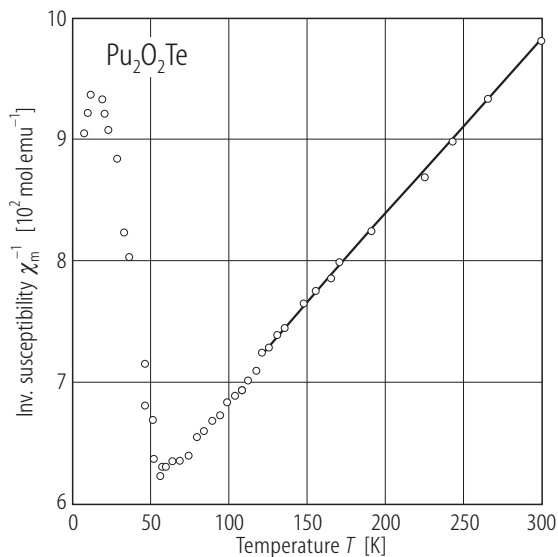


**Fig. 187.**  $\text{Pu}_2\text{O}_2\text{Te}$ . Reciprocal molar magnetic susceptibility,  $\chi_m^{-1}$ , vs. temperature,  $T$  [83CDDb2]. The compound orders antiferromagnetically at  $T_N = 56 \text{ K}$ . The Curie-Weiss fit (solid line) parameters are given in Table B. The magnetic behaviour the authors interpreted in terms of superexchange coupling interactions via nonmetal p orbitals (f-p mixing).

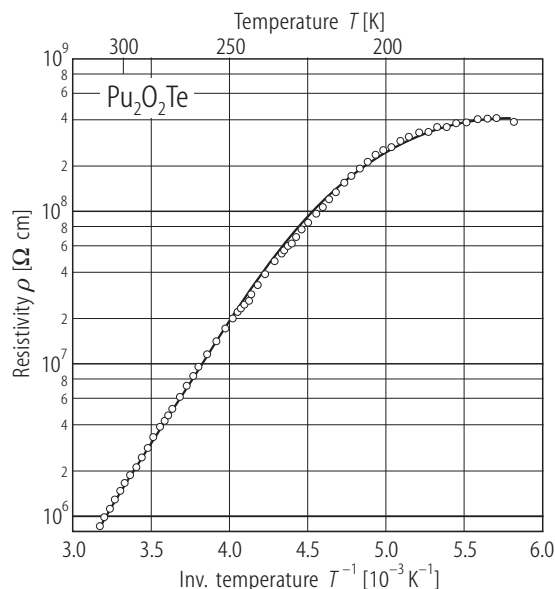


**Fig. 188.**  $\text{Pu}_2\text{O}_2\text{Te}$ . Electrical resistivity,  $\rho$ , vs. reciprocal temperature,  $1/T$  [83CDDb2]. Note a semiconducting behaviour. From the linear part of  $\rho(1/T)$  an intrinsic energy gap of 0.65 eV is deduced. The gap is ascribed by the authors to the energy difference between the 5p valence band and the 7s-6d conduction band. The 5f localised states are considered to overlap the bottom of 5p band.

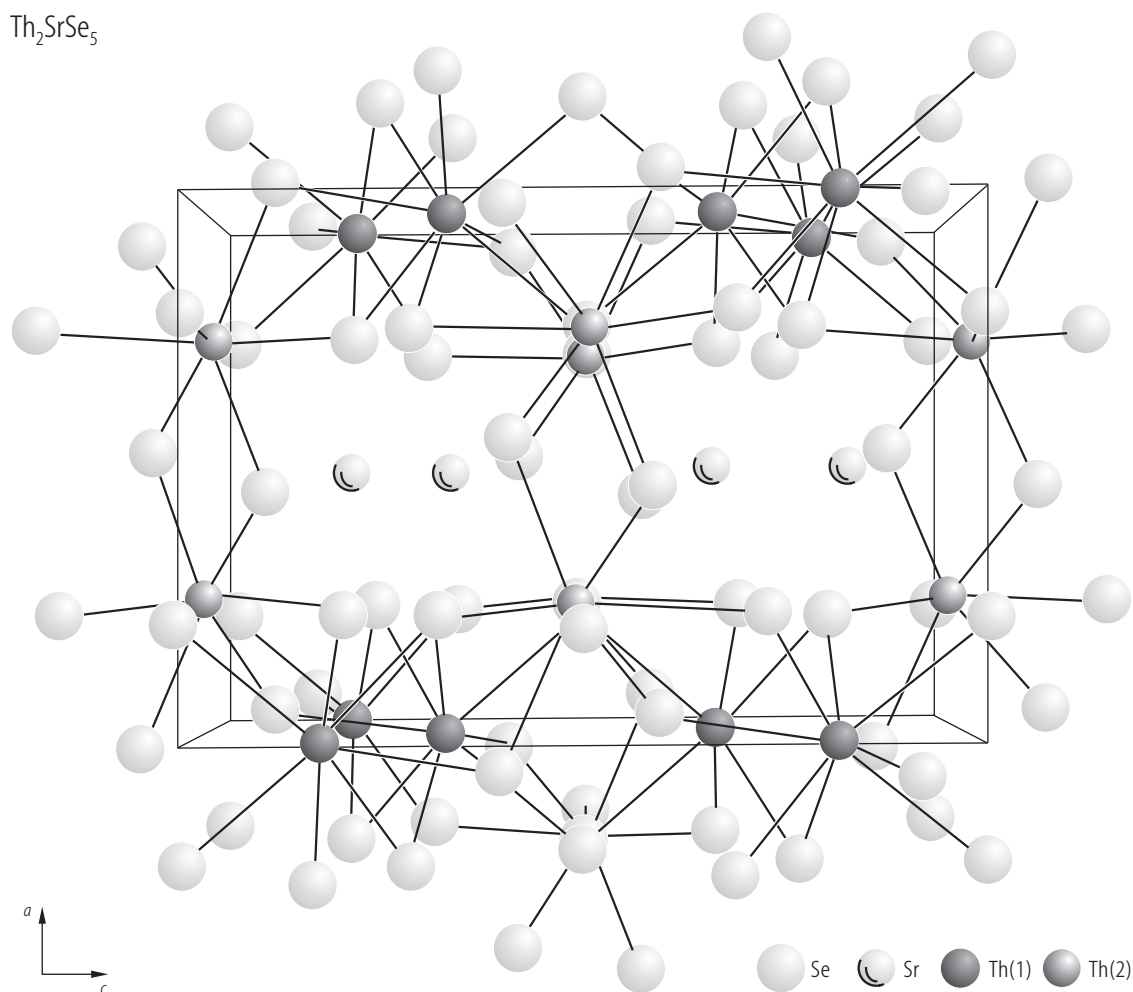
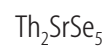


**Fig. 189.**  $\text{Th}_2\text{SrSe}_5$ . Crystal structure [98NI]. There are two distinct Th sites each with different environments. A three-dimensional framework is formed by the Th(1) net and the Th(2) chains with Sr cations located in one-dimensional channels.

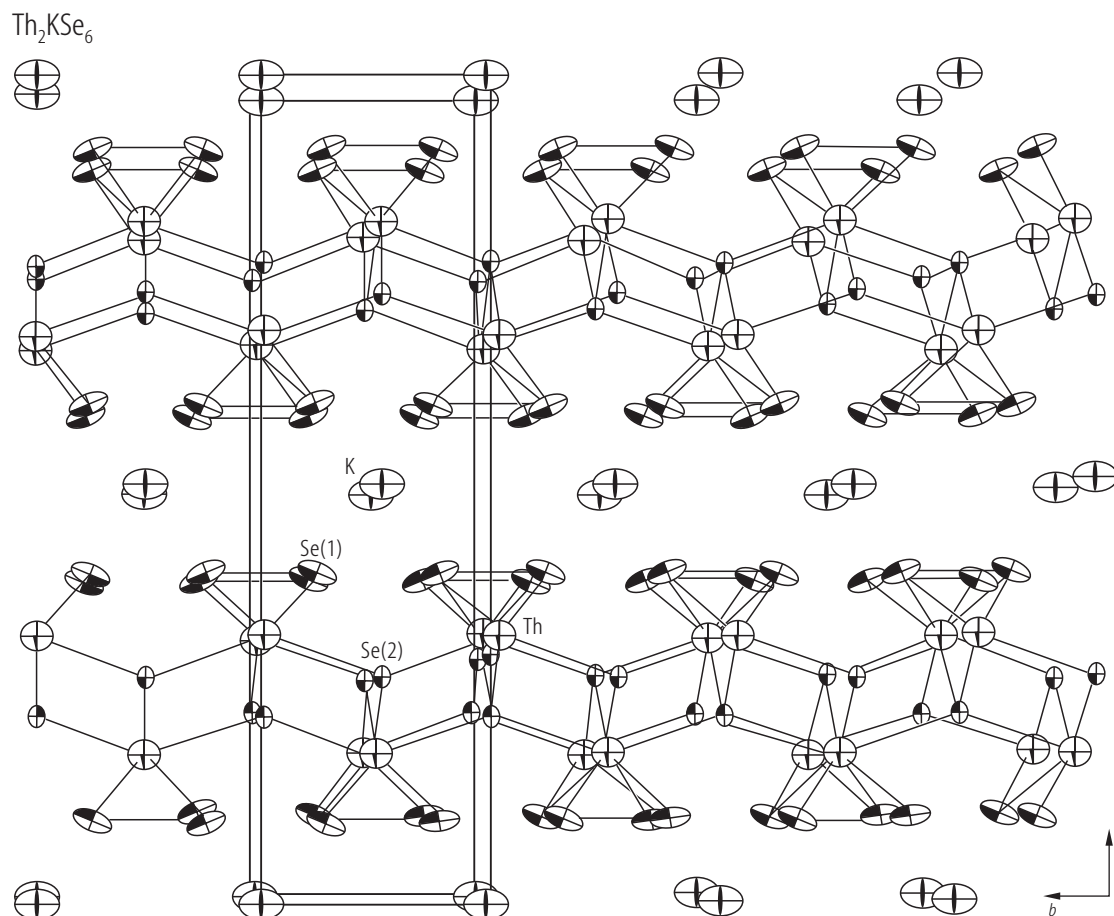
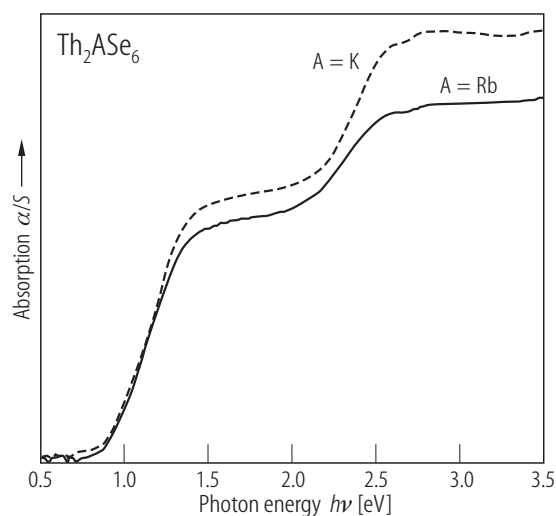


**Fig. 190.**  $\text{Th}_2\text{KSe}_6$ . Crystal structure viewed along the  $a$ -axis [98CPBW]. All atoms are represented by thermal vibrational ellipsoids. The unit cell is composed by infinite  $[\text{Th}_2\text{Se}_6]^-$  slabs that lie perpendicular to the  $[001]$  direction. These layers are stacked in an eclipsed manner with  $\text{K}^+$  cations accommodated in between them. The presented structure is only an average picture of the real atom

arrangement. TEM studies revealed a static charge density wave due to electron localization, which results in a  $4a \times 4b$  superstructure (for details see the original paper). The structure of  $\text{Th}_2\text{KSe}_6$  is closely related to that of  $\text{Th}_2\text{CsTe}_6$  (compare Fig. 193). The same structure type adopts  $\text{Th}_2\text{RbSe}_6$  [98CPBW].



←

**Fig. 191.**  $\text{Th}_2\text{AsSe}_6$ ,  $A = \text{K, Rb}$ . UV-Vis electronic absorption spectra [98CPBW]. Dashed curve:  $\text{Th}_2\text{KSe}_6$ ; solid curve:  $\text{Th}_2\text{RbSe}_6$ . The presence of abrupt optical transitions indicates that both materials are semiconductors. Dichroic nature of these transitions ( $E_g = 0.90$  and  $2.16$  eV for  $\text{Th}_2\text{KSe}_6$ ,  $E_g = 0.90$  and  $2.09$  eV for  $\text{Th}_2\text{RbSe}_6$ ) is unclear but may be due to strongly anisotropic electronic band structure caused by the lamellar character of the compounds.

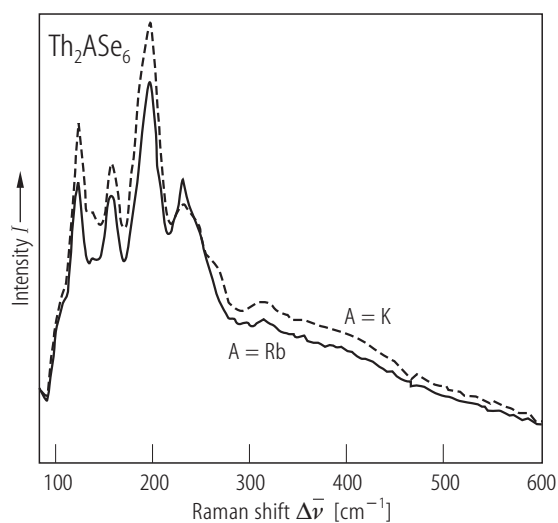


**Fig. 192.**  $\text{Th}_2\text{AsSe}_6$ ,  $A = \text{K, Rb}$ . Raman spectra measured on single crystals [98CPBW]. Dashed curve:  $\text{Th}_2\text{KSe}_6$ ; solid curve:  $\text{Th}_2\text{RbSe}_6$ . Both compounds exhibit shifts at similar energies. The structures at  $\sim 124$ ,  $\sim 160$  and  $\sim 199$   $\text{cm}^{-1}$  are attributed to Th-Se stretching and that one at  $\sim 234$   $\text{cm}^{-1}$  is assigned to  $\text{Se}_2^{2-}$  groups, which are involved in the formation a fourfold superstructure along the  $a$ - and  $c$ -axes (see Fig. 190).

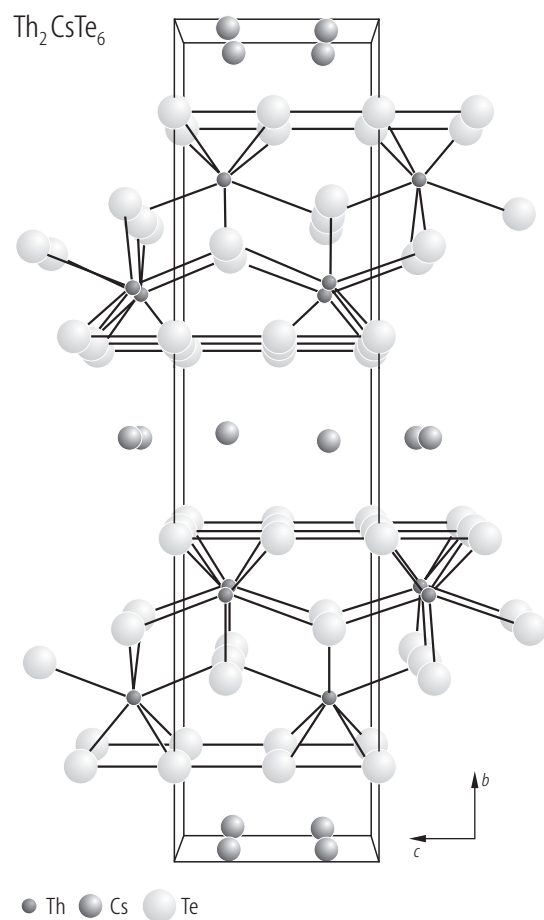


**Fig. 193.**  $\text{Th}_2\text{CsTe}_6$ . Unit cell viewed down the  $[100]$  direction [96CI]. The structure comprises two-dimensional infinite  $[\text{Th}_2\text{Te}_6]$  layers that stack perpendicular to the  $[010]$  axis. These slabs are interconnected by  $\text{Cs}^+$  cations. Isostructural to  $\text{Th}_2\text{CsTe}_6$  are the compounds  $\text{Th}_2\text{CsSe}_6$  and  $\text{Th}_2\text{KTe}_6$  [97WPI].

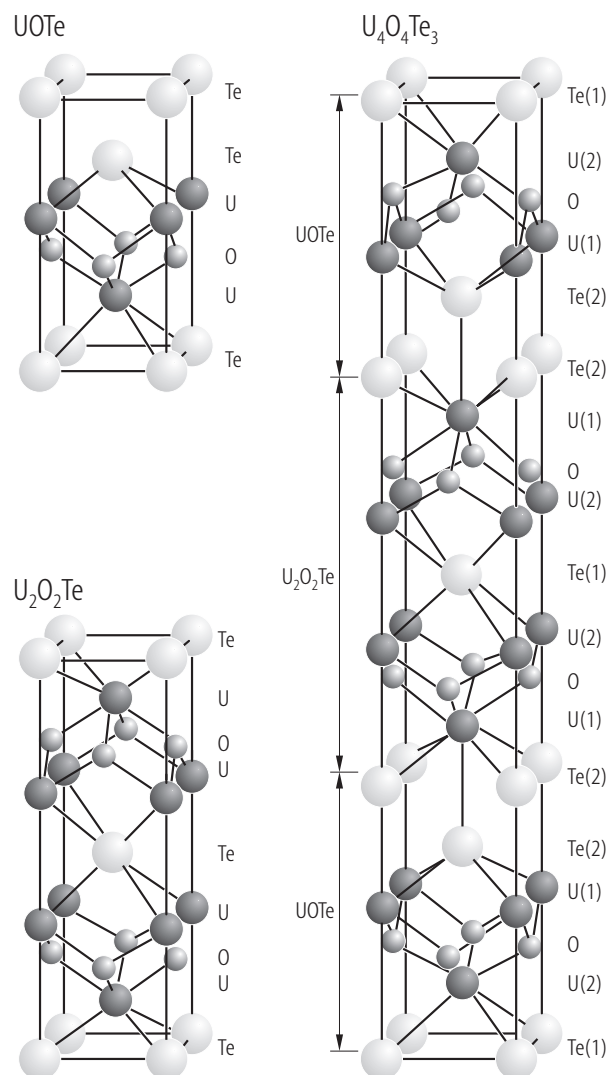


**Fig. 194.**  $\text{U}_4\text{O}_4\text{Te}_3$ . Crystal structure [95NPSK]. For comparison the structures of  $\text{UO}_4\text{Te}$  and  $\text{U}_2\text{O}_2\text{Te}$  are also shown.

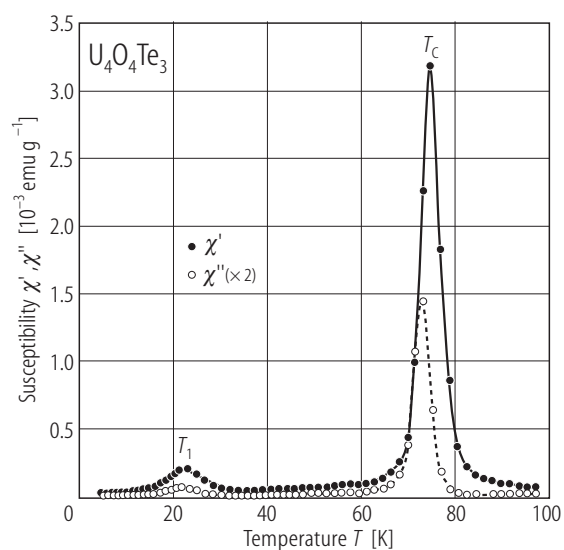


**Fig. 195.**  $\text{U}_4\text{O}_4\text{Te}_3$ . Complex magnetic susceptibility,  $\chi'$  and  $\chi''$ , vs. temperature,  $T$ , in the range 5...100 K, taken in an alternating field of 10 Oe with a frequency of 111.1 Hz in zero external static magnetic field [95KTSN]. For clarity,  $\chi''$  was multiplied by a factor of 2. The pronounced maxima occurring in both the real and imaginary components manifest two successive magnetic phase transitions. Below  $T_1 = 23$  K the compound is probably antiferromagnetic, while in the range  $23 < T < T_c = 80$  K it exhibits ferrimagnetic or canted-antiferromagnetic behavior (compare Fig. 196).



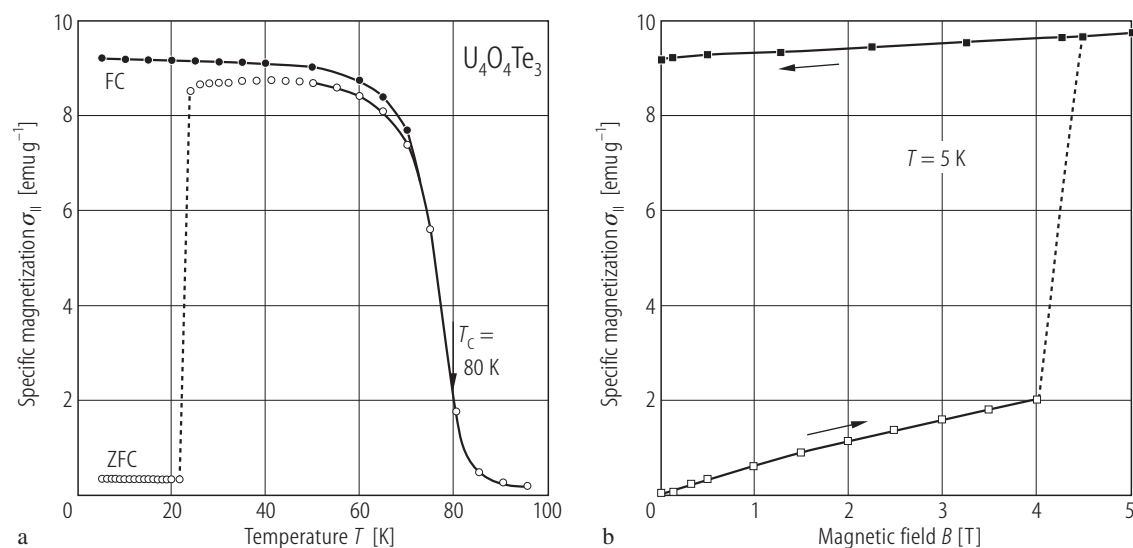


**Fig. 196.**  $\text{U}_4\text{O}_4\text{Te}_3$ . (a) Specific magnetization,  $\sigma_{||}$ , vs. temperature,  $T$ , measured on a single crystal with  $B \parallel c$ -axis in a magnetic field of 0.2 T upon cooling the sample in zero (ZFC) and non-zero (FC) magnetic field [95KTSN]. The arrow marks a phase transition at  $T_C = 80(2) \text{ K}$ . (b) Magnetization,  $\sigma_{||}$ , vs. magnetic field,  $B$ , measured at 5 K with increasing and decreasing magnetic field (indicated by the arrows). The magnetic moment measured at 5 T amounts

to  $0.6 \mu_B$ . The jumps occurring in  $\sigma_{||}(T)$  at  $T_1 = 23 \text{ K}$  (independent of  $B$ ; see also Fig. 195) and in  $\sigma_{||}(B)$  at about 4 T were interpreted by the authors as temperature and field induced metamagnetic-like transitions, respectively. Note a very large remanence, unusual for metamagnetic compounds, which may arise in the case of the magnetocrystalline anisotropy energy being comparable or larger than the magnitude of exchange interactions.

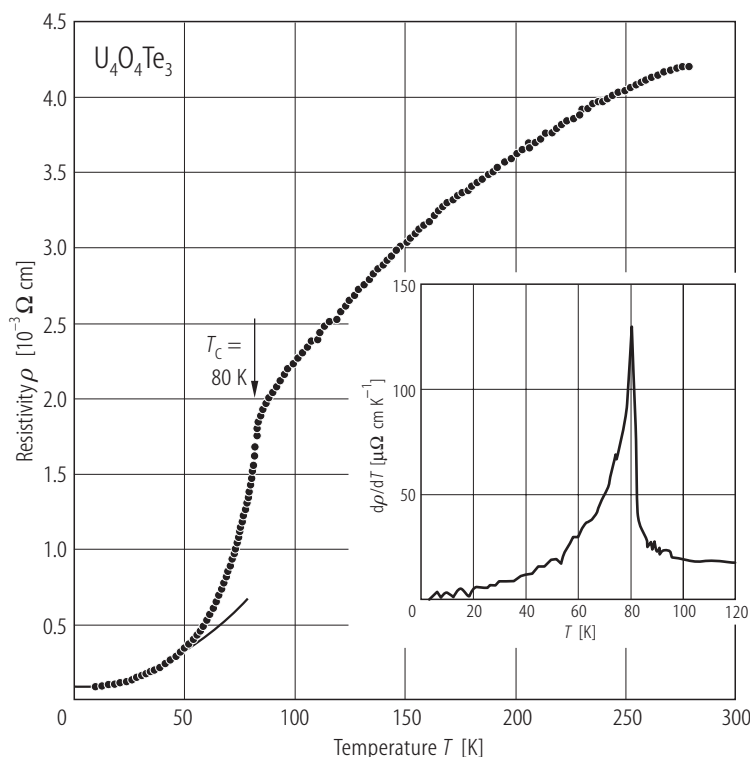


**Fig. 197.**  $\text{U}_4\text{O}_4\text{Te}_3$ . Electrical resistivity,  $\rho$ , vs. temperature,  $T$  measured on a single crystal with  $i \perp c$ -axis [95KTSN]. RRR = 53. Note a semimetallic behaviour. The arrow marks a magnetic phase transition at  $T_C = 80 \text{ K}$ . The other phase transition, found at  $T_1 = 23 \text{ K}$  in the magnetic studies (see Fig. 196), is visible neither in  $\rho(T)$  nor in  $d\rho/dT(T)$ . The solid line is a fit of the data below 50 K to the formula  $\rho(T) = a + bT^2 \exp(-\Delta/T)$ , with the parameters  $a = 80 \mu\Omega \text{ cm}$ ,  $b = 0.13 \mu\Omega \text{ cm/K}^2$  and  $\Delta = 15 \text{ K}$ , which may describe scattering of the conduction electrons on spin-wave excitations. Inset: temperature derivative of the resistivity,  $d\rho/dT$ , vs.  $T$ . Note a sharp maximum at  $T_C$ .

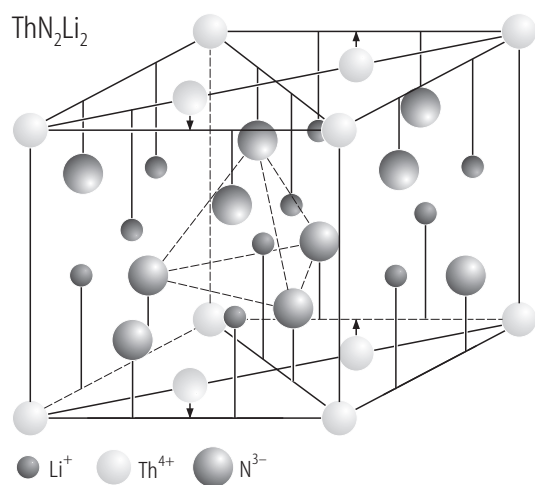


**Fig. 198.**  $\text{ThN}_2\text{Li}_2$ . Crystal structure [71PJ]. The arrows indicate the direction of small displacements of some Th atoms from the  $xy$ -plane.

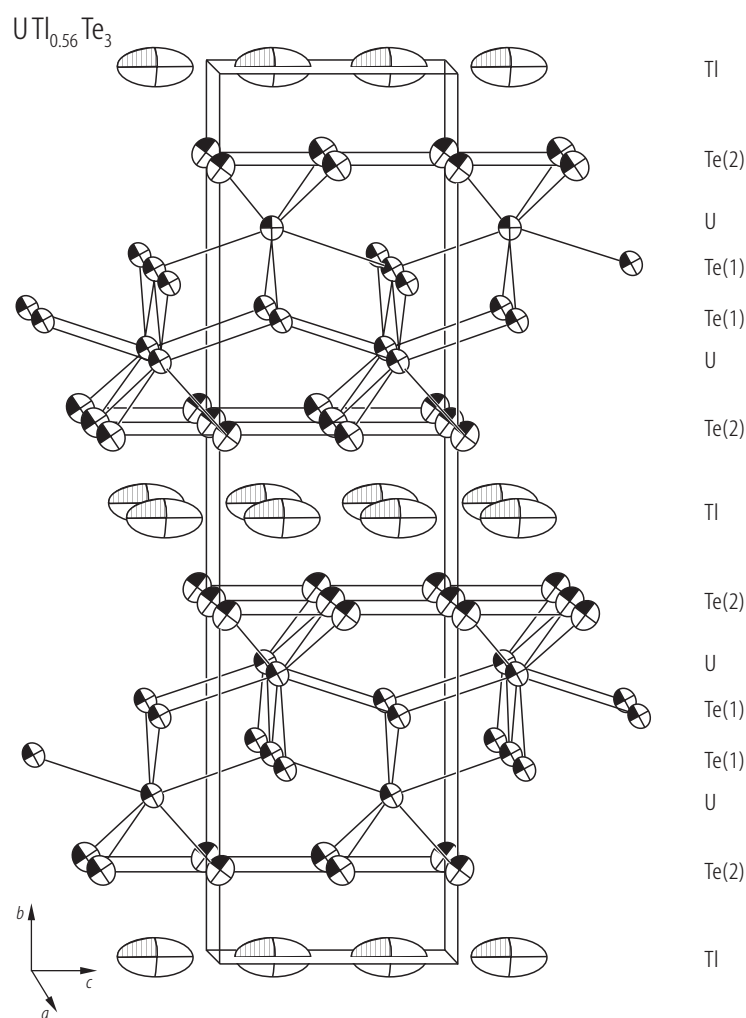


**Fig. 199.**  $\text{UTl}_{0.56}\text{Te}_3$ . Crystal structure [97TDPN]. The atoms are represented by ellipsoids corresponding to the anisotropic thermal atom displacement parameters.

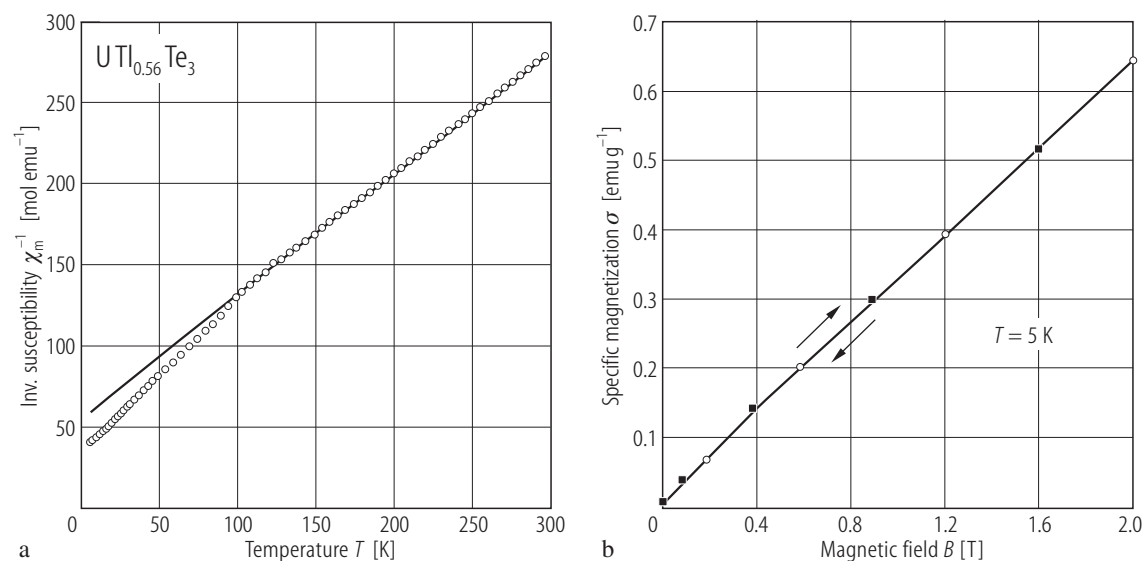


**Fig. 200.**  $\text{UTl}_{0.56}\text{Te}_3$ . (a) Reciprocal molar magnetic susceptibility,  $\chi_m^{-1}$ , vs. temperature,  $T$  [97TDPN]. The compound remains paramagnetic down to 2 K. The solid line denotes a Curie-Weiss fit with the parameters given in Table B. (b) Specific magnetization,  $\sigma$ , vs. field,  $B$ , taken at 5 K. Squares: increasing field; circles: decreasing field.

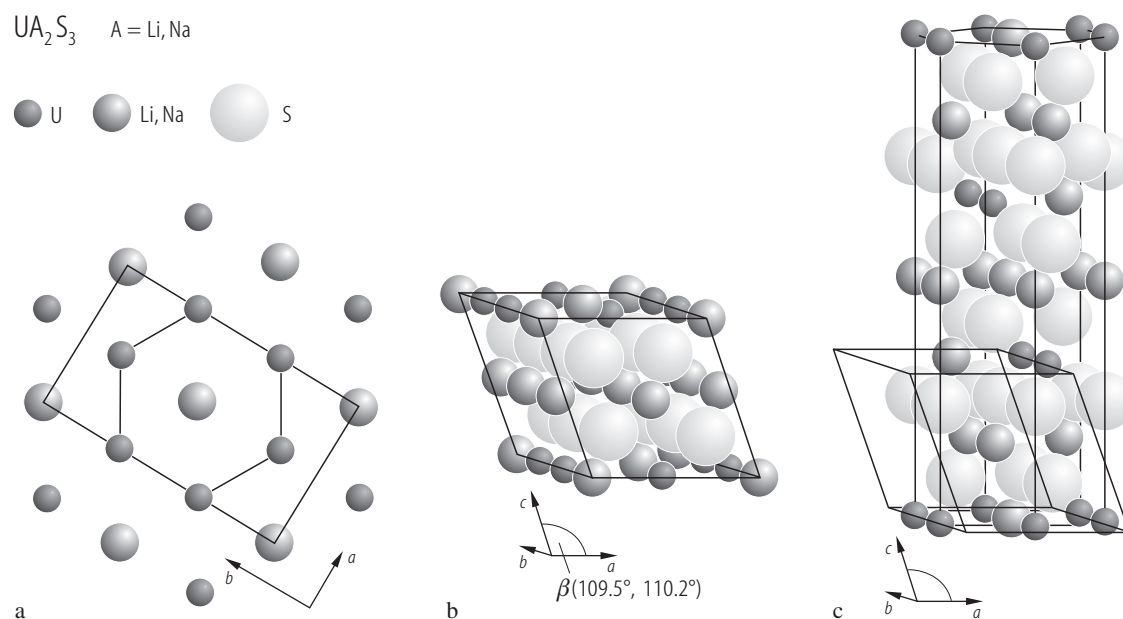


**Fig. 201.**  $\text{UA}_2\text{S}_3$ , A = Li, Na. (a) Schematic arrangement of U and A atoms in the unit cell; (b) crystal structure of the ordered form (monoclinic); (c) crystal structure of the disordered form (hexagonal) [99MFSY1]. Note a close similarity between the two structure types.

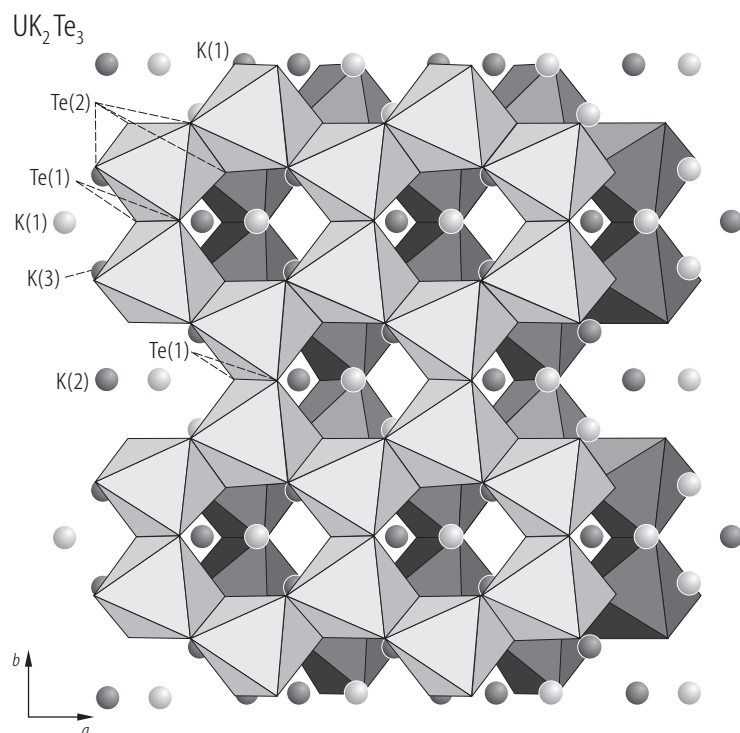


**Fig. 202.**  $\text{UK}_2\text{Te}_3$ . Part of the unit cell [99SA]. Emphasized are  $[\text{UTe}_6]$  octahedrons.

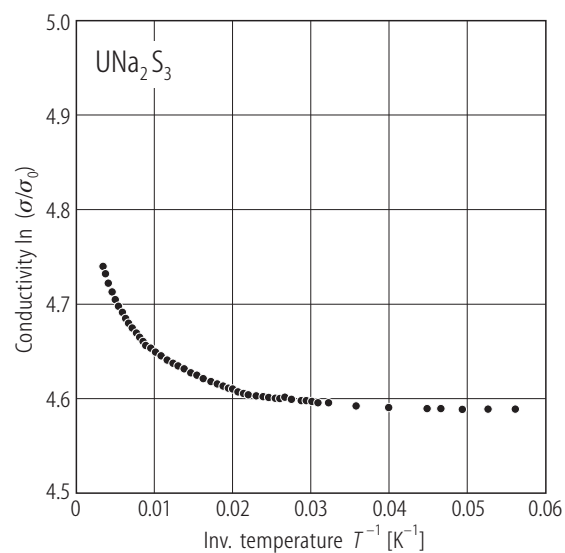


**Fig. 203.**  $\text{UNa}_2\text{S}_3$ . Electrical conductivity,  $\ln(\sigma/\sigma_0)$ , vs. reciprocal temperature,  $1/T$ , in the range 17...300 K [99MFSY2]. Note a semiconducting behaviour. Below 100 K the activation energy of conduction is of the order of only 0.1 meV. Above 200 K another conduction mechanism sets in with an activation energy of 1.87 meV.  $\sigma_0 = 1 \text{ } \Omega^{-1}\text{cm}^{-1}$ .

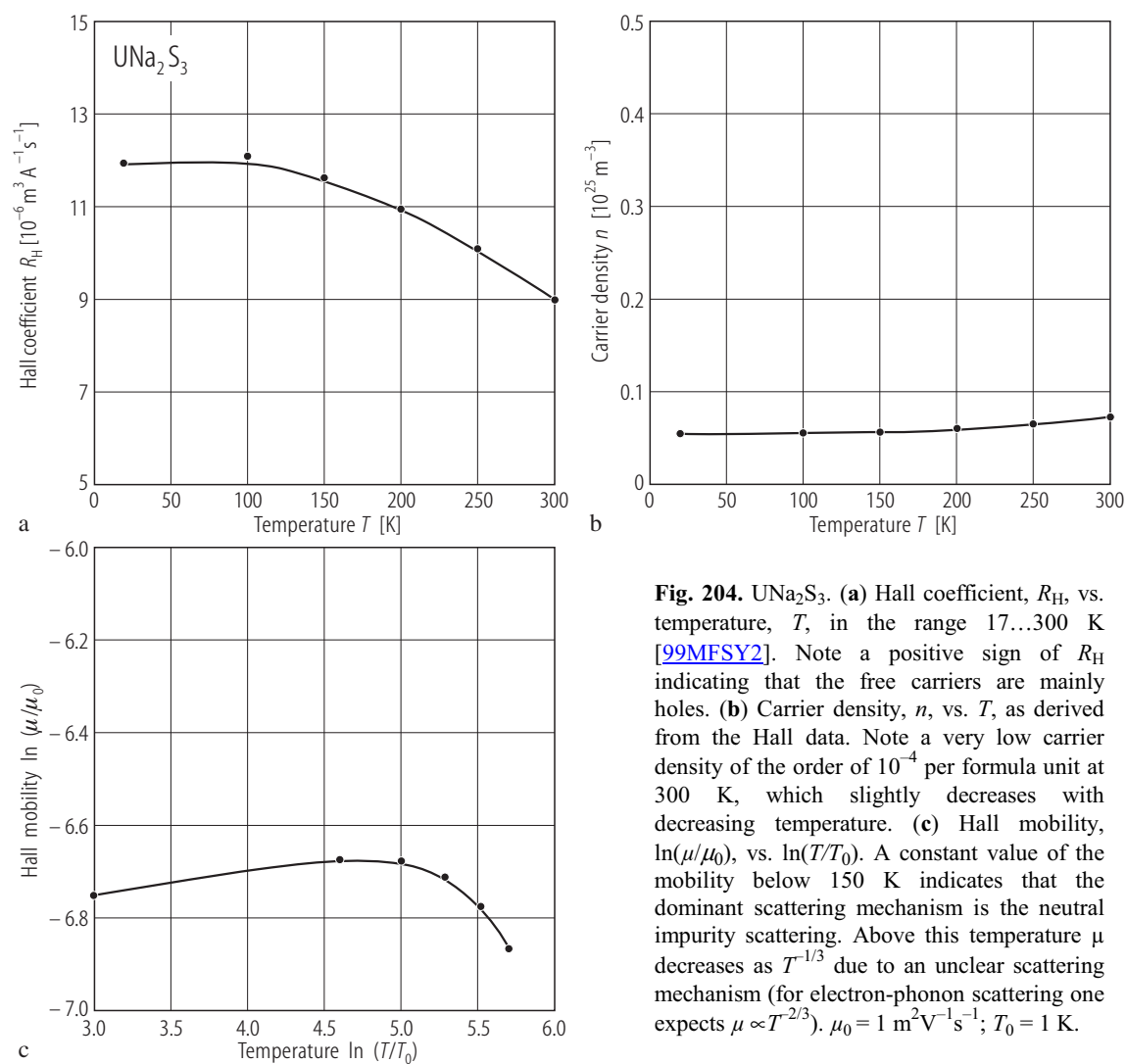


**Fig. 204.**  $\text{UNa}_2\text{S}_3$ . (a) Hall coefficient,  $R_H$ , vs. temperature,  $T$ , in the range 17...300 K [99MFSY2]. Note a positive sign of  $R_H$  indicating that the free carriers are mainly holes. (b) Carrier density,  $n$ , vs.  $T$ , as derived from the Hall data. Note a very low carrier density of the order of  $10^{-4}$  per formula unit at 300 K, which slightly decreases with decreasing temperature. (c) Hall mobility,  $\ln(\mu/\mu_0)$ , vs.  $\ln(T/T_0)$ . A constant value of the mobility below 150 K indicates that the dominant scattering mechanism is the neutral impurity scattering. Above this temperature  $\mu$  decreases as  $T^{-1/3}$  due to an unclear scattering mechanism (for electron-phonon scattering one expects  $\mu \propto T^{-2/3}$ ).  $\mu_0 = 1 \text{ m}^2 \text{ V}^{-1} \text{ s}^{-1}$ ;  $T_0 = 1 \text{ K}$ .

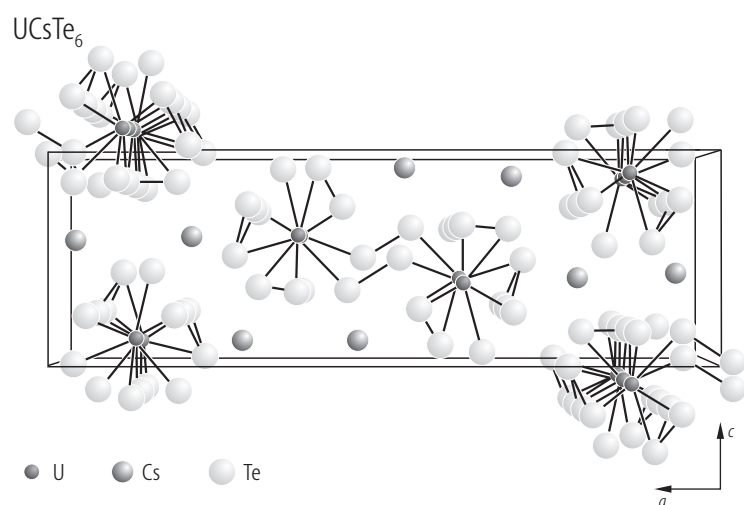


**Fig. 205.**  $\text{UCsTe}_6$ . Crystal structure [95CMPC].

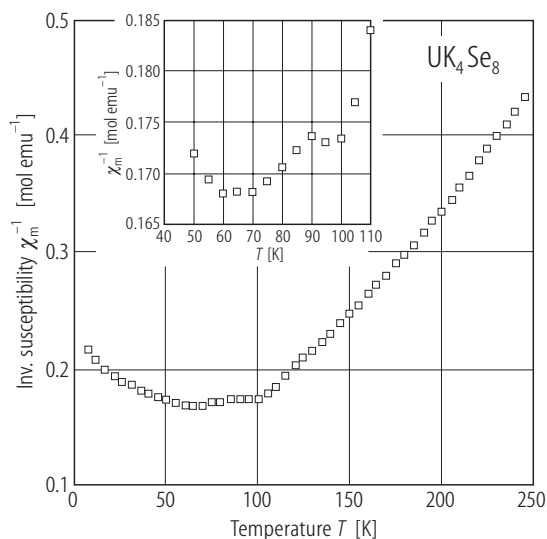


**Fig. 206.**  $\text{UK}_4\text{Se}_8$ . Reciprocal molar magnetic susceptibility,  $\chi_m^{-1}$ , vs. temperature,  $T$ , in the range 5...250 K taken in a field of 0.5 T [97SK]. Inset:  $\chi_m^{-1}$  vs.  $T$  from 50 to 110 K on an expanded scale. The maximum in  $\chi_m^{-1}(T)$  at 90 K was interpreted in the original paper as the onset of antiferromagnetic ordering, which is followed by a change of magnetic structure at about 65 K.

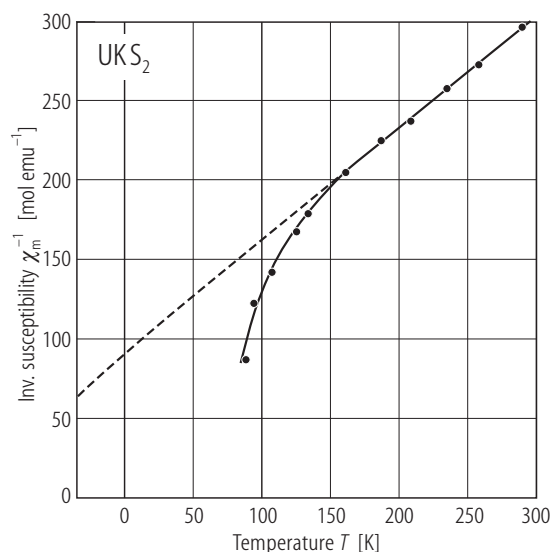


**Fig. 207.**  $\text{UKS}_2$ . Reciprocal molar magnetic susceptibility,  $\chi_m^{-1}$ , vs. temperature,  $T$ , in the range 86...295 K [66PL]. The dashed line denotes a Curie-Weiss fit with the parameters given in Table B. The compound probably orders ferro- or ferrimagnetically at temperatures lower than the experimental limit (86 K).

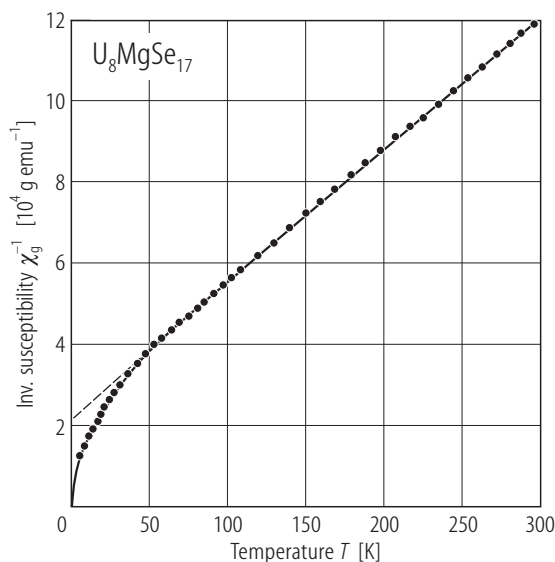


**Fig. 208.**  $\text{U}_8\text{MgSe}_{17}$ . Reciprocal mass magnetic susceptibility,  $\chi_g^{-1}$ , vs. temperature,  $T$  [79NT]. The dashed line marks a Curie-Weiss behaviour with the parameters given in Table B. The compound does not order magnetically down to 4.2 K.

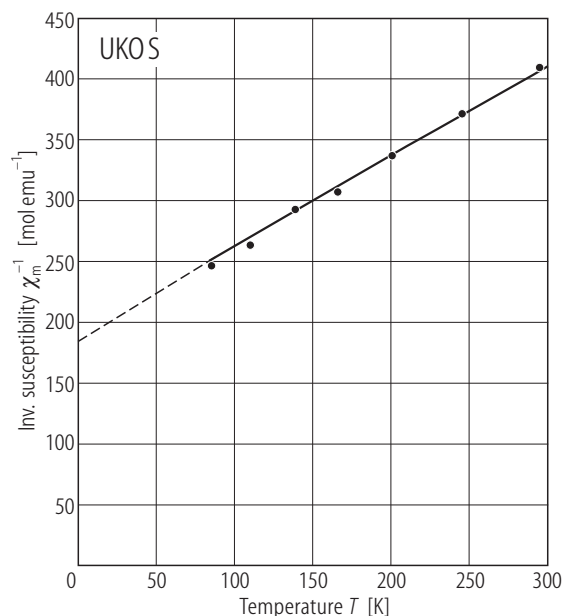


**Fig. 209.**  $\text{UKOS}$ . Reciprocal molar magnetic susceptibility,  $\chi_m^{-1}$ , vs. temperature,  $T$ , in the range 86...295 K [66PL]. The line denotes a Curie-Weiss fit with the parameters given in Table B.

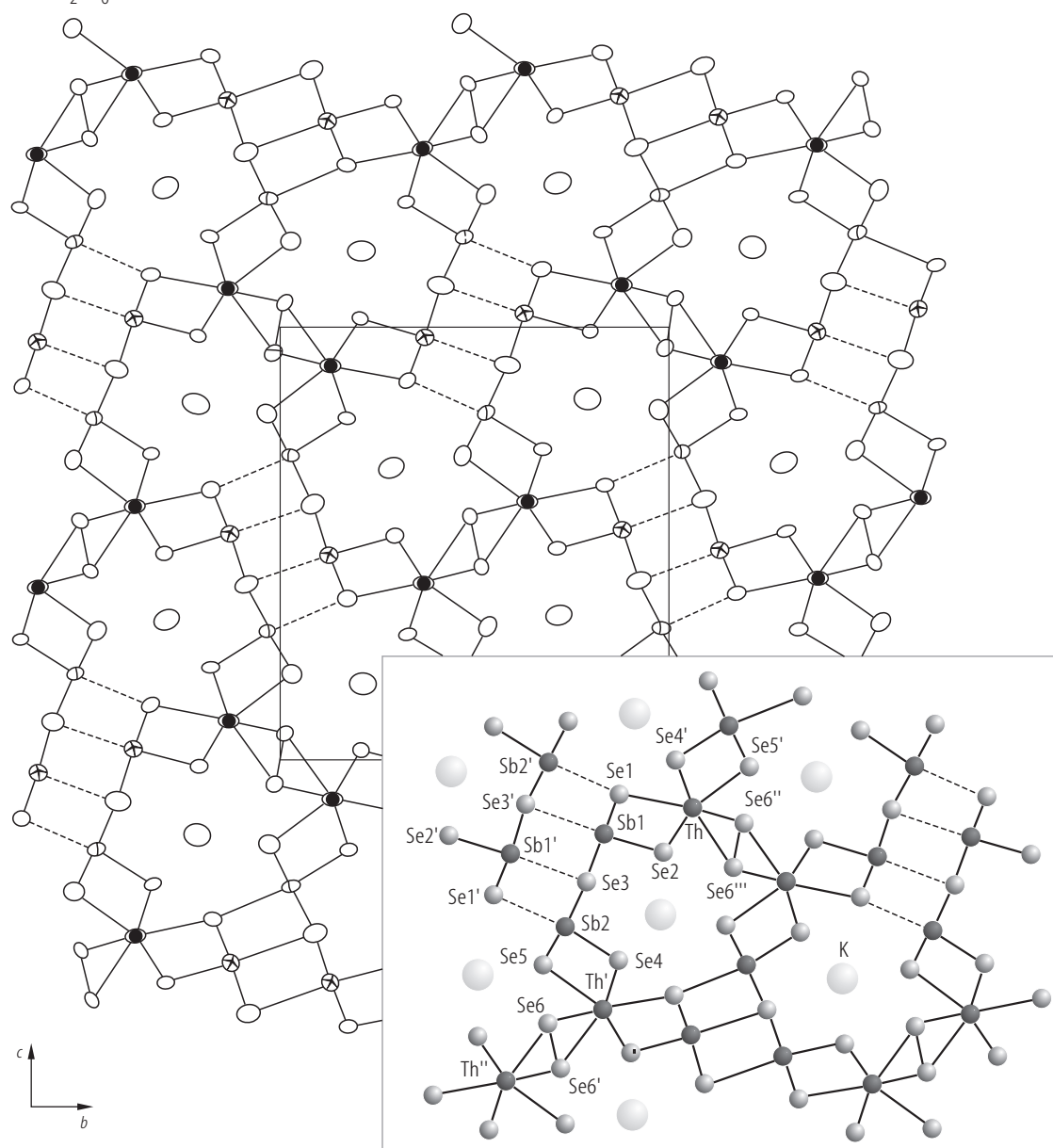


**Fig. 210.**  $\text{ThKSb}_2\text{Se}_6$ . Crystal structure viewed down the  $a$ -axis [97CICK]. The atoms are represented by thermal vibrational ellipsoids. Inset: atom labeling scheme.

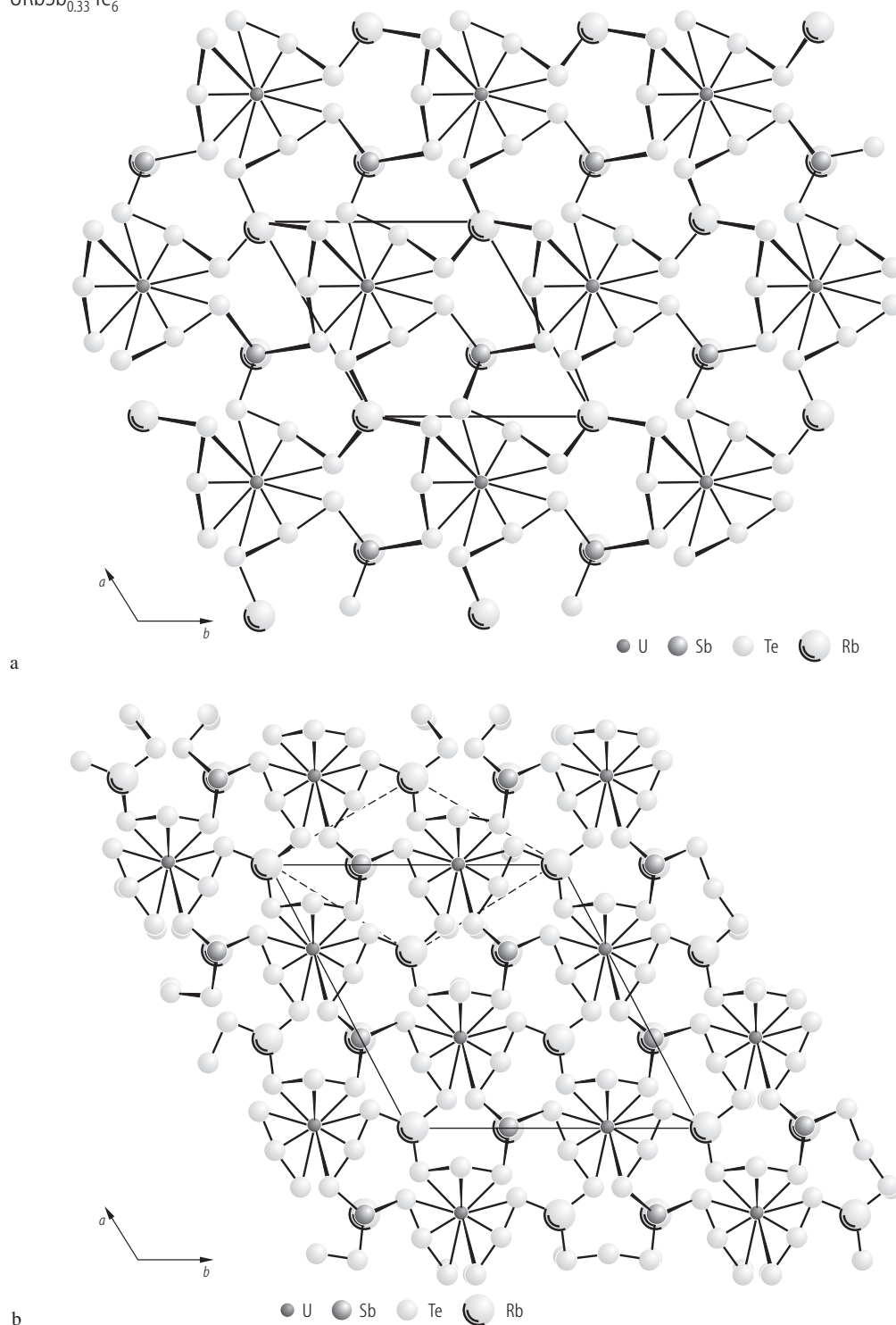


**Fig. 211.**  $\text{URbSb}_{0.33}\text{Te}_6$ . Crystal substructure (panel (a)) and superstructure (panel (b)) both viewed down the  $c$ -axis (solid lines) [01CK]. Dashed lines in panel (b) mark the unit cell of the substructure. The nine-fold superstructure ( $a_{\text{super}} = \sqrt{3}a_{\text{sub}}$ ,  $b_{\text{super}} = \sqrt{3}b_{\text{sub}}$ ,  $c_{\text{super}} = 3c_{\text{sub}}$ ) is caused by a periodic modulation of Te-Te distances in infinite zig-zag chains along the [001] direction.



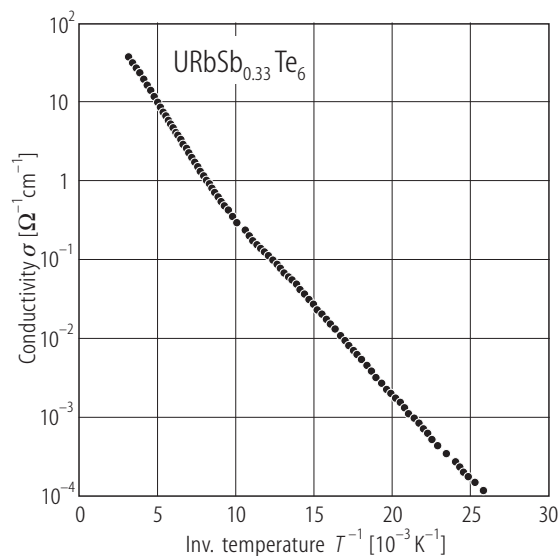


**Fig. 212.** URbSb<sub>0.33</sub>Te<sub>6</sub>. Electrical conductivity,  $\sigma$ , vs. inverse temperature,  $1/T$ , measured on a single crystal in the range 35...330 K [01CK]. The compound is a narrow gap semiconductor with an activation energy of  $\sim 0.05$  eV.

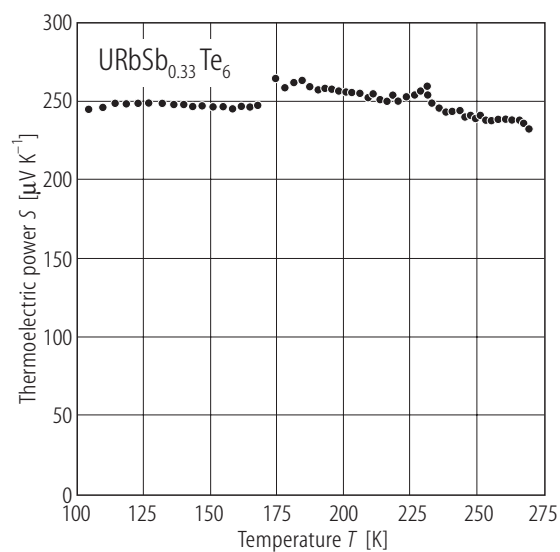


**Fig. 213.** URbSb<sub>0.33</sub>Te<sub>6</sub>. Thermoelectric power,  $S$ , vs. temperature,  $T$ , measured on a single crystal in the range 100...270 K [01CK]. Note a very large value of  $\sim 230$   $\mu\text{V/K}$  at room temperature, which hardly changes with decreasing temperature. The positive Seebeck coefficient indicates that holes are the dominant charge carriers.

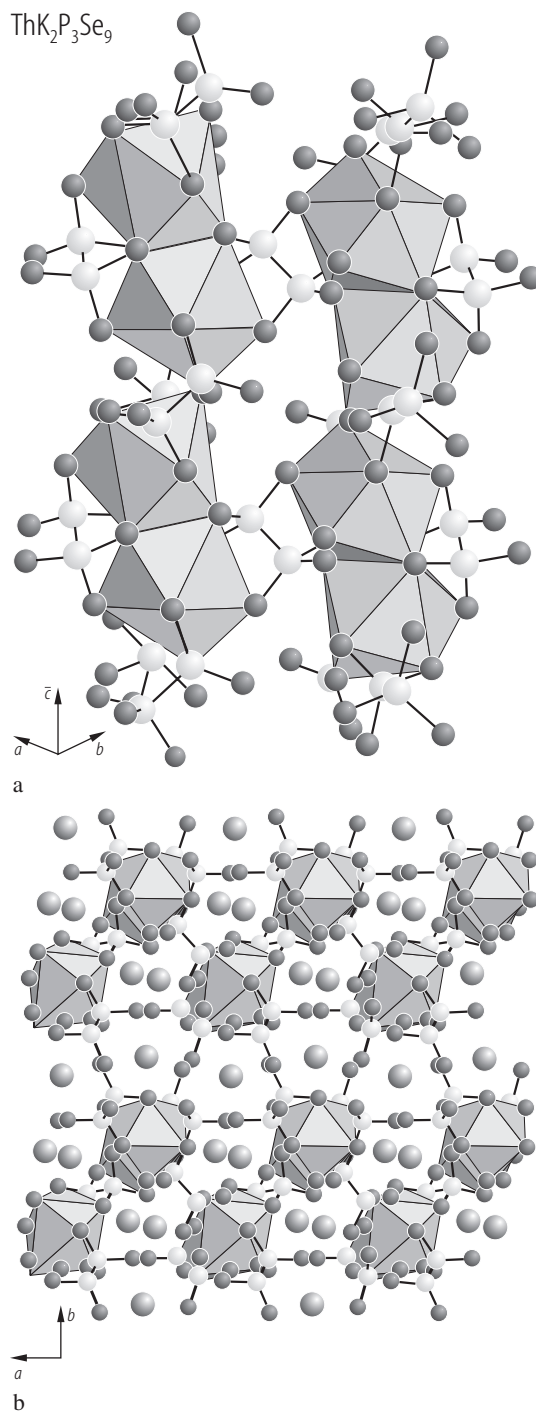


**Fig. 214.** ThK<sub>2</sub>P<sub>3</sub>Se<sub>9</sub>. Selected parts of the crystal structure [00BASD]. (a) Thorium selenophosphate chains viewed down the  $[110]$  direction. Polyhedra: Th atoms; dark gray circles: Se atoms; light gray circles: P atoms. The chains propagate along the  $[001]$  axis. (b) Puckered slabs viewed down the  $[001]$  direction. Polyhedra: Th atoms; small dark gray circles: Se atoms; small light gray circles: P atoms; large dark gray circles: K atoms. The slabs run left to right in the  $(101)$  plane.

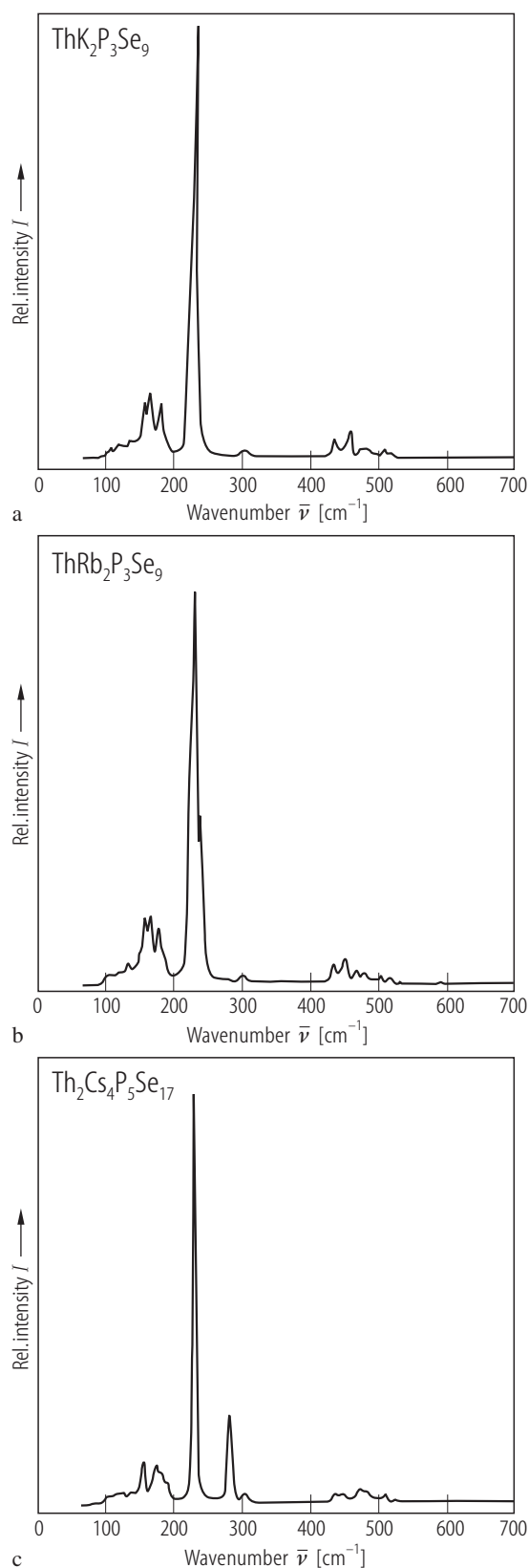


**Fig. 215.**  $\text{ThA}_2\text{P}_3\text{Se}_9$ ,  $A = \text{K, Rb}$ ,  $\text{Th}_2\text{Cs}_4\text{P}_5\text{Se}_{17}$ . Raman spectra taken on single crystals [00BASD]. (a)  $\text{ThK}_2\text{P}_3\text{Se}_9$ ; (b)  $\text{ThRb}_2\text{P}_3\text{Se}_9$ ; (c)  $\text{Th}_2\text{Cs}_4\text{P}_5\text{Se}_{17}$ . Note striking similarities between the data. A very strong peak at  $\sim 230 \text{ cm}^{-1}$  is assigned to  $\bar{\nu}_2 (A_{1g})$  stretching mode of  $(\text{P}_2\text{Se}_6)^{4-}$ . The other Raman active modes can be assigned as follows:  $\bar{\nu}_3 (A_{1g})$  at  $\sim 120 \dots 130 \text{ cm}^{-1}$ ,  $\bar{\nu}_9 (E_g)$  at  $\sim 150 \text{ cm}^{-1}$ ,  $\bar{\nu}_8 (E_g)$  at  $\sim 160 \dots 170 \text{ cm}^{-1}$ ,  $\bar{\nu}_7 (E_g)$  at  $\sim 430 \dots 480 \text{ cm}^{-1}$ ,  $\bar{\nu}_1 (A_{1g})$  at  $\sim 490 \dots 520 \text{ cm}^{-1}$ . The structures below  $120 \text{ cm}^{-1}$  are lower energy phonon modes. In the case of  $\text{Th}_2\text{Cs}_4\text{P}_5\text{Se}_{17}$  the strong band at  $283 \text{ cm}^{-1}$  is due to Se-Se stretching of the  $(\text{Se}_2)^{2-}$  anion.

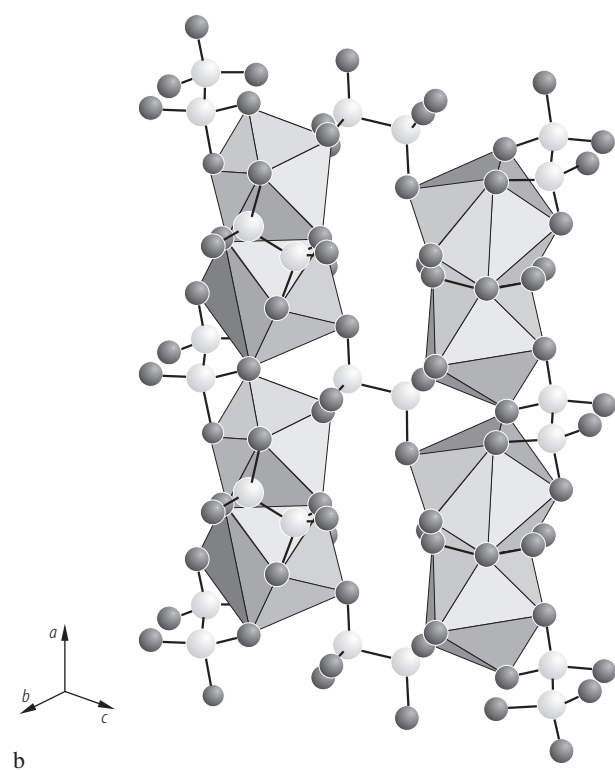
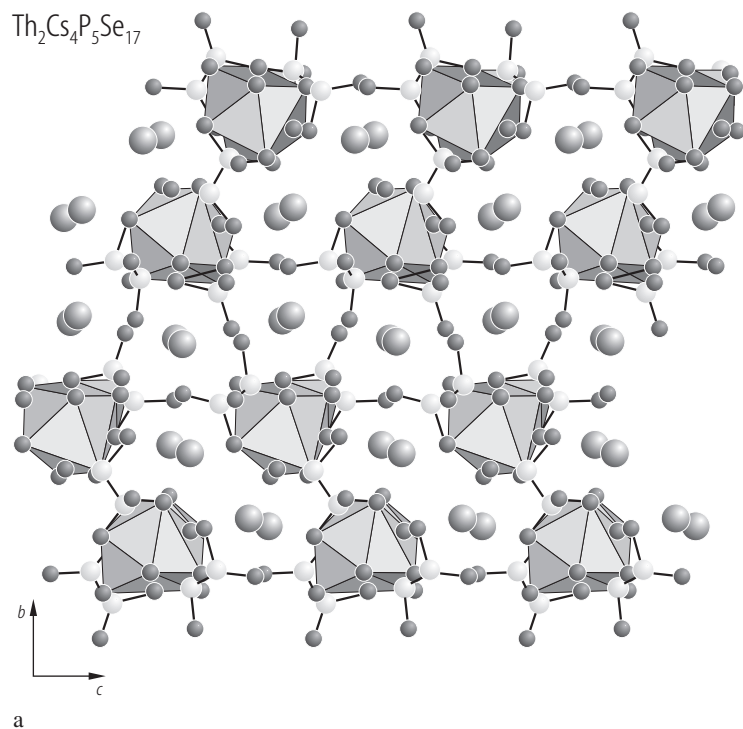


**Fig. 216.**  $\text{Th}_2\text{Cs}_4\text{P}_5\text{Se}_{17}$ . (a) Crystal structure viewed down the  $[\bar{1}00]$  direction [00BASD]. Polyhedra: Th atoms; large dark gray circles: Cs atoms; small light gray circles: P atoms; small, dark circles: Se atoms. The Th polyhedra in "dumbbell" ribbons run along the  $[\bar{1}00]$  direction. (b) "Dumbbell" chains of Th polyhedra viewed down the  $[011]$  direction [00BASD]. The chains are interconnected by  $(\text{P}_2\text{Se}_6)^{4-}$  units. Dark circles are Se atoms, light gray circles are P atoms.

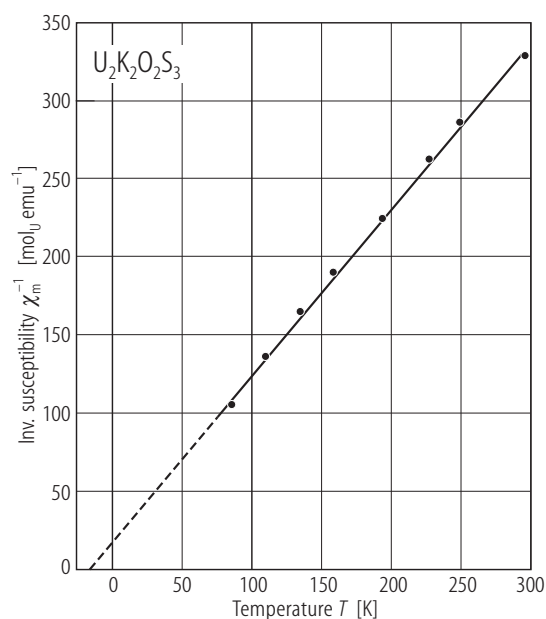


**Fig. 217.**  $\text{U}_2\text{K}_2\text{O}_2\text{S}_3$ . Reciprocal molar magnetic susceptibility,  $\chi_m^{-1}$ , vs. temperature,  $T$ , in the range 86...295 K [66PL]. The line denotes a Curie-Weiss fit with the parameters given in Table B.

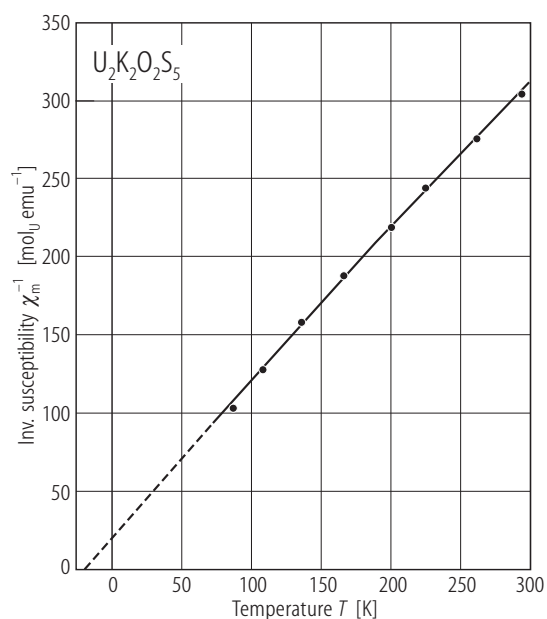


**Fig. 218.**  $\text{U}_2\text{K}_2\text{O}_2\text{S}_5$ . Reciprocal molar magnetic susceptibility,  $\chi_m^{-1}$ , vs. temperature,  $T$ , in the range 86...295 K [66PL]. The line denotes a Curie-Weiss fit with the parameters given in Table B.

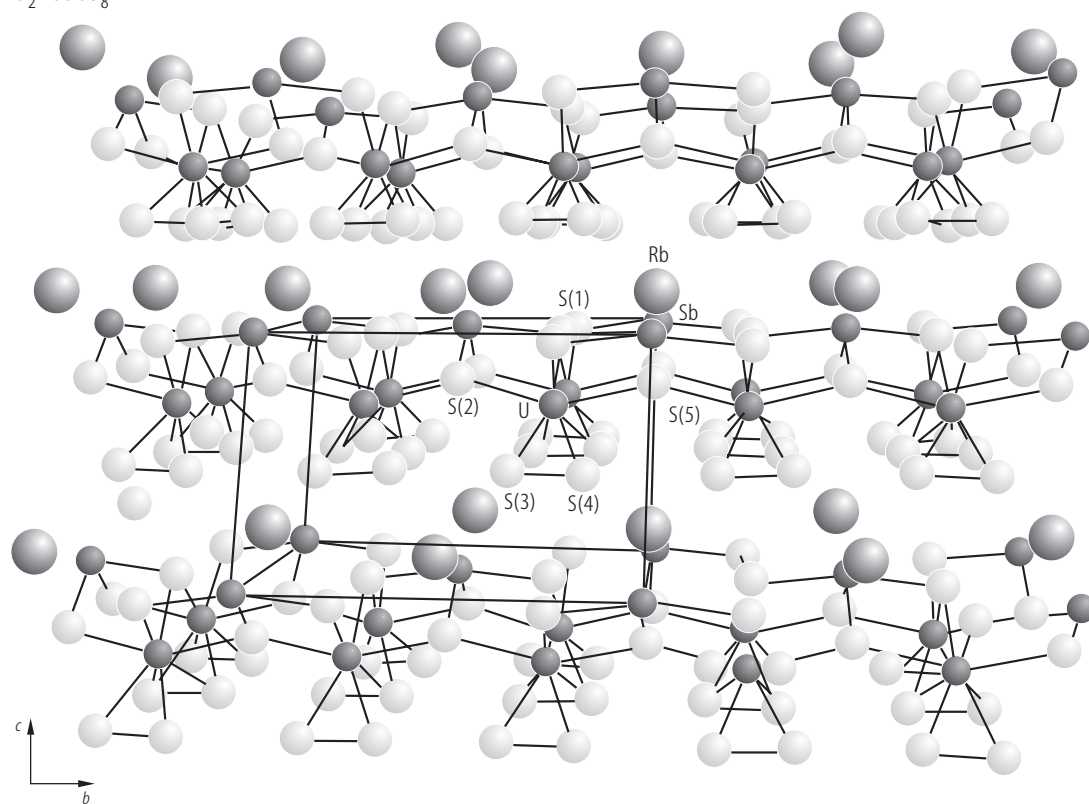


**Fig. 219.**  $\text{U}_2\text{RbSbS}_8$ . Crystal structure viewed down the  $a$ -axis [99CK]. The compound has a two-dimensional character with atom layers stacked perpendicular to the  $c$ -axis.

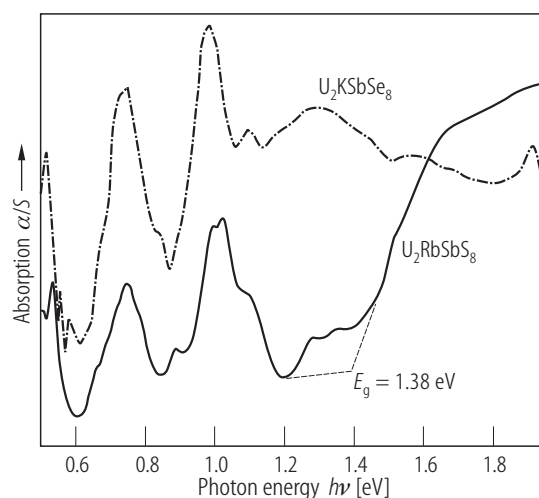


**Fig. 220.**  $\text{U}_2\text{RbSbS}_8$ ,  $\text{U}_2\text{KSbSe}_8$ . Optical absorption spectra [99CK]. For  $\text{U}_2\text{RbSbS}_8$  an abrupt gap is observed at 1.38 eV (emphasized by dashed lines) indicative of semiconducting properties. The intense bands at 0.52, 0.75 and 1.02 eV are assigned to f-f transitions. In the case of  $\text{U}_2\text{KSbSe}_8$  the optical gap occurs at about 0.6 eV but is poorly dissolved because of overlap with f-f transitions.

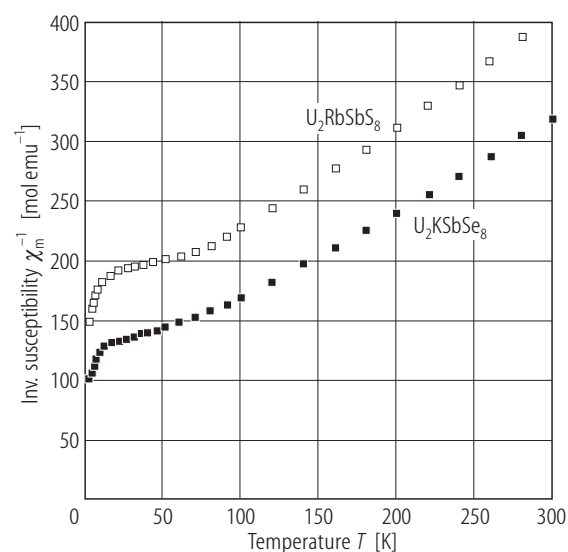


**Fig. 222.**  $\text{U}_2\text{RbSbS}_8$ ,  $\text{U}_2\text{KSbSe}_8$ . Reciprocal molar magnetic susceptibility,  $\chi_m^{-1}$ , vs. temperature,  $T$ , in the range 2...300 K [99CK]. Open squares:  $\text{U}_2\text{RbSbS}_8$ ; filled squares:  $\text{U}_2\text{KSbSe}_8$ . Above 90 K the susceptibility follows a Curie-Weiss law with the parameters given in Table B.

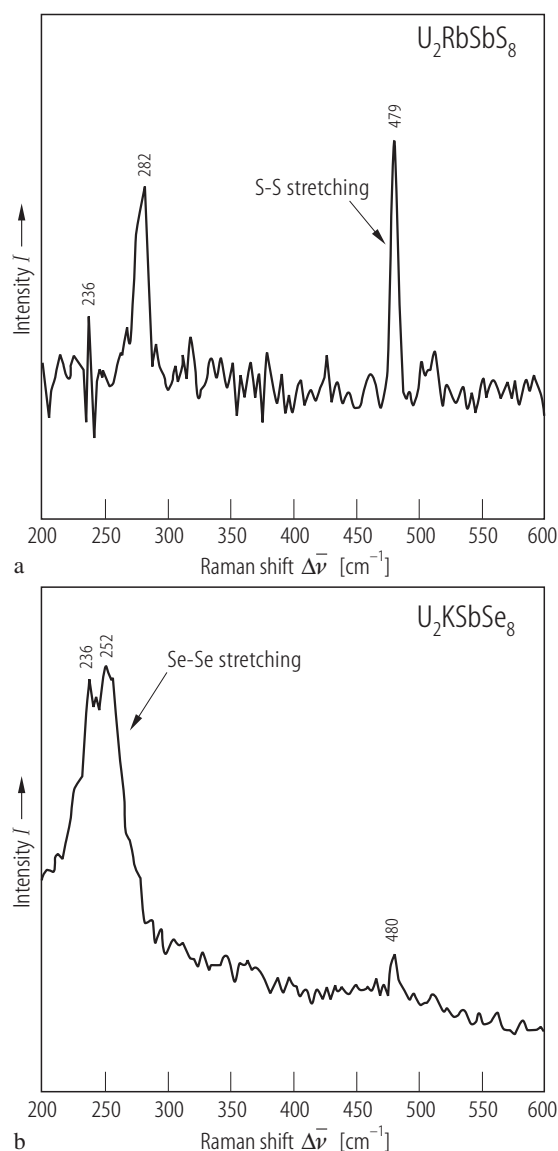


**Fig. 221.**  $\text{U}_2\text{RbSbS}_8$ ,  $\text{U}_2\text{KSbSe}_8$ . Raman spectra taken on single crystals [99CK]. (a)  $\text{U}_2\text{RbSbS}_8$  (b)  $\text{U}_2\text{KSbSe}_8$ . The shifts at 479  $\text{cm}^{-1}$  for  $\text{U}_2\text{RbSbS}_8$  and at 252  $\text{cm}^{-1}$  for  $\text{U}_2\text{KSbSe}_8$  are due to stretching vibration of dichalcogenide groups. The shift at 480 for  $\text{U}_2\text{KSbSe}_8$  is an overtone.

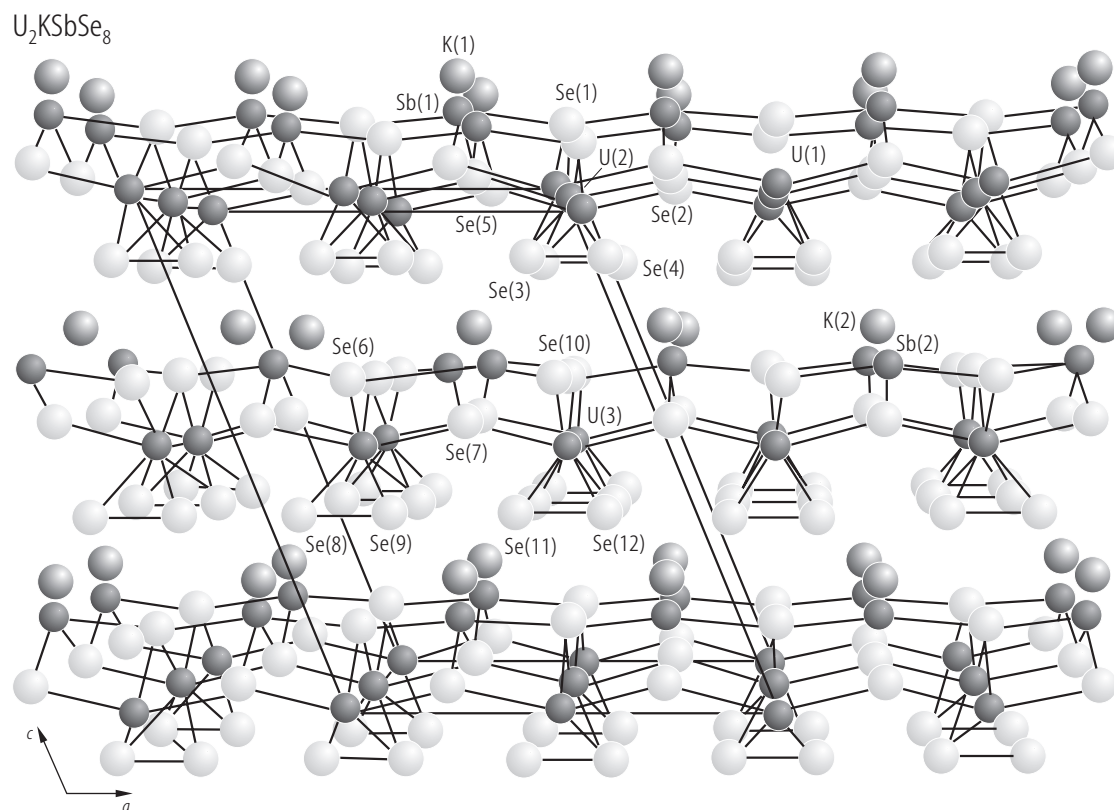


**Fig. 223.**  $\text{U}_2\text{KSbSe}_8$ . Crystal structure viewed down the  $b$ -axis [99CK]. The compound has a similar structure to that of  $\text{U}_2\text{RbSbSe}_8$  (compare Fig. 219) with the main difference that the  $\text{Sb}^{3+}$  and  $\text{K}^+$  ions are disordered in every other layer, resulting in a different unit cell.

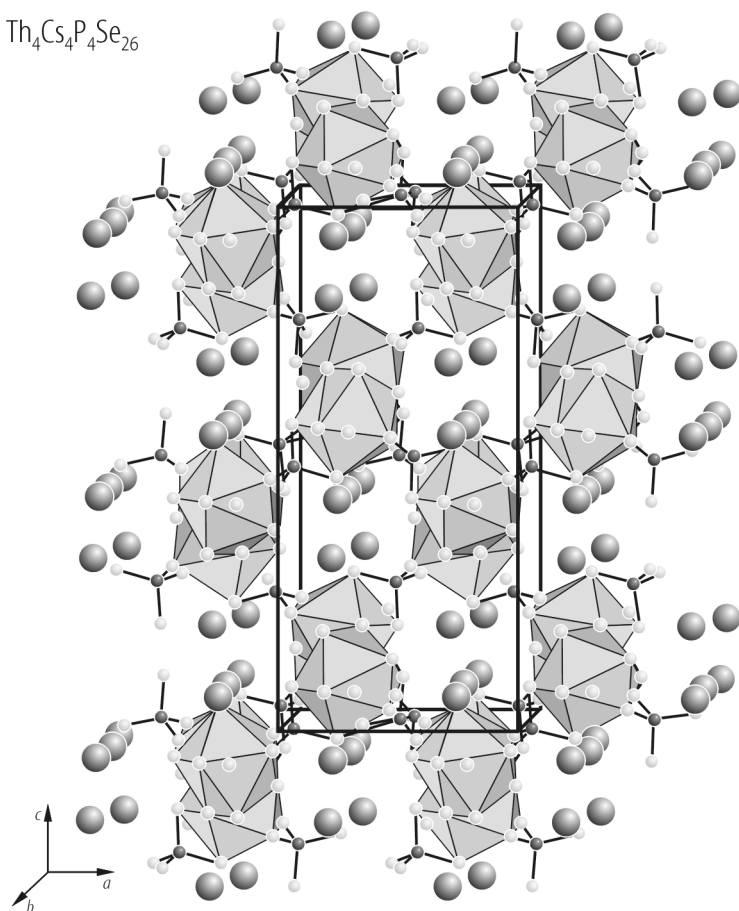


**Fig. 224.**  $\text{Th}_4\text{Cs}_4\text{P}_4\text{Se}_{26}$ . Crystal structure viewed down the  $[010]$  direction [01BASD]. Small light gray circles: Se; small dark gray circles: P; large circles: Cs. Emphasized are dimeric  $[\text{Th}_2\text{Se}_{13}]$  polyhedra.

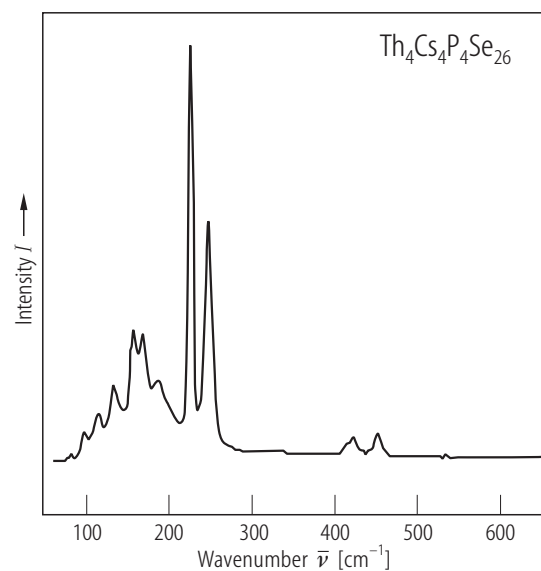


**Fig. 225.**  $\text{Th}_4\text{Cs}_4\text{P}_4\text{Se}_{26}$ . Raman spectrum [01BASD]. Four Raman active stretching modes are observed:  $\bar{\nu}_2(\text{E})$  with structures at 102 and 118  $\text{cm}^{-1}$ ,  $\bar{\nu}_4(\text{T}_2)$  with structures at 134, 162, 174 and 191  $\text{cm}^{-1}$ ,  $\bar{\nu}_1(\text{A}_1)$  with a very strong structure at 228  $\text{cm}^{-1}$ , and  $\bar{\nu}_3(\text{T}_2)$  with structures at 423 and 452  $\text{cm}^{-1}$ . The broad peak at 252  $\text{cm}^{-1}$  was assigned to Se-Se stretching.



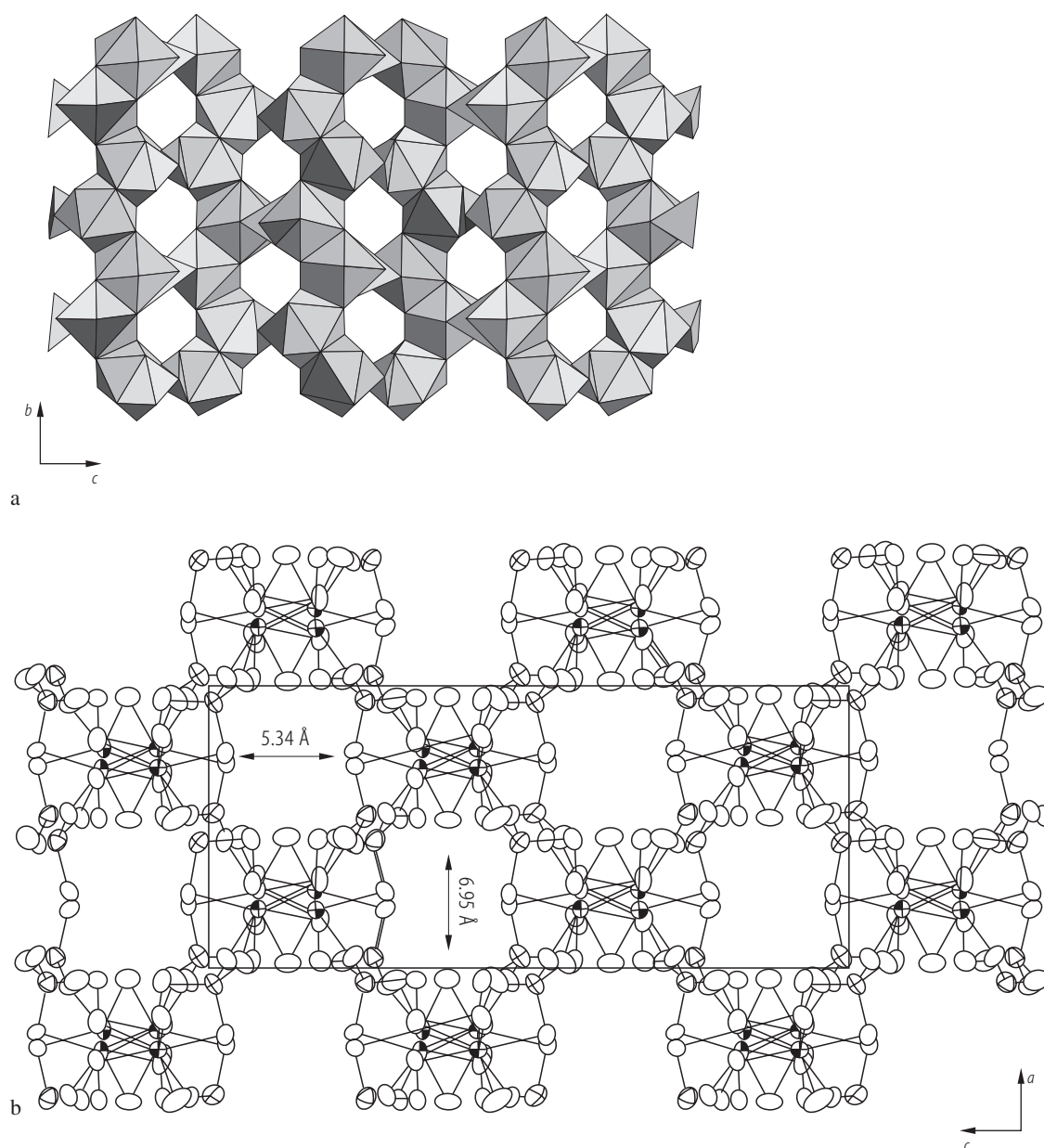
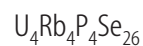


**Fig. 226.**  $\text{U}_4\text{Rb}_4\text{P}_4\text{Se}_{26}$ . **(a)** Crystal structure in a polyhedral representation down the  $[100]$  direction [97CK]. For clarity Rb atoms are omitted. Emphasized are intersecting narrow tunnels, which are accessible to Rb cations via

ion exchange. **(b)** Schematic representation of the tunnel framework in the  $(010)$  plane [97CK]. Note from both panels that the interconnected channels, filled by Rb ions, run in both the  $[100]$  and  $[010]$  directions.



**Table A.** Crystallographic data for actinide pnictides and chalcogenides containing s- and p-electron elements.

Compound	Sym- metry	Point group (structure type)	Lattice parameters				Ref.
			<i>a</i> [pm]	<i>b</i> [pm]	<i>c</i> [pm]	$\alpha, \beta, \gamma$	
<b>AnNY</b>							
UNSe	tetr.	P4/nmm (PbFCl)	384(1)		694(1)		<a href="#">86ABBG</a>
UNTe	tetr.	P4/nmm (PbFCl)	392.9(2) 391.6(1)		761.7(3) 748.5(1)		<a href="#">75TD</a> <a href="#">86ABBG</a>
<b>AnNZ</b>							
ThNCl	tetr.	P4/nmm (PbFCl)	409.7		689.5		<a href="#">74F</a>
ThNBr	tetr.	P4/nmm (PbFCl)	411.0		746.8		<a href="#">74F</a>
ThNI	tetr.	P4/nmm (PbFCl)	410.7		924.2		<a href="#">74F</a>
UNCl	tetr.	P4/nmm (PbFCl)	397.9		681.1		<a href="#">87B</a>
UNBr	tetr.	P4/nmm (PbFCl)	394		795		<a href="#">87B</a>
UNI	tetr.	P4/nmm (PbFCl)	399		920		<a href="#">87B</a>
<b>AnOY</b>							
ThOS	tetr.	P4/nmm (PbFCl)	395.5 396.3		673.3 674.6		<a href="#">67AD</a> <a href="#">74F</a>
ThOSe	tetr.	P4/nmm (PbFCl)	403 403.8		700.5 703		<a href="#">67AD</a> <a href="#">74F</a>
ThOTe	tetr.	P4/nmm (PbFCl)	411.2(5) 411.8		954.4(5) 754.9		<a href="#">54DS</a> <a href="#">74F</a>
PaOS	tetr.	P4/nmm (PbFCl)	383.2(1)		670.4(4)		<a href="#">54SFEZ</a> , <a href="#">67AD</a>
UOS	cub.	fcc (CaF <sub>2</sub> )	606(3)				<a href="#">70PA</a>
	tetr.	P4/nmm (PbFCl)	383.5 384.3 384.5(1) 384.36(2)		665.8 669.4 668.5(2) 669.38(6)		<a href="#">58PF</a> <a href="#">67AD</a> , <a href="#">74F</a> <a href="#">86LCB</a> <a href="#">98SMWY</a>
UOSe	tetr.	P4/nmm (PbFCl)	390.1 390.8 390.8 390.35(5) 390.8 390.38(5)		697.9 698.4 699.6 697.89(5) 699.6 698.05(9)		<a href="#">54F</a> <a href="#">57K</a> <a href="#">67AD</a> <a href="#">68MSTL</a> <a href="#">74F</a> <a href="#">93KPGZ</a>
UOTe	tetr.	P4/nmm (PbFCl)	401.2(3) 400.4 401.41(3)		750.1(3) 749.1 749.40(8)		<a href="#">61TNS</a> <a href="#">64KJ</a> <a href="#">71BBW</a>

Compound	Symmetry	Point group (structure type)	Lattice parameters				Ref.
			<i>a</i> [pm]	<i>b</i> [pm]	<i>c</i> [pm]	$\alpha, \beta, \gamma$	
NpOS	tetr.	P4/nmm (PbFCl)	382.5(2)		665.4(10)		<a href="#">49Z2</a>
			382.5		669.4		<a href="#">67AD</a>
			380.8(2)		662.7(4)		<a href="#">85TJP1</a>
			382(1)		665(1)		<a href="#">86CBBB</a>
			382.0(1)		665.2(2)		<a href="#">86LCB</a> , <a href="#">89ABBB</a>
NpOSe	tetr.	P4/nmm (PbFCl)	386.9(1)		691.1(3)		<a href="#">85TJP1</a>
PuOS	tetr.	P4/nmm (PbFCl)	388.2(1)		693.1(2)		<a href="#">89ABBB</a>
U <sub>0.5</sub> Pu <sub>0.5</sub> OS	tetr.	P4/nmm (PbFCl)	380(1)		659(1)		<a href="#">67M1</a>
PuOSe	tetr.	P4/nmm (PbFCl)	382.5(5)		663(1)		<a href="#">69M</a>
PuOSe	tetr.	P4/nmm (PbFCl)	415.1(3)		836.9(5)		<a href="#">57G</a>
<b>AnXX'</b> UP <sub>1.8</sub> As <sub>0.2</sub>	tetr.	P4/nmm (ZrSiS)	380.2(1)		779.8(2)		<a href="#">98HCPF</a>
UAsSb	tetr.	P4/nmm (Cu <sub>2</sub> Sb)	415.2(2)		846.3(4)		<a href="#">77TD</a>
<b>AnYY'</b> USSe	orth.	Pnma (PbCl <sub>2</sub> )	732	418	864		<a href="#">71PCS</a>
			733.63	417.42	860.12		<a href="#">77ZSM</a>
			732.8	416.7	859.6		<a href="#">94TKSP</a>
USTe			754	432	889		<a href="#">71PCS</a>
			763	428	885		<a href="#">75ES</a>
	orth.	Pnma (PbCl <sub>2</sub> )	766(1)	427(1)	884(1)		<a href="#">73RN</a>
			754.3	429.5	889.7		<a href="#">77ZSM</a>
			763.7	428.6	885.2		<a href="#">94TKSP</a>
US <sub>0.75</sub> Te <sub>1.25</sub>			760	428	880		<a href="#">75KG</a>
USETe	orth.	Pnma (PbCl <sub>2</sub> )	758	430	902		<a href="#">74ES</a>
			777.0	440.9	907.9		<a href="#">77ZSM</a>
			772.1	430.0	910.2		<a href="#">94TKSP</a>
<b>AnXY</b> ThPS	tetr.	P4/nmm (ZrSiS)	398.3		818.4		<a href="#">68H</a>
ThPSe	tetr.	P4/nmm (ZrSiS)	407.4		826.6		<a href="#">68H</a>
ThAsS	tetr.	P4/nmm (ZrSiS)	401.2		846.4		<a href="#">68H</a>
ThAs <sub>1.23</sub> S <sub>0.77</sub>	tetr.	P4/nmm (ZrSiS)	402.25(10)		848.3(1)		<a href="#">01HPWK</a>
ThAsSe	tetr.	P4/nmm (ZrSiS)	408.1		856.2		<a href="#">68H</a>
			408.40(10)		857.8(1)		<a href="#">01HPWK</a>

Compound	Symmetry	Point group (structure type)	Lattice parameters				Ref.
			<i>a</i> [pm]	<i>b</i> [pm]	<i>c</i> [pm]	$\alpha, \beta, \gamma$	
ThAsTe	tetr.	P4/nmm (ZrSiS)	426.0		881.2		<a href="#">68H</a>
ThSbSe	tetr.	P4/nmm (ZrSiS)	427.3		890.1		<a href="#">68H</a>
ThSbTe	tetr.	P4/nmm (ZrSiS)	436.8		914.7		<a href="#">68H</a>
ThBiTe	tetr.	P4/nmm (ZrSiS)	436.8(1)		913.1(2)		<a href="#">77CDW</a>
			446.8		917.4		<a href="#">68H</a>
UPS	tetr.	P4/nmm (ZrSiS)	381.3		798.1		<a href="#">68H</a>
			380.64(5)		798.1(2)		<a href="#">94KNPZ</a>
UPSe	tetr.	P4/nmm (ZrSiS)	396.1		817.8		<a href="#">68H</a>
			395.1(6)		818.5(8)		<a href="#">74ZLPL</a>
UPTe	tetr.	I4/mmm (UGeTe)	410.0		1702.6		<a href="#">73ZC</a>
UAsS	tetr.	P4/nmm (ZrSiS)	387.4		815.8		<a href="#">68H</a>
			388.4		817.6		<a href="#">72ZD</a>
			388.4(5)		817.6(6)		<a href="#">74ZLPL</a>
			387.8(2)		816.4(2)		<a href="#">75PL</a>
			387.6(2)		816(2)		<a href="#">90GSBD</a>
			386.00(1)		812.8(2)		<a href="#">98HCPF</a>
UAs <sub>1.5</sub> Se <sub>0.5</sub>	tetr.	P4/nmm (ZrSiS)	397.2		828.4		<a href="#">73LMZL</a>
UAs <sub>1.4</sub> Se <sub>0.6</sub>	tetr.	P4/nmm (ZrSiS)	397.5		832.5		<a href="#">73LMZL</a>
UAs <sub>1.35</sub> Se <sub>0.65</sub>	tetr.	P4/nmm (ZrSiS)	397.4		839.6		<a href="#">73LMZL</a>
UAs <sub>1.25</sub> Se <sub>0.75</sub>	tetr.	P4/nmm (ZrSiS)	397.9		839.0		<a href="#">73LMZL</a>
UAsSe	tetr.	P4/nmm (ZrSiS)	398.6		838.4		<a href="#">68H</a>
			396.2		842.2		<a href="#">72ZD</a>
			398.5(2)		839.8(5)		<a href="#">72LZ</a>
			398.5(2)		838.7(2)		<a href="#">90GSBD</a>
			398.70(1)		838.1(2)		<a href="#">98HCPF</a>
			398.1(2)		837.1(2)		<a href="#">75PL</a>
UAsTe	tetr.	P4/nmm (ZrSiS)	416.7		876.4		<a href="#">68H</a>
		I4/mmm (UGeTe)	414.83		1725.38		<a href="#">72ZD</a>
			415.0(2)		1727.0(2)		<a href="#">75PL</a>
USbS	tetr.	P4/nmm (ZrSiS)	393.7		853.0		<a href="#">68H</a>
			394(1)		852(1)		<a href="#">69KJ</a>
USbSe	tetr.	P4/nmm (ZrSiS)	411.6		867.8		<a href="#">68H</a>
			417.3(5)		868.1(7)		<a href="#">72LZ</a>
			411.6(3)		867.8(5)		<a href="#">69KJ</a>
USbTe	tetr.	P4/nmm (ZrSiS)	432.1		906.3		<a href="#">68H</a>
			431.85(2)		905.70(5)		<a href="#">69KJ</a>
UBiTe	tetr.	P4/nmm (ZrSiS)	443.4		915.7		<a href="#">68H</a>

Compound	Symmetry	Point group (structure type)	Lattice parameters				Ref.
			<i>a</i> [pm]	<i>b</i> [pm]	<i>c</i> [pm]	$\alpha, \beta, \gamma$	
NpPS	tetr.	P4/nmm (ZrSiS)	380.7		803.8		<a href="#">87B</a>
NpPSe	tetr.	P4/nmm (ZrSiS)	394.5		836.6		<a href="#">87B</a>
NpPTe	tetr.	P4/nmm (ZrSiS)	426.5		906.7		<a href="#">87B</a>
NpAsS	tetr.	P4/nmm (ZrSiS)	388.1		835.5		<a href="#">85W</a>
NpAsSe	tetr.	P4/nmm (ZrSiS)	397.2		857.1		<a href="#">85W</a>
NpAsTe	tetr.	P4/nmm (ZrSiS)	414.0		890.9		<a href="#">85W</a>
NpSbSe	tetr.	P4/nmm (ZrSiS)	416.9		886.9		<a href="#">87B</a>
NpSbTe	tetr.	P4/nmm (ZrSiS)	433.0(3)		918.5(7)		<a href="#">77CDW</a> , <a href="#">77CWD</a>
NpBiTe	tetr.	P4/nmm (ZrSiS)	441.3		924.9		<a href="#">87B</a>
PuPSe	tetr.	P4/nmm (ZrSiS)	406.8		841.5		<a href="#">87B</a>
PuPTe	tetr.	P4/nmm (ZrSiS)	428.9		909.8		<a href="#">87B</a>
PuAsS	tetr.	P4/nmm (ZrSiS)	388.9		850.8		<a href="#">87B</a>
PuSbSe	tetr.	P4/nmm (ZrSiS)	416.1		883.4		<a href="#">87B</a>
PuSbTe	tetr.	P4/nmm (ZrSiS)	432.8(4)		919.1(8)		<a href="#">77CDW</a>
PuBiTe	tetr.	P4/nmm (ZrSiS)	440.3		928.8		<a href="#">87B</a>
AmPTe	tetr.	P4/nmm (ZrSiS)	426.9		905.0		<a href="#">86DDT</a>
AmAsTe	tetr.	P4/nmm (ZrSiS)	423.8		908.7		<a href="#">86DDT</a>
AmSbTe	tetr.	P4/nmm (ZrSiS)	432.6(5)		917(1)		<a href="#">77CDW</a>
<b>AnMY</b>							
USiS	tetr.	P4/nmm (ZrSiS)	376.7(1)		828.5(2)		<a href="#">69KJ</a>
USiSe	tetr.	I4/mmm (UGeTe)	390(1)		1677(3)		<a href="#">69KJ</a>
UGeS	tetr.	P4/nmm (ZrSiS)	381.12(1)		830.54(5)		<a href="#">69KJ</a>
UGeSe	tetr.	I4/mmm (UGeTe)	382.0		832.3		<a href="#">77Z</a>
			382.0(2)		832(1)		<a href="#">78PLZ</a>
			393.23(2)		1696.9(1)		<a href="#">69KJ</a>
			393.3		1696.6		<a href="#">77Z</a>
			393.2(1)		1696.6(6)		<a href="#">78PLZ</a>

Compound	Sym- metry	Point group (structure type)	Lattice parameters				Ref.
			<i>a</i> [pm]	<i>b</i> [pm]	<i>c</i> [pm]	$\alpha, \beta, \gamma$	
UGeTe	tetr.	I4/mmm (UGeTe)	410.58(1) 411.0 411.0(1)		1760.14(5) 1759.9 1759.9(9)		<a href="#">69KJ</a> <a href="#">77Z</a> <a href="#">78PLZ</a>
USnTe	tetr.	P4/nmm (ZrSiS)	425.96(3)		913.13(4)		<a href="#">69KJ</a>
<b>An<sub>2</sub>N<sub>2</sub>O</b> Th <sub>2</sub> N <sub>2</sub> O	hex.	P $\bar{3}$ m1 (Ce <sub>2</sub> O <sub>2</sub> S)	388.3 388.3(1)		619.7 618.7(2)		<a href="#">67AD</a> <a href="#">67B</a>
<b>An<sub>2</sub>(N,O)<sub>2</sub>X</b> Th <sub>2</sub> (N,O) <sub>2</sub> P	hex.	P $\bar{3}$ m1 (Ce <sub>2</sub> O <sub>2</sub> S)	402.85(3)		683.5(1)		<a href="#">69BZ</a>
Th <sub>2</sub> (N,O) <sub>2</sub> As	hex.	P $\bar{3}$ m1 (Ce <sub>2</sub> O <sub>2</sub> S)	404.1(1)		697.9(2)		<a href="#">69BZ</a>
Th <sub>2</sub> N <sub>2</sub> Sb	tetr.	I4/mmm (La <sub>2</sub> O <sub>2</sub> Te)	404.9(1)		1357(1)		<a href="#">70BZ</a>
Th <sub>2</sub> (N <sub>0.75</sub> O <sub>0.25</sub> ) <sub>2</sub> Sb	tetr.	I4/mmm (La <sub>2</sub> O <sub>2</sub> Te)	404.5(3)		1318(4)		<a href="#">70BZ</a>
Th <sub>2</sub> (N <sub>0.5</sub> O <sub>0.5</sub> ) <sub>2</sub> Sb	tetr.	I4/mmm (La <sub>2</sub> O <sub>2</sub> Te)	404.1(1)		1284(1)		<a href="#">70BZ</a>
Th <sub>2</sub> N <sub>2</sub> Bi	tetr.	I4/mmm (La <sub>2</sub> O <sub>2</sub> Te)	407.5(1)		1362(1)		<a href="#">70BZ</a>
Th <sub>2</sub> (N,O) <sub>2</sub> Bi	tetr.	I4/mmm (La <sub>2</sub> O <sub>2</sub> Te)	407.4(2)		1353(3)		<a href="#">70BZ</a>
U <sub>2</sub> N <sub>2</sub> P	hex.	P $\bar{3}$ m1 (Ce <sub>2</sub> O <sub>2</sub> S)	380.3 380.2(1) 380.5(1)		655.6 655.2(2) 659.6(3)		<a href="#">67AD</a> <a href="#">69BZ</a> <a href="#">75LZLT</a>
U <sub>2</sub> N <sub>2</sub> As	hex.	P $\bar{3}$ m1 (Ce <sub>2</sub> O <sub>2</sub> S)	383.3(1) 383.0(1)		673.7(1) 673.9(2)		<a href="#">69BZ</a> <a href="#">75LZLT</a>
U <sub>2</sub> N <sub>2</sub> Sb	tetr.	I4/mmm (La <sub>2</sub> O <sub>2</sub> Te)	389.37(2) 389.25(6)		1233.71(7) 1231.91(28)		<a href="#">70BZ</a> <a href="#">78ZT</a>
U <sub>2</sub> N <sub>2</sub> Bi	tetr.	I4/mmm (La <sub>2</sub> O <sub>2</sub> Te)	392.92(5) 395(1)		1254.8(2) 1265(4)		<a href="#">70BZ</a> <a href="#">78ZT</a>
Pu <sub>2</sub> (N,O) <sub>2</sub> Sb	tetr.	I4/mmm (La <sub>2</sub> O <sub>2</sub> Te)	391.5		1320.6		<a href="#">87B</a>
Am <sub>2</sub> O <sub>2</sub> Bi	tetr.	I4/mmm (La <sub>2</sub> O <sub>2</sub> Te)	395.0		1343.4		<a href="#">87B</a>
Cm <sub>2</sub> O <sub>2</sub> Sb	tetr.	I4/mmm (La <sub>2</sub> O <sub>2</sub> Te)	392.0		1341		<a href="#">87B</a>
Cm <sub>2</sub> O <sub>2</sub> Bi	tetr.	I4/mmm (La <sub>2</sub> O <sub>2</sub> Te)	395.7		1335.9		<a href="#">87B</a>
<b>An<sub>2</sub>N<sub>2</sub>Y</b> Th <sub>2</sub> N <sub>2</sub> S	hex.	P $\bar{3}$ m1 (Ce <sub>2</sub> O <sub>2</sub> S)	400.8(1)		692.0(2)		<a href="#">69BZ</a>

Compound	Symmetry	Point group (structure type)	Lattice parameters				Ref.
			<i>a</i> [pm]	<i>b</i> [pm]	<i>c</i> [pm]	$\alpha, \beta, \gamma$	
Th <sub>2</sub> N <sub>2</sub> Se	hex.	P $\bar{3}$ m1 (Ce <sub>2</sub> O <sub>2</sub> S)	402.87(2)		715.6(1)		<a href="#">69BZ</a>
Th <sub>2</sub> N <sub>2</sub> Te	tetr.	I4/mmm (La <sub>2</sub> O <sub>2</sub> Te)	409.39(4)		1301.4(1)		<a href="#">70BZ</a>
U <sub>2</sub> N <sub>2</sub> S	hex.	P $\bar{3}$ m1 (Ce <sub>2</sub> O <sub>2</sub> S)	382.6 382.8(1) 381.8(2)		658.7 658.7(2) 661.0(2)		<a href="#">67AD</a> <a href="#">69BZ</a> <a href="#">75LZLT</a>
U <sub>2</sub> N <sub>2</sub> Se	hex.	P $\bar{3}$ m1 (Ce <sub>2</sub> O <sub>2</sub> S)	386.22(5) 386.3(1)		685.6(1) 686.7(2)		<a href="#">69BZ</a> <a href="#">75LZLT</a>
U <sub>2</sub> N <sub>2</sub> Te	tetr.	I4/mmm (La <sub>2</sub> O <sub>2</sub> Te)	396.31(2) 396.3 396.7(2) 397.7(2)		1256.1(2) 1256.1 1258(1) 1258.1(10)		<a href="#">70BZ</a> <a href="#">75TD</a> <a href="#">77LZT</a> <a href="#">78ZT</a>
<b>An<sub>2</sub>O<sub>2</sub>Y</b>							
U <sub>2</sub> O <sub>2</sub> Te	tetr.	I4/mmm (La <sub>2</sub> O <sub>2</sub> Te)	396.40(2)		1256.4(4)		<a href="#">71BB</a> , <a href="#">71BBW</a>
Np <sub>2</sub> O <sub>2</sub> S	hex.	P $\bar{3}$ m1 (Ce <sub>2</sub> O <sub>2</sub> S)	395(1)		680(1)		<a href="#">67M2</a>
Np <sub>2</sub> O <sub>2</sub> Se	hex.	P $\bar{3}$ m1 (Ce <sub>2</sub> O <sub>2</sub> S)	397.0		695		<a href="#">86DDT</a>
Np <sub>2</sub> O <sub>2</sub> Te	tetr.	I4/mmm (La <sub>2</sub> O <sub>2</sub> Te)	400.3		1273		<a href="#">85TJP2</a>
Pu <sub>2</sub> O <sub>2</sub> S	hex.	P $\bar{3}$ m1 (Ce <sub>2</sub> O <sub>2</sub> S)	392.7(3) 391.9 392.5(1) 392.9(1)		677.0(1) 675.5 676.8(2) 680.4(2)		<a href="#">49Z1</a> <a href="#">67AD</a> <a href="#">69M</a> <a href="#">83CDDDB1</a>
Pu <sub>2</sub> O <sub>2</sub> Se	hex.	P $\bar{3}$ m1 (Ce <sub>2</sub> O <sub>2</sub> S)	395.7 396.2(1)		697.7 698.6(1)		<a href="#">67AJ, 70ADJ</a> <a href="#">83CDDDB1</a>
Pu <sub>2</sub> O <sub>2</sub> Te	tetr.	I4/mmm (La <sub>2</sub> O <sub>2</sub> Te)	403 400.8(1)		1266 1265(2)		<a href="#">67AJ</a> <a href="#">83CDDDB2</a>
Am <sub>2</sub> O <sub>2</sub> S	trig.	P $\bar{3}$ m	391.0(3)		677.2(6)		<a href="#">77HF</a>
Am <sub>2</sub> O <sub>2</sub> Te	tetr.	I4/mmm (La <sub>2</sub> O <sub>2</sub> Te)	399.4		1272		<a href="#">86DDT</a>
Cm <sub>2</sub> O <sub>2</sub> S	trig.	P $\bar{3}$ m	392(3) 388.9(2)		677(6) 673.6(3)		<a href="#">75DCM</a> <a href="#">77HF</a>
Cm <sub>2</sub> O <sub>2</sub> Te	tetr.	I4/mmm (La <sub>2</sub> O <sub>2</sub> Te)	398		1258		<a href="#">86DDT</a>
Bk <sub>2</sub> O <sub>2</sub> S	trig.	P $\bar{3}$ m	386.1(1)		668.6(1)		<a href="#">77HF</a>
Cf <sub>2</sub> O <sub>2</sub> S	trig.	P $\bar{3}$ m	384.4(2)		665.6(4)		<a href="#">74BFH</a>
<b>An<sub>2</sub>BY<sub>5</sub>, An<sub>2</sub>MY<sub>5</sub></b>							
Th <sub>2</sub> SrSe <sub>5</sub>	mon.	P2 <sub>1</sub> /c	870.4(2)	786.1(2)	1245.8(4)	$\beta = 90.00(2)^\circ$	<a href="#">98NI</a>
U <sub>2</sub> PbS <sub>5</sub>	orth.	P2 <sub>1</sub> 22 <sub>1</sub>	744(1)	827(1)	1175(2)		<a href="#">72BPP</a>
U <sub>2</sub> CaS <sub>5</sub>	orth.	P2 <sub>1</sub> 22 <sub>1</sub>	741(2)	810(2)	1172(2)		<a href="#">70BPP</a>
U <sub>2</sub> SrS <sub>5</sub>	orth.	P2 <sub>1</sub> 22 <sub>1</sub>	746(2)	828(2)	1176(2)		<a href="#">70BPP</a>

Compound	Sym- metry	Point group (structure type)	Lattice parameters				Ref.
			<i>a</i> [pm]	<i>b</i> [pm]	<i>c</i> [pm]	$\alpha, \beta, \gamma$	
U <sub>2</sub> BaS <sub>5</sub>	orth.	P2 <sub>1</sub> 22 <sub>1</sub>	753(2)	849(2)	1182(2)	$\beta = 90^\circ$	<a href="#">70BPP</a>
U <sub>2</sub> PbSe <sub>5</sub>	orth.	P2 <sub>1</sub> 22 <sub>1</sub>	779(1)	861.0(5)	1227(2)		<a href="#">72BPP</a>
	mon.	P2 <sub>1</sub> /c	860.5(5)	778.8(5)	1227(1)		<a href="#">75BPB</a>
U <sub>2</sub> CaSe <sub>5</sub>	orth.	P2 <sub>1</sub> 22 <sub>1</sub>	775(1)	843.5(5)	1226(2)		<a href="#">72BPP</a>
U <sub>2</sub> SrSe <sub>5</sub>	orth.	P2 <sub>1</sub> 22 <sub>1</sub>	779(1)	860.0(5)	1227(2)		<a href="#">72BPP</a>
U <sub>2</sub> BaSe <sub>5</sub>	orth.	P2 <sub>1</sub> 22 <sub>1</sub>	786(1)	880.5(5)	1233(2)		<a href="#">72BPP</a>
<b>An<sub>2</sub>AY<sub>6</sub></b>							
Th <sub>2</sub> KSe <sub>6</sub>	orth.	Cmcm	414(2)	2188(4)	564(1)		<a href="#">97WPI</a>
		Immm	418.99(5)	563.37(5)	2186.0(4)		<a href="#">98CPBW</a>
Th <sub>2</sub> RbSe <sub>6</sub>	orth.	Immm	420.31(1)	563.47(1)	2247.14(1)		<a href="#">98CPBW</a>
Th <sub>2</sub> CsSe <sub>6</sub>	orth.	Cmcm	414(5)	2388(4)	567(5)		<a href="#">97WPI</a>
Th <sub>2</sub> KTe <sub>6</sub>	orth.	Cmcm	435.6(1)	2370.2(7)	634.1(3)		<a href="#">97WPI</a>
Th <sub>2</sub> CsTe <sub>6</sub>	orth.	Cmcm	436.7(2)	2511.9(10)	614.0(3)		<a href="#">96CI</a>
<b>An<sub>2</sub>O<sub>2</sub>Y<sub>3</sub></b>							
Pu <sub>2</sub> O <sub>2</sub> S <sub>3</sub>	tetr.	P4/nmm (Fe <sub>2</sub> As)	395.5(1)		795.5(1)		<a href="#">69M</a>
Pu <sub>2</sub> O <sub>2</sub> Se <sub>3</sub>	tetr.	P4/nmm (Fe <sub>2</sub> As)	?		?		<a href="#">70ADJ</a>
<b>An<sub>4</sub>O<sub>4</sub>Y<sub>3</sub></b>							
U <sub>4</sub> O <sub>4</sub> Te <sub>3</sub>	tetr.	I4/mmm	401.0(2)		2754(2)	$\beta = 118^\circ$	<a href="#">95NPSK</a>
Np <sub>4</sub> O <sub>4</sub> S <sub>3</sub>	mon.	?	1828(1)	676(1)	389(1)		<a href="#">67M2</a>
Pu <sub>4</sub> O <sub>4</sub> S <sub>3</sub>	mon.	?	1626(1)	672.8	387.2		<a href="#">67M1</a>
U <sub>2</sub> Pu <sub>2</sub> O <sub>4</sub> S <sub>3</sub>	mon.	?	1631(1)	677(1)	392(1)		<a href="#">67M1</a>
<b>others</b>							
ThN <sub>2</sub> Li <sub>2</sub>	hex.	$\bar{p}3$	639.8		554.7		<a href="#">71PJ</a>
			638.8	553.6	<a href="#">74BA</a>		
UN <sub>2</sub> Li <sub>2</sub>	hex.	$\bar{p}3$	590.2		532.1		<a href="#">71PJ</a>
ThN <sub>2</sub> Be	hex.		1050.1		395.5		<a href="#">71PJ</a>
ThMgTe <sub>3</sub>	orth.	Cmcm	428.54(6)	1404.2(2)	994.50(14)		<a href="#">00NI</a>
UBaS <sub>3</sub>	orth.	Pnma	744	1038	724		<a href="#">70BPG</a>
			748.23(5)	1038.01(7)	721.48(5)		<a href="#">80LI</a>
UTl <sub>0.56</sub> Te <sub>3</sub>	orth.	Cmcm	421.2(2)	2328.7(7)	609.1(3)		<a href="#">97TDPN</a>
ULi <sub>2</sub> S <sub>3</sub> (disord.)	hex.	$\bar{R}3m$	389.8		1839.1		<a href="#">99MFSY1</a>
ULi <sub>2</sub> S <sub>3</sub> (ord.)	mon.	C2/m	674.7	1167.9	653.7	$\beta = 110.2^\circ$	<a href="#">99MFSY1</a>
UNa <sub>2</sub> S <sub>3</sub> (disord.)	hex.	$\bar{R}3m$	403.6		1978.0		<a href="#">99MFSY1</a>
UNa <sub>2</sub> S <sub>3</sub> (ord.)	mon.	C2/m	699.0	1210.5	699.2	$\beta = 109.5^\circ$	<a href="#">99MFSY1</a>
UK <sub>2</sub> Te <sub>3</sub>	mon.	C2/m	800.41(3)	1387.67(5)	851.63(4)	$\beta = 108.495(3)^\circ$	<a href="#">99SA</a>
						$\beta = 107.7(1)^\circ$	
UCs <sub>2</sub> Te <sub>3</sub>	mon.	C2/m	816(1)	1407(2)	884(1)		<a href="#">99SA</a>
UKS <sub>2</sub>	tetr.		383.5		665.8		<a href="#">66PLP</a>
UCsTe <sub>6</sub>	orth.	Pnma	3080.1(7)	814.3(2)	917.4(2)		<a href="#">95CI</a>
UK <sub>4</sub> Se <sub>8</sub>	orth.	Fdd2	1733.1(4)	2058.4(3)	881.1(3)		<a href="#">97SK</a>

Compound	Sym- metry	Point group (structure type)	Lattice parameters				Ref.
			<i>a</i> [pm]	<i>b</i> [pm]	<i>c</i> [pm]	$\alpha, \beta, \gamma$	
Th <sub>2</sub> NS <sub>2</sub>	hex.	P $\bar{3}$ m1 (Ce <sub>2</sub> O <sub>2</sub> S)	382.2		665		<a href="#">71K</a>
U <sub>2</sub> C <sub>2</sub> Te	tetr.		656.4(1)		1395.9(3)		<a href="#">71BBW</a>
U <sub>8</sub> MgSe <sub>17</sub>	mon.	C2/m	1402(1)	877.1(5)	1101.6(7)	$\beta = 101.57(6)^\circ$	<a href="#">74N</a>
ThKSb <sub>2</sub> Se <sub>6</sub>	mon.	P2 <sub>1</sub> /c	426.76(1)	1517.46(4)	1699.09(4)	$\beta = 92.217(1)^\circ$	<a href="#">97CICK</a>
URbSb <sub>0.33</sub> Te <sub>6</sub> substruct.	trig.	P3	909.25(14)		812.9(2)		<a href="#">01CK</a>
superstruct.	rhomb.	R3	1574.1(2)		2438.2(4)		
ThK <sub>2</sub> P <sub>3</sub> Se <sub>9</sub>	tricl.	P $\bar{1}$	1045.82(5)	1653.84(8)	1022.45(5)	$\alpha = 107.637(1)^\circ$ $\beta = 91.652(1)^\circ$ $\gamma = 90.343(1)^\circ$	<a href="#">00BASD</a>
ThRb <sub>2</sub> P <sub>3</sub> Se <sub>9</sub>	tricl.	P $\bar{1}$	1053.69(5)	1669.14(8)	1028.64(5)	$\alpha = 107.614(1)^\circ$ $\beta = 92.059(1)^\circ$ $\gamma = 90.409(1)^\circ$	<a href="#">00BASD</a>
Th <sub>2</sub> Cs <sub>4</sub> P <sub>5</sub> Se <sub>17</sub>	mon.	P2 <sub>1</sub> /c	1023.78(5)	3218.2(2)	1074.92(6)	$\beta = 95.832(1)^\circ$	<a href="#">00BASD</a>
U <sub>2</sub> RbSbS <sub>8</sub>	mon.	Cm	795.43(9)	1109.87(13)	727.94(10)	$\beta = 106.03(2)^\circ$	<a href="#">99CK</a>
U <sub>2</sub> KSbSe <sub>8</sub>	mon.	Cm	1157.63(2)	820.33(1)	1527.42(1)	$\beta = 112.22(2)^\circ$	<a href="#">99CK</a>
Th <sub>4</sub> Cs <sub>4</sub> P <sub>4</sub> Se <sub>26</sub>	orth.	Pbca	1201.30(6)	1457.47(7)	2713.4(1)		<a href="#">01BASD</a>
U <sub>4</sub> Rb <sub>4</sub> P <sub>4</sub> Se <sub>26</sub>	orth.	Pbca	1199.79(1)	1448.74(1)	2713.77(2)		<a href="#">97CK</a>

**Table B.** Magnetic data for actinide pnictides and chalcogenides containing s- and p-electron elements.

Compound	<i>T<sub>N</sub></i> ( <i>T<sub>C</sub></i> ) [K]	Type of fit	Curie-Weiss parameters				Ref.
			$\Theta$ [K]	$p_{\text{eff}}$ [ $\mu_B$ ]	$\chi_0$ [emu/mol]	Temperature range [K]	
UOS	55	CW	−51	2.77		160...300	<a href="#">63BBP</a>
		CW	−108	3.10		500...1100	<a href="#">63BBP</a>
		CW	−55	2.8		?	<a href="#">68BH</a>
UOSe	72	CW	−30	2.9		?	<a href="#">68BH</a>
	90	CW	−10	2.87		100...300	<a href="#">68MSTL</a>
			−120	3.30		300...1150	<a href="#">68MSTL</a>
UOTe	162	CW	−56	3.26		?	<a href="#">61TNS</a>
	157	CW	−60	2.9		?	<a href="#">68BH</a>
NpOS	5	CW	−15	2.04		20...60	<a href="#">86CBBB</a>
UPS			120	2.1			<a href="#">68H</a>
	(118)						<a href="#">94KNPZ</a>
sc <i>B</i> $\parallel$ <i>c</i>		CW	123	2.57		120...300	
<i>B</i> $\perp$ <i>c</i>		CW	−2703	5.74		150...300	
UPSe P4/nmm			90	2.4			<a href="#">68H</a>
I4/mmm (55)							<a href="#">95KNZ</a>
sc <i>B</i> $\parallel$ <i>c</i>		CW	59	3.17		70...300	
<i>B</i> $\perp$ <i>c</i>		CW	−477	3.56		150...300	



Compound	$T_N(T_C)$ [K]	Type of fit	Curie-Weiss parameters			Temperature range [K]	Ref.
			$\Theta$ [K]	$p_{\text{eff}}$ [ $\mu_B$ ]	$\chi_0$ [emu/mol]		
UPTe	(85)	CW	−70	3.16		300...1000	<a href="#">73ZC</a>
	(85)						<a href="#">95KNZ</a>
sc $B \parallel c$		CW	86	2.83		90...300	
$B \perp c$		CW	−25	2.84		120...300	
UAsS	—	CW	120	2.1		?	<a href="#">68H</a>
	(128)	CW	−380	3.34		550...900	<a href="#">72ZD</a>
UAsSe	—	CW	110	2.4		?	<a href="#">68H</a>
	(118)	CW	−195	3.41		600...950	<a href="#">72ZD</a>
UAsTe	—	CW	120	2.8		?	<a href="#">68H</a>
	(< 77)	CW	−95	3.34		250...800	<a href="#">72ZD</a>
USbSe		CW	115	2.6		?	<a href="#">68H</a>
	(127)	CW	?	2.34		130...300	<a href="#">72LZ</a>
	(128)						<a href="#">95KNZ</a>
sc $B \parallel c$		CW	134	3.08		140...300	
$B \perp c$		CW	−709	4.24		200...300	
USbTe			110	3.0			<a href="#">68H</a>
	(127)						<a href="#">95KNZ</a>
sc $B \parallel c$		CW	131	3.18		140...300	
$B \perp c$		CW	−122	3.42		150...300	
UBiTe			110				<a href="#">68H</a>
USSe		CW	25	2.92		100...300	<a href="#">71PCS</a>
	(25)	CW	−12	3.23		100...300	<a href="#">77ZSM</a>
	(24)	MCW	30	3.16	$470 \cdot 10^{-6}$	30...300	<a href="#">94TKSP</a>
USTe		CW	74	2.90		100...300	<a href="#">71PCS</a>
	(87)	CW	52	2.91		160...300	<a href="#">77ZSM</a>
	(85)	MCW	87	2.92	$1090 \cdot 10^{-6}$	90...300	<a href="#">94TKSP</a>
USETe	(83)	CW	60	2.94		140...300	<a href="#">77ZSM</a>
	(69)	MCW	72	3.04	$570 \cdot 10^{-6}$	70...300	<a href="#">94TKSP</a>
UGeS	88	CW	77	2.60		100...300	<a href="#">77Z</a>
UGeSe	40	CW	−20	3.03		100...300	<a href="#">77Z</a>
UGeTe	73	CW	27	2.84		180...300	<a href="#">77Z</a>
NpAsTe	(25)			2.68		250...300	<a href="#">84BCFC</a>
				2.35		25...50	<a href="#">84BCFC</a>
NpSbTe		CW	−25(1)	2.68			<a href="#">84BCFC</a>
PuAsSe	(126)	MCW	?	0.5	$500 \cdot 10^{-6}$	?	<a href="#">77BCSW</a>
PuAsTe	(125)	MCW	?	0.64	$400 \cdot 10^{-6}$	?	<a href="#">77BCSW</a>
Pu <sub>2</sub> O <sub>2</sub> S	28	CW	−300	1.58		100...300	<a href="#">83CDDDB1</a>
Pu <sub>2</sub> O <sub>2</sub> Se	34	CW	−320	1.58		100...300	<a href="#">83CDDDB1</a>
Pu <sub>2</sub> O <sub>2</sub> Te	56	CW	−380	1.65		120...300	<a href="#">83CDDDB2</a>
U <sub>4</sub> O <sub>4</sub> Te <sub>3</sub>	(80)	MCW	78	2.47	$970 \cdot 10^{-6}$	100...300	<a href="#">95KTSN</a>
U <sub>2</sub> N <sub>2</sub> Sb	(166)	CW	45	2.83		450...1000	<a href="#">74TZ</a>
U <sub>2</sub> N <sub>2</sub> Bi	(160)	CW	−150	3.00		550...1000	<a href="#">74TZ</a>
U <sub>2</sub> N <sub>2</sub> Te	(75)	CW	20	2.86		400...1000	<a href="#">74TZ</a>
UTl <sub>0.56</sub> Te <sub>3</sub>		CW	−75	3.27		110...300	<a href="#">97TDPN</a>
UKS <sub>2</sub>	(<86)	CW	−130(6)	3.40(2)		160...300	<a href="#">66PL</a>
U <sub>8</sub> MgSe <sub>17</sub>		CW	−65	3.2		60...300	<a href="#">79NT</a>

Compound	$T_N(T_C)$ [K]	Type of fit	Curie-Weiss parameters			Temperature range [K]	Ref.
			$\Theta$ [K]	$p_{\text{eff}}$ [ $\mu_B$ ]	$\chi_0$ [emu/mol]		
UKOS		CW	−242(13)	3.25(2)		90...300	<a href="#">66PL</a>
URbSb <sub>0.33</sub> Te <sub>6</sub>		CW	−6.3	3.04		20...300	<a href="#">01CK</a>
U <sub>2</sub> K <sub>2</sub> O <sub>2</sub> S <sub>3</sub>		CW	−16(1)	2.81(2)		90...300	<a href="#">66PL</a>
U <sub>2</sub> K <sub>2</sub> O <sub>2</sub> S <sub>5</sub>		CW	−20(1)	2.83(2)		90...300	<a href="#">66PL</a>
U <sub>2</sub> RbSbS <sub>8</sub>		CW	−160	3.03		80...300	<a href="#">99CK</a>
U <sub>2</sub> KSbSe <sub>8</sub>		CW	−83	3.21		80...300	<a href="#">99CK</a>
U <sub>4</sub> Rb <sub>4</sub> P <sub>4</sub> Se <sub>26</sub>		CW	−42.6	1.85		70...300	<a href="#">97CK</a>

**Table C.** Thermodynamic characteristics of thorium and uranium compounds AnNY (Y = Se, Te) [[86ABBG](#)].

Compound	$T_C$ [K]	$C_p$ (298.15 K) [J/mol K]	$S$ (298.15 K) [J/mol K]	$5 < T < 11$ K		high temperatures	
				$\gamma$ [mJ/mol K <sup>2</sup> ]	$\Theta_D$ [K]	$\gamma$ (300K) [mJ/mol K <sup>2</sup> ]	$\Theta_D(\infty)$ [K]
ThNSe	—	68.40	94.06	0	210		474
UNSe	—	87.37	112.62	60	195	60	474
ThNTe	—	67.18	96.97	0	180		426
UNTe	52(3)	75.84	108.49	22	209	22	380

**Table D.** Crystal field parameters  $B^q_k$  (in cm<sup>−1</sup>), energy levels  $\Gamma_u$  (in K) and wavefunction coefficient  $\alpha$  of the level  $\Gamma_{t5}^{(1)}$  ( $|\Gamma_{t5}^{(1)}\rangle = \alpha|\pm 3\rangle + \beta|\mp 1\rangle$ ) calculated for UNSe and UNTe in the framework of lattice sum (LS) and nearest neighbours (NN) point-charge models as well as from a layer model (FINV; see description in the original paper) [[86ABBG](#)]. Sternheimer shielding included.

	UNSe			UNTe		
	LS	NN	FINV	LS	NN	FINV
$B^0_2$	8.528	10.884	9.275	6.887	8.895	7.326
$B^0_4$	0.3651	0.4162	0.3808	0.3474	0.3880	0.3562
$B^0_6$	0.007698	0.007510	0.007559	0.006269	0.006092	0.006195
$B^4_4$	3.012	3.223	3.002	2.567	2.781	2.561
$B^4_6$	−0.09195	−0.08361	−0.09178	−0.07852	−0.07172	−0.07843
$\Gamma_{t4}$	0	0	0	0	0	0
$\Gamma_{t5}^{(1)}$	13.1	32.0	26.8	15.3	36.8	22.8
$\Gamma_{t1}^{(1)}$	1291	1398	1325	1220	1313	1238
$\Gamma_{t5}^{(2)}$	1765	1880	1780	1561	1673	1569
$\Gamma_{t2}$	2092	2355	2166	1851	2079	1894
$\Gamma_{t3}$	2227	2276	2220	1899	1961	1895
$\Gamma_{t1}^{(2)}$	2095	2377	2169	1854	2101	1896
$\alpha$	0.8703	0.8696	0.8719	0.8833	0.8797	0.8842

**Table E.** Magnetic susceptibility characteristics of some equiatomic uranium compounds in terms of the equations:  $\chi_m^{-1} = (\frac{A}{T} + B)^{-1} + \lambda$  and  $\chi_m = \frac{C}{T - \Theta_p}$  [79TZ].  $p_p = \sqrt{8A}$ ,  $p_o$  is the uranium magnetic moment as determined by neutron powder diffraction.

Compound	Type of magnetic order	$T_{N/C}$ [K]	$A$ [K emu/mol]	$B \cdot 10^6$ [emu/mol]	$\lambda$ [mol/emu]	$\Theta_p$ [K]	$p_p$ [ $\mu_B$ ]	$p_o$ [ $\mu_B$ ]
UOS	AF	56	0.828	490	0	0	2.57	2.0
UOSe	AF	75	0.798	540	0	0	2.53	2.2
UOTe	AF	164	0.828	420	0	0	2.57	2.0
UNSe	(F)	90	0.517	400	-80	43	2.03	—
UNTe	F	59	0.437	400	-100	44	1.87	—
UPAs	AF	264	0.386	570	-320	151	1.76	—
USbBi	F	140	1.250 <sup>1)</sup> 2.069 <sup>2)</sup>	0 <sup>1)</sup> 0 <sup>2)</sup>	-120 <sup>1)</sup> 0 <sup>2)</sup>	150 <sup>1)</sup> 0 <sup>2)</sup>	3.16 <sup>1)</sup> 4.07 <sup>2)</sup>	—
USnTe	AF	70	1.046	270	-50	52	2.89	—

<sup>1)</sup> in the range 170...330 K    <sup>2)</sup> in the range 330...900 K

**Table F.** Thermodynamic characteristics of thorium and uranium compounds AnOY (Y = S, Se) [84ABCH].

Compound	$T_N$ [K]	$C_p$ (298.15 K) [J/mol K]	$S$ (298.15 K) [J/mol K]	$S_{\text{magn}}$ [J/mol K]	$\Theta_b$ (300K) [K]	$5 < T < 13$ K	
						$\gamma$ [mJ/molK <sup>2</sup> ]	$\Theta_b$ [K]
ThOS	—	67.25	76.34	—	500	—	—
UOS	55.35	76.23	94.20	6.3	500	2.0	306
ThOSe	—	72.65	93.50	—	400	1.0	368
UOSe	69.80	82.10	108.04	5.1	400	3.1	316

**Table G.** Crystal field parameters  $B_k^q$  (in  $\text{cm}^{-1}$ ) and wavefunction coefficients  $\alpha$ ,  $\beta$ ,  $\gamma$  and  $\varepsilon$  of the crystal field levels calculated for UOY compounds ( $Y = \text{S, Se, Te}$ ) in the framework of lattice sum (LS) or nearest neighbours (NN) point-charge models with Sternheimer shielding included [84ABCH]. The so-calculated uranium ordered moment is compared with that determined by neutron powder diffraction. The wave functions considered are:

$$|\Gamma_{t5}^{(1)}\rangle = \alpha|\pm 3\rangle + \beta|\mp 1\rangle$$

$$|\Gamma_{t5}^{(2)}\rangle = \beta|\pm 3\rangle - \alpha|\mp 1\rangle$$

$$|\Gamma_{t1}^{(1)}\rangle = \varepsilon|4\rangle + \gamma|0\rangle + \varepsilon|\bar{4}\rangle$$

$$|\Gamma_{t1}^{(2)}\rangle = \frac{1}{\sqrt{2}}\gamma|4\rangle - \sqrt{2}\varepsilon|0\rangle + \frac{1}{\sqrt{2}}\gamma|\bar{4}\rangle$$

$$|\Gamma_{t2}\rangle = \frac{1}{\sqrt{2}}|4\rangle - \frac{1}{\sqrt{2}}\gamma|\bar{4}\rangle$$

$$|\Gamma_{t3}\rangle = \frac{1}{\sqrt{2}}|2\rangle + \frac{1}{\sqrt{2}}\gamma|\bar{2}\rangle$$

$$|\Gamma_{t4}\rangle = \frac{1}{\sqrt{2}}|2\rangle - \frac{1}{\sqrt{2}}\gamma|\bar{2}\rangle$$

	UOS (LS)	UOSe (NN)	UOTe (NN)
$B_2^0$	8.528	10.884	7.326
$B_4^0$	0.3651	0.4162	0.3562
$B_6^0$	0.007698	0.007510	0.006195
$B_4^4$	3.012	3.223	2.561
$B_6^4$	-0.09195	-0.08361	-0.07843
$\alpha$	0.988	0.962	0.935
$\beta$	-0.156	-0.274	-0.353
$\gamma$	0.730	0.935	1.000
$\varepsilon$	0.484	0.250	0.000
$p_o(\text{calc})$	2.32	2.16	2.00
$p_o(\text{exp})$	2 [63BBP]	2.2 [68MSTL]	2.0 [69MSL]

**Table H.** Crystal field parameters (in  $\text{cm}^{-1}$ ) obtained for UOY (Y = S, Se, Te) compounds from various ab initio crystal field models [95G]. PCM: point charge model; ECM: extended charge model; GEM: generalized electrostatic model; OVP: overlap model; REN: renormalization model; GPM: generalized perturbation model. For definitions and discussion of the results refer to the original paper.

Compound	CF parameter	PCM	ECM	GEM	OVP	REN	GPM
UOS	B20	−2168	−1886	−187	−537	−751	−938
	B40	−3027	−1143	2168	−4028	−4284	−2116
	B60	1155	−650	−3126	5516	6581	3455
UOSe	B20	−1580	−1318	−154	−468	−756	−910
	B40	−3160	−1358	1906	−4188	−4656	−2750
	B60	1120	−616	−3041	5558	6776	3735
UOTe	B20	−2536	−2363	−308	−511	−710	−1018
	B40	−3059	−1812	852	−3734	−4727	−3975
	B60	1111	40	−1507	2906	3362	1862

Note that the parameters  $B_{kq}$  (see also Tables I, Q, P) are not equal to  $B_{kq}^a$  (see Tables D, G, L, M), and the relation between them is as follows:

$$B_{20} = B_{20}^0 \frac{1}{\alpha W_{20}}$$

$$B_{40} = B_{40}^0 \frac{1}{\beta W_{40}}$$

$$B_{60} = B_{60}^0 \frac{1}{\gamma W_{60}}$$

$$B_{44} = B_{44}^4 \frac{1}{\beta W_{44}}$$

$$B_{64} = B_{64}^4 \frac{1}{\gamma W_{64}}$$

where  $\alpha$ ,  $\beta$  and  $\gamma$  are the Stevens coefficients:

$$\alpha = -0.021$$

$$\beta = -7.346 \cdot 10^{-4}$$

$$\gamma = 6.099 \cdot 10^{-5}$$

and  $W_{kq}$  are the factors:

$$W_{20} = \frac{1}{2}$$

$$W_{40} = \frac{1}{8}$$

$$W_{60} = \frac{1}{16}$$

$$W_{44} = \frac{\sqrt{70}}{8}$$

$$W_{64} = 3 \frac{\sqrt{14}}{16}$$

**Table I.** Crystal field parameters (in meV) calculated for UOY (Y = S, Se, Te) compounds by means of the perturbative ab initio method and in the shielded point charge model (PCM) [00G]. Specified are the contributions of the particular ligands ( $4O^{2-}$  and  $5Y^{2-}$ ), and the contribution of further neighbours and electrical multipoles induced on all ions (lattice). For detailed discussion see the original paper. – For definition of parameters Bkq see also remark at Table H.

Compound	CF parameter		$4O^{2-}$	$5Y^{2-}$	Lattice	Total
UOS	B20	ab initio	–26.8	–82.1	–71.4	–180.4
		PCM	–8.6	–20.4	38.9	9.9
	B40	ab initio	–516.0	165.1	–193.7	–544.5
		PCM	–427.9	71.0	30.4	–326.5
	B44	ab initio	324.2	–346.2	–97.3	–119.4
		PCM	268.9	–149.4	–53.1	66.4
	B60	ab initio	109.9	308.4	5.6	423.9
		PCM	98.1	43.3	19.7	161.2
	B64	ab initio	189.4	–75.8	–9.2	104.4
		PCM	169.1	–10.9	22.7	180.8
UOSe	B20	ab initio	–50.8	–42.7	–23.6	–117.1
		PCM	–16.8	–4.3	40.8	19.7
	B40	ab initio	–497.9	65.5	–24.5	–457.0
		PCM	–401.5	28.7	27.0	–345.8
	B44	ab initio	329.8	–311.8	–108.1	–90.1
		PCM	265.9	–114.2	–48.5	103.2
	B60	ab initio	117.9	337.7	0.9	456.5
		PCM	99.1	37.6	16.0	152.7
	B64	ab initio	188.3	135.0	23.6	76.9
		PCM	158.3	–15.0	20.8	164.1
UOTe	B20	ab initio	–114.0	–55.0	10.2	–158.8
		PCM	–38.4	2.7	52.2	16.4
	B40	ab initio	–476.0	–76.7	–51.8	–604.6
		PCM	–358.7	–16.1	33.1	–341.7
	B44	ab initio	367.3	–260.9	–141.0	–34.6
		PCM	276.8	–78.1	–38.3	160.3
	B60	ab initio	140.2	266.5	6.6	413.3
		PCM	107.9	23.3	10.9	142.2
	B64	ab initio	187.6	–161.3	44.8	71.0
		PCM	144.4	–14.8	19.5	149.1

**Table J.** AOM parameters (in meV) calculated for UOY (Y = S, Se, Te) compounds within the angular overlap model [00G]. The parameters listed correspond to the ‘local’ contributions to the crystal field potential. The ‘U<sup>4+</sup>-Y<sup>2-</sup> average’ parameters are defined by the expression  $e_{\mu} \equiv \frac{1}{5}(4e_{\mu}^{Y(1)} + 4e_{\mu}^{Y(2)})$ . The ‘ligand average’ parameters are defined as  $e_{\mu} \equiv \frac{1}{9}(4e_{\mu}^O + 4e_{\mu}^{Y(1)} + 4e_{\mu}^{Y(2)})$ . For detailed discussion see the original paper.

Compound	AOM parameter	U <sup>4+</sup> -O <sup>2-</sup>	U <sup>4+</sup> -Y <sup>2-</sup> (1)	U <sup>4+</sup> -Y <sup>2-</sup> (2)	U <sup>4+</sup> -Y <sup>2-</sup> average	Ligand average
UOS	$e_{\sigma}$	340.1	214.7	194.5	210.7	268.2
	$e_{\pi}$	210.5	98.3	86.6	95.9	146.9
	$e_{\delta}$	62.8	33.0	28.6	32.1	45.8
UOSe	$e_{\sigma}$	324.1	211.0	174.8	203.8	257.3
	$e_{\pi}$	196.5	94.6	77.3	91.1	137.9
	$e_{\delta}$	55.2	32.2	26.5	31.1	41.8
UOTe	$e_{\sigma}$	316.3	204.2	106.4	184.7	243.2
	$e_{\pi}$	185.8	100.6	47.8	90.0	132.6
	$e_{\delta}$	46.4	34.7	17.2	31.2	37.9

**Table K** see next page

**Table L.** Crystal field parameters  $B^q_k$  (in units of the Lea-Leask-Wolf parameter W) calculated for UOS in the framework of model A and B as well as within the lattice sum (LS) and nearest neighbours (NN) point-charge models [89ABCF]. For the description of the models see the original paper. For the crystal field levels schemes resulting from the models A and B see Fig. 20.

	A	B	LS	NN
$B^0_2/W$	0.100	0.100	-0.132	0.236
$10B^0_4/W$	0.196	0.065	0.293	0.221
$10^3B^0_6/W$	0.236	1.240	0.538	0.327
$10B^4_4/W$	0.667	0.625	0.486	0.622
$10^2B^4_6/W$	-0.333	-0.417	-0.695	-0.423

**Table M.** Crystal field parameters  $B^q_k$  (in meV) calculated for UOS for the paramagnetic ( $T = 65$  K) and antiferromagnetic ( $T = 30$  K) regions - model C [95ABBC]. For the description of the model see the original paper. For the crystal field levels scheme resulting from this CF model see Fig. 21.

	$T = 65$ K	$T = 30$ K
$B^0_2$	-0.330(10)	-0.288(10)
$10^2B^0_4$	0.736(10)	0.712(10)
$10^2B^0_6$	0.227(1)	0.219(10)
$B^4_4$	0.0980(20)	0.102(2)
$10B^4_6$	-0.104(1)	-0.100(1)

**Table K.** Energies (in meV) and compositions of the lowest crystal field levels having dominating  $^3H_4$  components calculated for UOY (Y = S, Se, Te) compounds from first principles [00G]. The eigenstates are presented in the  $^{2S+1}L_{J,M}$  function basis. For UOS two sets are given, which correspond to two CF models considered in the original paper (see also Figs. 22 and 23).

State	Energy	Main components
UOS (model I)		
$\Gamma_{t5}^{(1)}$	0.0	$-0.9036^3H_{4,-3} - 0.2796^1G_{4,-3} + 0.2723^3H_{4,1}$
$\Gamma_{t1}^{(1)}$	37.0	$0.9006^3H_{4,0} - 0.2552^3F_{2,0} + 0.2392^1G_{4,0} - 0.1563^3H_{4,4} - 0.1563^3H_{4,-4}$
$\Gamma_{t4}$	39.4	$-0.6498^3H_{4,-2} + 0.6498^3H_{4,2} - 0.2519^1G_{4,-2} + 0.2519^1G_{4,2} + 0.1075^3F_{4,-2} - 0.1075^3F_{4,2}$
$\Gamma_{t3}$	68.9	$0.6578^3H_{4,2} + 0.6578^3H_{4,-2} + 0.2342^1G_{4,2} + 0.2342^1G_{4,-2}$
$\Gamma_{t5}^{(2)}$	76.0	$0.8956^3H_{4,1} + 0.2881^3H_{4,-3} + 0.2797^1G_{4,1} - 0.1045^3F_{3,1}$
UOS (model II)		
$\Gamma_{t5}^{(1)}$	0.0	$-0.9073^3H_{4,-3} - 0.2701^1G_{4,-3} + 0.2230^3H_{4,1} - 0.1150^3H_{5,-3} - 0.1008^3F_{3,1}$
$\Gamma_{t1}^{(1)}$	36.1	$0.8667^3H_{4,0} - 0.2492^3H_{4,-4} - 0.2492^3H_{4,4} - 0.2418^3F_{2,0} + 0.2047^1G_{4,0}$
$\Gamma_{t3}$	73.6	$0.6611^3H_{4,-2} + 0.6611^3H_{4,2} + 0.2277^1G_{4,-2} + 0.2277^1G_{4,2}$
$\Gamma_{t4}$	82.9	$0.6273^3H_{4,-2} - 0.6273^3H_{4,2} + 0.2810^1G_{4,-2} - 0.2810^1G_{4,2} - 0.1371^3F_{4,-2} + 0.1371^3F_{4,2}$
$\Gamma_{t5}^{(2)}$	88.0	$0.8966^3H_{4,1} + 0.2604^3H_{4,-3} + 0.2797^1G_{4,1} - 0.1192^3F_{3,1}$
$\Gamma_{t2}$	171.1	$0.6476^3H_{4,-4} - 0.6476^3H_{4,4} + 0.2177^1G_{4,-4} - 0.2177^1G_{4,4} - 0.1151^3H_{4,-4} + 0.1151^3H_{4,4} - 0.1418^3H_{5,0}$
$\Gamma_{t1}^{(2)}$	200.7	$0.5997^3H_{4,-4} + 0.5997^3H_{4,4} + 0.3253^3H_{4,0} + 0.2220^3G_{4,-4} + 0.2220^3G_{4,4} + 0.14271^1G_{4,0} - 0.1076^3H_{4,-4} - 0.1076^3H_{4,4}$
UOSe		
$\Gamma_{t5}^{(1)}$	0.0	$0.9266^3H_{4,-3} + 0.2819^1G_{4,-3} - 0.1988^3H_{4,1}$
$\Gamma_{t1}^{(1)}$	44.3	$-0.9111^3H_{4,0} - 0.2435^1G_{4,0} + 0.2196^3F_{2,0} + 0.1559^3H_{4,4} + 0.1559^3H_{4,-4}$
$\Gamma_{t4}$	47.1	$0.6500^3H_{4,-2} - 0.6500^3H_{4,2} + 0.2518^1G_{4,-2} - 0.2518^1G_{4,2} - 0.1074^3F_{4,-2} + 0.1074^3F_{4,2}$
$\Gamma_{t3}$	68.9	$0.6557^3H_{4,2} + 0.6557^3H_{4,-2} + 0.2385^1G_{4,2} + 0.2385^1G_{4,-2}$
$\Gamma_{t5}^{(2)}$	73.7	$-0.9172^3H_{4,1} - 0.2895^1G_{4,1} - 0.2096^3H_{4,-3} + 0.1075^3F_{3,1}$
UOTe		
$\Gamma_{t5}^{(1)}$	0.0	$0.9439^3H_{4,-3} + 0.2945^1G_{4,-3}$
$\Gamma_{t4}$	47.6	$0.6502^3H_{4,2} - 0.6502^3H_{4,-2} + 0.2475^1G_{4,2} - 0.2475^1G_{4,-2} - 0.1032^3F_{4,2} + 0.1032^3F_{4,-2}$
$\Gamma_{t1}^{(1)}$	53.8	$-0.9209^3H_{4,0} + 0.2548^3F_{2,0} - 0.2487^1G_{4,0}$
$\Gamma_{t3}$	54.2	$-0.6554^3H_{4,-2} - 0.6554^3H_{4,2} - 0.2381^1G_{4,-2} - 0.2381^1G_{4,2}$
$\Gamma_{t5}^{(2)}$	78.3	$-0.9330^3H_{4,1} - 0.2935^1G_{4,1} + 0.1188^3F_{3,1}$



**Table N.** Energies,  $E$ , of the crystal field levels and probabilities,  $P$ , of the transitions from the ground state for UOS in the paramagnetic region ( $T = 65$  K) and at different temperatures below  $T_N$  [95ABBC]. The CF levels are defined in Table G. Also given are the values of the molecular field,  $h$ , and the uranium magnetic moment along the  $c$ -axis,  $\langle p_z \rangle$ . The energies are relative to the lowest state  $\Gamma_{t5+}^{(1)}$  of the ground doublet, split by  $h$ . For the description of the model see the original paper.

	$T = 65$ K		$T = 50$ K		$T = 40$ K		$T = 30$ K		$T = 0$ K	
	$E$	$P$	$E$	$P$	$E$	$P$	$E$	$P$	$E$	$P$
	[meV]		[meV]		[meV]		[meV]		[meV]	
$\Gamma_{t5-}^{(1)}$	—	—	5.2	0.00	8.3	0.00	9.6	0.00	10.1	0.00
$\Gamma_{t1}^{(1)}$	8.8	0.02	11.9	0.01	13.4	0.01	14.0	0.01	14.3	0.00
$\Gamma_{t2}$	73.9	1.14	74.5	1.46	74.9	2.04	75.0	2.29	75.0	2.38
$\Gamma_{t4}$	82.3	3.34	81.1	2.78	82.5	3.42	83.2	3.70	83.4	3.81
$\Gamma_{t5-}^{(2)}$	83.4	0.58	83.1	0.00	84.2	0.00	84.7	0.00	84.9	0.00
$\Gamma_{t5+}^{(2)}$	83.4	0.58	84.4	0.48	86.4	0.57	87.2	0.60	87.6	0.61
$\Gamma_{t1}^{(2)}$	88.0	1.50	88.9	0.69	91.7	0.58	92.9	0.54	93.5	0.52
$\Gamma_{t3}$	170.0	0.98	168.5	0.72	170.1	0.86	170.8	0.92	171.0	0.94
$h$ [meV]	—		0.97		1.52		1.76		1.86	
$\langle p_z \rangle$ [ $\mu_B$ ]	—		1.15		1.81		2.09		2.20	

**Table O.** Comparison of various sets of the crystal field parameters Bkq (in meV) for UOS, used for calculating the magnetic excitations spectra, the magnetic susceptibility and the Schottky heat capacity, all presented in Fig. 23 [00G]. *a*: CF parameters derived from the parameters  $B^q_k$  reported in Ref. [95ABBC] for  $T = 65$  K (see also Table M); *b*: ab initio results (see also Table I); *c*: model I; *d*: model II (see Table K). For definition of parameters Bkq and  $B^q_k$  see remark at Table H.

	<i>a</i>	<i>b</i>	<i>c</i>	<i>d</i>
B20	31.4	−180.4	−116.6	−146.5
B40	−80.2	−544.5	−566.7	−579.4
B44	−127.6	−119.4	−10.6	−38.8
B60	595.5	423.9	632.3	595.1
B64	−243.0	104.4	250.0	447.1

**Table P.** Crystal field parameters Bkq (in meV; Wybourne's notation) calculated for UOSe by means of the perturbative ab initio model and in the point charge model (PCM) [93KPGZ]. Specified are the contributions of the particular ligands and further neighbours (FN). - For definition of parameters Bkq see also remark at Table H.

		$4O^{2-}$	$5Se^{2-}$	FN	Total
B20	ab initio	−410	−940	450	−910
	PCM	−1260	−320		−1580
B40	ab initio	−3750	630	370	−2750
	PCM	−3410	250		−3160
B44	ab initio	2480	−3090	−400	−1010
	PCM	2260	−970		1290
B60	ab initio	820	2770	140	3740
	PCM	810	310		1120
B64	ab initio	1310	−1080	180	410
	PCM	1290	−120		1170

**Table R.** Coefficients of the wavefunctions of the energy levels originating from the crystal field split  $^3H_4$  ground term in UOSe derived in a perturbative ab initio approach (see Table P for the crystal field parameters and Fig. 33 for the energy levels scheme) and in a point charge model (PCM) [93KPGZ]. The meaning of  $\alpha$ ,  $\beta$ ,  $\gamma$  and  $\varepsilon$  is as defined in Table G.

Coefficient	ab initio	PCM
$\alpha$	0.1971	0.2746
$\beta$	0.9804	0.9616
$\gamma$	0.9778	0.9354
$\varepsilon$	−0.1482	0.2501

**Table S.** Hyperfine parameters of NpOS and NpOSe [85TJP1]. Magnetic split: 1 mm/s = 0.0562 MG (where  $\mu_n = 2.8$  n.m. for  $^{237}\text{Np}$ ). Electrical split: 1 mm/s = 48.02 MHz. Isomer shifts (IS) are given with respect to  $\text{NpAl}_2$ .

Compound	$T$ [K]	IS [mm/s]	$e^2qQ$ [mm/s]	$g_0\mu_n H_{\text{eff}}$ [mm/s]	Width (FWHM) [mm/s]
NpOS	4.2	−4.8(2)		1.07(4)	5.2(2)
	77	−5.0(2)			4.3(1)
NpOSe	4.2	−3.2(3)	11.6(8)	53.7(1)	3.8(4)
	77	−3.2(3)	11(1)		4.0(4)

**Table T.** Crystal field parameters  $B^q_k$  (in  $\text{cm}^{-1}$ ) calculated for NpOS and NpOSe in the point charge model (PCM) within the Russell-Saunders coupling (RS) and intermediate coupling (IC) schemes using the nearest neighbours (NN) and lattice sum (LS) approximations [89ABBB]. The Sternheimer shielding coefficients included. For details see the original paper.

		RS		IC	
		NN	LS	NN	LS
NpOS	$B^0_2$	0.4583	−0.4664	0.3116	−0.3172
	$10B^0_4$	0.8006	0.7400	0.5765	0.5328
	$10^2B^0_6$	−0.1647	−0.1875	−0.1104	−0.1256
	$B^4_4$	0.2212	0.1143	0.1593	0.0823
	$10B^4_6$	0.2116	0.2401	0.1418	0.1609
NpOSe	$B^0_2$	0.4739	−0.5434	0.3222	−0.3695
	$10B^0_4$	0.8364	0.7746	0.6022	0.5577
	$10^2B^0_6$	−0.1609	−0.1793	−0.1078	−0.1201
	$B^4_4$	0.2868	0.1912	0.2065	0.1377
	$10B^4_6$	0.1945	0.2211	0.1303	0.1481

**Table U.** Reduced crystal field parameters  $b_q^k$  calculated for NpOS and NpOSe in the refined model as compared to  $b_q^k$  obtained in the point charge model (PCM) using the intermediate coupling nearest neighbours scheme [89ABBB]. For the definitions of  $b_q^k$ 's and description of the models see the original paper. In the case of NpOS two different directions of the magnetic moments are considered:  $p \parallel c$ -axis and  $p \perp c$ -axis. For NpOSe,  $p \parallel c$ -axis was assumed, as established in neutron diffraction studies.

	NpOS			NpOSe	
	$p \parallel c$ -axis	$p \perp c$ -axis	PCM	$p \parallel c$ -axis	PCM
$b_4^0$	1.318	5.534	3.460	2.651	3.613
$b_6^0$	-3.985	-4.451	-2.782	-3.076	-2.716
$b_4^4$	1.80	15.29	9.56	9.40	12.39
$b_6^4$	68.04	57.16	35.74	44.52	32.83

**Table V.** Energies of the crystal field levels (in K) calculated for NpOS and NpOSe in the point charge model (PCM) within the Russell-Saunders coupling (RS) and intermediate coupling (IC) schemes using the nearest neighbours (NN) and lattice sum (LS) approximations as well as in the refined model (RM) [89ABBB]. The eigenstates are of two different types  $|\psi\rangle$  and  $|\phi\rangle$ :

$$|\psi_i \pm\rangle = \alpha_i \left| \pm \frac{9}{2} \right\rangle + \beta_i \left| \pm \frac{1}{2} \right\rangle + \gamma_i \left| \mp \frac{7}{2} \right\rangle, \quad i = 1, 2, 3 \text{ (3 doublets)}$$

$$|\phi_k \pm\rangle = \delta_k \left| \pm \frac{5}{2} \right\rangle + \varepsilon_k \left| \mp \frac{3}{2} \right\rangle, \quad k = 1, 2 \text{ (2 doublets)}.$$

The compositions of the PCM ground states are specified. The magnetic moment components (in  $\mu_B$ ) calculated for the ground state are given for each model. In the case of RM two different directions of the magnetic moment in NpOS were considered:  $p \parallel c$ -axis and  $p \perp c$ -axis. For NpOSe,  $p \parallel c$ -axis was assumed in RM, as established in the neutron diffraction studies. For details on all the CF models applied see the original paper.

	RM		RS		IC	
	$p \parallel c$ -axis	$p \perp c$ -axis	NN	LS	NN	LS
NpOS	$ \phi\rangle$ 0	$ \phi\rangle$ 0	$ \phi\rangle$ 0	$ \phi\rangle$ 0	$ \phi\rangle$ 0	$ \phi\rangle$ 0
	$ \psi\rangle$ 84	$ \psi\rangle$ 166	$ \psi\rangle$ 157	$ \psi\rangle$ 204	$ \psi\rangle$ 104	$ \psi\rangle$ 139
	$ \phi\rangle$ 331	$ \phi\rangle$ 279	$ \phi\rangle$ 251	$ \psi\rangle$ 300	$ \phi\rangle$ 174	$ \psi\rangle$ 205
	$ \psi\rangle$ 354	$ \psi\rangle$ 343	$ \psi\rangle$ 305	$ \phi\rangle$ 322	$ \psi\rangle$ 214	$ \phi\rangle$ 220
	$ \psi\rangle$ 641	$ \psi\rangle$ 855	$ \psi\rangle$ 771	$ \psi\rangle$ 796	$ \psi\rangle$ 534	$ \psi\rangle$ 548
			$\delta = 0.9821$	$\delta = 0.9351$	$\delta = 0.9879$	$\delta = 0.9425$
			$\varepsilon = 0.1882$	$\varepsilon = 0.3544$	$\varepsilon = 0.1552$	$\varepsilon = 0.3343$
	$p_z = 0.88$		$p_z = 1.71$	$p_z = 1.45$	$p_z = 1.85$	$p_z = 1.58$
		$p_x = 0.83$	$p_x = 0.62$	$p_x = 1.10$	$p_x = 0.54$	$p_x = 1.11$
NpOSe	$ \phi\rangle$ 0		$ \phi\rangle$ 0	$ \phi\rangle$ 0	$ \phi\rangle$ 0	$ \phi\rangle$ 0
	$ \psi\rangle$ 84		$ \psi\rangle$ 135	$ \psi\rangle$ 162	$ \psi\rangle$ 90	$ \psi\rangle$ 109
	$ \phi\rangle$ 168		$ \phi\rangle$ 241	$ \psi\rangle$ 279.9	$ \phi\rangle$ 171	$ \psi\rangle$ 193
	$ \psi\rangle$ 207		$ \psi\rangle$ 314	$ \phi\rangle$ 280.1	$ \psi\rangle$ 223	$ \phi\rangle$ 195
	$ \psi\rangle$ 537		$ \psi\rangle$ 774	$ \psi\rangle$ 779	$ \psi\rangle$ 539	$ \psi\rangle$ 538
			$\delta = 0.9992$	$\delta = 0.9717$	$\delta = 1.0000$	$\delta = 0.9780$
			$\varepsilon = 0.0400$	$\varepsilon = 0.2364$	$\varepsilon = 0.0046$	$\varepsilon = 0.2084$
	$p_z = 1.68$		$p_z = 1.81$	$p_z = 1.66$	$p_z = 1.92$	$p_z = 1.79$
			$p_x = 0.13$	$p_x = 0.76$	$p_x = 0.02$	$p_x = 0.72$

**Table W.** Thermodynamic characteristics of uranium compounds UAsY (Y = S, Se, Te) [80BLWZ].

Compound	$T_C$ [K]	$C_p$ (298.15K) [J/mol K]	$S$ (298.15K) [J/mol K]	$S_{\text{magn}}$ [J/mol K]	5 < $T$ < 300 K		1.5 < $T$ < 15 K	
					$\gamma$ [mJ/molK <sup>2</sup> ]	$\Theta_b$ [K]	$\gamma$ [mJ/molK <sup>2</sup> ]	$\Theta_b$ [K]
UAsS	125.8	80.90	114.5	1.80	0	291	23.5	308
UAsSe	108.8	83.48	131.9	0.63	39.7	231	41	233
UAsTe	62.8	81.32	139.9	2.75	32.5	217	56	238.5

**Table X.** Magnetic data for the UAs<sub>2-x</sub>Se<sub>x</sub> system derived from neutron powder diffraction [73LMZL].

x	Type of magnetic order	$T_N$ [K]	$T_C$ [K]	$p_o$ (4 K) [ $\mu_B$ ]
0.00	AF-II	283		1.6(1)
0.50	AF-II	160(5)		1.35(8)
0.60	AF <sup>1)</sup>	170(5)		
0.65	F <sup>2)</sup>		107(5)	
0.75	F		95(3)	1.1(1)
1.00	F		113(3)	1.5(1)

<sup>1)</sup> Distinct traces of F phase<sup>2)</sup> Distinct traces of AF phase**Table Y.** Magnetic susceptibility characteristics of hexagonal uranium compounds U<sub>2</sub>N<sub>2</sub>X and U<sub>2</sub>N<sub>2</sub>Y in terms of the equations:  $\chi_m^{-1} = (\frac{A}{T} + B)^{-1} + \lambda$  and  $\chi_m = \frac{C}{T - \Theta_p}$  [74TZ].  $p_p = \sqrt{8A}$ ,  $p_o$  is the uranium magnetic moment as determined by neutron powder diffraction,  $p_s$  is the uranium saturation magnetic moment as determined by bulk magnetization measurement [75LZLT, 78ZT].

Compound	$T_N$ ( $T_C$ ) [K]	$A$ [K emu/mol]	$B \cdot 10^6$ [emu/mol]	$\lambda$ [mol/emu]	$\Theta_p$ [K]	$p_p$ [ $\mu_B$ ]	$p_o$ ( $p_s$ ) [ $\mu_B$ ]
U <sub>2</sub> N <sub>2</sub> P	363	0.350	320	390	156	1.67	1.65
U <sub>2</sub> N <sub>2</sub> As	400	0.320	330	505	195	1.60	1.60
U <sub>2</sub> N <sub>2</sub> Sb	(166)	0.395	330	360	161	1.78	(1.80)
U <sub>2</sub> N <sub>2</sub> Bi	(154)	0.426	370	300	144	1.85	(1.95)
U <sub>2</sub> N <sub>2</sub> S	231	0.270	420	-180	45	1.47	1.45
U <sub>2</sub> N <sub>2</sub> Se	243	0.560	430	-120	-65	2.12	2.25
U <sub>2</sub> N <sub>2</sub> Te	(71)	0.878	148	52	46	2.65	2.50 (2.78)